

NATIONAL CENTRE FOR NUCLEAR RESEARCH

DOCTORAL THESIS

**The star formation activity of galaxies:
multi-wavelength constraints based on
Spectral Energy Distribution fitting**

Author:
Gabriele Riccio

Supervisor:
Katarzyna Małek
Auxiliary supervisor:
Junais

*A thesis submitted in fulfillment of the requirements
for the degree of Doctor of Philosophy*

in the

Astrophysics Division
Fundamental Research Department



May 8, 2023

Declaration of Authorship

I, Gabriele Riccio, declare that this thesis titled, “The star formation activity of galaxies: multi-wavelength constraints based on Spectral Energy Distribution fitting” and the work presented in it are my own. I confirm that:

- This work was done wholly or mainly while in candidature for a research degree at the National Centre for Nuclear Research.
- Where any part of this thesis has previously been submitted for a degree or any other qualification at the National Centre for Nuclear Research or any other institution, this has been clearly stated.
- Where I have consulted the published work of others, this is always clearly attributed.
- Where I have quoted from the work of others, the source is always given. With the exception of such quotations, this thesis is entirely my own work.
- I have acknowledged all main sources of help.
- Where the thesis is based on work done by myself jointly with others, I have made clear exactly what was done by others and what I have contributed myself.

Signed:

Date:

Abstract

The star formation activity of galaxies: multi-wavelength constraints based on Spectral Energy Distribution fitting

Gabriele RICCIO

From the beginning of the 20th century, the study of galaxies' properties has become an important matter among astronomers, and uncovering their formation and evolution is considered one of the greatest challenges in modern astronomy. It is known that galaxies may have very different properties, starting from morphology (e.g., spiral, elliptical, irregular) to the dust or gas content, the mass of the stellar component, the rate at which stars are formed, and so on. For this reason, it is crucial to fully understand the processes that lead to the observed galaxy emission by estimating and analyzing their main physical parameters. The goal of my scientific project is to uncover, with a multi-wavelength approach, the physical properties of galaxies, especially their star formation activity, and test the reliability of their estimation with Spectral Energy Distribution (SED) fitting methods. Such an investigation is crucial nowadays, with new upcoming large galaxy surveys, which are constantly expanding in the number of observations, but only sometimes gather the information necessary to constrain the star formation activity straightforwardly. This work mainly focuses on the ultraviolet (UV)-infrared (IR) spectrum, as it is widely demonstrated to trace the formation of young stars, and on the X-ray regime, which presents promising results in constraining physical parameters such as star formation rate (SFR) and stellar mass (M_{star}).

The first part of this work focuses on how the upcoming optical Legacy Survey of Space and Time (LSST) data from the Vera C. Rubin Observatory can be employed to constrain the physical properties of normal star-forming galaxies (Chapter 2). It presents a catalog of simulated LSST observations and uncertainties of $\sim 50\,000$ real galaxies, within the redshift range $0 < z < 2.5$, from the COSMOS and ELAIS-N1 fields of the *Herschel Extragalactic Legacy Project* (HELP) survey. I chose HELP as a reference survey because, at the moment, it provides the biggest dataset with the best mid-infrared (MIR) and far-infrared (FIR) data available, necessary for the estimation of the galaxies' physical properties. The actual estimation was performed by fitting the SED of galaxies using the Code Investigating GALaxy Emission (CIGALE). We compared the properties, such as the SFR, the M_{star} , and the dust luminosity (L_{dust}), obtained from the fit of the observed multi-wavelength photometry (from the UV to the FIR) to those obtained from the simulated LSST optical measurements alone. This work shows a clear difference for the dust-related parameters (SFR, dust luminosity, dust mass), highly dependent on redshift. The stellar masses estimated based on the LSST measurements are instead in good agreement with the full UV to far-IR estimates. To correct the difference, I find it necessary to have prior knowledge of the sample, such as employing auxiliary rest-frame MIR observations, simulated UV observations, or the far-UV attenuation (A_{FUV})- M_{star} relation.

The second part of this work, Chapters 3 and 4, focuses on the properties of X-ray binaries (XRBs), how they affect the total X-ray luminosity of a galaxy, and what kind of correlation exists between their integrated X-ray luminosity and galaxies' physical properties. In fact, it is well known that the XRBs emission traces a galaxy's

stellar population and was found to scale with the SFR and the M_{star} of the host galaxy.

First, I study the physical properties of the population of low-mass X-ray binaries (LMXBs) hosted by globular clusters (GCs) in the Fornax galaxy cluster. The data used are a combination of *VLT Survey Telescope* (VST) and *Chandra* observations. I found that, as was already observed for the innermost regions of galaxies, LMXBs tend to form in red and bright GCs, as these properties are, respectively, a proxy of the total number of stars and of the compactness of the globular cluster. These characteristics are essential for the formation of LMXBs in such environments. However, I find that the likelihood of a red GC hosting an LMXB decreases with galactocentric distance. Still, it remains approximately constant for the blue GC population. Regarding the X-ray properties of the hosted LMXBs (GC-LMXBs), I find a difference in the X-ray luminosity function (XLF) between the intra-cluster and host-galaxy samples. I further investigated the spectral properties of the GC-LMXBs, and found a puzzling difference in the X-ray hardness ratio of the two populations, where the intra-cluster GC-LMXBs appear to have harder spectra than the host-galaxy objects. The same trend was found between the blue and red samples of GC-LMXBs. This trend was never observed before. Furthermore, I find that the total X-ray luminosity of the galaxies is dominated by the field LMXBs, with little contribution from the GC-LMXBs. This suggests that the well-known scatter of the X-ray luminosity-SFR scaling relation at low SFR is mainly driven by field LMXBs.

Second, this work presents measurements of the relation between X-ray luminosity and star formation activity for a sample of normal galaxies spanning the redshift range between 0 and 0.25. I use data acquired by the next-generation X-ray observatory SRG/eROSITA, for the Performance-and-Verification-Phase program named the eROSITA Final Equatorial Depth Survey (eFEDS). Making use of a wide range of ancillary data, spanning from the UV to MIR, I estimate the SFR and M_{star} of 888 galaxies, using the CIGALE code. In order to study sources with negligible X-ray components attributable to active galactic nuclei (AGN), I perform the identification of AGN systems making use of the observed fluxes in the X-ray, optical, and MIR range, and using the results from the SED fitting. I validate the results from the SED fitting and the AGN identification using FIR data from HELP and spectral lines from MPA/JHU catalog based on the *Sloan Digital Sky Survey* DR7 release. To isolate the contribution of High-mass X-ray binaries (HMXBs) and LMXBs, that scale with the SFR and stellar mass, respectively, I subtract the contribution of hot gas, coronally active binaries, and cataclysmic variables from the total X-ray emission. I divide our sample into star-forming (SFGs) and quiescent, according to their position on the main sequence relation. I find a linear correlation between the X-ray luminosity and the SFR for our sample of SFGs. However, I find this relation to be strongly biased by the X-ray luminosity completeness limit of the eFEDS survey. Correcting for completeness, I find the calibrated L_x -SFR to be consistent with the literature. The X-ray emission of normal galaxies is not only dominated by the contribution of HMXBs but also by the contribution of LMXBs, which is expected to scale with the M_{star} . It was shown that the ratio of HMXB-to-LMXB emission is sensitive to the specific SFR (sSFR), defined as SFR/M_{star} . To consider this, I quantify the scaling factors $\alpha \equiv L_{x,LMXB}/M_{star}$ and $\beta \equiv L_{x,HMXB}/SFR$. Even correcting for completeness, I find a consistently higher contribution of LMXBs than observed in previous works. I conclude that, due to completeness issues, without performing a stacking process it is not possible to employ eFEDS data to study the redshift evolution of the LMXBs and HMXBs contributions to the scaling relation. Nevertheless, I find our sources

to largely scatter from the expected L_X/SFR vs $s\text{SFR}$ relation at high redshift. I discuss the dependence of the scatter on stellar mass, metallicity, and globular cluster content of the galaxy.

In summary, this Ph.D. thesis presents important results on using broadband observations from next-generation instruments to estimate the star-formation activity of galaxies. I have shown that LSST survey data can, when used without additional observations at other wavelengths, give misleading estimates of the SFR. A correction of this estimate can be obtained with additional observations in the ultraviolet range or at least one detection coming from the infrared spectrum. In addition, another possibility to correct the SFR parameter is to use the relation describing the dust attenuation in the far-UV and the galaxy's stellar mass. Also, using information from a much shorter wavelength, namely the X-ray range, I achieve important results in the study of X-ray binaries. I show that this type of radiation carries hints of the galaxy's stellar mass and star-formation activity through components derived from low- and high-mass X-ray binaries. In this paper, however, I have shown that the most recent survey in the X-ray regime, the eROSITA survey, can empirically scale the relation between X-ray luminosity and galaxy star-formation activity but is burdened by incompleteness for normal star-forming galaxies, i.e. without strong contributions from AGN.

Streszczenie

The star formation activity of galaxies: multi-wavelength constraints based on Spectral Energy Distribution fitting

Gabriele RICCIO

Od początku XX wieku analiza własności galaktyk stała się niezwykle ważną kwestią badawczą astronomów. Obecnie próba zrozumienia powstania różnych typów galaktyk i ich ewolucji uważane jest za jedno z największych wyzwań współczesnej astronomii. Wiadomo, że galaktyki mogą mieć bardzo różne właściwości, począwszy od morfologii (np. budowa spiralna, eliptyczna, nieregularna) po zawartość pyłu lub gazu, masę składnika gwiazdnego, czy tempo powstawania gwiazd. Z tego powodu, aby dobrze scharakteryzować galaktykę, kluczowe jest pełne zrozumienie zachodzących w niej procesów fizycznych prowadzących do obserwowanej emisji w różnych zakresach fal elektromagnetycznych. Dzięki połączeniu obserwacji z procesami zachodzącymi w galaktyce (czy też w jej otoczeniu, interakcjami z inną galaktyką) możliwe jest oszacowanie i analiza głównych parametrów fizycznych opisujących daną galaktykę. Jest to jeszcze ważniejsze obecnie, w czasach wielkich przeglądów nieba, które ustawicznie zwiększają liczbę obserwacji, zarówno znanych galaktyk, jak i takich obserwowanych po raz pierwszy. Niestety w większości przypadków zebrane dane nie wystarczają, aby w pełni opisać najważniejsze parametry fizyczne obserwowanych galaktyk bądź też tylko niektóre z nich. W szczególności niezwykle rzadko przeglądy te gromadzą informacje niezbędne do bezpośredniego oszacowania tak wymagającego parametru, jakim jest aktywność formowania się gwiazd w galaktykach. Celem mojej pracy doktorskiej jest wyznaczenie podstawowych własności fizycznych galaktyk, w tym ich aktywności gwiazdotwórczej, za pomocą obserwacji galaktyk w różnych długościach fal elektromagnetycznych. Równocześnie moim celem jest wyznaczenie wiarygodności ich oszacowania za pomocą modelowania widmowego rozkładu energii (*ang. spectral energy distribution, SED*) galaktyk. W swojej pracy koncentruję się głównie na zakresie długości fal od ultrafioletu (UV) do podczerwieni (*ang. infrared, IR*), gdyż właśnie w tym zakresie można bezpośrednio śledzić młode obszary gwiazdotwórcze w galaktykach, oraz emisję pyłu, który częściowo przysłania te obszary, pochłaniając promieniowanie pochodzące z młodych, masywnych gwiazd. Promieniowanie to jest następnie reemitowane przez pył w zakresie IR. Dodatkowo skupiam się również na widmie w zakresie rentgenowskim, który daje obiecujące wyniki w wyznaczaniu parametrów fizycznych, takich jak tempo powstawania nowych gwiazd (*ang. star formation rate, SFR*) i masę gwiazdową galaktyki (M_{star}).

Pierwsza część poniższej pracy koncentruje się na tym, w jaki sposób dane z nadchodzącego Optycznego Przeglądu Przestrzeni i Czasu (*ang. Legacy Survey of Space and Time, LSST*) z Obserwatorium Vera C. Rubin mogą zostać wykorzystane do wyznaczenia własności fizycznych normalnych galaktyk gwiazdotwórczych (Rozdział 2). W tej części przedstawiłem przygotowany przeze mnie katalog symulowanych obserwacji i niepewności dla przeglądu LSST dla $\sim 50\,000$ prawdziwych galaktyk, w zakresie przesunięcia ku czerwieni $0 < z < 2.5$. Galaktyki te obserwowane były na polach COSMOS i ELAIS-N1, a ich obserwacje w zakresie od UV do dalekiej podczerwieni zostały zebrane, ujednolicone i opublikowane w przeglądzie *Herschel*

Extragalactic Legacy Project (HELP). Wybraliśmy galaktyki obserwowane przez HELP jako dane referencyjne, ponieważ obecnie przegląd ten zapewnia największy zbiór danych galaktyk z dedykowaną redukcją podczerwonych map z przeglądu *Herschel*: od średniej (MIR) do dalekiej (FIR) podczerwieni. Pomiary te są niezwykle istotne do oszacowania właściwości samego pyłu oraz właściwości fizycznych galaktyk związanych z pyłem. Ponieważ przegląd LSST będzie zbierał dane jedynie w pasmach optycznych, analiza symulowanych obserwacji LSST galaktyk obserwowanych w pełnym widmie od UV do FIR pozwala na porównanie wyznaczonych właściwości fizycznych w przypadku tylko-LSST i LSST–dane podczerwone. Główna analiza została przeprowadzona poprzez dopasowanie SED galaktyk za pomocą Code Investigating GALaxy Emission (CIGALE) - programu umożliwiającego modelowanie widma energetycznego galaktyk. Porównywałem właściwości takie jak SFR, M_{star} i jasność pyłu (L_{dust}), otrzymane z dopasowania obserwowanej fotometrii wielofalowej (od UV do FIR) z tymi samymi parametrami uzyskanymi jedynie na podstawie symulowanych pomiarów optycznych LSST. Wyniki mojej pracy pokazują wyraźną różnicę oszacowań dla głównych parametrów fizycznych związanych z pyłem (SFR, jasność pyłu, masa pyłu), dodatkowo silnie zależnych od przesunięcia ku czerwieni. Masy gwiazdowe oszacowane na podstawie pomiarów LSST są natomiast zgodne z szacunkami uzyskanymi na podstawie zakresu UV–FIR. Aby skorygować różnice zależne od pyłu, niezbędne jest posiadanie informacji o detekcji w MIR, obserwacje w zakresie UV bądź zastosowanie relacji pomiędzy tłumieniem pyłu w dalekim UV (FUV) a masą gwiazdową galaktyki ($A_{FUV}-M_{star}$).

Druga część tej pracy, opisana w Rodziałach 3 i 4, koncentruje się na właściwościach rentgenowskich układów podwójnych (*ang. X-ray binaries, XRB*), ich wpływie na całkowitą jasność galaktyki w zakresie promieniowania rentgenowskiego oraz na tym, jaki rodzaj korelacji istnieje między ich zintegrowaną jasnością w zakresie rentgenowskim, a właściwościami fizycznymi galaktyk. W rzeczywistości dobrze wiadomo, że emisja XRB śledzi populację gwiazd w galaktyce i stwierdzono, że skaluje się z parametrami SFR i M_{star} galaktyki macierzystej.

W pierwszym kroku mojej analizy zbadałem właściwości populacji podwójnych układów rentgenowskich o małej masie (*ang. low-mass X-ray binaries, LMXB*) znajdujących się w gromadach kulistych (*ang. globular clusters, GCs*) w gromadzie galaktyk Fornax. Użyte dane są kombinacją obserwacji pochodzących z instrumentów *VLT Survey Telescope (VST)* i *Chandra*. Na podstawie dokładnej analizy wykazałem, że, jak już zaobserwowano w przypadku najbardziej wewnętrznych obszarów galaktyk, LMXB mają tendencję do tworzenia się w czerwonych i jasnych GCs, ponieważ te właściwości są odpowiednio przybliżeniem całkowitej liczby gwiazd w gromadzie kulistej. Jednak zauważyłem, że prawdopodobieństwo, że czerwony GC będzie gospodarzem LMXB, maleje wraz z odległością galaktocentryczną. Prawdopodobieństwo to pozostaje jednak stałe dla niebieskiej populacji GC. Analizowałem również właściwości rentgenowskie galaktyk, w których znajdują się LMXB (GC-LMXB). Znalazłem różnicę w funkcji jasności promieniowania rentgenowskiego (*ang. X-ray luminosity function, XLF*) pomiędzy próbkami wewnątrz gromady i próbkami galaktyk macierzystych. Sprawdziłem również właściwości widmowe GC-LMXB i znalazłem zagadkową różnicę w stosunku "twardości" dwóch populacji, gdzie GC-LMXB wewnątrz gromady wydają się mieć twardsze widma niż obiekty galaktyki macierzystej. Ten sam trend jest widoczny między niebieskimi i czerwonymi próbkami GC-LMXB. Nigdy wcześniej nie zaobserwowano takiej zależności. Co więcej, całkowita jasność galaktyk w zakresie rentgenowskim jest zdominowana przez LMXB znajdujące się w polu galaktycznym, z niewielkim udziałem GC-LMXB. Sugeruje to, że dobrze znane rozproszenie relacji Lx-SFR przy niskich wartościach SFR jest

napędzane głównie właśnie przez LMXB znajdujące się w polu.

Równocześnie, łącząc oba tematy przedstawione powyżej, niniejsza praca w swojej ostatniej części przedstawia pomiary zależności między jasnością promieniowania rentgenowskiego a aktywnością gwiazdotwórczą dla próbki normalnych galaktyk obejmujących zakres przesunięcia ku czerwieni między 0 a 0,25. W tej części skupiłem się na danych pochodzących z obserwatorium rentgenowskiego nowej generacji SRG/eROSITA na potrzeby programu Performance-and-Verification-Phase o nazwie eROSITA Final Equatorial Depth Survey (eFEDS). Korzystając z szerokiego zakresu danych pomocniczych, od UV do MIR, oszacowałem parametry SFR i M_{star} dla 888 galaktyk, ponownie używając programu CIGALE. W celu zbadania źródeł o znikomej składowej X związanej z aktywnymi jądrami galaktycznymi (AGN) zidentyfikowałem układy AGN wykorzystując detekcje w zakresie promieniowania X, optycznym i MIR oraz wykorzystując wyniki modelowania SED. Dodatkowo potwierdziłem wyniki dopasowania SED i identyfikację AGN za pomocą danych FIR ponownie pochodzących z przeglądu HELP oraz analizy linii widmowych otrzymanych z katalogu MPA/JHU w oparciu o wydanie *Sloan Digital Sky Survey* DR7. Aby wyizolować wkład układów podwójnych rentgenowskich o dużej masie (*ang. High mass X-ray binaries*, HMXB) i LMXB, które skalują się odpowiednio z SFR i masą gwiazdową, wyekstrachowałem z całkowitej emisji promieniowania rentgenowskiego udział gorącego gazu, aktywnych układów podwójnych i zmiennych kataklizmicznych. Podzieliłem próbkę na galaktyki aktywne (*ang. star forming galaxies*, SFG) i pasywne gwiazdotwórczo, zgodnie z ich pozycją w relacji SFR- M_{star} . Jak już zaobserwowano w poprzednich pracach, istnieje liniowa korelacja między jasnością promieniowania rentgenowskiego, a SFR dla próbki SFG. Jednak z mojej analizy wynika, że ta zależność jest silnie obciążona przez niekompletność przeglądu eFEDS. Uwzględniając w analizie kompletność próbki, wyznaczona przeze mnie relacja Lx-SFR jest bardziej zgodna z tą studiowaną poprzednio w literaturze. Dodatkowo emisja promieniowania rentgenowskiego w normalnych galaktyk jest zdominowana nie tylko przez wkład HMXB, ale także przez wkład od LMXB, który, jak się oczekuje, skaluje się wraz z M_{star} . W swojej pracy pokazałem, że stosunek emisji HMXB do LMXB jest wrażliwy na specyficzny SFR, zdefiniowany jako SFR/M_{star} . Aby to uwzględnić, określiłem ilościowo współczynniki skalowania relacji $\alpha \equiv L_{x,LMXB}/M_{star}$ i $\beta \equiv L_{x,HMXB}/SFR$. Nawet poprawiając kompletność, uzyskałem konsekwentnie wyższy wkład LMXB niż obserwowany w poprzednich pracach. Z mojej analizy wynika, że ze względu na problemy z kompletnością przeglądu eFEDS nie jest możliwe zbadania ewolucji przesunięcia ku czerwieni wkładów pochodzących od LMXB i HMXB w relacje skalowania bez dodawania poszczególnych (tzw. stackowania). Niemniej jednak pojedyncze źródła z badanej próbki w dużej mierze rozpraszają się od oczekiwanej relacji Lx / SFR w funkcji sSFR przy wysokim przesunięciu ku czerwieni. W pracy skupiłem się na omówieniu wielkości tego rozproszenia od masy gwiazdowej, metaliczności czy zawartości gromad kulistych w galaktyce.

Podsumowując, praca doktorska przedstawia ważne wyniki dotyczące wykorzystania obserwacji szerokopasmowych pochodzących z instrumentów nowej generacji do oszacowania aktywności gwiazdotwórczej galaktyk. Wykazałem, że dane pochodzące z przeglądu LSST mogą, używane bez dodatkowych obserwacji w innych długościach fal, mylnie szacować tempo tworzenia nowych gwiazd. Korektę tego oszacowania możemy uzyskać przy włączeniu dodatkowych obserwacji w zakresie ultrafioletowym bądź przynajmniej jednej obserwacji pochodzącej z zakresu

podczerwieni. Dodatkowo, inną możliwością korekcji parametru SFR jest skorzystanie z relacji opisującej attenuację pyłu w zakresie FUV i masy gwiazdowej galaktyki. Sprawdziliśmy również możliwość użycia do szacowania parametru SFR informacji pochodzącej ze znacznie krótszej długości fali, a mianowicie z zakresu promieniowania rentgenowskiego. Ten typ promieniowania również niesie ze sobą wskazówki dotyczące zarówno masy gwiazdowej jak i aktywności gwiazdotwórczej galaktyki poprzez składowe pochodzące z podwójnych układów rentgenowskich o małej i wysokiej masie. W pracy jednak wykazałem, że najnowszy przegląd w zakresie promieniowania X, eROSITA, może być użyty do empirycznego skalowania zależności pomiędzy jasnością promieniowania X, a aktywnością gwiazdotwórczą galaktyki, jednak obciążony jest niekompletnością dla normalnych galaktyk tworzących gwiazdy, bez silnego wkładu pochodzącego od AGN.

Acknowledgements

I would like to thank my supervisor, Prof. Katarzyna Małek, for giving me the opportunity to improve myself during my Ph.D study. I would also like to thank my colleagues Dr. Mederic Boquien and Prof. Maurizio Paolillo for the insightful comments and valuable scientific discussions. But most importantly, I would like to thank my friend Misha Hamed for accompanying me in these 4 difficult years.

Contents

| | |
|--|-------------|
| Declaration of Authorship | iii |
| Abstract | v |
| Streszczenie | ix |
| Acknowledgements | xiii |
| 1 Introduction | 1 |
| 1.1 The Extra-Galactic Universe: a "relatively" new field | 2 |
| 1.2 Star formation rate and Initial Mass Function | 3 |
| 1.3 Star formation rate history | 5 |
| 1.4 The multi-wavelength picture of galaxies | 6 |
| 1.4.1 X-ray regime: compact objects and diffuse hot ISM | 7 |
| X-ray binaries: contribution from different stellar populations | 8 |
| Old XRB population: LMXBs | 9 |
| Young XRB population: HMXBs | 11 |
| 1.4.2 UV, optical and NIR: stellar emission | 14 |
| 1.4.3 MIR and FIR indicators: dust and PAH | 17 |
| Extinction | 17 |
| Attenuation | 19 |
| Dust emission | 20 |
| 1.4.4 Fitting of the spectral energy distribution | 22 |
| Results of the SED fitting: physical properties | 24 |
| 1.4.5 This Thesis | 25 |
| 2 Preparing for LSST data: Estimating the physical properties of $z < 2.5$ main-sequence galaxies | 27 |
| 2.1 Abstract | 27 |
| 2.2 Introduction | 28 |
| 2.3 Data | 30 |
| 2.3.1 ELAIS N1 field | 30 |
| 2.3.2 COSMOS field | 31 |
| 2.3.3 Total sample | 31 |
| 2.4 Method: SED fitting, starbursts, and outlier detection | 32 |
| 2.4.1 SED fitting with CIGALE | 32 |
| 2.4.2 Selection of starburst galaxies | 34 |
| 2.4.3 Selection of passive galaxies | 35 |
| 2.4.4 AGN contribution | 36 |
| 2.4.5 Outlier selection | 37 |
| 2.4.6 Final sample | 37 |
| 2.5 Estimation of the LSST physical properties | 37 |
| 2.5.1 Estimating LSST-simulated data and uncertainties | 38 |

| | | |
|--|--|------------|
| 2.5.2 | Fiducial parameters and LSST data alone | 39 |
| 2.5.3 | Fiducial parameters, LSST, and ancillary data | 43 |
| 2.6 | Testing different input parameters in CIGALE | 44 |
| 2.6.1 | Dust emission and mass | 44 |
| 2.6.2 | Dust attenuation laws and star formation history | 46 |
| 2.7 | Application of the $A_{FUV}-M_{star}$ relation to correct for the SFR overesti- mation | 47 |
| 2.8 | Conclusions | 49 |
| 2.9 | Appendix | 51 |
| 2.9.1 | Outlier selection | 51 |
| 2.9.2 | AGN selection | 52 |
| 2.9.3 | Scatter of the MS | 53 |
| 3 | Properties of low-mass X-ray binaries in Fornax globular clusters | 55 |
| 3.1 | Abstract | 55 |
| 3.2 | Introduction | 56 |
| 3.3 | Dataset | 57 |
| 3.3.1 | Optical data | 57 |
| 3.3.2 | X-ray data | 61 |
| 3.4 | Identification of X-ray sources in GCs | 62 |
| 3.5 | Properties of GC-LMXBs | 64 |
| 3.5.1 | Optical properties of the host GCs | 64 |
| 3.5.2 | X-ray properties of the GC-LMXB | 66 |
| 3.6 | Summary and conclusions | 72 |
| 4 | X-ray luminosity - star formation rate scaling relation: constraints from the eROSITA Final Equatorial Depth Survey (eFEDS) | 77 |
| 4.1 | Abstract | 77 |
| 4.2 | Introduction | 78 |
| 4.3 | Data and sample selection | 79 |
| 4.4 | Methodology | 81 |
| 4.4.1 | SED fitting | 81 |
| Star formation history and SSP | 81 | |
| Dust attenuation and emission | 82 | |
| AGN and X-ray emission | 83 | |
| 4.4.2 | Identification of AGN systems | 83 |
| 4.5 | SFR estimates and reliability check | 86 |
| 4.5.1 | Mock analysis | 86 |
| 4.5.2 | SFR estimates with FIR data | 86 |
| 4.5.3 | Spectral counterpart and BPT diagram | 87 |
| 4.5.4 | Galaxies distribution on the SFR- M_* relation | 89 |
| 4.6 | Subtraction of other contributions to the total X-ray luminosity | 90 |
| 4.6.1 | Quiescent galaxies | 91 |
| 4.6.2 | Star forming galaxies | 91 |
| 4.6.3 | AGN contamination to the total X-ray luminosity | 92 |
| 4.7 | Lx-SFR relation | 94 |
| 4.8 | Lx-sSFR relation | 97 |
| 4.9 | Summary and conclusions | 101 |
| 5 | Summary | 105 |

Bibliography

List of Figures

- 1.1 Tuning fork diagram representing Hubble’s morphology classification. Credits: University of Iowa. 3
- 1.2 SFR- M_{star} relation at $1.5 < z < 2.5$. The red-filled circles, cyan squares, black-filled circles, and black dots represent four different samples of galaxies, observed by *Herschel*-PACS over the COSMOS and GOODS fields. The solid black line represents the MS for SFGs at $z = 2$ calibrated by (Daddi et al., 2007). Dotted and dashed lines mark respectively the loci 10 and 4 times above the MS. 4
- 1.3 SFR density estimated using FUV+IR rest-frame measurements as a function of redshift. Credits: Madau et al. (2014) 6
- 1.4 Multi-wavelength picture of the Andromeda galaxy, from radio to the X-ray. Credits: ESA / NASA. 7
- 1.5 Evolution of an XRB population formed from a single-burst population of stars. Top panel: specific bolometric X-ray luminosity, i.e., luminosity per unit M_{star} , as a function of the population’s age. The HMXBs evolution is presented as a blue dotted line while the LMXBs’ one as red long-dashed line. Bottom panel: XRB evolution for the cases of metallicities $Z = 0.1 Z_{\odot}$ (green short-dashed) and $Z = 1.5 Z_{\odot}$ (magenta dot-dashed) compared to solar. Credits: Fragos et al. (2013) 9
- 1.6 The combined XLFs of LMXBs in different environments plotted in the cumulative form. The solid black line represents the XLF of field LMXBs. The red dashed line picture the XLF of GC-LMXBs, while the blue dotted line is the XLF of LMXBs restricted to the nucleus of the galaxy. The shaded areas around the curves show 1σ statistical uncertainty. Credits: Zhang et al. (2011) 10
- 1.7 Number of sources with luminosity $L_x > 10^{37}$ erg/s and their collective X-ray luminosity versus M_{star} . Circles represent the early-type galaxies, while triangles are the late-type galaxies. The solid lines represent the fitted linear relations. Credits: Gilfanov (2004) 11
- 1.8 Left panel: Scaling relation between the X-ray luminosity in the 0.5-8 KeV band as a function of the SFR estimated with UV and IR indicators. Credits: Mineo et al. (2014). Right panel: Same relation using H_{α} based SFR. The thick points indicate the median X-ray luminosity in each SFR bin. The dashed line shows the relation of Mineo et al. (2014) which is clearly steeper than the trend shown in the data (grey dashed-dotted line). The right panel of this figure shows the residuals with respect to the best-fit linear relation. Credits: Kouroumpatzakis et al. (2020). 13

| | | |
|------|--|----|
| 1.9 | X-ray luminosity in the 0.5-7 KeV band per unit SFR as a function of the specific SFR (SFR/M_{star}). Black circles represent the sources detected in the full band (0.5-7 KeV). Green circles are the sources also observed in the hard band (2-7 KeV) while pink circles are upper limits. The solid curve represents the best-fit solution to Eq. 1.1. the long-dashed blue curve represents the mean value found by Mineo et al. (2014). Credits: Lehmer et al. (2016). | 14 |
| 1.10 | Integrated emission of SSPs at a fixed solar metallicity. The numbers specify the assumed age of the modeled SSP in Gyr. Credits: Bruzual et al. (2003). | 15 |
| 1.11 | Dark nebula Barnard 68 in the MW. The stars behind the nebula are not visible due to the extinction of the dust in the cloud. When observed in the IR, it is possible to uncover the underlying stellar content. Credits: ESO | 17 |
| 1.12 | Comparison between the Extinction (left panel) and Attenuation (right panel) scenario. | 18 |
| 1.13 | Extinction curves for the MW and the Small and Large Magellanic Clouds. A bump at 217.5 nm is observed probably due to the presence of graphite or Polycyclic Aromatic Hydrocarbons (PAH). | 18 |
| 1.14 | Comparison between different attenuation laws (Calzetti et al. 2000, Charlot et al. 2000, Lo Faro et al. 2017) normalized at $0.5\mu m$. Credits: Hamed et al. (2023). | 20 |
| 1.15 | Example of the SED of a galaxy observed by Herschel. The best-fit SED model is plotted in black while the intrinsic model without dust extinction is plotted in blue. Red dots represent the observed fluxes. The green line represents the spectral features. Credits: Timmons et al. (2015). | 21 |
| 1.16 | Left panel: Illustration of different PAH molecules. Right panel: Principal spectral feature of PAHs in the mid-IR spectrum. Credits: Draine (2003) | 22 |
| 1.17 | Example of a fit from the X-ray to the IR performed by CIGALE. The blue solid line represents the AGN emission, the orange solid line represents the galaxy emission, and the black solid line is the total AGN+galaxy SED. Credits: Yang et al. (2022) | 24 |
| 1.18 | Comparison of SFRs of star-forming galaxies derived from SED fitting to SFRs from the DR7 MPA/JHU catalog. The blue dashed line is the best-fit relation, the yellow solid line represents the 1:1 relation, and the white solid line is a comparison with the literature. Credits: Salim et al. (2016) | 25 |
| 2.1 | <i>left panel</i> : Example of the sSFR distribution of ELAIS N1 galaxies in the redshift range $1 < z < 1.5$ obtained with the delayed SFH plus an additional burst. The orange line represents the Gaussian fit, and the dashed black line corresponds to the division of starburst (SB galaxies are located on the right side of the line) and MS galaxies. The division is located 3σ away from the centre of the Gaussian. <i>Right panel</i> : MS distribution for the same redshift bin. Magenta circles represent SB galaxies selected from the sSFR distribution shown in the left panel. The dashed black line represents the Speagle et al. (2014) MS. | 35 |

| | | |
|-----|---|----|
| 2.2 | sSFR distribution in four different redshift bins obtained with delayed SFH plus an additional burst. Open histograms are the galaxy distributions (MS+SB) derived in this work, the dashed black line is the division between SBs (right side of the line) and MS (left side of the line) in our sample, and the cyan full histograms represent the simulated SB sample from B17. The division is located at about 3σ from the Gaussian centre. The sample is the same as for Fig. 2.1, but the binning is different. | 36 |
| 2.3 | Redshift distribution of ELAIS-N1 and COSMOS samples based on the approach of Duncan et al. (2018). | 38 |
| 2.4 | Magnitude errors vs observed apparent magnitudes for simulated LSST observations from the ELAIS N1 sample. Simulations are cut to the maximum LSST limit. The choice to vary simulation parameters allows us to obtain different errors for similar magnitude values, as we would expect in the case of real observations. The brightest end we reached is 13 mag, but for clarity of the plot, we cut it at 21 mag. | 39 |
| 2.5 | Comparison of SEDs evaluated for the same object at $z \sim 1$ using the full UV-to-IR observations (<i>left panel</i>) and the LSST optical bands alone (<i>right panel</i>). The blue square represents the observed fluxes, and the red dots represent the fluxes predicted by the model. The magenta lines delimit the division between optical and IR bands, which is taken into account by CIGALE. The IR emission is not constrained for the LSST estimate. | 40 |
| 2.6 | Main-sequence (SFR vs M_{star}) relation for the ELAIS N1 and COSMOS fields in four redshift bins. In blue we show the LSST-like sample, and in black the real sample. The solid black line represents the MS by Speagle et al. (2014), and the dashed lines mark the loci two times above and below the MS. This plot shows a clear SFR overestimate obtained using LSST bands alone, which tends to disappear at higher redshift ranges. | 41 |
| 2.7 | Ratios of different physical properties obtained from fitting the simulated LSST data alone and from the UV-FIR SED (e.g. $SFR_{ratio} = SFR_{LSST}/SFR_{UV-FIR}$) as a function of redshift for the ELAIS N1 and COSMOS fields. The properties obtained from the UV-FIR SED fitting are considered as the true values. From the upper left panel we show clockwise the SFR, M_{star} , L_{dust} , and M_{dust} comparisons. The dashed lines represent polynomial fits performed on the samples. The points are the median values in each redshift bin, with the median absolute deviation as errors. A ratio equal to zero corresponds to a perfect agreement between the estimates obtained based on the LSST-like sample and the real values. The distributions calculated for ELAIS N1 and COSMOS are comparable within the errors. | 42 |
| 2.8 | LSST coverage of an example SED at different redshifts indicated in the panel. | 43 |

| | | |
|------|---|----|
| 2.9 | <i>Upper left panel:</i> SFR ratio, defined as in figure 2.7, estimated with LSST observations alone (red) and with LSST+IRAC observations (blue). The two samples disagree at low redshift, but the comparison improves at high redshift, highlighting the redshift dependence of the results. With the addition of MIR observations, the LSST-only estimates are consistent with the UV-IR estimates. <i>Upper right panel:</i> Same comparison, but adding FIR SPIRE observations. In this case we did not fully remove the overestimation, which highlights that the problem lies in the lack of rest-frame MIR data. <i>Lower left panel:</i> Same as in the other panels, but adding GALEX observations. We obtain a slight decrease in the overestimation. For this comparison we considered the $\sim 3\,000$ objects that have a counterpart in the GALEX database. <i>Lower right panel:</i> M_{dust} ratio evaluated with LSST observations alone (red) and with LSST+SPIRE observations (blue). The results are consistent with the ‘real’ ratio with a very low scatter. | 45 |
| 2.10 | SFR overestimation as a function of redshift for the Charlot et al. (2000) (red) and Calzetti et al. (2000) (cyan) attenuation laws. | 46 |
| 2.11 | A_{FUV} as a function of stellar mass estimated from the UV-FIR SED fitting (blue density plot) compared with the A_{FUV} estimated by employing M_{star} from the relation of Bogdanoska et al. (2020). | 48 |
| 2.12 | Difference between A_{FUV} estimated from $A_{FUV}-M_{star}$ relations: Bogdanoska et al. (2020) (green) and Eq. 2.2 with the coefficients reported in Table 2.5 (blue) and A_{FUV} estimated from the UV-FIR SED fitting as a function of redshift. | 49 |
| 2.13 | SFR ratio, defined as in Fig. 2.7, as a function of redshift. The result from the SED fitting employing LSST data alone is shown in red. Green and blue lines represent results from the SED fitting, adding as prior the A_{FUV} from the relations of Bogdanoska et al. (2020) and Eq. 2.2, respectively. | 50 |
| 2.14 | Outlier selection. Comparison of $L_{dust,IR}$ and $L_{dust,all}$ (<i>upper panel</i>), and $M_{star,OPT}$ and $M_{star,all}$ (<i>bottom panel</i>). L_{dust} inconsistent objects are represented as magenta stars, and full blue stars correspond to the M_{star} outliers. Grey circles represent objects with a consistent estimate of the L_{dust} and M_{star} parameters. Inside each panel we present an example SED of the respective outliers represented with a black star. | 51 |
| 2.15 | IRAC color-color diagrams for the ELAIS N1 (left column) and COSMOS (right column) fields. The AGNs (magenta points) are selected following the criteria described in Donley et al. (2012) (upper row, black line) and Stern et al. (2005) (lower row, black line). | 52 |
| 2.16 | AGN redshift distribution for the full sample of ELAIS N1 +COSMOS fields. | 53 |
| 2.17 | SFR ratio, defined as in Fig. 2.7, estimated with LSST data alone (red) and LSST plus simulated GALEX observations ($GALEX_{true}$, in blue). Differently from the result shown in Fig. 2.9, in this case we are able to correct the overestimation, underlining the effect that high-quality UV observations would have on the SFR estimate, when available for the entire sample. | 54 |

| | | |
|------|---|----|
| 2.18 | Intrinsic scatter of our objects around exemplar MS compared with the results found in previous works. Red and green points represent the scatter of our objects from the Speagle et al. (2014) and Whitaker et al. (2017) MS, respectively, blue points represent the results found in Pearson et al. (2018), and grey stars, triangles, and diamonds represent the results presented in Speagle et al. (2014). | 54 |
| 3.1 | Spatial distribution of the GCs (grey points) and the X-ray sources (red crosses) centered on NGC1399. The solid black circles represent bright galaxies in the cluster from Ferguson (1997). The size is proportional to their effective radii. The dashed line highlights the FoV of <i>Chandra</i> observations. | 58 |
| 3.2 | Luminosity function in <i>g</i> band for the sample of candidate GCs. The dashed black line corresponds to the expected theoretical GC luminosity function (with values $\mu = 24$ and $\sigma = 1.4$). | 60 |
| 3.3 | $g - i$ color distribution of GC candidates in the central square degree of the Fornax cluster. The smooth solid black, red, and blue lines show the GMM model for the total, red, and blue populations. | 61 |
| 3.4 | Mean values calculated by the GMM for different distances from each galaxy in terms of R_{eff} for red and blue GCs, and the separation performed by the GMM. The error bars correspond to the standard deviation of the mean. | 62 |
| 3.5 | Cumulative X-ray luminosity function for the sources from the catalog of Jin et al. (2019) and for the CSC catalog. The shaded region represents the 1σ error. | 63 |
| 3.6 | Spatial distribution of intra-cluster (cyan crosses) and host-galaxy (magenta crosses) GC-LMXBs. Cluster galaxies are solid black circles, and the sizes are proportional to their effective radii. The dashed circle shows the $6 R_{eff}$ distance from the galaxy center. The dashed line depicts the FoV of the <i>Chandra</i> observations. | 65 |
| 3.7 | Fraction of XGC as a function of the distance in units of R_{eff} for the total, red, and blue sample of GCs. The fraction is defined as the number of total, red, or blue XGC divided by the respective total number of GCs in the distance bin. The distances on the X-axis are from the nearest galaxy to the object. | 65 |
| 3.8 | Magnitude in <i>g</i> band as a function of the distance in terms of R_{eff} . Grey circles and triangles represent red and blue GCs, respectively. Black crosses are GCs that host an LMXB. Dashed lines represent the mean <i>g</i> magnitude of the GC in each distance range for the red and blue sample. The dashed lines show a computer cut of the <i>g</i> magnitude at $g < 23.5$. | 66 |
| 3.9 | Fraction of GCs hosting LMXBs as a function of luminosity. The different types of lines correspond to different galactocentric distances. The magnitude range is restricted to $g \leq 23.5$. The fraction is defined as the number of XGCs divided by the number of GCs in the magnitude bin. The result for the inner region agrees with the results obtained in Paolillo et al. (2011). These authors covered almost the same FoV with <i>HST</i> . | 67 |

| | | |
|------|---|----|
| 3.10 | Left panels: Magnitude distribution of GCs hosting (grey shaded) and GCs without (black line) LMXBs in intra-cluster space (upper panel) and in the host-galaxy environment (lower panel). Right panels: Color distribution of GCs hosting (grey shaded) and GCs without (black line) LMXBs in intra-cluster space (upper panel) and in the host-galaxy environment (lower panel). | 67 |
| 3.11 | Cumulative X-ray luminosity function for the host-galaxy and intra-cluster sample of GC-LMXBs. The solid lines represent the completeness-corrected LFs, and the dotted lines show the observed LFs. The shaded region represents the 1σ error. | 69 |
| 3.12 | Cumulative X-ray luminosity functions comparison. <i>Upper panel:</i> red and blue samples of GC-LMXB. Lines and shaded areas are represented as in Figure 3.11. <i>Bottom panel:</i> completeness-corrected luminosity functions for red and blue intra-cluster and host-galaxy sources separately. | 69 |
| 3.13 | X-ray luminosity as a function of distance from each galaxy. Grey dots represent the whole sample of X-ray sources. Blue triangles and red crosses represent the respective GC-LMXBs. The mean errors in each X-ray luminosity order of magnitude are shown in black. | 70 |
| 3.14 | Left panel: Cumulative X-ray luminosity function for field and GC-LMXBs. The solid lines represent the completeness-corrected LF for the sample of GC-LMXBs, and the dotted lines show the observed LFs. The shaded region represents the 1σ error. Right panel: X-ray luminosity in the 0.5-8 KeV band in function of the distance from the nearest galaxy. Blue points represent the GC-LMXBs, while grey stars the field LMXBs. The dashed lines represent the median value of the X-ray luminosity in each bin of distance, with the shaded region representing the 1σ dispersion | 71 |
| 3.15 | Hardness ratios between host-galaxy (grey) and intra-cluster (black) GC-LMXBs. The error bar is the median value of the errors associated with the HR of the sources. | 72 |
| 3.16 | Hardness ratios between red (grey) and blue (black) GC-LMXBs. The error bar is the median value of the errors associated with the HR of the sources. | 73 |
| 3.17 | Hardness ratio as a function of the distance for field X-ray objects (upper panel) and GC-LMXBs (bottom panel) with counterparts in the CSC catalog. Black dots represent the HR estimates in the CSC catalog, and grey triangles show the HR we used. Dashed green and magenta lines again represent the mean value in each distance bin. | 73 |
| 4.1 | Exemplary SED fitted for an object at $z = 0.32$, adopting the procedure described in Section 4.4. The black solid line represents the total modeled spectrum, the red solid line the dust emission, the yellow solid line the attenuated stellar emission, the orange solid line the AGN emission and the dashed blue line the unattenuated stellar emission. The observed fluxes employed for the fitting are represented as purple empty circles, while the modeled fluxes are the red-filled circles. The bottom panel shows the residuals of the fit. | 82 |

- 4.2 Left panel: Optical r-band AB magnitude vs the X-ray flux for the final selected sample. Diagonal lines indicate a constant flux ratio between the r-band and X-ray. Right panel: WISE1-WISE2 color vs WISE2-band VEGA magnitude. The lines represent the MIR WISE selection criteria, 95% reliability (solid line), 90% reliability (dashed black line) 75% reliability (dashed green), respectively. Black circles represent the WISE-selected AGNs in this work. For all panels, the grey circles represent the normal galaxies, the red circles the X-ray luminosity selected AGN, blue circles the K band selected AGNs. . . . 85
- 4.3 X-ray luminosity vs redshift for the selected final sample. The dashed black line indicates $L_x = 3 \times 10^{42}$ erg/s. The solid black line represent the eFEDS sensitivity limit of $f_{limit} = 6.5 \times 10^{-15}$ erg s⁻¹cm⁻² Brunner et al. (2022). Grey and white circles represent AGN and normal galaxies respectively for the final selected sample. 85
- 4.4 Comparison between the true value of the SFR provided by the best-fit model for the mock catalog (x-axis) and the value estimated by the code (y-axis). The Pearson product-moment correlation coefficient is given as the 'r' value. The black line corresponds to the 1:1 relation, while the red dashed line is the regression line with the equation given in the legend. 86
- 4.5 Left panel: Comparison between the SFR evaluated with data up to WISE (y-axis) and SFR estimated adding SPIRE FIR data (x-axis). The black solid line corresponds to the 1:1 relation, red dashed line to the linear fit of the data. Right panel: Comparison between $frac_{AGN}$ parameter estimated by the two runs. The solid line corresponds to the 1:1 relation. 88
- 4.6 Left panel: Comparison between the SFR evaluated with the SED fitting up to WISE (y-axis) and SFR estimated using H_α lines (x-axis). The black solid line corresponds to the 1:1 relation, red dashed line to the linear fit of the data. Right panel: BPT diagram for the sources having spectral counterparts. The solid line delimits the division between SFG, AGNs, and composite. For both panels, the blue dots represent the SFGs, yellow triangles the LINERs, green pentagons the Seyferts and purple crosses the composite galaxies 89
- 4.7 Left panel: 724 galaxies from the final sample shown in in the SFR- M_* plot. Blue points represent the SFGs, red points show the location of the quiescent galaxies, and grey points the AGNs classified as described in section 4.4.2. Right panel: the same plot showing star-forming and quiescent galaxies color-coded by the $f_{0.25\mu m}$ parameter. The solid black line represents the MS from Aird et al. (2017) at redshift 0.15 (the mean redshift of our sample of normal galaxies). The dashed line shows the threshold 1.3 dex above and below the MS. . . . 90
- 4.8 X-ray luminosity distribution over redshift for our sample of quiescent (left panel) and SFGs (right panel). The uncorrected values are presented as solid circles while the change in the L_x after the correction is shown by a solid line. 92

| | | |
|------|---|-----|
| 4.9 | Mock analysis for the $L_{AGN,0.2-2.3keV}$ (top panel), $L_{XRB,0.2-2.3keV}$ (middle panel) and $fracAGN_{0.2-2.3keV}$ (bottom panel). The Pearson product-moment correlation coefficient is given as an 'r' value. The black solid line corresponds to the 1:1 relation, while the red dashed line is the regression line with the equation given in the legend. The magenta star represents the superposition of 44 sources. The red stars are the sources having $f_{0.25\mu m} > 0.1$ from the initial run described in Section 4.4. | 95 |
| 4.10 | X-ray luminosity as a function of the SFR. Black dots represent the full sample of SFGs. Red crosses and blue triangles represent the sources having <i>Herschel</i> and SDSS counterparts respectively. The solid black line represents the fit of our sample of data, while Lehmer et al. (2016) scaling relation is represented by the dashed black line. The size of the dots is proportional to the redshift of the sources. | 96 |
| 4.11 | X-ray luminosity per SFR unit ($L_{0.2-2.3keV}/SFR$) in the function of redshift for the sample of SFGs. The solid black line represents the X-ray luminosity sensitivity limit of the eFEDS sample, rescaled by the max value of the SFR in each interval. | 97 |
| 4.12 | Right panel: Cumulative X-ray luminosity function for the sample of SFGs. The black solid line represents the completeness-corrected XLF, while the dotted line shows the observed XLF. The shaded region represents the 1σ error. Right panel: X-ray luminosity in the 0.2-2.3 keV band as a function of the SFR. The size of the dots is proportional to the redshift of the sources. The red line shows the linear fit corrected for completeness, while the black line is the observed fit already shown in Fig. 4.10. | 98 |
| 4.13 | X-ray luminosity in the 0.2-2.3 keV band scaled by the SFR in the function of the sSFR for the full sample of normal galaxies, selected in this work, both quiescent (red dots) and SFGs (blue dots). The solid black line represents the observed fit of the sources, while the red solid line represents the completeness corrected fit. Lehmer et al. (2016) fit at $z = 0.09$ is pictured as a black dashed line, with the shaded region representing the 3σ dispersion. The size of the dots scales with the redshift of the sources. | 99 |
| 4.14 | X-ray luminosity in the 0.2-2.3 keV band scaled by the SFR in the function of the sSFR for the full sample of normal galaxies divided into three redshift bins. The points size is scaled by the M_{star} , The solid black lines represent the observed fit of the sources, while the red dashed lines represent Lehmer et al. (2016) relation estimated at the mean value of the redshift for each bin. The shaded red region represents the 3σ dispersion. | 100 |
| 4.15 | X-ray luminosity in the 0.2-2.3 keV band scaled by the SFR as a function of the sSFR, color-coded by the number of globular clusters. The lines are the same as Fig. 4.14. | 102 |

List of Tables

| | | |
|-----|---|----|
| 2.1 | List of filters for the ELAIS N1 and COSMOS fields. | 32 |
| 2.2 | Input parameters for the code CIGALE. | 33 |
| 2.3 | Total number of galaxies and SB percentage for ELAIS and COSMOS fields in each redshift range. | 35 |
| 2.4 | Number of AGNs selected based on the MIR features for the ELAIS N1 and COSMOS fields. The last column shows the total number (and percentage) of AGNs in the full sample. | 37 |
| 2.5 | Obtained a and b coefficients from fitting Eq. 2.2 in the four redshift bins. | 48 |
| 3.1 | Selection criteria for the GC candidates. | 59 |
| 3.2 | List of galaxies from Ferguson (1997) in the <i>Chandra</i> FoV. | 59 |
| 4.1 | List of photometry available as ancillary data for the X-ray sources. The number of detections corresponds to the sample of 888 galaxies initially selected as normal galaxies. | 81 |
| 4.2 | Input parameters for the code CIGALE. | 84 |
| 4.3 | Summary of the fits performed on the completeness corrected eFEDS sample. | 99 |

Alla mia famiglia, Palu', Malu' e Fiolu', per avermi sempre sostenuto con ogni mezzo disponibile. Tutto cio' che sono lo devo a voi.

1

Introduction

Understanding the laws governing the universe has always fascinated mankind since ancient times. Babylonians were the first to recognize that astronomical phenomena are periodic and to apply mathematics to them. Greeks developed the first geometrical, three-dimensional model to explain the apparent motion of the planets, and Egyptians found the position of Sirius, who they believed was the ancient god Anubis. Still, all of them came to their conclusions by observing the same thing, light. Stars emit light that may reach our telescopes, allowing us to study the history of galaxies and uncover the mysteries of galaxies' evolution, dark matter, and dark energy. Also, this light may change the physical condition of the galaxy from which it originated, affecting its chemical abundances and ionizing the neutral gas. For this reason, the formation of stars is of crucial importance in the fields of galaxy evolution and cosmology. The detailed physics of the formation of individual stars is still the subject of study, as it depends on several processes (such as gravity collapse, magnetic field, cooling and heating of the matter) and occurs on different scales (from nuclear reactions in the core to the collapse of enormous molecular clouds). But, focusing on galactic scales, star formation is a global process that plays the fundamental role of transforming interstellar gas into stars and metals. For these reasons, it is crucial to determine the Star Formation Rate (SFR) of galaxies with high reliability. In this Thesis, I will present different methods to estimate or correct the SFR using prior information about the galaxy's main properties.

Galaxies are complex structures formed not only by stars but by many other components such as stellar remnants, the interstellar medium (ISM), dust, and supermassive black holes (Walcher et al. 2011, Conroy 2013). A detailed study and understanding of each of them is required to fully comprehend the processes that lead to the observed galaxy emission. In the past decades, we saw an explosion of data from local and distant Universe across the entire electromagnetic spectrum. This gave us the opportunity to explore the physics of various galaxy components and to constrain important physical parameters (e.g. SFR, stellar mass, ISM, and dust properties) needed to understand the formation and evolution of galaxies. Nevertheless, both processes still remain largely unknown (Mo et al. 2010, Jones et al. 2015).

The availability of multi-wavelength data, together with the advances reached in each field of astrophysics, led to the development of a variety of methods for estimating the galaxies' physical properties. For example, the SFR can be estimated using many different approaches, using both photometric and spectroscopic information: from the study of specific spectral lines to the use of the ultraviolet (UV) and

infrared (IR) continuum, up to the use of empirical relations (e.g. X-ray luminosity-SFR). As we will discuss in the following sections, each method has advantages and disadvantages. Therefore, developing new methodologies is of crucial importance, especially in anticipation of future large surveys, such as the optical *Legacy Survey of Space and Time* (LSST), the IR *James Webb Space Telescope* (JWST) or the X-ray eROSITA.

For this reason, one method that has recently acquired popularity, due to its reliability when multi-wavelength data are available, is to model the Spectral Energy Distribution (SED) of the galaxy (Walcher et al. 2011).

In this work, we test the reliability of the physical parameters estimated using SED fitting methods, with a view to future surveys such as LSST and eROSITA. We then study possible relations between these parameters and the total X-ray output of the galaxy. We begin with the discussion on galaxies physical properties, focusing mainly on their star formation activity. Then we discuss the SED fitting as an important tool to estimate galaxies' properties. We finally show how to use LSST data to estimate the parameters, followed by a study of the X-ray properties of the population of X-ray binaries in galaxies.

1.1 The Extra-Galactic Universe: a "relatively" new field

Nowadays, it is common knowledge of the existence of other galaxies outside our own, the Milky Way (MW), but this was not the case for our great-grandparents. In fact, the concept of the extra-Galactic universe was taken into account only in the 1920s, when Edwin Hubble succeeded in resolving one field in the Andromeda Galaxy (M31) into a collection of distinct stars. Some of the stars proved to be variables of a type similar to those found by Shapley in globular clusters. Measurements of the properties of these variables yielded estimates of their distances. As it turned out, the distance to M31 put it well outside the confines of even Shapley's huge model of the MW and proved that M31 must be an independent system of stars. With this discovery, Hubble inaugurated the era of extra-Galactic astronomy. From that moment, the newborn field of extra-Galactic astrophysics developed considerably, improving our knowledge of the properties of galaxies and proving that they can be very different from each other. Hubble himself would then portray the morphological differences of galaxies through a classification scheme, still widely used, known as the tuning fork diagram (Hubble 1926, shown in Fig. 1.1). According to this diagram, galaxies can be divided into spiral, elliptical, lenticular and irregular. Ellipticals and lenticulars are known as early-type galaxies (E0-E7, S0), while spiral and irregular are known as late-type galaxies (classes Sa, Sb, Sc, Irr <). Early-type galaxies usually have smooth and spheroidal shapes, consisting of an old stellar population, and undergo a quiescent period of star formation (Holmberg 1958). Late-type galaxies, instead, are characterized by circular discs containing spiral arms and a central nuclear bulge. In the spiral arms, an active star formation boosts the stellar content of the galaxy.

Soon after, it would be discovered the connection between the visual shape of galaxies and their fundamental properties, such as colors, masses, luminosity and gas content (Kennicutt 1992, Roberts et al. 1994). For example, observing two or more color filters made it possible to divide galaxies into red and blue. Early-type galaxies, being mainly dominated by old stellar populations and undergoing a quiescent state with no significant star formation, appears as significantly red (Renzini 2006, Kormendy et al. 2009, Graham 2013). Late-type galaxies, instead, being dominated by young and hot stars, appear significantly bluer (Graham 2013, Dobbs et al.

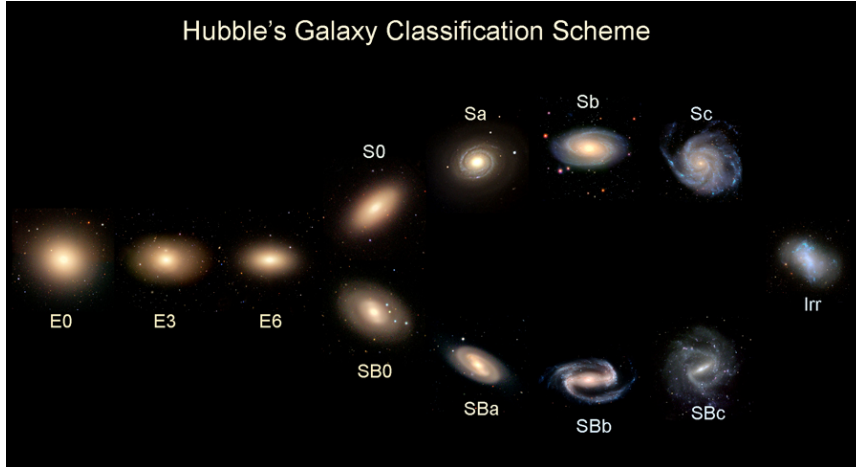


FIGURE 1.1: Tuning fork diagram representing Hubble's morphology classification. Credits: University of Iowa.

2014). They also differ in total stellar mass (M_{star}), with early-type galaxies being on average much more massive than spirals. Nevertheless, the most crucial difference between elliptical and spiral galaxies is their star formation activity, quantified with the SFR parameter (Kennicutt 1998, Brinchmann et al. 2004). In this Thesis, we will focus mainly on the connection between SFR and other properties of galaxies. Therefore it is important to give an adequate background on this parameter, why is important, and how to measure it.

1.2 Star formation rate and Initial Mass Function

The SFR is by definition the rate at which materials such as gas and dust are turned into stars. The unit of choice is usually solar masses per year ($M_{\odot} yr^{-1}$). It is also useful to define the SFR density, in volume or surface density, respectively ψ_{SFR} (in $M_{\odot} kpc^{-3} yr^{-1}$) and Σ_{SFR} (in $M_{\odot} pc^{-2} yr^{-1}$). These quantities, when normalized over large scales, are often used by cosmologists to show the cosmic history of star formation. Also, the surface densities can be easily related to quantities, such as the surface brightness, that we can directly observe from galaxies. The above definition describes an SFR that is instantaneous. However, determining instantaneous SFR is very difficult from the observational point of view as most SFR tracers are associated with a timescale on which they are sensitive. For example, the SFR indicator that traces the smallest timescales ($\sim 1-10$ Myr) is the H_{α} emission line. The connection between the H_{α} luminosity and the SFR is well known (Kennicutt 1998) since young stars tend to ionize the neutral hydrogen surrounding the star-forming regions, whose recombination generates the H_{α} emission. Also, other indicators such as the UV and IR continuum trace the SFR at timescales of 10-100 Myr. In the next sections, I will introduce some of the most common SFR indicators and discuss more in detail the ones used in this work. I previously introduced that galaxies can be classified according to various parameters, such as their morphology, color, and of course, their efficiency to form stars. The position of the galaxies in the famous SFR- M_{star} plot, known as main sequence (MS, Speagle et al. 2014; Schreiber et al. 2015; Pearson et al. 2018), highlights the existence of three primary populations: "starburst" (SB), star-forming (SFGs) and quiescent galaxies. The first group, composed

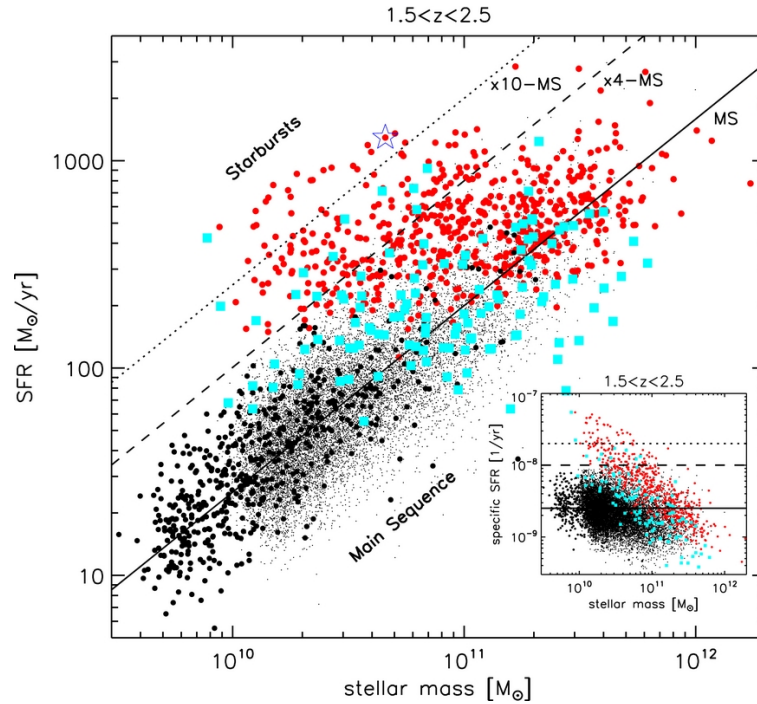


FIGURE 1.2: SFR- M_{star} relation at $1.5 < z < 2.5$. The red-filled circles, cyan squares, black-filled circles, and black dots represent four different samples of galaxies, observed by *Herschel*-PACS over the COSMOS and GOODS fields. The solid black line represents the MS for SFGs at $z = 2$ calibrated by (Daddi et al., 2007). Dotted and dashed lines mark respectively the loci 10 and 4 times above the MS.

of SB galaxies, is characterized by a violent phase of star formation, probably triggered by catastrophic events. The second group, known as ‘star-forming’ galaxies, exhibit continuous star formation processes, less violent than SB, and possess late-type morphologies with prominent disk components (Faber et al. 2007, Noeske et al. 2007, Blanton et al. 2009, Aird et al. 2017). The last group is composed of ‘quiescent’ galaxies that have early-type morphologies and passively evolving stellar populations. Figure 1.2 shows a famous example of the MS for a sample of galaxies at redshift $1.5 < z < 2.5$ (Rodighiero et al. 2011). It is possible to notice that the majority of the galaxies tend to follow a linear relation, marked as a solid black line in the plot. These galaxies are classified as SFGs. The outliers of this relation are instead classified as SB or quiescent galaxies, depending on whether they are above or below the relation. At the present state-of-art, the boundaries dividing these classifications are not precisely defined, as different authors use different methods to distinguish SBs from MS galaxies (i.e. Rodighiero et al. 2011, Speagle et al. 2014, Elbaz et al. 2018, Donevski et al. 2020). No universally accepted method exists. Nevertheless, it is generally accepted that the three groups differ in regard to their physical properties, such as star formation history, dust and gas content, and others (Silverman et al. 2018, Elbaz et al. 2018). In this work, we will make extensive use of these classifications, which is why such a long introduction was needed.

A last introductory point, important for what follows, is to define the Initial Mass Function (IMF) as the distribution of masses of stars when they are formed in the galaxy. This is, of course, extremely important, as the type of chemical elements produced by the evolution of stars and their emitted light strictly depends on the initial mass of the star, given by the IMF. So, precisely, the IMF is defined as a mass function

$\xi(m)$ describing the number of stars per mass interval dm , i.e. $dN = \xi(m)dm$. There exist several IMF laws (Salpeter 1955; Miller et al. 1979; Chabrier 2003), describing in a different way the galaxies' stellar content. Steeper laws picture galaxies with much less massive and old stellar content, while flatter laws predict the presence of a bigger population of young and massive stars.

To summarize, the SFR describes the amount of material going into stars, while the IMF describes the statistical distribution in stellar masses of this material.

1.3 Star formation rate history

SFR and IMF are the essential building blocks to uncover the formation and evolution of galaxies but to understand how to use this information it is necessary to describe how the Universe works on cosmological scales. Electromagnetic radiation is the only source of information when observing galaxies. However, any description that involves distances traveled by light highly depends on the cosmological framework adopted. The standard model universally accepted in the scientific community is the Λ -cold dark matter model (Λ CDM). The Λ CDM is a model based on the equations of general relativity (Einstein 1916), that describes the Universe energy content as dominated by dark energy (69.2%) and dark matter (26.8%), while baryons represent only the 4%. This model predicts that the Universe is expanding in an accelerated manner, as confirmed by the observations (Riess et al. 1998, Perlmutter et al. 1999). A factor of great importance to galaxy evolution studies is that this model considers the radiation traveling at a constant speed of $c = 3 \times 10^8 \text{ m s}^{-1}$. Therefore, the light emitted by far objects would take time to arrive to the detectors, allowing us to study the properties of these objects in their early life. Also, the radiation traveling toward us is "stretched" to longer wavelengths due to the expansion of the Universe, in a phenomenon called redshift. As the expansion speed-up farther we travel in the Universe, the redshift phenomena is higher at earlier epochs, serving as a time reference for events. Thus, observing galaxies at different redshifts can give us information about their evolution through cosmic time.

It was shown that galaxies' star formation activity evolves with cosmic time (Madau et al. 2014). Figure 1.3 shows the cosmic evolution of the SFR density, as a function of redshift, estimated from UV and far-infrared (FIR) data, under the assumption of a universal IMF. This astonishing result provides a remarkably consistent picture of the cosmic star formation history (SFH): a rising phase of formation between $3 \lesssim z \lesssim 8$, scaling as $\psi \propto (1+z)^{-2.9}$, a peak of SF activity between $z = 2$ and 1.5, when the universe was ~ 3.5 Gyr old, followed by a gradual decline to present days, dropping exponentially with an e-folding timescale of 3.9 Gyr. A consistent picture is emerging, the Universe was a much more active place in the past: stars formed at a peak rate of almost nine times higher than is seen today. Considering that the evolution of galaxies strictly depends on their star formation activity, this could suggest that the galaxies we observe in the Local Universe are at the end of their life, giving us insight into their formation and evolutionary channels. For this reason, precise estimates of the SFR are of crucial importance, especially for the high redshift regime. Also, Fig. 1.3 shows a decrease in the number of observations going to higher redshift. This trend can be explained by considering that the intensity of the radiation decreases as a function of the inverse of the luminosity distance it has traveled toward us. This implies a decrease in the flux density measured by the instruments that go as $\propto (1+z)^{-4}$. Thus, it is extremely challenging to detect the

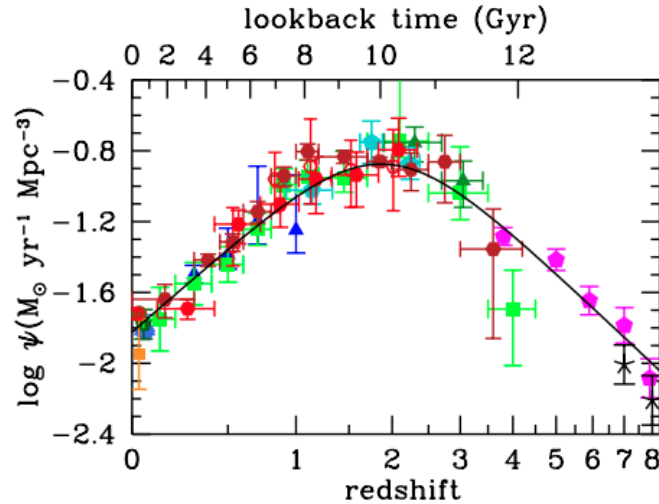


FIGURE 1.3: SFR density estimated using FUV+IR rest-frame measurements as a function of redshift. Credits: Madau et al. (2014)

most distant galaxies, resulting in little information on the SF activity in the earlier epochs.

The advent of the next generation high resolution and sensitivities telescopes, such as LSST (Ivezić et al. 2019), JWST (Gardner et al. 2006), and EUCLID (Euclid Collaboration et al. 2022) will allow the study of high redshift objects with a resolution never achieved before, making the need for reliable estimates of SFR all the more compelling. In the next sections of this introductory chapter I will introduce the intrinsic multi-wavelength nature of galaxies, and what are the milestones achieved so far in estimating SFR. I will then conclude the chapter by describing the advantages and possibilities of the SED fitting method, comparing it with other SFR indicators.

1.4 The multi-wavelength picture of galaxies

Figure 1.4 shows the view of the spiral galaxy Andromeda observed in different bands of the electromagnetic spectrum. As I will explain in the next sections, each band gives insight into specific physical processes that, due to their nature, emit radiation in that specific range of wavelengths. For example, IR and UV images distinguish in detail the arms of the Andromeda spirals, which is where star formation events occur. However, these spirals are not as detailed when observed in the visible spectrum, but it is possible to notice a diffused white light coming from the center of the galaxy, where the oldest stellar population resides. Instead, in the X-ray spectrum, the galaxy is completely unrecognizable and it is possible to observe only a few point-like sources together with a diffuse light distributed around the center. These emissions are contributions from high-energy binary systems and diffused hot ISM. These, considering that these are just some of the processes that contribute to the total emission of a galaxy, their intrinsic differences make clear the need for multi-band studies to have a complete and detailed view of these objects.

A representation of the complexity of the electromagnetic spectrum emitted by galaxies can be achieved by sampling their SED. The SED is the distribution of the energy output of the galaxy over a wide range of wavelengths and it is usually constructed using broadband photometric (and sometimes spectroscopic) observations. All the physical processes responsible for the emission of galaxies, including the

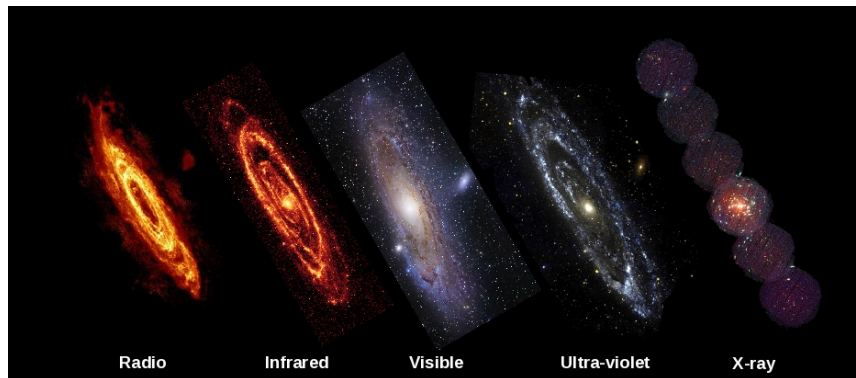


FIGURE 1.4: Multi-wavelength picture of the Andromeda galaxy, from radio to the X-ray. Credits: ESA / NASA.

ones mentioned above, are imprinted in the shape of the SED (see Section 1.4.4). For this reason, the modeling of the processes that shape the SED and the subsequent fit to the real data has become a largely employed method to translate the observed light in the knowledge of the galaxy's physics. Early versions of the SED models were mostly limited to fitting the stellar emission in the UV-NIR regime (Bolzonella et al. 2000, Brinchmann et al. 2000), but recently other SED-fitting approaches allowed the modeling of other regimes of the electromagnetic spectrum, from radio to the X-ray (Burgarella et al. 2005, da Cunha et al. 2008, Boquien et al. 2019, Yang et al. 2022). In this thesis, we largely make use of the SED-fitting method to estimate galaxies' physical parameters. Below, we describe the physics behind the integrated panchromatic emission of galaxies, in order to better comprehend how to model it, focusing particularly from the high energy regime (X-ray) to the lower energy end (IR). We do not use radio bands in our analysis.

1.4.1 X-ray regime: compact objects and diffuse hot ISM

It has been established that the X-ray emission from galaxies have three primary components, namely: discrete stellar sources (X-ray binaries), Active Galactic Nuclei (AGN) and diffuse hot ISM with temperatures of $10^6 - 10^7$ K (Trinchieri et al. 1985, Sarazin et al. 2001, Revnivtsev et al. 2008). AGNs are essentially supermassive black holes (SMBH) at the center of galaxies, accreting matter which gravitationally collapses at their core. This accretion is thought to take the form of a thin accretion disk ($\sim 10^{-3} - 10^{-2}$ pc in radius) surrounded by a hot ($T > 10^6$ K) corona. X-ray binaries (XRBs) are binary systems composed of an extremely dense object (a neutron star or black hole, called *accretor*) and a secondary star (called *donor*) that are gravitationally bounded and rotate around each other. In these systems, matter is flowing from the donor to the accretor, forming an accretion disk similar to the AGN one, but considerably smaller. For both objects, the accretion disk converts the fraction of the gravitational energy released in the accretion process into thermal emission, approximately as a black body peaking at ultraviolet wavelengths. Some of this UV emission is upscattered by the surrounding corona by inverse Compton scattering into hard (>few KeV) X-rays. In case of the AGNs, the UV emission is also reprocessed by the surrounding dust into mid-IR (MIR) and FIR. Both components are visually recognizable in nearby resolved galaxies, with the AGN appearing as a strong emission in the center of the galaxy, while the XRBs appear as point-like sources scattered around the center. However, in some cases it is possible to observe a diffuse X-ray emission, especially in galaxies residing in the center of a galaxy cluster, due to the

emission of ionized hot gas. This hot ISM can form in different ways, from mass loss of old stellar populations (e.g., stellar winds from evolved stars, planetary nebulae, and Type Ia supernovae), accretion of the intergalactic medium (IGM), as well as mergers of small galaxies.

The main effort of the community in the past decades has been focused on studying the galactic X-ray emission and source populations to understand their relation with the host galaxy and to infer its SFR and M_{star} . In fact, stellar remnants such as the compact objects forming XRBs, bear the imprint of the star-formation activity responsible for the formation of their parent stellar population. Therefore, being able to divide the contributions of each component to the total X-ray luminosity is of crucial importance for tracing the star formation activity of galaxies.

X-ray binaries: contribution from different stellar populations

It is clear that the X-ray emission from galaxies traces their stellar populations. This has been observed for the first time with the Einstein Observatory which showed strong correlations between the integrated galactic X-ray emission and their B-band or K-band luminosity, which trace the young and old stellar populations respectively (Fabbiano 1989). However, only with the advent of high-resolution telescopes, such as the *Chandra X-ray Observatory* and *XMM-Newton*, it has been possible to resolve the discrete X-ray sources (typically XRBs, but also supernovae remnants, AGN, or stars) in our Local Universe and study in detail the connection between X-ray emission and stellar content. These studies produced scaling relations between the soft (0.5-2 KeV) or hard (2-8 KeV) band luminosity and their SFR and M_{star} (Gilfanov 2004, Mineo et al. 2014). These relations have also been extended beyond our local Universe (Lehmer et al. 2016, Aird et al. 2017). To understand the physics behind these relations, a more accurate description of the XRBs is required.

X-ray binaries can be classified, on the basis of their donor stars, into two broad categories: those accreting material from an early-type star (OB star, or a supergiant), and those accreting from a late-type star (typically of M,K spectral type). These are referred to as High-Mass X-ray binaries (HMXBs) and Low-Mass X-ray binaries (LMXBs) respectively since their donor stars have masses typically above $8M_{\odot}$ and below $1-2M_{\odot}$.

HMXBs have a relatively short lifetime (10-100 Myr) due to the short life of their massive donor star. The onset of the X-ray emitting phase takes place soon after the formation of the compact object. On the other hand, due to the small mass of their donor star, LMXBs survive for longer periods (in Gyr order of magnitude) providing the necessary time for orbital decay to bring the donor star and the accretor compact object close enough to initiate mass transfer through Roche-Lobe overflow. The resulting different timescales make the relative number of the two sub-populations in galaxies depend on the star-formation history. For example, Fig. 1.5 shows the evolution of the HMXBs and LMXBs population after a single event of star formation, as predicted by the theoretical XRBs population-synthesis model of Fragos et al. (2013). After an initial ~ 5 Myr ramp-up, HMXBs dominate the X-ray power output for $\sim 100 - 300$ Myr. Following this, the LMXBs take over the spectrum, peaking in formation at $\sim 0.5-1$ Gyr, and then passively fading with increasing age. Also, the type of the donor star plays an important role to understand the correlation of these objects with SFR and M_{star} .

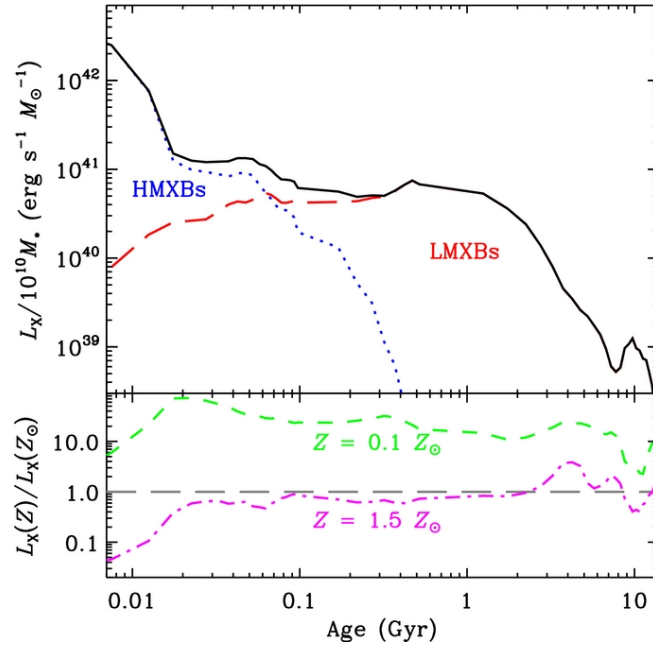


FIGURE 1.5: Evolution of an XRB population formed from a single-burst population of stars. Top panel: specific bolometric X-ray luminosity, i.e., luminosity per unit M_{star} , as a function of the population's age. The HMXBs evolution is presented as a blue dotted line while the LMXBs' one as red long-dashed line. Bottom panel: XRB evolution for the cases of metallicities $Z = 0.1 Z_{\odot}$ (green short-dashed) and $Z = 1.5 Z_{\odot}$ (magenta dot-dashed) compared to solar. Credits: Fragos et al. (2013)

Old XRB population: LMXBs

A statistical analysis of a large sample of early-type galaxies, observed with Chandra, so far confirms the conclusion that LMXBs can account for a very large fraction of the X-ray emission of some early-type galaxies. For example, in NGC1316, the integrated LMXBs emission, including non-detected sources below the sensitivity threshold, could reach luminosity of 4×10^{40} erg/s (Fabbiano 2006). Ignoring the contribution of this hidden emission can be a source of errors in estimating galaxies' properties, thus a proper characterization is required.

A popular way to characterize different XRB populations is to infer their X-ray luminosity function (XLF). In this work, we study the XLF shape of a sample of LMXBs in the Fornax cluster (see Chapter 3), so a brief introduction is required. The XLF is by definition the distribution of the number of sources according to their X-ray luminosity. Usually, it is shown as a cumulative distribution, which represents the distribution of the cumulative number of sources having X-ray luminosities greater than a certain value. Figure 1.6 shows the cumulative XLFs for LMXBs in different environments. The reader can notice that the shape changes according to the environment. In fact, the XLF shape may be connected with the age and/or metallicity of the host environment and can give us an important observational basis for the LMXBs population synthesis. For example, similarities in the XLF of field LMXBs and LMXBs residing in globular clusters (GC-LMXBs), can support a scenario where the entire population of LMXBs in galaxies, including those in the field, may have been produced dynamically in globular clusters (GCs) and later expelled into the field. We will discuss this possibility in Chapter 3.

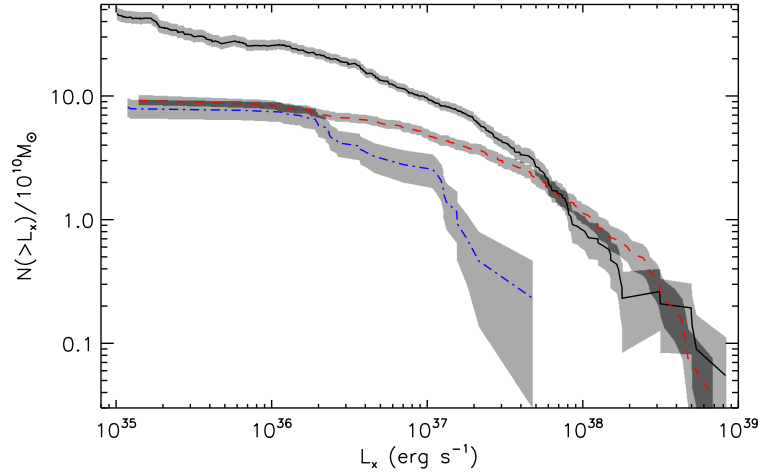


FIGURE 1.6: The combined XLFs of LMXBs in different environments plotted in the cumulative form. The solid black line represents the XLF of field LMXBs. The red dashed line picture the XLF of GC-LMXBs, while the blue dotted line is the XLF of LMXBs restricted to the nucleus of the galaxy. The shaded areas around the curves show 1σ statistical uncertainty. Credits: Zhang et al. (2011)

Several works have studied the XLF of LMXBs in nearby elliptical galaxies, finding that the shape can be parameterized as a power-law or a broken power-law (Kim et al. 2006; Paolillo et al. 2011; Zhang et al. 2011). The overall shape, ranging from 10^{36} to a few 10^{39} erg/s is fairly steep, but the presence of breaks has been extensively a matter of controversy. For example, the first main break (at $2 - 5 \times 10^{38}$ erg/s) can be related to the transition of the sources between a neutron star and black hole binaries (Fabbiano 2006). Instead, the second high luminosity break ($\sim 10^{39}$ erg/s) is still the subject of controversial discussions.

I previously discussed that the lifetime of LMXBs exceeds, by several orders of magnitudes, the characteristic time scales of a star formation event and can be even comparable to the lifetime of the host galaxy. For this reason, their contribution is defined by the several cumulative effects of the star formation episodes experienced by the host galaxy during its life, i.e. it is proportional to the M_{star} . Different studies have found that the XLF and the number of LMXBs, scale linearly with the M_{star} of the host galaxy (e.g. Gilfanov 2004; Kim et al. 2006; Lehmer et al. 2014, Fig. 1.7).

This relation is also predicted in simulations of large-scale population synthesis (Fragos et al. 2013). These simulations model the formation and evolution of XRBs from the first galaxies of the Universe until today. The predictions from these models can be very accurate, estimating the number of XRBs formed after an event of star formation and their evolution across cosmic time. Although, these models only consider the formation of XRBs via the evolution of isolated binaries, i.e. XRBs that reside in the field of the galaxy. Dynamically formed LMXBs, such as GC-LMXBs, that can have a significant contribution to the integrated X-ray emission of some elliptical galaxies, are usually not taken into account by simulations. The high density of GCs may facilitate the formation of LMXBs through gravitational processes, such as three-body interactions or tidal capture. This could connect the efficiency of LMXBs formation to the properties of the GCs population, such as luminosity, density, and color, critically complicating the global picture of the LMXBs population in galaxies.

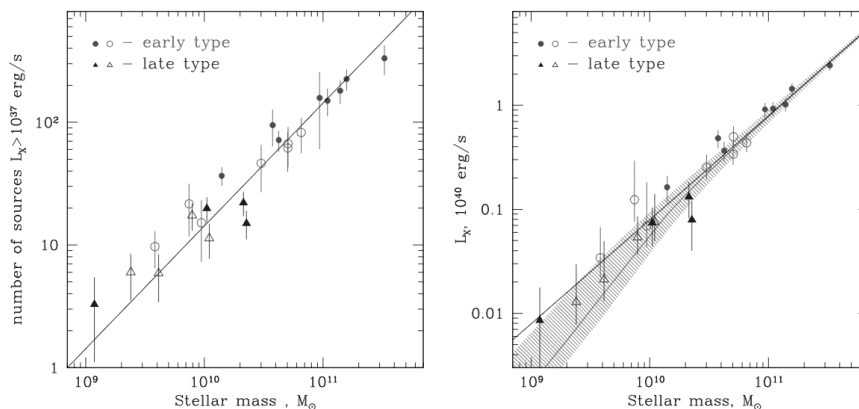


FIGURE 1.7: Number of sources with luminosity $L_x > 10^{37}$ erg/s and their collective X-ray luminosity versus M_{star} . Circles represent the early-type galaxies, while triangles are the late-type galaxies. The solid lines represent the fitted linear relations. Credits: Gilfanov (2004)

Several works showed that a considerable portion of LMXBs is found to be located in globular clusters, with a range from 10-20% in small galaxies to approximately 70% in large galaxies, depending on the morphological type of the galaxy and the abundance of GCs (Kim et al. 2009). LMXBs have a tendency to form in bright GCs, as their luminosity is a proxy of the number of stars they contain. However, factors such as size and concentration, which impact the efficiency of dynamical interactions, also play a role in binary formation. Additionally, the mass, size, and metallicity of GCs can influence LMXBs formation, with red, metal-rich GCs being three times more likely to host LMXBs compared to blue, metal-poor GCs due to their higher average density (Jordán et al. 2004, Fabbiano 2006, Paolillo et al. 2011, D’Ago et al. 2014). Despite this correlation, the role of metallicity in LMXBs’ formation remains uncertain, and further research is needed to understand how these objects form and if the properties of their environment (the host GC or the galaxy) affect their structure and emission. Thus, the presence of GCs in galaxies and in galaxy clusters can affect the LMXBs population and the respective X-ray output. The fact that the spatial distribution of LMXBs in early-type galaxies better resembles the distribution of the GC population (more extended) than that of the optical light of the galaxy (Kim et al. 2009, Paolillo et al. 2011) suggests that the likelihood of LMXBs formation is mainly driven by the internal GC properties. This supports the scenario for which GCs may be the principal (or the sole) birthplace of LMXBs.

In the next section, we will discuss how the simulation-neglected contribution from GC-LMXBs could cause a scatter in the empirical relation between X-ray luminosity and SFR. For this reason, a better understanding of the formation scenario of LMXBs in GCs, and thus their contribution to the galaxy’s X-ray emission, is crucial. In chapter 3 we try to address this problem by studying the X-ray properties of LMXBs in the field and in GCs, as a function of the distance from the center of the parent galaxy, in the local universe.

Young XRB population: HMXBs

The association of HMXBs with the young stellar population has been known since the beginning of X-ray astronomy (see [X-ray astronomy 1974](#)). The X-ray population

– SFR connection was initially proposed based on the analysis of a sample of normal galaxies observed with the Einstein satellite. The study revealed a strong correlation between the global X-ray and FIR emission of late-type, star-forming galaxies (Fabbiano 2006). This can be explained considering that, in general, SFR indicators link the direct or reprocessed stellar emission to the number of young stars present in the galaxy. For example, as young stars emit mainly in the UV regime, the total UV emission of a galaxy is a direct proxy of the SFR. However, considering the fast evolution of massive stars, these are consequently also young. For this reason HMXBs, and consequently their X-ray emission, are expected to correlate with the SFR, as their number correlate with the number of young stars in the galaxy. This connection was found by Grimm et al. (2003) studying a sample of 10 star-forming galaxies observed with Chandra and XMM-Newton. They propose the existence of a universal XLF for star-forming populations that follow a simple power law with a cumulative slope of $\alpha = -0.6$. This conclusion is based on the assumption that the XLF of star-forming galaxies is primarily influenced by the presence of young and luminous HMXBs. They suggest that the relative number of HMXBs in a galaxy is proportional to the SFR per unit of M_{star} , and when normalized to this quantity, the cumulative XLFs studied collapse into a power-law with a slope of $\alpha = -0.6$. Grimm et al. (2003) also first reported a linear relation between the number of X-ray binaries in star-forming galaxies (or equivalently their integrated X-ray luminosity), and their SFR (see also Mineo et al. 2014, and Fig. 1.8). An important trait of this relation is that, while there is a tight correlation at high X-ray luminosities and SFRs, there is a significant scatter at low SFR. This can be the result of stochastic events and variability of the sources. In fact, galaxies with integrated X-ray emission of even $10^{39} - 10^{40}$ erg/s can be dominated by few HMXBs, sometimes even a single one. An additional source of scatter in these scaling relations can be the different sensitivity of the SFR indicators on the age of the stellar population, which may lead to a mismatch between the age of the XRB population and the stellar population contributing to the SFR indicator (Kouroumpatzakis et al. 2020). Also, in the extremely low SFR regime, a scatter from the X-ray luminosity - SFR relation can occur due to the contribution of an underlying LMXB population. This has led astronomers to try to quantify this contribution (e.g. Gilfanov 2004). For example, a way to quantify the HMXB-to-LMXB ratio is to introduce joint relations between X-ray luminosity, SFR, and M_{star} , which account for both HMXBs and LMXBs components (Lehmer et al. 2008, Mineo et al. 2014. The SFR in these studies is generally based on IR indicators, although in some cases IR-UV hybrid indicators, or even SED-fitting have been used (e.g. Basu-Zych et al. 2013a, Aird et al. 2017). Figure 1.9 shows the joint relation between X-ray luminosity, SFR and M_{star} found by Lehmer et al. (2016). The solid black line highlights the fit of the empirical relation in the form:

$$Lx(XRB) = \alpha M_{star} + \beta SFR \quad (1.1)$$

where $Lx(XRB)$ is the total X-ray luminosity due to the XRB population, and $\alpha \equiv Lx(LMXB)/M_{star}$ and $\beta \equiv Lx(HMXB)/SFR$ are fitting constants that parameterize the relative contribution of LMXBs and HMXBs. The reader can notice that in the high specific SFR ($sSFR \equiv SFR/M_{star}$) regime, where the contribution of HMXBs is dominant, the sources are tightly grouped around the fitted relation. The slight scatter of the single sources can be traced to various factors, such as differences in metallicity. In fact, HMXBs are expected to be more numerous and more luminous with decreasing metallicity, since weaker stellar winds allow more mass

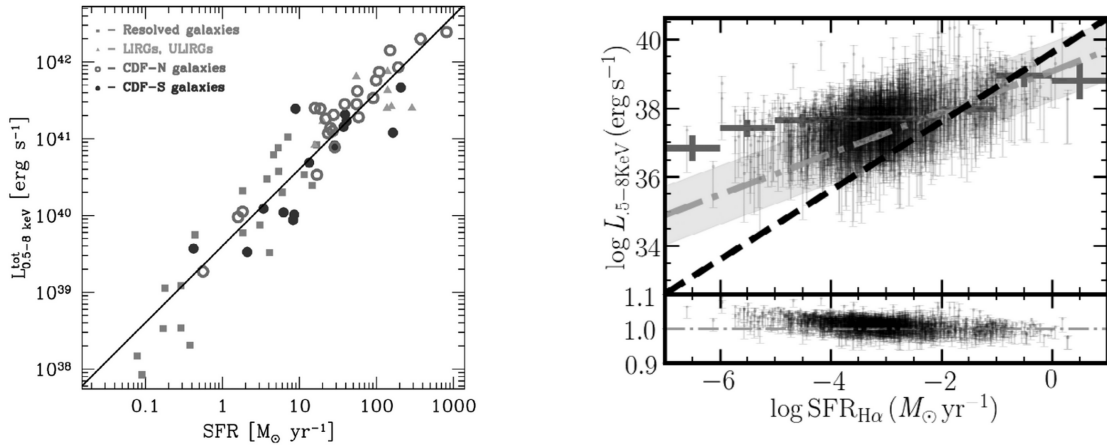


FIGURE 1.8: Left panel: Scaling relation between the X-ray luminosity in the 0.5–8 KeV band as a function of the SFR estimated with UV and IR indicators. Credits: Mineo et al. (2014). Right panel: Same relation using H_{α} based SFR. The thick points indicate the median X-ray luminosity in each SFR bin. The dashed line shows the relation of Mineo et al. (2014) which is clearly steeper than the trend shown in the data (grey dashed-dotted line). The right panel of this figure shows the residuals with respect to the best-fit linear relation. Credits: Kouroumpatzakis et al. (2020).

retention and tighter binary orbits, as demonstrated in X-ray binary population synthesis models (Linden et al. 2010, Fragos et al. 2013, Basu-Zych et al. 2016). Going to lower sSFR, where the contribution of LMXBs dominates the X-ray emission, the scatter from the relation is more marked. This suggests intrinsic differences in how LMXBs contribute to the emission, which may depend on several factors, such as the presence of a rich population of GCs. Furthermore, Lehmer et al. (2016) found that the relative contribution of LMXBs and HMXBs increase with redshift, due to declining host galaxy stellar ages and metallicities, respectively. Therefore, it is clear that the study of these relations is of crucial importance both to understand the synthesis of XRBs, and to have a reliable connection with the physical parameters involved.

To conclude, the results from previous studies on the X-ray luminosity from nearby and distant galaxies show a correlation with the SFR and M_{star} . This demonstrates that the X-ray output of the galaxy can be used as an indicator of its star-formation activity. However, there are still complications and limitations in the calibration of these scaling relations. The most important one is the strong age dependence of the HMXBs population, as the SFR used to calibrate the relation should come from indicators that probe similar timescales. For example, the most used SFR indicators, such as UV and/or IR, probe stellar populations with lifetimes up to 100 Myr or longer, that could exceed the lifetimes of HMXBs. Recently, SED-fitting based SFRs are starting to be used to calibrate the Lx-SFR relation, as different SFHs (sometimes quite complex) can be used in the estimation. However, right now only the H_{α} indicator probes stellar populations with similar ages as the formation scales of the HMXBs, but spectral analysis of large samples of galaxies along with X-ray observations are not often available. Future X-ray observatories such as eROSITA and ATHENA, will enable us to fully utilize the SFR indicators mentioned in this section. In Chapter 4 we make use of early eROSITA data and SED fitting methods to study the connection between X-ray emission and galaxies' physical parameters.

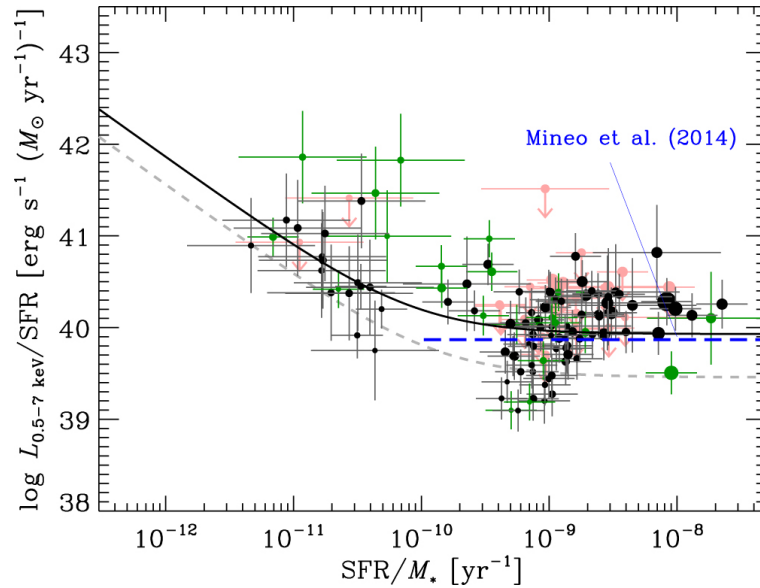


FIGURE 1.9: X-ray luminosity in the 0.5-7 KeV band per unit SFR as a function of the specific SFR (SFR/M_{star}). Black circles represent the sources detected in the full band (0.5-7 KeV). Green circles are the sources also observed in the hard band (2-7 KeV) while pink circles are upper limits. The solid curve represents the best-fit solution to Eq. 1.1. the long-dashed blue curve represents the mean value found by Mineo et al. (2014). Credits: Lehmer et al. (2016).

1.4.2 UV, optical and NIR: stellar emission

To understand the properties of a galaxy, its evolution and the interaction between the various components, it is necessary to have a clear picture of its stellar content. The wavelength ranges of the SED that trace the galaxy's stellar population emission are UV, optical, and near-infrared (NIR). Although the entire electromagnetic spectrum contains contributions from the full range of stellar spectral types, the majority of the emission is concentrated in this range of wavelengths. For example, the visible and NIR wavelengths are dominated by intermediate-type main-sequence stars (A to early F) and G-K giants. Young stars (O, B) and supergiants have the majority of their emission in the UV region. To study the contribution of these stars to the total SED of the galaxy, stellar population synthesis models are commonly used, which rely on stellar evolution theory to determine the ensemble of possible stellar types at a given metallicity and age (Bruzual et al. 2003, Conroy 2013 for a review). These models are called Simple Stellar Populations (SSPs). The emission of SSPs is built as the superposition of the different stellar types in number dictated by the assumed IMF. By adopting stellar spectra (as a function of temperature and metallicity) from libraries, it is possible to model the integrated emission of stars. Figure 1.10 shows the emission of integrated SSPs at a fixed solar metallicity, assuming a certain IMF, and for different ages. The models show that in the early stage of their life (~ 10 Myr), stars strongly emit in the UV spectrum ($0.1-0.4 \mu\text{m}$), while old stars ($\sim \text{Gyr}$) have the majority of their emission in the optical ($0.4-0.7 \mu\text{m}$) and near-IR ($0.7-2.5 \mu\text{m}$) wavelengths. An important feature of the integrated SSPs is their very bright spectrum at wavelengths longer than 912 \AA , but very dim at shorter wavelengths. This threshold is the *Lyman limit* and coincides with the emission of ground state-free transition of neutral hydrogen. Radiation at higher energies than the Lyman limit is almost completely absorbed by neutral gas around star-forming regions. However,

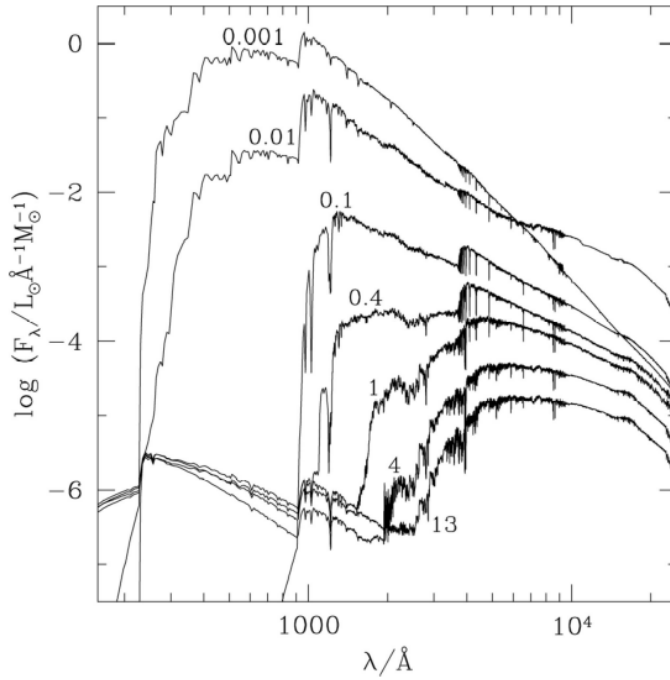


FIGURE 1.10: Integrated emission of SSPs at a fixed solar metallicity. The numbers specify the assumed age of the modeled SSP in Gyr. Credits: Bruzual et al. (2003).

very young stars can ionize the surrounding neutral hydrogen, decreasing the absorption effect caused by the transition. This ionization explains the smaller breaks of the 10 and 100 Myr curves. The total contribution from the stellar component is then constructed by building composite stellar populations (CSPs), as a superimposition of SSPs of different ages and metallicities, employing the SFH and the metallicity evolution of the galaxy.

The intensity of the blue end of the integrated emission is essential to determine the SFR of the galaxy. On the other hand, the optical/NIR end of the SED, dominated by the reddest, oldest stars, is a direct proxy of the M_{star} . Thus, the UV continuum is often used to have estimates of the SFR. The optimal wavelength range is 1250-2500Å, to avoid systematic errors from contamination of older stellar populations, and farther enough from the *Lyman limit* to avoid possible relevant contribution from neutral hydrogen absorption. Usually, the SFR equation linearly depends on the integrated UV luminosity in a certain range of wavelengths (Kennicutt 1998 for a review, Figueira et al. 2022 for a summary of the different relations). An example of a common formula for SFR using the UV luminosity (Madau et al. 1998), using Salpeter (1955) IMF is:

$$SFR(M_{\odot}yr^{-1}) = 1.4 \times 10^{-28} L_{\nu}(ergs s^{-1} Hz^{-1}) \quad (1.2)$$

Where L_{ν} represent the luminosity density at the frequency ν . This equation applies to galaxies with continuous SF over timescales of 100 Myrs or longer. During the past years, several relations were computed, applying to different types of galaxies and populations. The main advantage of the UV continuum estimation is that it directly traces the emission of the young stellar population and can be applied to a wide range of redshifts. On the other hand, the absorption of UV light by dust and gas can lead to considerable errors in the estimation, which may require corrections

ranging from 0 to 3 magnitudes (Buat 1992). However, since the spatial distribution of dust and gas can be very inhomogeneous, the calibration of the extinction is problematic. For this reason, it is considered more reliable to combine the UV continuum with the total IR emission, to account for the UV light absorbed and reprocessed by dust.

Another way to connect the stellar emission to the SF activity of galaxies is through emission lines due to the ionization of gas by the UV radiation emitted by young stars. In particular, hydrogen emission lines are tracing the star formation within HII regions, where the far-UV starlight exceeds the 13.6 eV ionization potential of the neutral hydrogen. For example, the Lyman- α line is the strongest hydrogen emission in the UV regime but, as we said, can be strongly attenuated by dust and gas. Another line that is largely used for the estimation of the SFR is the H_α line, emitted when the electron falls from its third to second lowest energy level. Being a recombination line, emitted due to the reprocessing of the ionizing radiation emitted by young stars, it directly traces young stellar populations with ages up to 20 Myr. For this reason, the H_α indicator is a more direct measure of the instantaneous star formation. Calibrations have been published by numerous authors (i.e., Kennicutt et al. 1983, Kennicutt et al. 1994, Madau et al. 1998). Considering the same Salpeter (1955) IMF of equation 1.2, an example of calibration formula is:

$$SFR(M_\odot yr^{-1}) = 7.9 \times 10^{-42} L(H_\alpha) (ergs/s) \quad (1.3)$$

The primary advantage of this method is the high sensitivity and the direct tracing of the massive young stars. In nearby galaxies, it is largely used as it can also be traced with small telescopes. The major drawback of this calibration is its high sensitivity to uncertainties due to extinction from dust and gas. Most of the time, the observed H_α flux has to be corrected for extinction using IR recombination lines or attenuation law models.

Other emission lines can be used to quantify the SFR of galaxies, especially when the hydrogen lines are unavailable or impossible to use. For example, the [OII] doublet at 3726 Å and 3729 Å have largely been used as a SFR indicator, as its bluer rest-frame wavelength allows us to observe it in the optical range at higher redshift than the H_α line (Kennicutt 1998, Kewley et al. 2004). However, since bluer wavelengths require greater corrections for extinction, the SFRs derived from OII are less precise than from H_α but can provide very useful estimates of the systematics in samples of distant galaxies, and are useful for consistency check on SFRs derived with other indicators.

Nowadays, several surveys, both space and ground-based, allow us to explore this range of wavelengths. For example, the Galaxy Evolution Explorer (GALEX, Martin et al. 2005), the first UV space survey, made it possible to calibrate relations between the UV emission and the star formation rate up to redshift ~ 2 . Also, optical space telescopes, such as the Hubble Space Telescope (HST), or ground-based optical surveys, such as VLT Survey Telescope (VST), made possible a detailed characterization of the optical emission of very distant galaxies. In the coming years, the successor of these optical surveys will undoubtedly be the *Legacy Survey of Space and Time* (LSST, Ivezić et al. 2019). The LSST survey is expected to provide around 20 TB of data per night, in the *ugrizy* bands, observing about 20 billion galaxies during ten years of observations. This enormous amount of data will allow us to statistically study samples of galaxies at high redshifts and, for this reason, adequate methods to study their properties are essential. In Chapter 2 we discuss a possible way to reliably estimate the SFR using only LSST data.

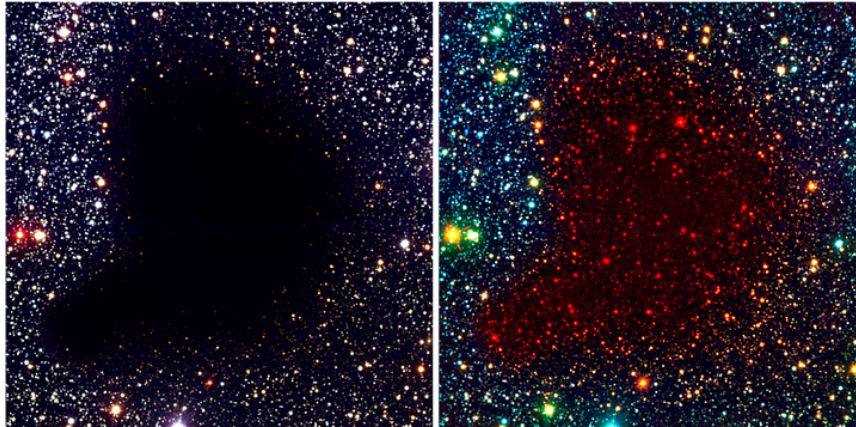


FIGURE 1.11: Dark nebula Barnard 68 in the MW. The stars behind the nebula are not visible due to the extinction of the dust in the cloud. When observed in the IR, it is possible to uncover the underlying stellar content. Credits: ESO

1.4.3 MIR and FIR indicators: dust and PAH

Most of the time UV indicators are not enough to characterize a galaxy's star formation activity. In fact, dust strongly impacts the observations by absorbing the stellar light coming from the star-forming region and re-emitting it in the IR spectrum. Therefore, galaxies could appear extremely red not because they are dominated by old stellar populations, or undergoing a quenching period of star formation, but because their star-forming regions are extremely attenuated by dust. Correctly accounting for the effect of dust allows for more accurate studies of galaxies' properties. In order to better understand the role of dust as a SFR indicator, in this section I briefly introduce the concept of extinction, attenuation, and dust emission.

Extinction

Interstellar dust extinction is the result of photons being absorbed or scattered out of the line of sight by dust grains. The extinction can be so strong to completely hide the underlying stellar component (Fig. 1.11). The general picture can be summarized as a background point source (in general a star) positioned behind a column of dust (Fig 1.12). Given these geometric assumptions, the distribution of the foreground dust is irrelevant to the total extinction value, i.e. the value is only proportional to the amount of dust along the line of sight. The ratio between the extinguished star's flux (I_λ) over the input star's flux (I_{λ_0}), in a specific wavelength, defines the dust extinction $A(\lambda)$ as:

$$A(\lambda) = -2.5 \log\left(\frac{F_\lambda}{F_{\lambda_0}}\right) \quad (1.4)$$

As the extinction is only proportional to the amount of dust in the line of sight, the ratio of the extinction at two different wavelengths does not vary with different amounts of identical dust. For this reason, dust extinction is often measured as a relative value between two bands. Conveniently, we can define the color excess:

$$E(\lambda_1 - \lambda_2) \equiv A(\lambda_1) - A(\lambda_2) \quad (1.5)$$

Dust extinction is usually measured relative to the V band $A(\lambda)/A(V)$. As blue light is more absorbed than red light, the color excess between B and V bands,

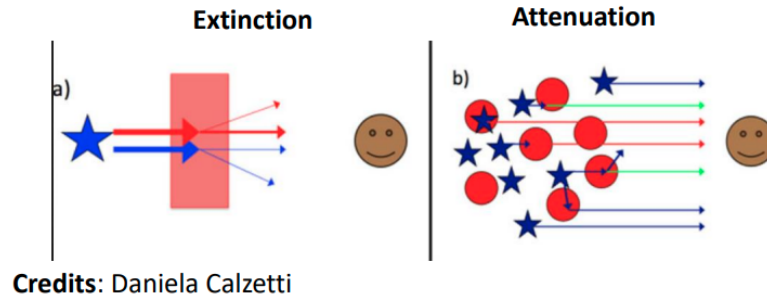


FIGURE 1.12: Comparison between the Extinction (left panel) and Attenuation (right panel) scenario.

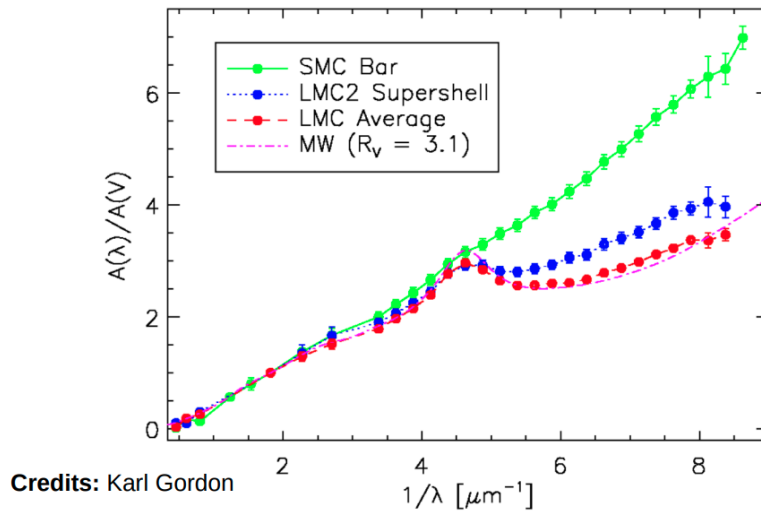


FIGURE 1.13: Extinction curves for the MW and the Small and Large Magellanic Clouds. A bump at 217.5 nm is observed probably due to the presence of graphite or Polycyclic Aromatic Hydrocarbons (PAH).

namely $E(B-V)$, is a commonly used measure of the amount of dust extinction and is used as a normalization parameter. In fact, we can write:

$$\frac{A(\lambda)}{A(V)} = \frac{E(\lambda - V)}{E(B - V)} \frac{1}{R_V} + 1 \quad (1.6)$$

where $R_V = A(V)/E(B - V)$ is called the total-to-selective extinction in V band. The effect of dust extinction on a star's flux is then:

$$F(\lambda) = F_0(\lambda)e^{-\tau(\lambda)} \quad (1.7)$$

where $\tau(\lambda) = 0.921A(\lambda)$ is the optical depth. Extinction curves have been largely measured towards stars in our Galaxy and in other galaxies of the Local Group (Valencic et al. 2004, Fitzpatrick et al. 2007, Gordon et al. 2009). Figure 1.13 shows different extinction curves estimated for the MW, the Small Magellanic Cloud, and the Large Magellanic Cloud. The MW value of $R_V = 3.1$ is largely used as the average value in many computational models. Larger values of R_V (up to 5) correspond to flatter curves, i.e. denser regions and/or larger dust grains.

Attenuation

Measurements of dust extinction outside the Local Group are problematic as require individual stars to be resolved from their neighbors. This is when the attenuation plays a bigger role in determining the amount of light extinguished by dust. Attenuation refers to the net effect of dust absorption and scattering in a complex geometrical distribution, where the light sources can be distributed within the dust at different ranges of depths, and their light can be attenuated by different amounts of dust or scattered into or outside the line-of-sight (Fig. 1.12). The main advantage of extinction curves is that their shape is invariant to the amount of dust along the line of sight. This is not the case with attenuation, where the more complex geometries (both of the dust and the stars) result in attenuation curves that vary with the amount of dust in the system.

Measuring attenuation curves (or laws) is more complex than the Extinction counterpart. In fact, with the knowledge of the intrinsic spectrum of a star from either observations in regions without foreground dust along the line of sight or from stellar atmosphere models, extinction curves can be directly measured by observing the same star type in regions with dust along the line of sight. In the case of attenuation, this is not possible due to the complexity of the systems. For example, it is unlikely to find two identical galaxies, one with specific dust properties and geometry and one dust-free, to compare the amount of observed light. Thus, using the pairing method to measure attenuation curves is not possible. Theoretically predicting attenuation curves is also a complex task. In fact, the radiative transfer of light through dust is described by an integro-differential equation that depends on the properties of the dust and on its capability to interact with photons. Solving this equation results in attenuation curves with complex and non-linear dependence on dust amount and dust/stars geometry (Steinacker et al. 2013).

However, it is possible to measure average attenuation curves for samples of galaxies. Numerous studies have focused on the observational determination of attenuation laws in a statistical sample of galaxies, finding a remarkable diversity (Calzetti et al. 2000, Charlot et al. 2000, Lo Faro et al. 2017, Buat et al. 2018, Salim et al. 2018). The attenuation curve from Calzetti et al. 1994 is a good example of such an average attenuation curve. In fact, it is calibrated by studying the behavior of the attenuation in a sample of UV-bright SB galaxies and is appropriate to correct for the effect of the dust in similar galaxies. Different methods can be employed to determine the average extent of dust attenuation in galaxies. For example, a multi-wavelength analysis of the UV-NIR SED can give an idea of the total dust attenuation as the obscuring effects of dust intensify at shorter wavelengths. Also, the Balmer line ratio (H_α/H_β), known as the Balmer decrement, can be used to measure dust reduction towards HII regions (Domínguez et al. 2013). In the absence of dust, this ratio can be calculated based on first principles and is only slightly dependent on the temperature of the gas. So, comparing the observed ratio with the expected value can provide evidence of attenuation by dust. Lastly, it is possible to employ the IR-to-UV luminosity ratio (called IRX) to reveal the total dust absorption as photons absorbed in the UV/optical must be re-radiated in the IR due to energy conservation. Calzetti et al. (1994) discovered that the dust optical depth measured from the Balmer line ratio H_α/H_β was almost double the estimation made from the UV continuum slope in a sample of 39 SB and blue compact galaxies. They believed that this discrepancy could be explained by young, hot stars being surrounded by dusty clouds while older stars only experience attenuation from the diffuse ISM. Later, Charlot et al. (2000) developed a two-component model to describe dust absorption

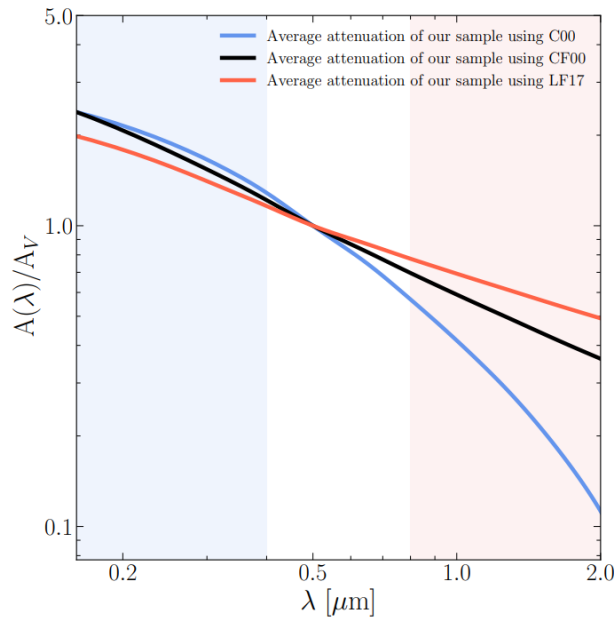


FIGURE 1.14: Comparison between different attenuation laws (Calzetti et al. 2000, Charlot et al. 2000, Lo Faro et al. 2017) normalized at $0.5\mu\text{m}$. Credits: Hamed et al. (2023).

that supported this idea, where young stars are surrounded by natal clouds and all stars face dust reduction from the diffuse ISM. In this model, a transition time is specified when the natal cloud is dispersed (usually 10^7 years) and attenuation curves are created for both the natal cloud and diffuse ISM, both being power-laws with the same exponent ($\tau \propto \lambda^{-0.7}$). The natal cloud curve is typically set to have twice the normalization of the diffuse ISM. Figure 1.14 shows the comparison between Calzetti et al. (1994), Charlot et al. (2000), and Lo Faro et al. (2017) attenuation curves, commonly used for modeling the SED of dusty galaxies.

However, other authors (Wild et al. 2011, Buat et al. 2012) found that the mean attenuation curves can significantly vary as a function of the galaxies' physical properties, such as sSFR, inclination, and stellar mass surface density. For example, Buat et al. (2012) modeled the UV-FIR SEDs of a sample of galaxies at $1 < z < 2$ and found evidence for a steeper attenuation curve (i.e., a faster rise in the UV) than the Calzetti law in 20-40% of their sample. This confirms the need to perform further studies on attenuation curves and the high-quality optical and IR data, such as LSST and JWST, will make an incredible contribution to the task.

Dust emission

Extinction and attenuation model how starlight is dimmed by the dust, but the energy absorbed in this process is generally thermalized and re-emitted in the IR. Figure 1.15, showing a galaxy's SED with and without the presence of dust, is a perfect example of how models are predicting the reprocessed stellar light in the IR regime. Understanding the physics behind this emission is crucial to correct the observations to the dust attenuation, in order to reliably estimate physical properties such as the SFR. For example, by combining observations in the UV or H_α with observations in the total IR or $24\mu\text{m}$, it is possible to create a composite indicator that takes into account both the obscured and un-obscured star formation (Calzetti et

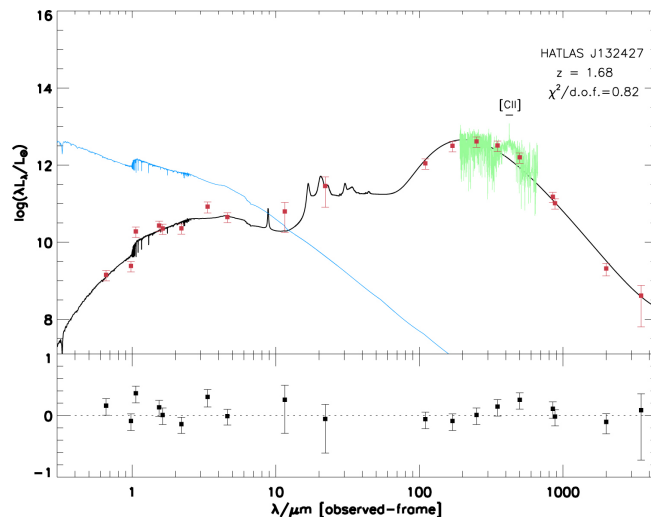


FIGURE 1.15: Example of the SED of a galaxy observed by Herschel. The best-fit SED model is plotted in black while the intrinsic model without dust extinction is plotted in blue. Red dots represent the observed fluxes. The green line represents the spectral features. Credits: Timmons et al. (2015).

al. 2007, Kennicutt et al. 2009). For this reason, several authors tried to model the emission spectrum of dust, taking into account different types of dust grains (composition, geometry) and sizes. The models can be divided into 3 broad categories: the silicate-graphite-PAH model (e.g. Draine et al. 2007, Dale et al. 2014), the silicate core carbonaceous mantle model (e.g. Li et al. 1997) and the composite model (e.g. Zubko et al. 2004) which assume dust to be a mixture of low-density silicate and carbonaceous particles. These models can be constrained by comparing the expected emission with observations. In this thesis, I will concentrate mostly on the silicate-graphite-PAH model, as it was shown to well reproduce the observations in the mid and far IR range (Draine et al. 2007, Draine et al. 2014).

The MIR part of the SED of star-forming galaxies is characterized by the emission from Poly-Cyclic Aromatic Hydrocarbons (PAHs) (Tielens 2008). PAHs are molecules composed of carbon atoms bound with hydrogen in a ring-shaped composition. These molecules emit the brightest emission lines across the MIR spectrum, specifically at 6.2, 7.7, 8.6, 11.3, 12.0, 12.7, and 13.55 μm (Fig. 1.16). These spectral features are the result of the absorption of far-UV photons, whose energy is subsequently re-emitted in the MIR spectrum as vibrational energy (Leger et al. 1984, Allamandola et al. 1985). The PAH's population is currently estimated to contribute 10-15% of the total interstellar carbon, with their emission accounting for 20-30% of the total IR emission of star-forming galaxies. For this reason, their emission is directly connected to the star formation.

The far-IR and sub-millimeter wavelengths of the galaxy's SED are instead dominated by the thermal emission of cold dust, which can be generally modeled as a black body modified by dust emissivity laws. As interstellar-dust grains have sizes ranging from nanometers to microns, the total emission is the sum of the contributions from different grain sizes and compositions. For example, large grains (about 0.1 μm) are generally in thermal equilibrium with the radiation field and so their emission is characterized by a black body with a single temperature. Due to their size, these grains are generally colder than their smaller counterpart, which results in the peak of the blackbody emission shifting at longer wavelengths. Instead, small

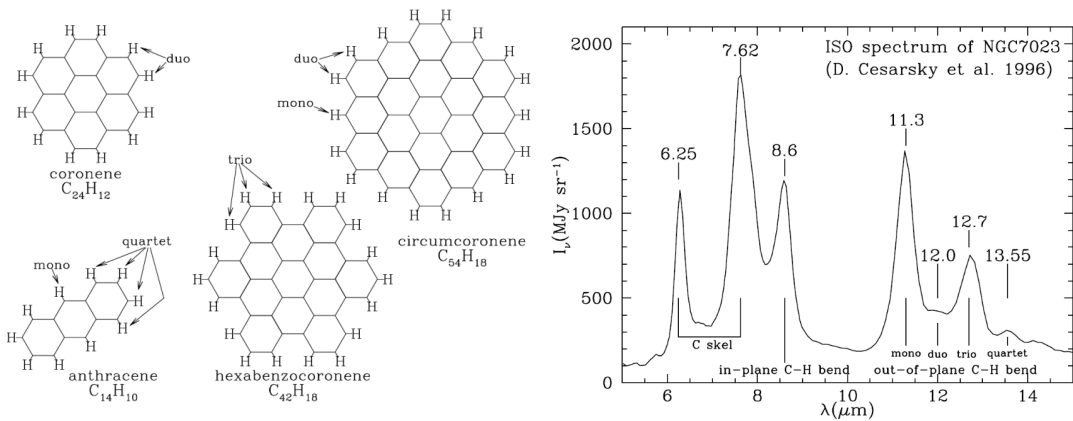


FIGURE 1.16: Left panel: Illustration of different PAH molecules. Right panel: Principal spectral feature of PAHs in the mid-IR spectrum. Credits: Draine (2003)

grains are generally not in equilibrium with the interstellar radiation field as the time between absorbing photons can be long enough, due to their low cross-section, to allow the grain to cool down (Draine et al. 2007). This could result in significant miscalculations of the dust emission if approximations of global thermal equilibrium are taken into account.

Therefore, to take into account the energy balance between the UV and IR emission when estimating the physical properties of galaxies, both accurate dust emission models and good coverage of the IR SED are absolutely necessary. Neglecting these aspects could lead to serious miscalculations (Buat et al. 2019, Riccio et al. 2021). Unfortunately, it is not often possible to have available high-quality IR observations, due to the characteristic lower sensitivity and resolution of wide IR cameras or extremely expensive sub-millimeter observations such as those with ALMA. In Chapter 2 we explore the possibility to estimate the SFR for a sample of galaxies without any IR counterpart, as it is expected for the next generation of large optical surveys such as LSST.

1.4.4 Fitting of the spectral energy distribution

In the previous sections, I largely discussed how different physical processes occurring in galaxies leave their imprint on the global and detailed shape of the spectrum, emitting across a large range of wavelengths, from the X-rays to the IR regime. Thus, it becomes clear how the study of the integrated SED is one of the primary sources of information about the properties of unresolved galaxies. Detailed analysis of the SED of a galaxy should therefore, in principle, allow us to gain insight into various properties of galaxies, such as SFH, SFR, gas content, dust content, AGNs. In this section, we briefly explain the SED fitting tool as galaxies' physical parameters estimator, as it is largely used in this project.

By simple definition, the SED of a galaxy is the representation of the distribution of its energy as a function of wavelength. This information is gathered through observations with various telescopes and instruments that cover different parts of the electromagnetic spectrum. Thus, SED fitting is the attempt to analyze a galaxy SED and to estimate its physical properties by fitting models to an observed SED. There are two main approaches for modeling the SED:

- Radiative Transfer Modeling: This method models the scattering, absorption, and re-emission of the light from stars by dust grains in the surrounding environment. The resulting spectrum provides valuable information about the embedded stellar populations. Radiative transfer codes use the radiation transport equation and incorporate factors such as the chemical composition, SFH, and dust/star geometry of galaxies to model the transport of radiation in dusty environments. The distribution of stars and dust must be specified before running the calculations, which will then determine the temperature distribution of dust grains and result in the modeled SED. Finally, by integrating over all positions in a given galaxy, the modeled SED is obtained (Silva et al. 1998, Baes et al. 2011, Popescu et al. 2011). This allows for exquisitely detailed modeling, at the expense of high computing time, which increases exponentially as the size of the model grid grows. This has mostly limited the use of radiative transfer models to theoretical studies and to few observational studies on edge-on galaxies. Examples of such studies include Popescu et al. (2000), Gordon et al. (2001), Tuffs et al. (2004), and Trayford et al. (2017).
- Physically motivated and fast broadband SED modeling using discrete emission components and energy balance: this approach uses a different philosophy in modeling the impact of the processes on the integrated SED: the energy emitted by dust in the mid- and far-IR exactly corresponds to the energy absorbed by dust in the UV-optical range. The option of adding X-ray and AGN counterparts, as well as radio emission, helps in modeling a wider range of observed galaxies. It takes into account several options for factors such as stellar populations, dust attenuation laws, and dust emission processes. The majority of the components are either modeled directly within the code or are taken from published models/templates that are available to the user. Examples of codes that employ the energy balance in modeling SEDs and fitting observed ones include MAGPHYS (da Cunha et al. 2008) and CIGALE (Noll et al. 2009; Boquien et al. 2019). This method is a good compromise between speed, precision, and accuracy and has been applied to study a wide variety of systems (Buat et al. 2012; Lo Faro et al. 2017; Małek et al. 2018; Salim et al. 2018; Riccio et al. 2021). The difference between different tools are discussed in Pacifici et al. (2023)

In this project we make use of energy balance methods of SED fitting (using the code CIGALE), to study statistical samples of galaxies at low and intermediate redshift ($0 < z < 2.5$), an impossible task for the computationally demanded radiative transfer modeling. A key aspect of this model is its use of a Bayesian approach. Starting from a set of input parameters controlled by the user, a grid of mock SEDs is created employing models of the galaxy's physical processes in each of the wavelength ranges. The models are progressively computed by a series of independent modules called successively, each corresponding to a unique physical component or process. The generated mock SEDs are then fitted to the observed photometry. The physical properties are then not evaluated from the best-fit SED but by weighting all the SEDs depending on their goodness of fit, with the best-fit SED having the heaviest weight. This method is particularly useful for multi-wavelength data as the problem of finding the physical parameters is not straightforward when considering effects such as dust attenuation, line emission, and dust emission. Also, this takes into account the uncertainties on the observations while considering the intrinsic degeneracies between physical parameters (different models with widely different

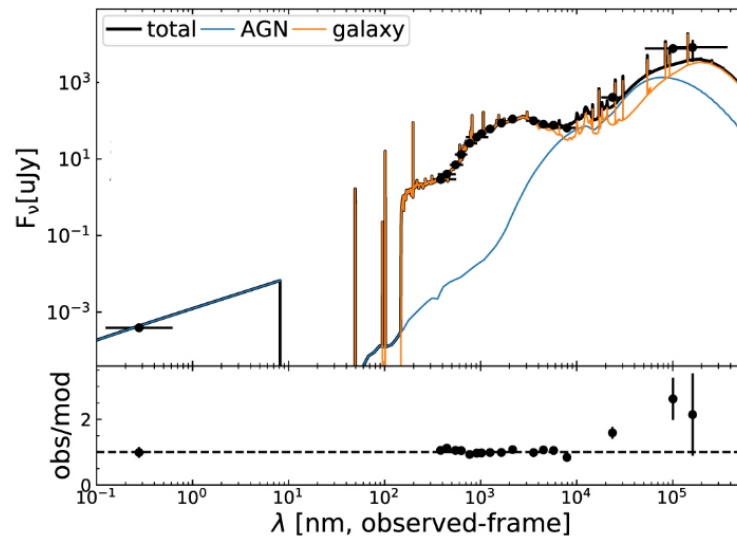


FIGURE 1.17: Example of a fit from the X-ray to the IR performed by CIGALE. The blue solid line represents the AGN emission, the orange solid line represents the galaxy emission, and the black solid line is the total AGN+galaxy SED. Credits: Yang et al. (2022)

physical parameters, can sometimes yield similar SEDs). The typical sequence to build each model is the following:

1. Computation of the SFH.
2. Computation of the stellar spectrum from the SFH and SSP models.
3. Computation of the nebular emission.
4. Computation of the attenuation of the stellar and nebular emission assuming an attenuation law.
5. Computation of the dust emission in the mid and far IR.
6. Computation of the AGN emission.
7. Computation of the X-ray emission.
8. Computation of the radio emission (not used in this thesis)
9. Redshifting of the model and computation of the absorption by the intergalactic medium (IGM).

Figure 1.17 shows an example of a best-fitting SED model to observed data, from the X-ray to the IR, performed with CIGALE (Yang et al. 2020; Yang et al. 2022).

Results of the SED fitting: physical properties

SED fitting is a very powerful tool when it comes to estimating the galaxies' physical parameters. Pretty much all of the parameters mentioned before in this thesis can be estimated by SED fitting, covering the adequate spectral range. For example, good coverage of the stellar emission (UV, optical, NIR) results in reliable estimation of

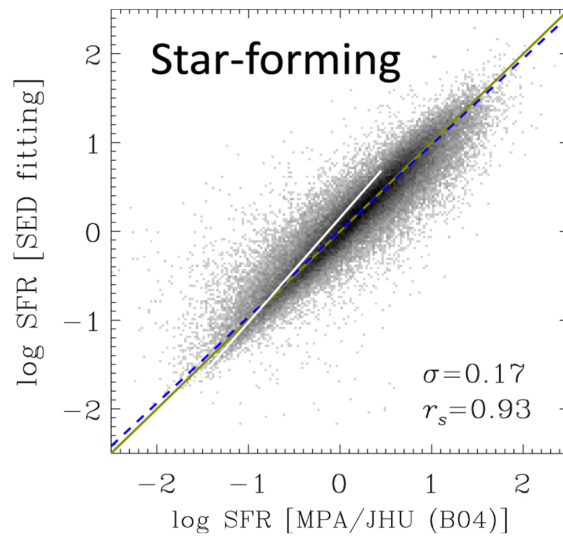


FIGURE 1.18: Comparison of SFRs of star-forming galaxies derived from SED fitting to SFRs from the DR7 MPA/JHU catalog. The blue dashed line is the best-fit relation, the yellow solid line represents the 1:1 relation, and the white solid line is a comparison with the literature. Credits: Salim et al. (2016)

the M_{star} , while parameters like dust mass, dust luminosity, AGN properties, PAH fraction, are well estimated with a good IR coverage. Estimating the SFR through SED fitting has the advantage of utilizing information from a broad range of the electromagnetic spectrum (Conroy 2013, for a review). For this reason, it's important to assess how these SFR values compare to those estimated using other methods. Figure 1.18 shows an example of SED-based SFRs versus SFRs obtained from the DR7 MPA/JHU catalog (Salim et al. 2016). They find a satisfying agreement between the two SFRs, where the latter is a hybrid SFR derived from emission lines, D4000 and SED fitting. Other works studied the reliability of the SFR estimation with SED fitting, finding comparable results with other indicators (e.g. Figueira et al. 2022 for an extensive study). Therefore, we conclude that the SFRs estimated from SED fitting can be considered as reliable, especially for SFGs studied in this Thesis.

However, the reliability of the estimations depends on many factors, such as the quality of the observed photometry, or the coverage of the SED. For instance, to determine the total SFR of dusty galaxies, high-quality data in the rest-frame MIR to FIR range are required. However, these data are not often available or of poor quality. In fact, collecting deep MIR or FIR data can be a major challenge for galaxies at high redshift. Without reliable IR data, key parameters such as dust mass, temperature, and SFR cannot be accurately inferred (see also Chapter 2).

1.4.5 This Thesis

This thesis presents extensive work on the panchromatic emission of normal star-forming galaxies at low and intermediate redshift. Using observed and simulated data from next-generation telescopes (LSST and eROSITA), together with the state-of-the-art SED fitting method, this thesis focuses on exploring possible relations between the physical properties of galaxies and their star formation activity.

In Chapter 2 we explore the limits and the expectations of the physical parameters estimated with LSST. In order to do so, we simulate LSST observations for a

sample of 50385 real galaxies within the redshift range $0 < z < 2.5$. In order to estimate the physical parameters, and to compare them with the one estimated employing optical LSST data, we study the panchromatic emission of these galaxies, from the UV to FIR, making use of *Herschel* data. In this chapter, we show that LSST data alone will not be able to give reliable constrain of the SFR, and other prior knowledge on the sample of galaxies is required. Specifically, we show that to correct the estimated SFR it is enough to combine LSST data with UV or MIR ancillary data. However, considering the huge amount of data LSST will deliver in the 10 years survey, we do not expect to have ancillary data for all the galaxies that LSST will uncover. Considering that the M_{star} is well estimated using optical LSST data, we show that the usage of far-UV attenuation (A_{FUV})- M_{star} relations is a prosperous method to employ only LSST data in the estimation of SFR. These results were presented in Riccio et al. (2021).

In the picture of galaxies' star formation activity and properties, we discussed how the contribution of an underlying LMXBs population to the total X-ray luminosity of the galaxies could cause a significant scatter of the sources from the empirical Lx-SFR scaling relation. As it is known that a consistent population of LMXBs resides in globular clusters, in **Chapter 3** we study the population of GC-LMXBs in the galaxies forming the central region of the most GC-rich galaxy cluster of the nearby Universe: the Fornax galaxy cluster. We make use of a combination of VST and Chandra observation to study the properties of the population of GC-LMXBs as function of distance and GC properties. We find that LMXBs tend to form in red and bright GCs, with the likelihood of a red GC to host a LMXB decreasing with galactocentric distance, while it remains approximately constant for the blue GC population. We find no significant difference in the X-ray luminosity function between the field and GC-LMXBs, both following a single power law in agreement with the literature. We assess a minor contribution of GC-LMXBs to the total X-ray luminosity of the cluster, suggesting that the well-known scatter of the Lx-SFR scaling relation at low SFR is mainly driven by field LMXBs. We then investigate the spectral properties of the GC-LMXBs, finding an unprecedented dependence on the environment (GC color/distance). The majority of these results were presented in Riccio et al. (2022)

In **Chapter 4** we explore the relation between X-ray luminosity and galaxies' physical properties making use of the first release of data acquired by SRG-eROSITA for the Performance-and-Verification-Phase program named the eROSITA Final Equatorial Depth Survey (eFEDS). Thanks to the combination of X-ray data and ancillary data from UV-to-MIR, we are able to model the X-ray emission from XRBs, AGN and hot gas and to estimate the SFR and M_{star} of the galaxies. We then isolate the HMXBs and LMXBs emissions (that scale with SFR and M_{star} respectively) removing AGNs systems and subtracting the contribution of hot gas. We are able to confirm a linear correlation between X-ray luminosity and SFR for our sample of SFGs, finding comparable results with literature when correcting for completeness. Analyzing the combined contributions from LMXBs and HMXBs, we find an allegedly enhanced LMXBs' emission, that scatter our objects away from the empirical relation observed in previous works. We discuss the dependence of this scatter on the M_{star} , metallicity, and globular cluster content of the galaxy. These results have been submitted to the *Astronomy & Astrophysics* journal (Riccio et al. submitted).

2

Preparing for LSST data: Estimating the physical properties of $z < 2.5$ main-sequence galaxies

This chapter originally appeared as ‘Preparing for LSST data. Estimating the physical properties of $z < 2.5$ main-sequence galaxies’ by G. Riccio et al. 2021, *Astronomy & Astrophysics*, Volume 653, article number A107 (Riccio et al. 2021)

2.1 Abstract

We study how the upcoming *Legacy Survey of Space and Time* (LSST) data from the Vera C. Rubin Observatory can be employed to constrain the physical properties of normal star-forming galaxies (main-sequence galaxies). Because the majority of the observed LSST objects will have no auxiliary data, we use simulated LSST data and existing real observations to test the reliability of estimates of the physical properties of galaxies, such as their star formation rate (SFR), stellar mass (M_{star}), and dust luminosity (L_{dust}). We focus on normal star-forming galaxies because they form the majority of the galaxy population in the universe and are therefore more likely to be observed with the LSST. We performed a simulation of LSST observations and uncertainties of 50 385 real galaxies within the redshift range $0 < z < 2.5$. In order to achieve this goal, we used the unique multi-wavelength data from the *Herschel Extragalactic Legacy Project* (HELP) survey. Our analysis focused on two fields, ELAIS N1 and COSMOS. To obtain the physical properties of the galaxies, we fit their spectral energy distributions (SEDs) using the Code Investigating GALaxy Emission (CIGALE). We simulated the LSST data by convolving the SEDs fitted by employing the multi-wavelength observations. We compared the main galaxy physical properties, such as SFR, M_{star} , and L_{dust} obtained from the fit of the observed multi-wavelength photometry of galaxies (from the UV to the far-IR) to those obtained from the simulated LSST optical measurements alone. We present the catalog of simulated LSST observations for 23 291 main-sequence galaxies in the ELAIS N1 field and for 9 093 galaxies in the COSMOS field. It is available in the HELP virtual observatory. The stellar masses estimated based on the LSST measurements agree with the full UV to far-IR SED estimates because they mainly depend on the UV and optical emission, which is well covered by LSST in the considered redshift range. Instead, we obtain a clear overestimate of the dust-related properties (SFR, L_{dust} , M_{dust}) estimated with the LSST alone. They are highly correlated

with redshift. We investigate the cause of this overestimation and conclude that it is related to an overestimation of the dust attenuation in both UV and near-IR. We find that it is necessary to employ auxiliary rest-frame mid-IR observations, simulated UV observations, or the far-UV attenuation (AFUV)- M_{star} relation to correct for the overestimate. We also deliver the correction formula $\log_{10}(\text{SFR}_{\text{LSST}}/\text{SFR}_{\text{real}}) = 0.26 \cdot z^2 - 0.94 \cdot z + 0.87$. It is based on the 32 384 MS galaxies detected with *Herschel*.

2.2 Introduction

In the past 20 years, the study of the multi-wavelength emission of galaxies from X-rays to radio was found to be necessary to properly analyse the physical properties of galaxies. Because the spectral energy distribution (SED) is the result of a complex interplay of several components, such as old and young stars, stellar remnants, the interstellar medium, dust, and supermassive black holes (Walcher et al. 2011, Conroy 2013), only the panchromatic view of galaxies can give the full information about their physical properties. For example, the emission from the hot interstellar medium, active galactic nuclei (AGN), or stellar remnants can be observed in the X-ray band (Fabbiano, 2006), while the emission of the dust heated by interstellar radiation can be observed in the mid- and far-IR band (Silva et al. 1998, Noll et al. 2009, da Cunha et al. 2010, Hao et al. 2011, Calzetti et al. 2012, Schreiber et al. 2018, Leja et al. 2018). To fully comprehend the interactions between these parts, the simultaneous use of different spectral ranges is needed. As broad-band photometry is much less expensive than spectroscopy in terms of observation time, modeling the broad-band SED of galaxies has become one of the most commonly employed methods to evaluate and constrain the physical properties. In this way, properties such as the star formation rate (SFR) and stellar mass (M_{star}), which are essential for a complete understanding of galaxy formation and evolution, can be evaluated.

However, modeling the SED can be an intricate problem because galaxies with very different properties can look similar over some wavelength range: that is, a young dusty galaxy can appear to be an old dust-free galaxy because they both look red in the optical. This is particularly the case when restricted wavelength ranges, instead of the full SED, are considered. The full SED is rarely available. This makes estimating the physical properties with only a limited wavelength range a great challenge for SED modeling.

In the literature (i.e. Kennicutt 1998, Le Flocc'h et al. 2005, Schreiber et al. 2015, Whitaker et al. 2017) it has been shown that the ultraviolet (UV) to infrared (IR) SED contains important information about the star formation activity of galaxies. For example, some knowledge about newborn stars can be directly inferred from the UV band, making it a very efficient tracer of the SFR. The region in which these stars are created, however, is highly obscured by dust, which makes them very difficult to observe. Dust is composed of carbonaceous and silicate grains and absorbs part of the UV emission and re-emits it in the IR band. For example, Fig. 10 of Buat et al. (2019) shows that the total SFR of a galaxy is the sum of the SFR obtained from UV/optical measurements and the SFR estimated from IR data. Because the role played by dust is so important, it is fundamental for the SED fitting process to introduce attenuation laws that describe how dust obscures the light emitted by the stars.

The attenuation law developed by Calzetti et al. (1994) for nearby UV-bright starburst galaxies is by far the most common law used in literature. However, other laws such as those proposed by Charlot et al. (2000) and Lo Faro et al. (2017) are widely

employed in the SED fitting codes. Małek et al. (2018) used a combination of UV and IR observations to determine the best approach to fit SEDs of millions of galaxies from the *Herschel Extragalactic Legacy Project* (HELP) across a wide redshift range ($0 < z < 6$) to obtain homogeneous estimates of the main physical properties. They found that using three different attenuation laws, the estimate of stellar masses can change by a factor of 2 on average. Similar results were found in a sample of Ultra-Luminous IR Galaxies at $z \sim 2$ for instance by Lo Faro et al. (2017), for galaxies obtained from the semi-analytic galaxy formation model GALFORM by Mitchell et al. (2013), and by Burgarella et al. (2013), who combined UV to IR measurements up to $z = 3.6$ to calculate the redshift evolution of the total SFR and dust attenuation. They found that the attenuation increases up to $z = 1.2$ and then decreases at higher redshift. The ratio of UV and far-IR (FIR) emission also serves as an indicator of dust attenuation in galaxies (Buat et al. 2005, Takeuchi et al. 2005). All these factors require the combined usage of UV and IR observations to provide a better understanding of the star formation history (SFH), SFR, and dust attenuation properties of the galaxies. In order to perform the SED fitting of galaxies, different methods and codes were developed, such as STARLIGHT (Cid Fernandes et al., 2005), VESPA (Tojeiro et al., 2007), Hyperz (Bolzonella et al., 2000), Le Phare (Arnouts et al. 1999, Ilbert et al. 2006), PÉGASE.3 (Fioc et al. 2019), and COSMOS2020 (Weaver et al. 2021) together with Bayesian SED fitting codes such as GOSSIP (Franzetti et al., 2008), PROSPECTOR (Leja et al., 2017), CIGALE (Noll et al. 2009; Boquien et al. 2019), and BayeSED (Han et al., 2014).

The main problem of the multi-wavelength fitting technique is the lack of high-quality IR observations, which is due to instrumental sensitivity and the lower resolution of wide IR cameras or extremely expensive sub-millimeter observations such as those with ALMA. In contrast, a very large and high-quality coverage of the optical part of the spectrum is usually available for wide-field surveys and narrow and deep-field imaging with several ground and space telescopes. With the upcoming *Legacy Survey of Space and Time* (LSST, Ivezić et al. 2019) from the Vera C. Rubin Observatory, we will obtain even higher-quality optical images in the *ugrizy* bands. The LSST survey will observe about 20 billion galaxies during ten years of observations. Most of these galaxies will not have any counterparts in the available IR catalogs. Moreover, IR astronomy often has blending issues, which makes a precise match of optical and IR sources even more difficult (Hurley et al. 2017, Pearson et al. 2018).

The LSST will be the largest (8.4 meters of the primary mirror) wide-field ground telescope designed to obtain repeated images covering the sky that is visible from Cerro Pachón in Chile. The survey will observe about $30\,000\text{ deg}^2$ of the southern sky, covering the wavelength range 320-1 050 nm. At the end of the ten-year survey, it will reach a magnitude depth ~ 27.5 in *r* band and similar in the other bands. Considering the depth of forthcoming observations, it is expected that the LSST will unveil a significant number of faint galaxies that have remained undetected in current wide-area surveys. These potentially large datasets will raise multifold questions, such as how we can use only LSST optical observations to obtain estimates of the main physical properties of galaxies, and how realistic and reliable they would be. We investigate these topics by performing a simulation of LSST observations of main-sequence (hereafter MS) galaxies that form a nearly linear relation (in log-log space) between their stellar mass and SFR (Noeske et al. 2007, Elbaz et al. 2010, Rodighiero et al. 2011, Speagle et al. 2014, Schreiber et al. 2015, Whitaker et al. 2015, Pearson et al. 2018). Main-sequence galaxies constitute the dominant population in deep fields such as COSMOS and ELAIS N1, which can reach very faint optical magnitudes ($\sim 29\text{-}30$ mag). The LSST is expected to expand the observed MS population

of galaxies to other fields that are not currently covered by deep-field surveys. For this reason, we decided to focus on the MS galaxies.

The paper is organised as follows. In Section 4.3 we describe the data and the HELP project. In Section 4.4 we present the sample selection, outliers, and starburst, and the method we used for this work. In Section 4.7 we discuss the simulated LSST magnitude and errors. The same section, together with Section 2.6 and 2.7, presents the results. Our conclusions are presented in Section 4.9. Throughout this paper we use the WMAP7 cosmology (Komatsu et al., 2011): $\Omega_m = 0.272$, $\Omega_\Lambda = 0.728$, and $H_0 = 70.4 \text{ km s}^{-1} \text{ Mpc}^{-1}$.

2.3 Data

The HELP collaboration provides extremely valuable multi-wavelength data over the HerMES (Oliver et al., 2012) and the H-ATLAS survey fields (Eales et al., 2010) and other relevant *Herschel* fields. The total area of HELP is $1\,269.1 \text{ deg}^2$ (Oliver et al. in prep, Shirley et al. 2019). *Herschel* was equipped with two imaging instruments, the Photodetector Array Camera and Spectrometer (PACS; Poglitsch et al. 2010), which observed the FIR at 100 and 160 μm , and the Spectral and Photometric Imaging Receiver (SPIRE; Griffin et al. 2010), which covered the 250, 350, and 500 μm wavelength ranges.

Surveys that combine a wide range of wavelengths have particular identification issues because the spatial resolution of the sources is different in different bands. To correct for this issue, HELP builds a master list catalog of objects as complete as possible for each field and uses the near-IR (NIR) sources of this catalog as prior information to deblend the *Herschel* maps. A detailed description can be found in Shirley et al. (2019). The tool developed to obtain the photometry of *Herschel* sources, XID+ (Hurley et al., 2017), is a probabilistic deblending algorithm that extracts source flux densities from photometry maps that show source confusion. It uses Bayesian inference to explore the posterior probability distribution and provide probability density functions (PDFs) for all prior sources, and thus flux and uncertainties can be estimated. A detailed description can be found in Hurley et al. (2017). The whole procedure is described in Notebook and stored in a GitHub repository¹.

We use two HELP fields because many multi-wavelength data are available within their wide-field coverage: the European Large Area ISO Survey North 1, hereafter ELAIS N1 (Oliver et al., 2000), and the COSMOS field (Laigle et al., 2016). In addition to data from two PACS and three SPIRE maps, we used available sets of photometric data at shorter wavelengths for both fields (listed in Table 2.1 and described below in Sections 2.3.1 and 2.3.2). Based on true galaxy observations from these fields, we evaluate the LSST-like observations we used for further analysis.

2.3.1 ELAIS N1 field

According to the HELP strategy, all sources detected in any of the Spitzer IRAC bands were used as a prior for XID+ to obtain FIR fluxes. XID+ was run on the Spitzer MIPS 24 μm and *Herschel* PACS and SPIRE maps. The flux level at which the average posterior probability distribution of the source flux becomes Gaussian is 20 $m\text{Jy}$ for MIPS, 12.5 and 17.5 $m\text{Jy}$ for 100 μm and 160 μm PACS bands, respectively, and 4 $m\text{Jy}$ for all three (250, 350, and 500 μm) SPIRE bands (for more details, see Hurley et al. 2017; indicating that information from data dominates those of the prior). In the

¹https://github.com/H-E-L-P/dmu_products

deblending procedure, the priors used to compute the fluxes satisfied two criteria: they must have an IRAC 1 band detection, and they must have been detected in either the optical or NIR wavelengths to eliminate artifacts. More information about the catalog can be found in Małek et al. (2018), Shirley et al. (in prep.), and on the main webpage of the HELP project².

In addition to the FIR bands, the catalog is built on a position cross-match of all the public survey data available in the optical and mid-IR (MIR) range. This comprises observation from the *Isaac Newton* Telescope/Wide Field Camera (INT/WFC) survey (González-Solares et al., 2011), the Subaru Telescope/Hyper Suprime-Cam Strategic Program catalogs (HSC-SSP; Aihara et al. 2018), the Panoramic Survey Telescope and Rapid Response System (Pan-STARRS; Chambers et al. 2016), the UK Infrared Telescope Deep Sky Survey – Deep Extragalactic Survey (UKIDSS–DXS) (Swinbank 2013; Lawrence et al. 2007), the *Spitzer* Extragalactic Representative Volume Survey (SERVS; Mauduit et al. 2012), and the *Spitzer* Wide InfraRed Extragalactic Survey (SWIRE; Lonsdale et al. 2003; Stauffer et al. 2005). We show the list of filters for ELAIS N1 in Table 2.1. The whole matching procedure is described in Shirley et al. (2019).

2.3.2 COSMOS field

For the COSMOS field, the XID+ analysis was performed on *Spitzer* and *Herschel* maps for all the sources with fluxes greater than $1 \mu Jy$ in any of the IRAC bands from the COSMOS2015 catalog (Laigle et al., 2016). The fluxes obtained follow the criterion of goodness defined in XID+ and correspond to a Gaussian posterior distribution of the estimated flux.

Starting with this multi-wavelength catalog, COSMOS2015 (Laigle et al., 2016), ancillary photometry was added with a position cross-match with other public surveys, again containing optical and MIR observations. Other than the one already mentioned for ELAIS N1, this comprises the WIRCam Deep Survey (WIRDS, WIRCam bands J, H, Ks), the VLT Survey Telescope (VST; Arnaboldi et al. 1998), the Victor Blanco 4 m Telescope, the Visible and Infrared Survey Telescope for Astronomy (VISTA; Emerson et al. 2006, Dalton et al. 2006), and the UKIDSS-LAS (WFCAM bands J, H, K) catalogs. (The merging strategy is the same as for ELAIS N1 and is described in detail in Shirley et al. (2019)). The list of filters used for COSMOS survey is shown in Table 2.1.

Detailed description of both fields (the area, mean depths in different filters, all raw files and ancillary data, and many others) can be found on the http://hedam.lam.fr/HELP/dataproducts/dmu31/dmu31_Field_overviews/ webpage.

2.3.3 Total sample

As part of the HELP database, both field catalogs include photometric redshifts generated using a template fitting method that is based on the Bayesian combination approach described in Duncan et al. (2018). The authors investigated the performance of three photometric redshift template sets as a function of redshift, radio luminosity, and infrared/X-ray properties over the NOAO Deep Wide Field Survey Bootes and COSMOS fields. The three template sets are (1) the default EZY reduced galaxy set (Brammer et al., 2008), (2) XMM COSMOS templates (Salvato et al., 2009), and (3) the atlas of Galaxy SEDs (Brown et al., 2014).

²<http://hedam.lam.fr/HELP/>

TABLE 2.1: List of filters for the ELAIS N1 and COSMOS fields.

| Telescope | Instrument | Elais-N1 filters | COSMOS filters |
|-----------------|-----------------|--------------------------------|--------------------------------|
| CFHT | MegaCam | u, g, r, y, z | u, g, r, i, y, z |
| | WIRcam | | H, J, Ks |
| Subaru | HSC | g, r, i, z, N921, y | g, r, i, z, N921, y |
| Isaac Newton | Wide Field Cam. | u, g, r, i, z | |
| PanSTARRS1 | Gigapixel Cam.1 | g, r, i, z, y | g, r, i |
| UKIRT | WFCam | J, K | J, H, K |
| VST | OmegaCAM | | u,g,r,i |
| BLANCO | DEcam | | g, r, z |
| VISTA | Vircam | | J, H, Ks, y |
| <i>Spitzer</i> | IRAC | 3.6, 4.5, 5.8, 8.0 (μm) | 3.6, 4.5, 5.8, 8.0 (μm) |
| | MIPS | 24 (μm) | 24 (μm) |
| <i>Herschel</i> | PACS | 100, 160 (μm) | 100, 160 (μm) |
| | SPIRE | 250, 350, 500 (μm) | 250, 350, 500 (μm) |

The total sample includes 39 329 objects for the ELAIS N1 survey and 14 864 for COSMOS, with FIR detections in at least two photometric bands with a signal-to-noise ratio (S/N) ≥ 3 . This cut is performed to remove objects with unreliable photometry and thus improves the quality of the SED fitting process. We kept in mind that by employing the selection described above, we restricted our analysis to only a subsample of galaxies that LSST will observe, which are objects that are bright in the FIR. Then, as we show in the next section, we selected only the so-called MS galaxies observed in the spectral range from UV to FIR because these are the most commonly observed types of galaxy. The considered bands are u, g, r, i, z, N921, y, J, H, K, Spitzer IRAC 3.6, 4.5, 5.8, and 8.0 μm , Spitzer MIPS 24 μm , and five passbands from Herschel, two from PACS (100 and 160 μm), and three from SPIRE (250, 350 and 500 μm) across the ELAIS N1 and COSMOS fields.

2.4 Method: SED fitting, starbursts, and outlier detection

2.4.1 SED fitting with CIGALE

The SED fitting was performed with the Code Investigating GALaxy Emission³ (CIGALE). For a detailed description of the code, we refer to Boquien et al. (2019). We provide a brief summary here. CIGALE is a Bayesian SED fitting code that combines modeled stellar spectra with dust attenuation and emission. CIGALE preserves the energy balance considering the energy emitted by massive stars, which is partially absorbed by dust grains and then re-emitted in the MIR and FIR. The quality of the fit is expressed by the best χ^2 (and a reduced best χ^2 defined as $\chi_r^2 = \chi^2 / (N - 1)$, with N the number of data points). The minimum value of χ_r^2 corresponds to the best model selected from the grid of all possible computed models from the input parameters. The physical properties and their uncertainties are estimated as the likelihood-weighted means and standard deviations.

To obtain the starting MS sample of galaxies with the correct physical properties to compare them with those obtained with LSST alone, we ran CIGALE on

³<https://cigale.lam.fr>

TABLE 2.2: Input parameters for the code CIGALE.

| Parameters | Values |
|---|--|
| Star formation history: | |
| <i>Delayed star formation history + additional burst</i> | |
| e-folding time of the main stellar population model (Myr) | 1000, 2000, 3000, 5000, 7000 |
| e-folding time of the late starburst population model (Myr) | 5000 |
| Mass fraction of the late burst population | 0.001, 0.01, 0.03, 0.1, 0.3 |
| Age (Myr) | 1000, 2000, 3000, 4000, 5000, 6500, 10000 |
| Age of the late burst (Myr) | 10, 40, 70 |
| <i>Delayed star formation history</i> | |
| e-folding time of the main stellar population model (Myr) | 1000, 2000, 3000, 4000, 5000, 6500, 8000 |
| Age (Myr) | 500, 1000, 3000, 4000, 5000, 6000, 7000, 8000, 9000, 10000, 12000 |
| Mass fraction of the late burst population | 0.0 |
| Single stellar population: Bruzual et al. 2003 Bruzual et al. (2003) | |
| Initial mass function | Chabrier et al. 2003 Chabrier (2003) |
| Metallicities (solar metallicity) | 0.02 |
| Age of the separation between the young and the old star population (Myr) | 10 |
| Dust attenuation law: Charlot & Fall 2000 Charlot et al. (2000) | |
| A_V in the Birth Clouds | 0, 0.05, 0.1, 0.3, 0.8, 1.2, 1.7, 2.3, 2.8, 3.3, 3.8, 4.0, 4.2 |
| Power law slopes of the attenuation in the birth clouds | -0.7 |
| BC to ISM factor (A_V ISM / A_V BC) | 0.5, 0.8 |
| slope ISM | -0.7 |
| Dust emission: | |
| <i>Draine & Li 2014 Draine et al. (2014)</i> | |
| Mass fraction of PAH | 1.12, 2.5, 3.19 |
| Minimum radiation field (U_{min}) | 5.0, 10.0, 25.0 |
| Power law slope dU/dM (U^α) | 2.0, 2.8 |
| Fraction illuminated from U_{min} to U_{max} (γ) | 0.02 |
| <i>Dale et al. 2014 Dale et al. (2014)</i> | |
| AGN fraction | 0 |
| Power law slope dU/dM (U^α) | 2.0 |

the ELAIS N1 and COSMOS samples with the physical modules and parameters reported in Table 2.2. We did not use the AGN module (see App. 2.9.2 and Sec. 2.4.5). As shown in Małek et al. (2018), this set of parameters corresponds to the set that best fits a large sample of IR-detected galaxies in the 23 HELP fields for the redshift range $0 < z < 6$. We used an SFH modeled as a delayed exponential function with an additional exponential burst to select and remove starburst galaxies from our sample in order to retain MS galaxies alone. We performed the SED fitting by employing the modified version of the Charlot et al. (2000) attenuation law, which was employed in Małek et al. (2018) for a large sample of multi-wavelength HELP data. We used the Draine et al. (2014) dust emission module. A detailed description of each module can be found in Boquien et al. (2019) and Małek et al. (2018).

To improve the quality of our selection, we selected only objects with redshift lower than 2.5 from the full sample. Our cut in redshift was not related with the LSST redshift range because the photometric redshifts for the LSST will be applied and calibrated over the range $0 < z < 4$ for galaxies to $r \sim 27.5$ LSST Science Collaboration et al. (2009). The $z < 2.5$ is related to the redshift distribution in the ELAIS N1 and COSMOS fields that were used in this analysis, and it also restricts us to high-quality data and so maximises the accuracy of the estimation of physical properties. Moreover, we removed all the objects recognized as possible stars by

GAIA (*flag GAIA* > 0 in the database). In this way, we removed 2 921 objects (7.5% of the sample) from ELAIS N1 and 887 (6% of the sample) from the COSMOS catalog. From now on, we refer to the remaining 36 408 and 13 977 galaxies from the ELAIS N1 and COSMOS fields as the real sample

2.4.2 Selection of starburst galaxies

Galaxies can be classified according to their different properties: morphology, color, environment, mass, etc. A property that is often used in the literature is the rate at which stars are forming out of gas, the SFR. This leads to a definition of three different types of galaxies: passive, normal/MS, and starburst (SB). The boundaries dividing these classifications are not precisely defined because different authors use different methods to distinguish starbursts from MS galaxies (i.e. Rodighiero et al. 2011, Speagle et al. 2014, Elbaz et al. 2018, Donevski et al. 2020). No universally accepted method exists. Nevertheless, there is agreement that the three groups differ in regard to their evolution and physical properties, such as SFH, dust and gas content, and others (Silverman et al. 2018, Elbaz et al. 2018).

Most galaxies observed with the LSST will be composed of active IR galaxies, but the majority of them are likely to be normal, MS-like, or passive galaxies. For example, the current estimate for the contribution of SB galaxies to the full star formation population is about 5% (Schreiber et al. 2016, Béthermin et al. 2017). However, this contribution increases when we isolate brighter IR galaxies (e.g. Miettinen et al. 2017).

To interpret possible bias for the physical parameter estimation, we have to ensure that the selection effects do not produce artificial trends in the analysis. To quantify the accuracy of the physical property estimates of LSST galaxies, we decided to focus on MS objects alone because we can select a large number of these galaxies from the HELP data to obtain a statistically important sample of real and simulated galaxies. The method we used to separate MS galaxies is described in detail in Rodighiero et al. (2011). We divided our sample into four redshift bins (Table 2.3) because the definition of starbursts changes with redshift. It was shown by Schreiber et al. (2015) that the average SFR of star-forming galaxies in the same mass ranges increases with redshift. In this work starbursts are defined according to their specific SFR distribution ($\text{SFR}/M_{\text{star}}$, hereafter sSFR). Figure 2.1 shows that the sSFR follows a Gaussian distribution. We followed the same definition for starbursts as Rodighiero et al. (2011), that is, objects with sSFR that lie above $\overline{\text{sSFR}} + 3\sigma$, where $\overline{\text{sSFR}}$ is the Gaussian mean of the sSFR distribution. The right panel in Fig. 2.1 shows the selected starbursts and the MS galaxies.

To further test the reliability of the SB selection, we compared our distribution and the position of starbursts with the distribution found in Béthermin et al. (2017) (hereafter: B17), a catalog of simulated galaxies. B17 was built on IR/sub-millimeter data, and it is one of only a few models that is able to simultaneously match the total IR number counts and the evolution of the sSFR. It simulates a 2 deg^2 field including physical clustering from a dark matter simulation, and is thus perfectly suited for comparison purposes. Figure 2.2 shows the comparison of the SB distribution derived in this paper with the sample of simulated SBs from B17 (cyan distribution). The simulated SB sample extends to sSFR values that are lower than the sSFR range obtained from our analysis. The discrepancy arises because two different selection methods were used in our work and in B17. On the one hand, B17 randomly drew the SFR of each source using a continuous log-normal distribution (in agreement with the observational results, e.g. Rodighiero et al. 2011) and then

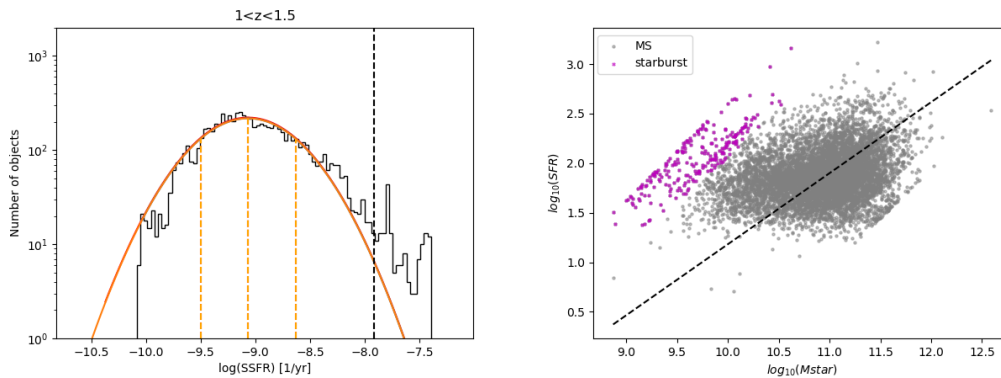


FIGURE 2.1: *left panel*: Example of the sSFR distribution of ELAIS N1 galaxies in the redshift range $1 < z < 1.5$ obtained with the delayed SFH plus an additional burst. The orange line represents the Gaussian fit, and the dashed black line corresponds to the division of starburst (SB galaxies are located on the right side of the line) and MS galaxies. The division is located 3σ away from the centre of the Gaussian. *Right panel*: MS distribution for the same redshift bin. Magenta circles represent SB galaxies selected from the sSFR distribution shown in the left panel. The dashed black line represents the Speagle et al. (2014) MS.

TABLE 2.3: Total number of galaxies and SB percentage for ELAIS and COSMOS fields in each redshift range.

| Redshift range | ELAIS N1 | SB% | COSMOS | SB% |
|----------------|----------|-------|--------|-------|
| 0 - 0.5 | 7 718 | 0.64% | 2 629 | 1.35% |
| 0.5 - 1 | 11 353 | 1.54% | 5 081 | 1.65% |
| 1 - 1.5 | 8 120 | 2.96% | 2 526 | 2.09% |
| 1.5 - 2.5 | 9 214 | 3.19% | 3 733 | 0.83% |

used the Schreiber et al. (2015) definition of the MS to select the galaxies, with an additional offset correction for galaxies at $z < 0.5$. Specifically, B17 defined MS objects as those belonging to the distribution centred on $0.87 \times \text{SFR}_{\text{MS}}$ with 0.2 dex of width and SBs as those belonging to the distribution centred at $5.3 \times \text{SFR}_{\text{MS}}$ with 0.3 dex of width. On the other hand, our selection is based on the statistical analysis presented in Rodighiero et al. (2011), who used the sSFR distribution over a broad redshift range. This makes our selection more discrete, while the selection of B17 is continuous. Figure 2.2 shows that the purity of our selection is very high, but at the same time, it can be incomplete for less active galaxies.

We removed 763 SB galaxies from ELAIS N1 and 228 from COSMOS. Table 2.3 shows the fraction of SB galaxies in the ELAIS N1 and COSMOS field. Our findings for the ELAIS N1 field agree with the literature because it is expected that the fraction of SBs rises from 1% at low redshift to about 3% at higher redshift, and remains flat thereafter (i.e. Béthermin et al. 2012).

2.4.3 Selection of passive galaxies

The SFH with two or more stellar populations is suitable to fit active galaxies with moderate or high SFR. For this reason, we analyzed the remaining objects without

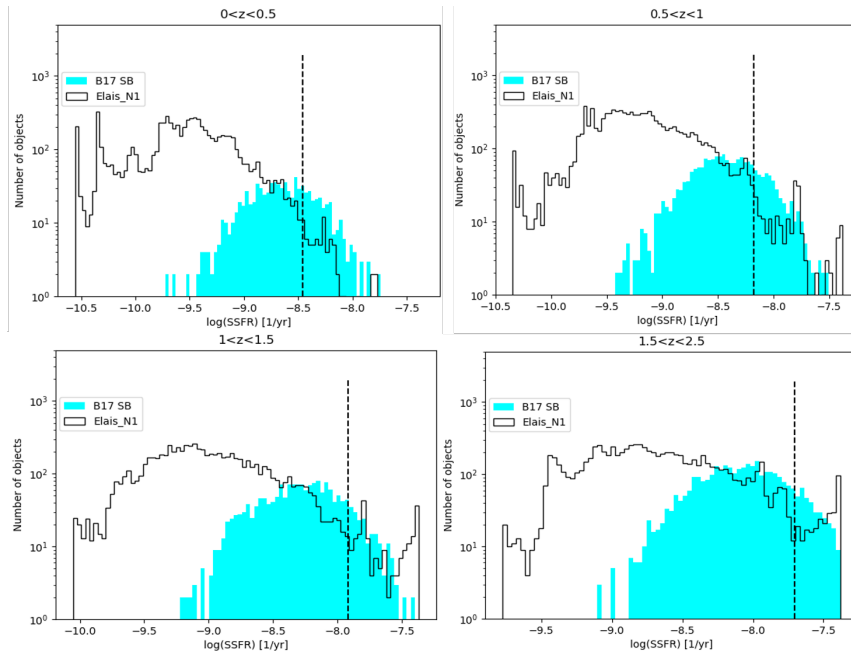


FIGURE 2.2: sSFR distribution in four different redshift bins obtained with delayed SFH plus an additional burst. Open histograms are the galaxy distributions (MS+SB) derived in this work, the dashed black line is the division between SBs (right side of the line) and MS (left side of the line) in our sample, and the cyan full histograms represent the simulated SB sample from B17. The division is located at about 3σ from the Gaussian centre. The sample is the same as for Fig. 2.1, but the binning is different.

SBs employing the delayed SFH in the SED fitting, which is more suitable for normal MS galaxies (Ciesla et al., 2016). All parameters we used for the SED fitting are listed in Tab. 2.2. We again performed the SED fitting to obtain real physical properties of the sample of real MS galaxies. These values were then used to simulate the LSST observations (see Section 2.5.1).

To ensure the purity of the MS sample, we additionally removed possible passive galaxies. As for the starburst evaluation, many different methods were employed in the literature to select red passive galaxies, that is, a UVJ and NUVrK color diagram analysis (Williams et al. 2009, Arnouts et al. 2013), a division based on sSFR (Vulcani et al. 2015, Salim et al. 2016, Salim et al. 2018), or unsupervised machine learning (Siudek et al. 2018). We decided to follow the method described by Salim et al. 2018 by removing all objects with $\log_{10}(\text{sSFR}[\text{yr}^{-1}]) < -11$. In this way, we removed 340 (1%) and 63 (0.5%) galaxies from the ELAIS N1 and COSMOS field, respectively. The almost negligible number of passive galaxies in the HELP sample is related to our initial sample selection, which required at least two *Herschel* measurements with $S/N > 3$.

2.4.4 AGN contribution

Taking advantage of an IRAC detection for all galaxies included in our analysis, we used MIR detections to determine how numerous the AGN population in our sample is. We employed two different selection criteria based on MIR photometry (IRAC bands) analysis. They are explained in detail in Stern et al. (2005) and Donley et al. (2012). Fig. 2.15 shows the IRAC color-color selection using the methods of Donley

TABLE 2.4: Number of AGNs selected based on the MIR features for the ELAIS N1 and COSMOS fields. The last column shows the total number (and percentage) of AGNs in the full sample.

| Method | ELAIS N1 | COSMOS | Total sample |
|----------------------|---------------|---------------|---------------|
| Stern et al. (2005) | 1 269 (3.48%) | 1 334 (9.50%) | 2 603 (5.16%) |
| Donley et al. (2012) | 497 (1.36%) | 291 (2.08%) | 788 (1.56%) |

et al. (2012) (upper panels) and Stern et al. (2005) (lower panels). Using both criteria, we find a negligible number of AGN in comparison to the final sample (1.56% and 5.16% for the criterion of Donley et al. (2012) and Stern et al., 2005, respectively; see Table 2.4 for detailed information for both fields). The redshift distribution of selected AGNs is shown in Fig. 2.16. For consistency with the cuts made previously, we removed AGNs from our sample. We decided to use a conservative approach, and we removed all 2 603 possible AGNs found with the method of Stern et al. (2005) because this selection includes all the AGNs that are detected with the approach of Donley et al. (2012).

2.4.5 Outlier selection

Because the number of galaxies' free parameters is large and unknown, a simple χ_r^2 selection cannot reliably remove the majority of the outliers from our sample. Along with a χ_r^2 selection, we used an estimation of the physical properties L_{dust} and M_{star} (see appendix 2.9.1) in order to eliminate possible outliers and to ensure a high quality of the SED fitting. A similar procedure was used by Matek et al. (2018) for the HELP ELAIS N1 field. Based on these criteria, we removed 2 117 galaxies from ELAIS-N1 and 640 from the COSMOS field. This is 5.81% and 4.75%, respectively.

2.4.6 Final sample

To obtain the final sample of normal star-forming galaxies, we removed possible starbursts (Sec. 2.4.2), passive galaxies (Sec. 2.4.3), and possible AGNs (Sec. 2.4.4). We also performed additional cleaning using outlier selection (Sec. 2.4.5) to remove all galaxies with possibly incorrect photometry, or incorrect matches of UV-optical and FIR measurements. At the end of the process, 31 936 objects were left for ELAIS-N1 (87% of the total sample) and 11 716 galaxies for COSMOS (84% of the total number). Furthermore, in order to validate the photometric redshift estimates used for these objects, we performed a comparison with spectroscopic redshift estimates, which are available for ~ 5000 galaxies in the ELAIS N1 and COSMOS fields. Following the Duncan et al. (2018) definition of critical outliers ($\frac{|\Delta z|}{1+z_s} > 0.2$), we find that the fraction of outliers in our sample is at a level of 4%, which agrees with what was found in previous works (Ilbert et al. 2009, Hildebrandt et al. 2010, Duncan et al. 2018). The final redshift distributions of both samples are shown in Fig. 2.3.

2.5 Estimation of the LSST physical properties

In the following section we discuss the LSST data and uncertainties from simulations and the estimation of the physical properties of the galaxies obtained by performing the SED fitting of i) the fiducial input parameters plus LSST data alone and ii) the fiducial input parameters plus LSST data coupled with other observations.

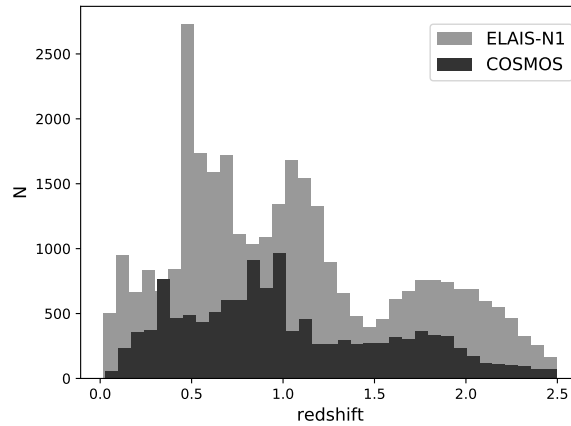


FIGURE 2.3: Redshift distribution of ELAIS-N1 and COSMOS samples based on the approach of Duncan et al. (2018).

2.5.1 Estimating LSST-simulated data and uncertainties

Simulating LSST data has been a popular topic in the past years because of the upcoming start of the survey Ivezić et al. (2019). We derive an ‘LSST-like catalog’ from the best fit of the observational data as described in Sect. 4.3. In this way, we are able to quantify the difference between estimating the physical properties based on the LSST measurements alone and the UV-to-FIR wavelength of the real, observed objects. Considering the depth reached with ten years of survey data, it is very likely that LSST will observe objects that are not visible with the current ground-based survey telescopes, and this work will be a starting point to learn how these objects should be treated with SED fitting methods.

We simulated the observed fluxes in the six LSST bands (*ugrizy*; the filter response curve is provided by the LSST developers team, Ivezić et al. 2019). To obtain LSST fluxes, we ran CIGALE by fitting the photometric measurements and providing the LSST filter response curves for the code. We used a CIGALE module (called *fluxes*) that is specifically designed to estimate the fluxes in the defined filters. We computed LSST fluxes from the best-fit model of each object. We included in our sample all the galaxies that will be detected in all bands at the depth of the ten-year survey: $u < 26.1$, $g < 27.4$, $r < 27.5$, $i < 26.8$, $z < 26.1$, $y < 24.9$. In this way we discard 8 645 objects (23% of the total sample) from ELAIS N1 and 2 623 (19% of the total sample) from COSMOS.

To incorporate an LSST-like observational uncertainty in our catalog, we must take random phenomena into account that might occur during a real observation, such as a change in the sky seeing or the number of visits. The predicted magnitude errors that we converted into flux errors following the conversion provided in the LSST manual (Ivezić et al., 2019) depend on the galaxy magnitude, the sky seeing, and the total survey exposure time in a given filter. We used the LSST simulation software package *CatSim*⁴ to calculate magnitude errors. The error evaluation was based on Eq. 5 of Ivezić et al. (2019) and took variations in the photometry due to hardware and observational components (e.g. detector, darksky, and atmosphere) into account. The evaluated random error was then divided by the square root of

⁴<https://www.lsst.org/scientists/simulations/catsim>

the number of visits during the survey. The LSST manual provides mean values for all these components.

To mimic the real conditions, we added a value that was randomly chosen from a Gaussian distribution centred on the provided mean value to the average value of each component provided in the LSST manual, which had a standard deviation the 10% of the mean. In this process, we varied the number of visits and sky seeing. The assumed standard conditions for these components are 0.8 arcsec for the seeing and a uniform progression that assumes a total of 56, 80, 184, 184, 160, and 160 visits in filters *ugrizy*, respectively, in ten years, where each visit is 30 seconds of integration time.

At the end, to further mimic a possible divergence of the ‘real’ observed flux from the simulated value evaluated from the best-fit SED, we again added a value randomly chosen from a Gaussian distribution centred on 0 to the best-fit SED with the standard deviation of the flux error calculated before. Figure 2.4 shows the magnitude errors as a function of the simulated observed magnitude for our sample of galaxies. We only selected objects that would be observed in all six bands according to our simulation. As a result, we reached the LSST magnitude limit only for the *u* band. The final catalog contains simulated LSST fluxes and uncertainties for 23 291 galaxies in the ELAIS N1 field and 9 093 in the COSMOS field. The catalogs, together with the photometric redshifts and HELP IDs, are available at the HELP virtual observatory⁵.

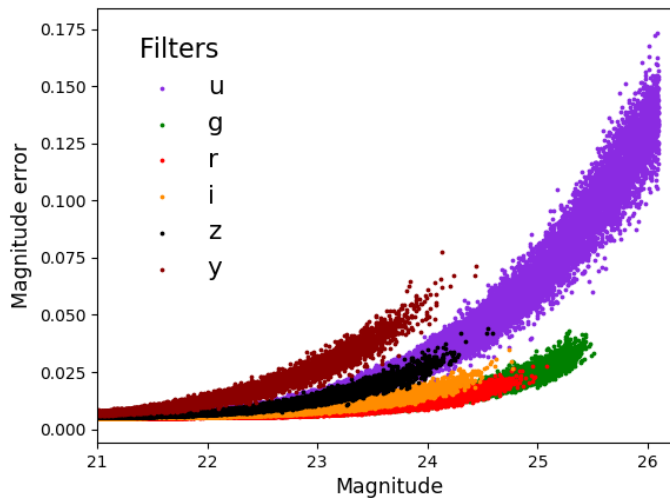


FIGURE 2.4: Magnitude errors vs observed apparent magnitudes for simulated LSST observations from the ELAIS N1 sample. Simulations are cut to the maximum LSST limit. The choice to vary simulation parameters allows us to obtain different errors for similar magnitude values, as we would expect in the case of real observations. The brightest end we reached is 13 mag, but for clarity of the plot, we cut it at 21 mag.

2.5.2 Fiducial parameters and LSST data alone

To estimate the main physical properties of the LSST sample, we ran CIGALE on simulated LSST observations and uncertainties employing the same modules and

⁵<https://www.herschel-vos.phys.susx.ac.uk>

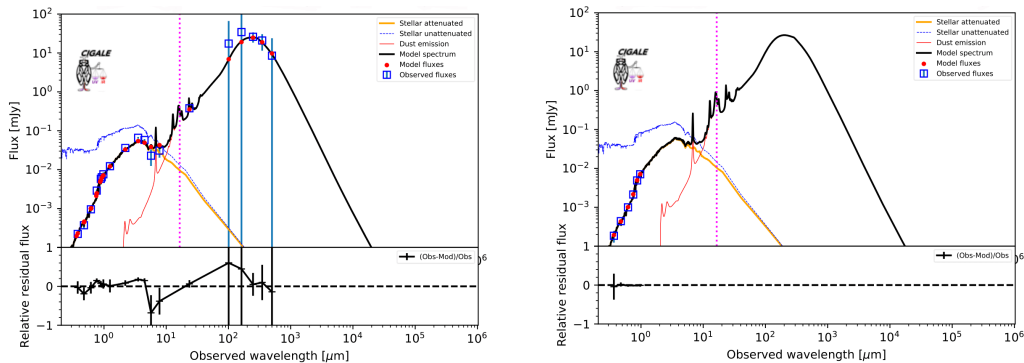


FIGURE 2.5: Comparison of SEDs evaluated for the same object at $z \sim 1$ using the full UV-to-IR observations (*left panel*) and the LSST optical bands alone (*right panel*). The blue square represents the observed fluxes, and the red dots represent the fluxes predicted by the model. The magenta lines delimit the division between optical and IR bands, which is taken into account by CIGALE. The IR emission is not constrained for the LSST estimate.

parameters as were used for the HELP MS sample (Table 2.2, with delayed SFH). Figure 2.5 shows two example SEDs of the same galaxy at redshift 0.92, obtained with the UV-FIR and LSST photometric-only data set, respectively. For this specific case, we found an agreement of estimated stellar masses ($M_{star\ real} = 6.05 \cdot 10^{10} \pm 5.62 \cdot 10^9 M_{\odot}$, $M_{star\ LSST} = 5.59 \cdot 10^{10} \pm 1.80 \cdot 10^{10} M_{\odot}$). Instead, the SFR calculated for the LSST-like photometric data alone is highly overestimated (by a factor of six) with respect to the real value obtained by employing the UV-FIR data set ($SFR_{real} = 11.9 \pm 2.16 M_{\odot} yr^{-1}$ and $SFR_{LSST} = 67.4 \pm 45.9 M_{\odot} yr^{-1}$). Moreover, the residuals for the LSST are very small (but never null), as we can easily find a model that almost perfectly fits just six observations in the optical part. However, the IR part of the SED, and so the dust emission module, is completely unconstrained (we used the same dust emission module from Draine et al. (2014) as was used for the original HELP data with the same grid of parameters).

The relation of SFR and M_{star} in the four redshift bins is shown in Fig. 2.6. In this figure, we compare the MS relation obtained for the LSST-like sample with the relation obtained from the full UV-FIR SED fitting. We show the MS from Speagle et al. (2014) as a reference. At low redshift, the LSST estimation fails to probe low-SFR objects, and this leads to a clear division between the respective MS relations, which overlap at higher redshifts, however. In Appendix 2.9.3 we discuss the scatter between our sample and the MS law. Figure 2.7 shows this overestimation as a function of redshift separately for ELAIS N1 and COSMOS (*left upper panel*). We also plot in the same figure the ratio of the LSST-derived stellar mass, L_{dust} , and M_{dust} and those from the full UV-IR SED fitting. We obtain an overestimation of the dust related properties (SFR, L_{dust} , and M_{dust}) but the values of M_{star} are comparable. The overestimation of the SFR is strongly dependent on the redshift. The ratio of the stellar masses is evenly distributed around zero, leading to comparable results between the two runs because stellar masses mostly rely on optical data. This result holds for the ELAIS N1 and COSMOS fields and shows that there is no dependence on the field.

These results can be explained when we consider how the physical properties are evaluated by the Bayesian method. This is basically done through a likelihood estimation. Each model in the grid of models built from the starting input parameters

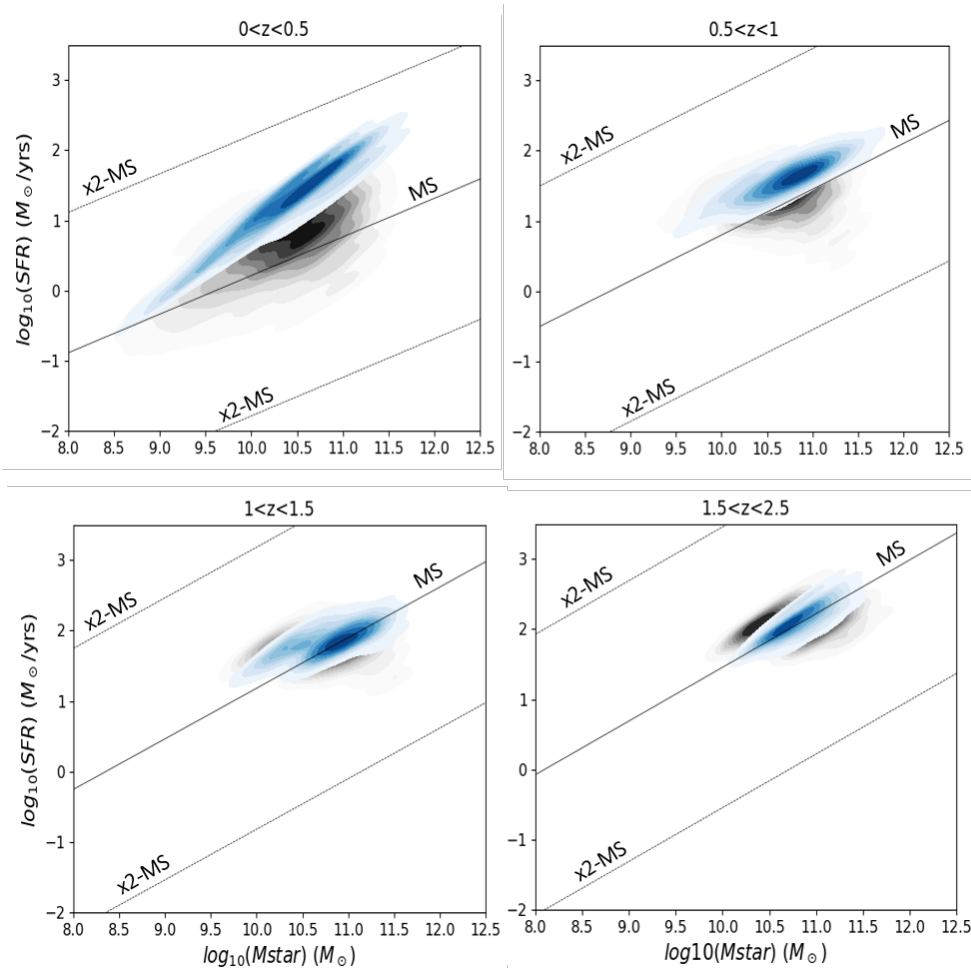


FIGURE 2.6: Main-sequence (SFR vs M_{star}) relation for the ELAIS N1 and COSMOS fields in four redshift bins. In blue we show the LSST-like sample, and in black the real sample. The solid black line represents the MS by Speagle et al. (2014), and the dashed lines mark the loci two times above and below the MS. This plot shows a clear SFR overestimate obtained using LSST bands alone, which tends to disappear at higher redshift ranges.

will have an associated likelihood taken as $\exp(-\chi^2/2)$ that is used as weight to estimate the physical parameters (the likelihood-weighted mean of the physical parameters attributed to each model) and the related uncertainty (see Sec. 4.3 of Boquien et al. 2019). Fitting just LSST optical observations results in high likelihood values even for templates that do not reflect the real physical properties of the modelled galaxy. Because the SFR is partly estimated from the UV emission of the massive young stars in star-forming regions and because this emission is attenuated by the dust and is re-emitted in the IR band, we find that the lack of information about the UV and MIR rest-frame wavelengths for the LSST sample causes CIGALE to overestimate the attenuation. Overestimated attenuation also results in an overestimation of the SFR.

The fluxes observed by the LSST in the optical at high redshift are in the UV rest-frame. Because the UV wavelengths trace young stellar populations, the estimates of the SFR from the SED fitting with CIGALE, significantly improves as a consequence. Figure 2.8 shows an example of an SED superimposed with LSST coverage at different redshifts. Even at $z = 1$, the LSST bands are almost entirely shifted to

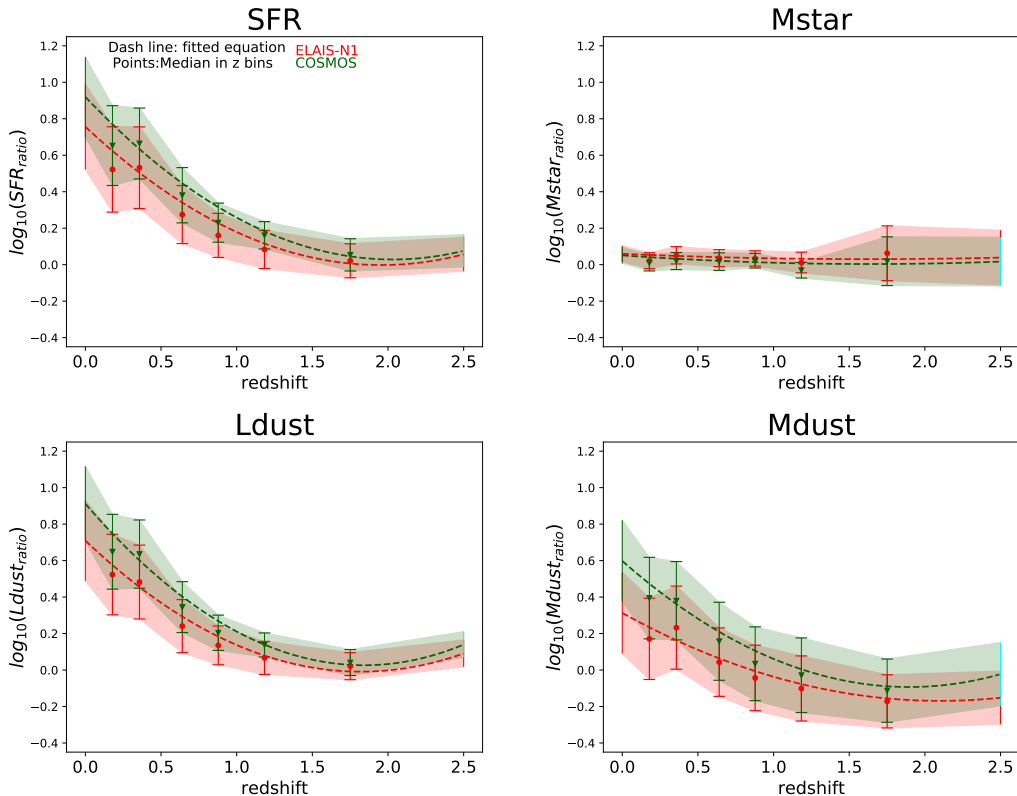


FIGURE 2.7: Ratios of different physical properties obtained from fitting the simulated LSST data alone and from the UV-FIR SED (e.g. $SFR_{ratio} = SFR_{LSST}/SFR_{UV-FIR}$) as a function of redshift for the ELAIS N1 and COSMOS fields. The properties obtained from the UV-FIR SED fitting are considered as the true values. From the upper left panel we show clockwise the SFR, M_{star} , L_{dust} , and M_{dust} comparisons. The dashed lines represent polynomial fits performed on the samples. The points are the median values in each redshift bin, with the median absolute deviation as errors. A ratio equal to zero corresponds to a perfect agreement between the estimates obtained based on the LSST-like sample and the real values. The distributions calculated for ELAIS N1 and COSMOS are comparable within the errors.

the rest-frame UV bands, which range between 0.01 and 0.38 μm . As a result, the dust attenuation is better probed because the LSST bands cover a larger portion of the UV rest-frame spectra, where dust attenuates more effectively, and a better constraint of the SFR is provided. As shown in Fig. 2.7, the differences in the estimated SFR become negligible for $z \gtrsim 1.3$.

In order to obtain a useful function with which to correct for the overestimation of the SFR, we performed a polynomial fit on the SFR ratio distribution of ELAIS N1 and COSMOS combined,

$$\log_{10}(SFR_{ratio}) = 0.26 \cdot z^2 - 0.94 \cdot z + 0.87, \quad (2.1)$$

where SFR_{ratio} stands for SFR_{LSST}/SFR_{real} . However, this formula is highly dependent on the input parameters.

To determine whether the complex set of parameters used for the Draine et al. (2014) model is responsible for the overestimation of the SFR, we ran the whole analysis and adopted the Dale et al. (2014) model. Dust emission in this model is

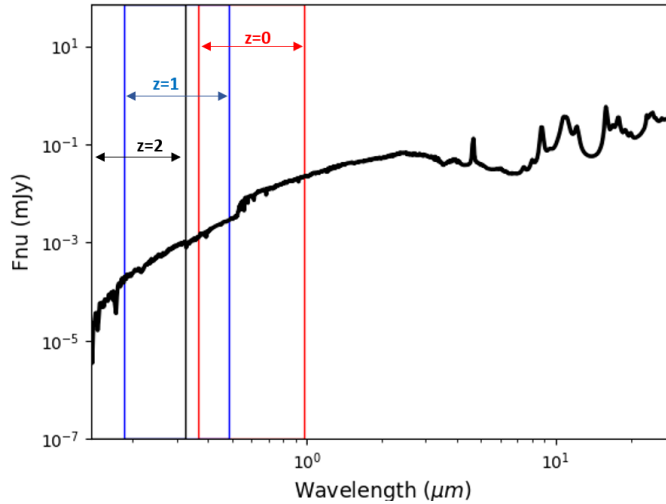


FIGURE 2.8: LSST coverage of an example SED at different redshifts indicated in the panel.

parametrised by a single parameter α defined as $\frac{dU}{dM} = U^\alpha$, where M is the dust mass heated by a radiation field at intensity U . We used the parameter $\alpha = 2$ to better describe the stellar emission from MS galaxies. The module also allows adding an optional AGN component, which we set to 0 for this test. Comparing the LSST physical properties with the real one using the Dale et al. (2014) module, we obtain the same overestimation of the SFR and L_{dust} as was obtained with the Draine et al. (2014) dust emission. We were not able to compare dust mass because it is not an output parameter of the Dale et al. (2014) module. As we found no improvement by employing a simpler model, we decided to keep the results obtained with Draine et al. (2014) for homogeneity with the results published by HELP project (Malek et al., 2018, Shirley et al., in prep.).

2.5.3 Fiducial parameters, LSST, and ancillary data

A different approach to correct for the overestimation consists of applying the SED procedure on the LSST data together with other available observations in different bands (e.g. MIR *Spitzer* bands, FIR *Herschel* Spire bands). Figure 2.9 shows the results for SFR ratios obtained by adding IRAC MIR and SPIRE FIR observations. We expect that by adding the rest-frame NIR part of the SED, the attenuation of the old stellar population will be better constrained, while the MID and FIR mainly constrain the dust emission from the star-forming regions and the missing SFR, which is hidden by dust. The upper left panel of Fig. 2.9 shows that when MIR observations alone are added, the overestimation of the SFR is fully corrected, regardless of the considered redshift range.

The combined use of UV and LSST data might also be expected to correct for the overestimation of the SFR at low redshift. We tested this hypothesis by adding the UV observations from GALEX and performing the SED fitting. We performed a 1.5 arcsec cross-match with the HELP catalog and identified ~ 3000 galaxies with a GALEX counterpart. Figure 2.9 (bottom left panel) shows the comparison of the SFR estimation for LSST-like and the UV-FIR data set of these 3000 galaxies. We conclude from this plot that by adding GALEX observations, we obtain a slightly

lower overestimation in general, which is still consistent with previous results, however, meaning that the observed UV fluxes are not enough to completely correct the differences. Furthermore, for $0.5 < z < 1.5$, we obtain a slight underestimation of the parameter. Nevertheless, we stress that this result can be biased by the low number of GALEX counterparts of the LSST-like catalog and the low quality of GALEX observations for higher-redshift sources. To confirm this statement, we simulated GALEX near-UV (NUV) and far-UV (FUV) observations for the whole sample (we refer to it as $GALEX_{true}$), again using the CIGALE module *fluxes*, and employed it together with the LSST to estimate the physical properties. We decided to cut objects with $z > 1.5$ because after this limit, both NUV and FUV GALEX bands probe emissions below the Lyman break. Fig. 2.17 shows the comparison of the SFR evaluated in this way and the SFR evaluated using LSST observations alone. We find a clear correction of the overestimation, highlighting the great effect that UV observations have on the SFR estimation. We confirm that the overestimation is partially due to the lack of the direct tracer of the young stellar population. Unfortunately, no new UV missions are planned in the near future, therefore we do not expect a UV coverage that large enough to be used in conjunction with the LSST in order to correctly estimate the physical parameters.

Figure 2.9 (bottom right panel) also shows the correction of M_{dust} estimates that we obtained by adding the SPIRE FIR observations. The good agreement of the LSST plus SPIRE and the real estimates arises because the FIR emission is a direct probe of the dust mass.

2.6 Testing different input parameters in CIGALE

As discussed in section 2.4.1, the set of parameters we employed for the analysis presented so far corresponds to the best set to fit the large sample of objects in the area of $\sim 1300 \text{ deg}^2$ of the HELP field. However, we also investigated how much the results obtained by fitting the LSST simulated data alone are dependent on the CIGALE input parameters. In particular, we tested possible variations of the derived galaxy physical quantities as a function of the input radiation field, PAH fraction, and dust attenuation law. To test how the variations in the dust attenuation laws change our results, we refitted the UV to IR photometry and rederived the LSST simulated data that were later refitted by adopting a different attenuation law.

2.6.1 Dust emission and mass

Dust continuum emission is only determined by the energy balance, and therefore it only depends on the amount of absorbed radiation. As a consequence, the total dust emission is not affected by the parameter U_{min} , but is only sensitive to the total absorbed radiation. In contrast, we find that M_{dust} is not constrained by using the LSST data alone, and its estimate is largely affected by the U_{min} parameter. When U_{min} is changed, the amount of radiation that irradiates the dust is modified, but the amount of dust emission is unaltered. As a consequence, higher input values of U_{min} are translated into lower M_{dust} and vice versa. High values of the U_{min} ($U_{min}=25$) parameter yield an underestimation of M_{dust} . As a consequence, because the shape of dust emission is completely unconstrained using the LSST coverage alone, the Bayesian method cannot evaluate the U_{min} parameter and assigns an average value from all considered input parameters to all galaxies. This results in a strong dependence of dust mass estimates on the input parameters. When the dust emission is

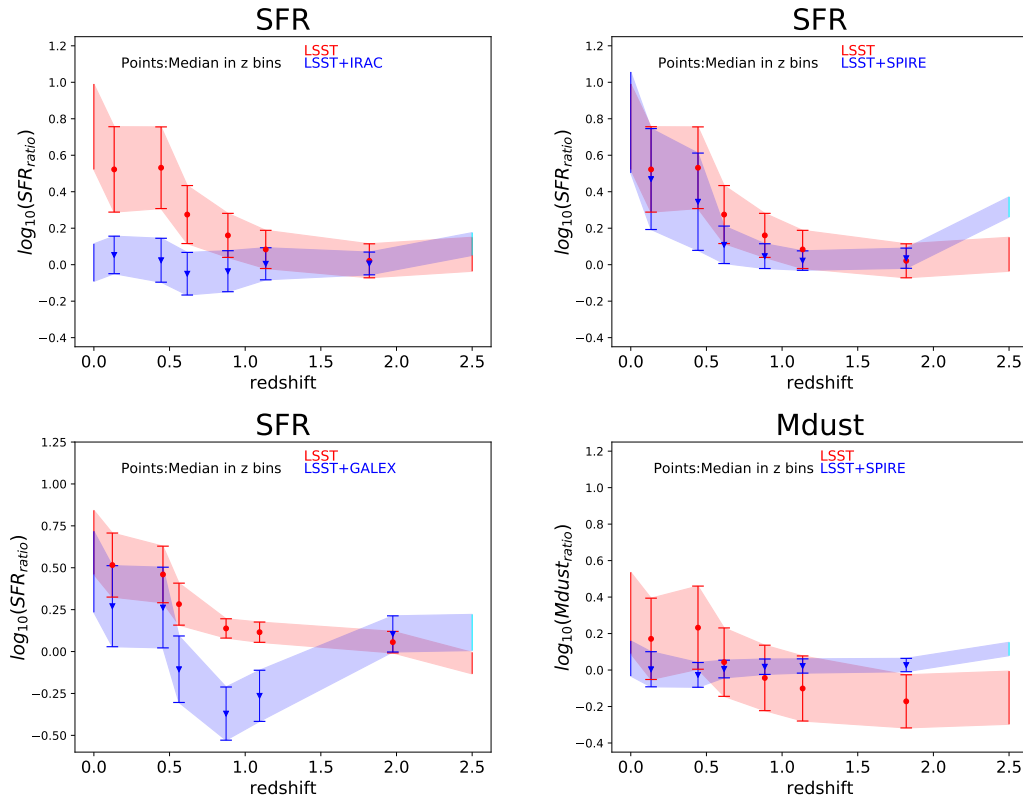


FIGURE 2.9: *Upper left panel*: SFR ratio, defined as in figure 2.7, estimated with LSST observations alone (red) and with LSST+IRAC observations (blue). The two samples disagree at low redshift, but the comparison improves at high redshift, highlighting the redshift dependence of the results. With the addition of MIR observations, the LSST-only estimates are consistent with the UV-IR estimates. *Upper right panel*: Same comparison, but adding FIR SPIRE observations. In this case we did not fully remove the overestimation, which highlights that the problem lies in the lack of rest-frame MIR data. *Lower left panel*: Same as in the other panels, but adding GALEX observations. We obtain a slight decrease in the overestimation. For this comparison we considered the ~ 3000 objects that have a counterpart in the GALEX database. *Lower right panel*: M_{dust} ratio evaluated with LSST observations alone (red) and with LSST+SPIRE observations (blue). The results are consistent with the ‘real’ ratio with a very low scatter.

constrained using SPIRE observations, the U_{min} parameter is well evaluated by the Bayesian method, and so is the dust mass.

The use of different attenuation laws also changes the estimates of dust emission and mass because the radiation absorbed and the re-emitted by dust grains is modified. By using either the Calzetti et al. (2000) and Charlot et al. (2000) attenuation laws, we obtain an overestimation of the dust luminosity over the entire redshift range. The trends of the dust luminosity ratios and the redshift are different, however. When we adopt Calzetti et al. (2000), we obtain a constant slight overestimation of the dust mass, centered around 0.3 dex throughout the whole redshift range, and when we use Charlot et al. (2000), the dust mass is overestimated for local galaxies, and underestimated for redshift greater than ~ 1 .

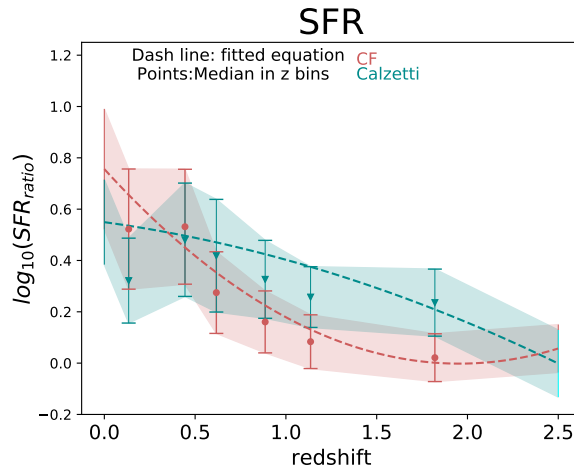


FIGURE 2.10: SFR overestimation as a function of redshift for the Charlot et al. (2000) (red) and Calzetti et al. (2000) (cyan) attenuation laws.

2.6.2 Dust attenuation laws and star formation history

We find that the SFR to is not affected by the PAH fraction or the input radiation field (U_{min} and α parameters) because the input quantities only shape dust emission. The SFR is instead affected by our choice of attenuation law. When the Calzetti et al. (2000) modified attenuation law is employed, we obtain the results shown in Fig. 2.10. The results using the Calzetti et al. (2000) attenuation curve agree well with those obtained with the Charlot et al. (2000) prescription at low redshift but change in shape at higher z . The overestimation with the Calzetti et al. (2000) curve is more constant throughout the redshift range, but it decreases faster when the Charlot et al. (2000) prescription is used.

Furthermore, we also examined the dependence of SFR estimates on the SFH module. Performing the entire process using a delayed plus additional burst SFH, we obtain an even higher overestimation when estimated using LSST observations alone, which again decreases at higher redshift.

We also inspected changes in the SFR difference when the best values were used instead of Bayesian values for the LSST-like sample. We find a consistency between the SFR from the LSST best fit and the one estimated from the UV-FIR best fit, finding $\log_{10}(SFR_{LSST,best}/SFR_{UV-FIR,best})$ very well distributed around zero with a scatter of 0.05 dex. This result shows a good agreement of the best templates of the two runs. It can be understood as follows: The fluxes for the LSST-like run were calculated based on the best template of the UV-FIR run. We confirm that the differences we found must be sought in the Bayesian analysis, which tends to overestimate the attenuation when it is employed on LSST data alone. Unfortunately, being estimated directly from the SED that best fits our data, the best-fit value has several drawbacks that make it unsuitable for this type of analysis. For example, it ignores the degeneracies that can be encountered because models with equally good fits can have very different properties. Moreover, the best fit in itself does not provide information about the uncertainties.

2.7 Application of the $A_{FUV}-M_{star}$ relation to correct for the SFR overestimation

Previous results show major miscalculations of the SFR when LSST data alone are used. Due to the lack of information in the UV and MIR part of the spectrum, the SED fitting results in an overestimation of the attenuation, which leads to the general overestimation of the SFR. At the same time, as it is probed mainly from the optical emission of the galaxy, M_{star} seems to be well estimated using LSST data alone. When we take into account that M_{star} is the result of the previous star formation activity of the galaxy, which is responsible for producing the dust, it could be used as a promising tracer of the dust content.

Several works have recently explored possible relations of M_{star} and dust attenuation (Xu et al. 2007, Martin et al. 2007, Buat et al. 2009, Bogdanoska et al. 2020). Most of them suggest a possible linear relation between A_{FUV} and $\log_{10}(M_{star})$ over a wide mass range ($9 \leq \log_{10}(M_{star}) \leq 12$). According to the literature, this relation is highly dependent on redshift.

Recently, Bogdanoska et al. (2020), hereafter BB2020, modeled a single parameter linear function, assuming a non-zero constant dust attenuation for low-mass galaxies (Eq. 6 in BB2020). They used a sample of galaxies based on the selection criterion that requires IR excess⁶ (IRX) to be directly calculated from the IR-to-UV ratio or by SED fitting. This selection can introduce a bias in the local Universe and above redshift 2–3 due to the IR detection (at high redshift, only very dusty and massive galaxies are detected, while in the local universe, the IR-detected galaxies are rather rare). BB2020 found that the $A_{FUV} - M_{star}$ relation cannot be described with a simple linear function, and they concluded their work with a new relation between A_{FUV} and M_{star} as a function of redshift. In this section, we try to use the $A_{FUV} - M_{star}$ relation provided by BB2020 to estimate the A_{FUV} (we refer to it as $A_{FUV\ BB20}$) of the LSST sample. The procedure is as follows: (1) from the LSST data we estimated the M_{star} , (2) using Eqs. 5 and 6 from BB2020, we calculated $A_{FUV\ BB20}$, and finally, (3) we used $A_{FUV\ BB20}$ as a prior of the new LSST CIGALE run.

Fig. 2.11 shows the $A_{FUV\ BB20}$ compared with the A_{FUV} obtained from the full UV-FIR SED fitting as a function of M_{star} . We find that the estimates $A_{FUV\ BB20}$ are substantially lower than those obtained with the SED fitting process. The difference between $A_{FUV\ BB20}$ and $A_{FUV\ UV-FIR}$ is shown in Fig. 2.12 (green line). The underestimation is accentuated for low-redshift objects. As expected, employing the $A_{FUV\ BB20}$ as prior in the SED fitting process along with LSST observations results in an underestimation of the SFR, as shown in Fig. 2.13, where the ratios of the true SFR and the one derived by different methods are shown. We suspect that the reason for the substantial difference between the two estimates of A_{FUV} can be traced back to the choice of the sample, as the sample used in BB2020 is more general, while in our case, we focused on IR-bright galaxies to ensure the highest quality of the UV-FIR SED fitting process. It is clear from these results that we cannot directly employ the relation of Bogdanoska et al. (2020) to correct for the SFR overestimation for our sample.

We decided to incorporate the general idea presented in Bogdanoska et al. (2020) and to use the $A_{FUV} - M_{star}$ relation in order to correct the SFR for an LSST sample of

⁶The IR excess is defined as $IRX = \log(L_{IR}/L_{UV})$, where L_{IR} stands for total integrated luminosity in the IR, and L_{UV} is the UV luminosity derived from flux measured with a filter, such as GALEX or estimated through a SED process.

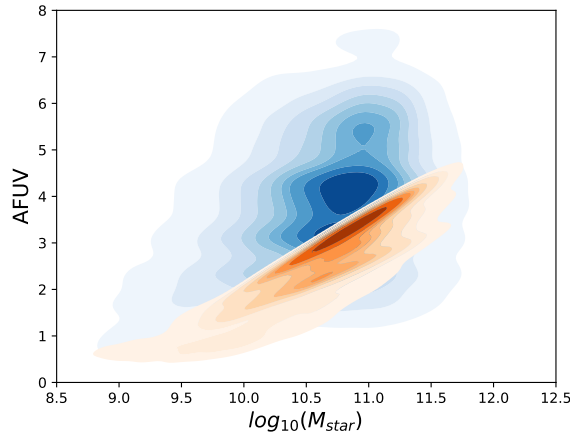


FIGURE 2.11: A_{FUV} as a function of stellar mass estimated from the UV-FIR SED fitting (blue density plot) compared with the A_{FUV} estimated by employing M_{star} from the relation of Bogdanoska et al. (2020).

TABLE 2.5: Obtained a and b coefficients from fitting Eq. 2.2 in the four redshift bins.

| Redshift | a | b |
|----------|-----------------|------------------|
| 0-0.5 | 0.41 ± 0.02 | -1.39 ± 0.21 |
| 0.5-1 | 0.44 ± 0.03 | -0.49 ± 0.30 |
| 1-1.5 | 0.72 ± 0.03 | -3.42 ± 0.34 |
| 1.5-2.5 | 0.83 ± 0.04 | -5.19 ± 0.39 |

data. We built a simplified relation that represented our sample of IR-bright main-sequence galaxies by following a procedure similar to that described by Bogdanoska et al. (2020). For this purpose, we fit the A_{FUV} estimated from the UV-FIR SED fitting as a function of the $\log_{10}(M_{star})$. We used four redshift bins (0-0.5, 0.5-1.0, 1.0-1.5, and 1.5-2.5) to include the redshift dependence of the $A_{FUV} - M_{star}$ relation. Linear, power-law, and exponential functions were tested to obtain the best fit, but we found a negligible difference between them. To be as consistent as possible with the results obtained in the previous works, we decided to use the linear function in the form

$$A_{FUV-LSST} = a \cdot \log_{10}(M_{star-LSST}) + b. \quad (2.2)$$

From the fitting process, we obtained a and b coefficients for each redshift bin. Table 2.5 shows all coefficients together with the uncertainties.

The blue line in Fig. 2.12 shows the difference between the $A_{FUV-LSST}$ calculated with our four linear relations and the one estimated from the UV-FIR SED fitting as a function of redshift. Our relation reproduces the AFUV derived from the fitting of the full SED better than the Bogdanoska et al. (2020) relation. By employing the $A_{FUV-LSST}$ as a prior in the SED fitting along with LSST observations, we obtain the blue relation shown in Fig. 2.13. This figure shows that the SFR overestimation is fully corrected for when the $A_{FUV-LSST}$ prior is employed. This result also proves that knowing the $A_{FUV} - M_{star}$ relation for a given sample of galaxies, it is possible to estimate SFR without the IR counterpart. This requires prior knowledge of the

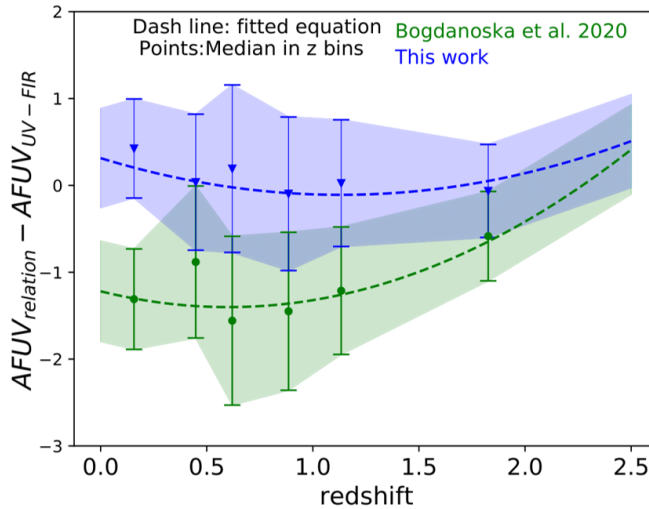


FIGURE 2.12: Difference between A_{FUV} estimated from $A_{FUV} - M_{star}$ relations: Bogdanoska et al. (2020) (green) and Eq. 2.2 with the coefficients reported in Table 2.5 (blue) and A_{FUV} estimated from the UV-FIR SED fitting as a function of redshift.

sample, which is often not available. We are aware that the relation constructed in this work may be applicable only to our sample, or at most to IR-bright normal star-forming galaxies, but further generalization of our results is beyond the scope of this paper. However, considering the extreme usefulness of this relation for future surveys such as the LSST, we are planning to extend our analysis to a more general sample of galaxies in the next work.

2.8 Conclusions

We performed a reliability check of the physical properties estimation of MS galaxies by employing simulated LSST observations. For this purpose, we selected 50 135 and 15 754 objects from the ELAIS N1 and COSMOS fields, respectively, of the *Herschel* Extragalactic Legacy Project (HELP), in order to build the starting set of data to simulate observed LSST fluxes and to obtain reliable estimates of the physical properties of galaxies.

An important part of our analysis was the sample selection. We selected only galaxies from the so-called main sequence by removing all possible SBs from the sample using the same method as Rodighiero et al. (2011), and we removed passive galaxies using the method described in Salim et al. (2018). Furthermore, we also removed galaxies that contain AGN according to the selection of Stern et al. (2005). We also cleaned the sample from all non-typical galaxies by implementing additional quality criteria on physical properties following Małek et al. (2018): for our analysis, we removed all galaxies for which L_{dust} and M_{star} estimated from the full SED fitting (from UV to FIR) were different from those obtained from only the optical or only the infrared part of the spectrum. At the end of the sample selection, we selected 43 652 galaxies. This is 86% of the total sample.

We used this sample of MS galaxies as a prior to calculate the corresponding LSST fluxes in the *ugrizy* bands. We used the LSST simulation software package *CatSim* in order to simulate the uncertainties on the photometric measurements. We took the possible effects due to the hardware and observational components (e.g.

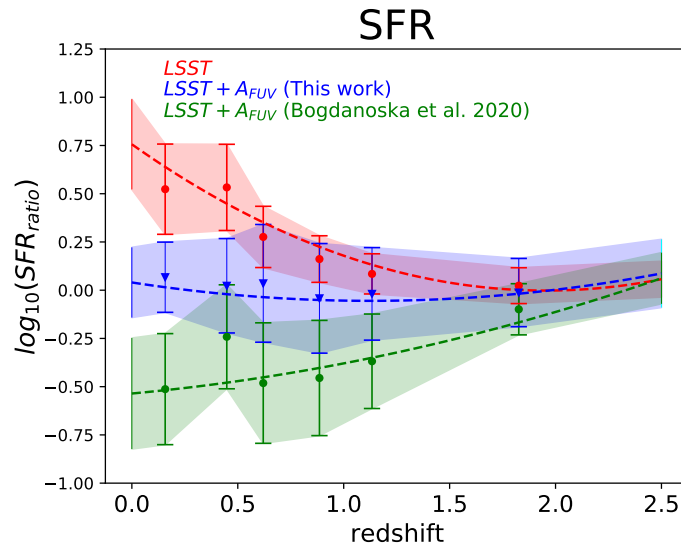


FIGURE 2.13: SFR ratio, defined as in Fig. 2.7, as a function of redshift. The result from the SED fitting employing LSST data alone is shown in red. Green and blue lines represent results from the SED fitting, adding as prior the A_{FUV} from the relations of Bogdanoska et al. (2020) and Eq. 2.2, respectively.

detector, dark sky, and atmosphere) into account. We then estimated the main physical properties of galaxies by performing the SED fitting of the simulated LSST data by employing the same sets of modules and parameters as for the originally used HELP galaxies (Shirley et al. in prep., Shirley et al. (2019)).

We found that M_{star} is well estimated by the LSST-like data set. At the same time, SFR, L_{dust} are overestimated using the LSST-like sample alone, while M_{dust} is completely unconstrained and dependent on the input parameters. The overestimation of the SFR is redshift dependent and clearly decreases with redshift. It disappears at about redshift ~ 1 . We found the relation that can correct the overestimation for the SFR parameter: $\log_{10}(\text{SFR}_{ratio}) = 0.26 \cdot z^2 - 0.94 \cdot z + 0.87$.

We determined the photometric data that can be combined with the LSST data to remove the overestimation. In our analysis we used not simulated but real and sometimes uncompleted data to fully mimic the auxiliary data for the LSST because we do not expect to have better UV or FIR data soon. We found that the most efficient way to correct for the overestimation of the SFR is adding mid-IR observations (IRAC data), while M_{dust} is corrected for by adding the far-IR bands (SPIRE data). The addition of UV observations from GALEX does not correct the differences. Our findings suggest that the main problem of the pure LSST-like sample in the local Universe will be the inability to mimic the real attenuation for the old and young stellar populations.

By testing the input parameters of CIGALE, we found that the SFR overestimation is preserved using different attenuation laws that are commonly employed in the literature (e.g. Calzetti et al. 2000, Charlot et al. 2000), but its trend as a function of the redshift changes. The estimate of M_{dust} is instead found to be dependent on both the input radiation field (U_{min}) and the attenuation law and is unconstrained if LSST data alone are employed for the SED fitting.

In Section 2.7 we showed that another efficient way to correct for the SFR is by

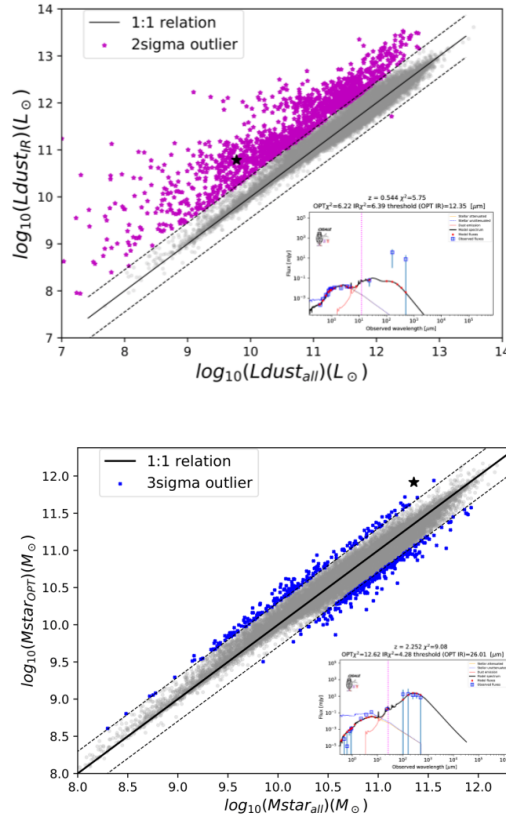


FIGURE 2.14: Outlier selection. Comparison of $L_{dust,IR}$ and $L_{dust,all}$ (upper panel), and $M_{star,OPT}$ and $M_{star,all}$ (bottom panel). L_{dust} inconsistent objects are represented as magenta stars, and full blue stars correspond to the M_{star} outliers. Grey circles represent objects with a consistent estimate of the L_{dust} and M_{star} parameters. Inside each panel we present an example SED of the respective outliers represented with a black star.

exploiting a prior knowledge of A_{FUV} , if this is available. We stress that the further analysis of the $A_{FUV} - M_{star}$ relation can be useful for future surveys and help to properly estimate main physical parameters of galaxies without IR observations. As future work, we plan to extend this test to different SED fitting methods and HELP fields to confirm the systematics of our results.

2.9 Appendix

2.9.1 Outlier selection

To implement additional quality criteria based on the physical properties of the sample, we run CIGALE two more times: (1) for optical data alone to estimate the stellar mass based on the optical measurements alone (from now, $M_{star,OPT}$), and (2) for FIR data alone to calculate the dust luminosity (hereafter $L_{dust,IR}$). In Fig. 2.14 we compare the physical properties obtained by employing this method with the properties from full-wavelength UV-FIR fits ($M_{star,all}$ and $L_{dust,all}$, respectively).

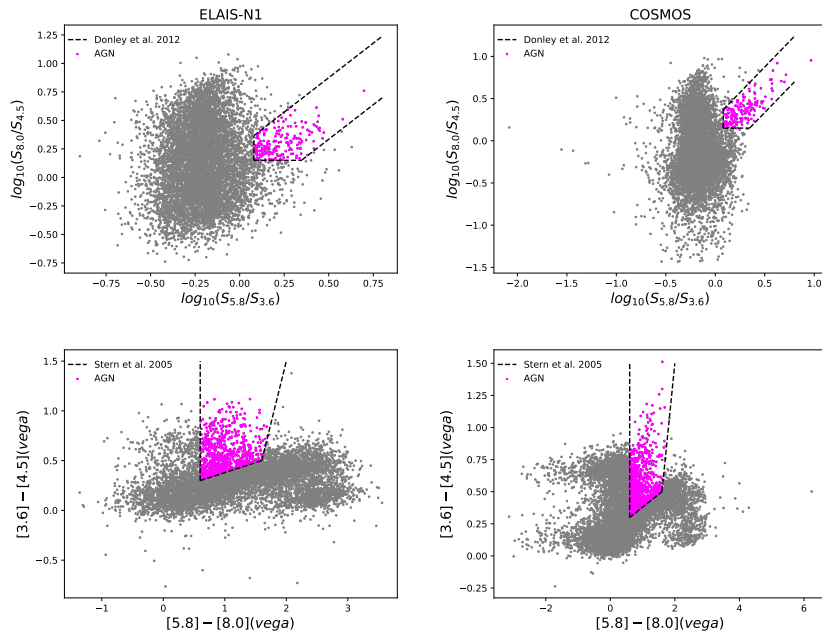


FIGURE 2.15: IRAC color-color diagrams for the ELAIS N1 (left column) and COSMOS (right column) fields. The AGNs (magenta points) are selected following the criteria described in Donley et al. (2012) (upper row, black line) and Stern et al. (2005) (lower row, black line).

Based on this analysis, we eliminated galaxies that showed an L_{dust} and/or M_{star} inconsistency with those estimated from the full SED fitting. Outliers were selected based on the distance from the 1:1 relation:

- criterion 1: L_{dust} inconsistent (within the 2σ level) with the $L_{dust,IR}$
- criterion 2: M_{star} inconsistent (within the 3σ level) with the $M_{star,OPT}$

As shown in Małek et al. (2018), the inconsistency between estimated L_{dust} values might be induced by energy balance issues of heavily dust-obscured galaxies or lensed objects. We also removed galaxies with an inconsistent M_{star} estimation, mostly due to problems with optical and IR catalogs matching. Figure 2.14 also shows two example SEDs for objects considered as outliers. Based on these criteria, we removed 1 642 ELAIS N1 sources (4.5% of the total sample) and 460 COSMOS sources (3.2% of the total sample) with inconsistent estimates of L_{dust} . The M_{star} inconsistency removed 475 (1.3% of the total sample) and 214 (1.5% of the total sample) galaxies for the ELAIS N1 and the COSMOS field, respectively.

2.9.2 AGN selection

The AGN selection in ELAIS N1 and COSMOS fields. We used two different selection criteria based on the MIR features (IRAC bands) analysis: Stern et al. (2005) and Donley et al. (2012). Figure 2.15 shows the IRAC color-color selection using the methods of Donley et al. (2012) (upper panels) and Stern et al. (2005) (lower panels). The redshift distribution of selected AGNs is shown in Fig. 2.16.

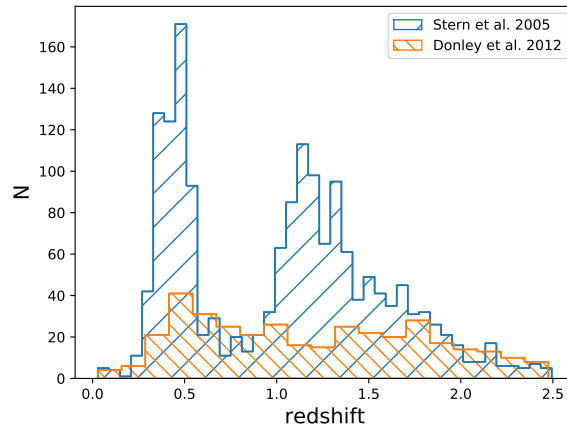


FIGURE 2.16: AGN redshift distribution for the full sample of ELAIS N1 +COSMOS fields.

2.9.3 Scatter of the MS

Star-forming galaxies follow a relatively tight, almost linear relation between SFR and M_{star} that is known as the MS. One of the most noticeable feature is that the MS relation at any given redshift shows a rather small scatter of σ_{MS} that can vary from ~ 0.2 to ~ 0.4 dex (Whitaker et al. 2012, Speagle et al. 2014, Pearson et al. 2018). Here we discuss the scatter of our sample from the MS, given that high scatter could lead to an incorrect estimate of the physical parameters. Figure 2.18 shows the scatter of our objects from two reference main-sequence laws (Speagle et al. 2014, Whitaker et al. 2017), and we compare the results with the MS intrinsic scatter in the literature (Speagle et al. 2014, Pearson et al. 2018). The scatter found in our sample agrees with the scatter found previously in literature within the error bars. This is also valid for the lowest redshift bin where the scatter appears to be the largest. Therefore we are confident that these are MS objects and that the input parameters are adequate to provide us with reliable physical properties for the purposes of this analysis. The origin of this scatter can be traced back to different enhancement or decrement events of star formation that could occur during the galaxy lifetime. Large-scale gas inflow or outflow events can trigger gas compaction or depletion phenomena that can lead to an enhancement or decrement of the SFR of the galaxy (Tacchella et al. 2016).

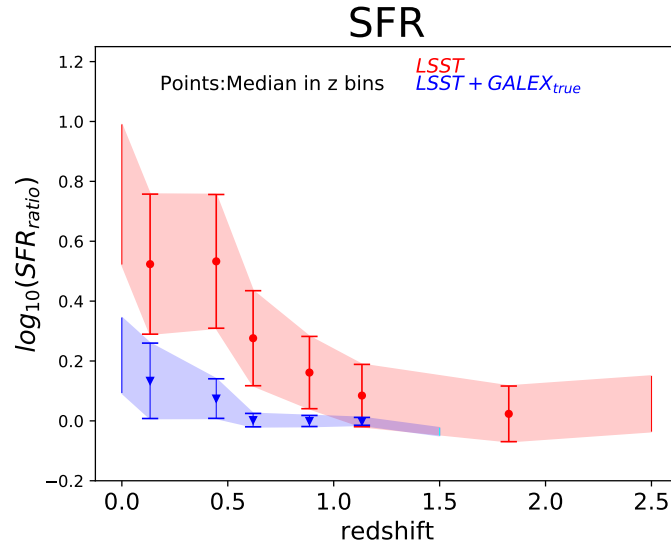


FIGURE 2.17: SFR ratio, defined as in Fig. 2.7, estimated with LSST data alone (red) and LSST plus simulated GALEX observations ($GALEX_{true}$, in blue). Differently from the result shown in Fig. 2.9, in this case we are able to correct the overestimation, underlining the effect that high-quality UV observations would have on the SFR estimate, when available for the entire sample.

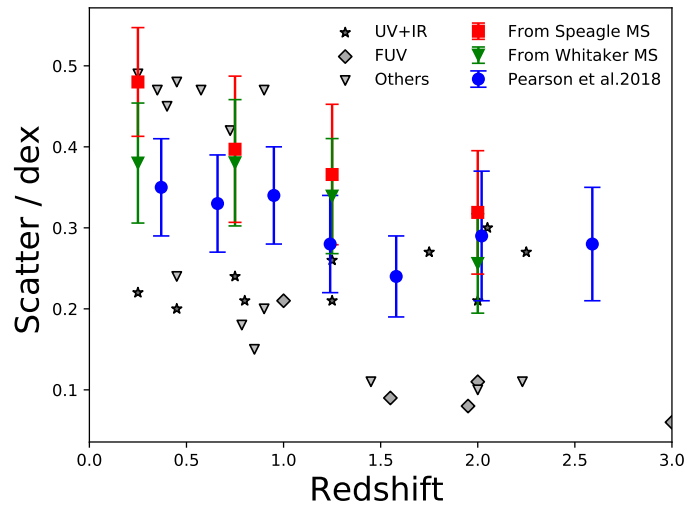


FIGURE 2.18: Intrinsic scatter of our objects around exemplar MS compared with the results found in previous works. Red and green points represent the scatter of our objects from the Speagle et al. (2014) and Whitaker et al. (2017) MS, respectively, blue points represent the results found in Pearson et al. (2018), and grey stars, triangles, and diamonds represent the results presented in Speagle et al. (2014).

3

Properties of low-mass X-ray binaries in Fornax globular clusters

The majority of this chapter originally appeared as ‘Properties of intra-cluster low-mass X-ray binaries in Fornax globular clusters’ by G. Riccio et al. 2022, *Astronomy & Astrophysics*, Volume 664, article number A41 (Riccio et al. 2022)

3.1 Abstract

We present a study of the intra-cluster population of low-mass X-ray binaries (LMXB) residing in globular clusters (GC) in the central 1 deg^2 of the Fornax galaxy cluster. Differently from previous studies, which were restricted to the innermost regions of individual galaxies, this work is aimed at comparing the properties of the intra-cluster population of GC-LMXBs with those of the host galaxy. The data used are a combination of *VLT Survey Telescope* (VST) and *Chandra* observations. We perform a cross-match between the optical and X-ray catalog, in order to identify the LMXBs residing in GCs. We divide the GC-LMXBs into host-galaxy and intra-cluster objects based on their distance from the nearest galaxy in terms of effective radius (R_{eff}). We found 82 intra-cluster GC-LMXBs and 86 objects that are hosted in galaxies. As the formation of LMXBs also depends on the host GC color, we performed a Gaussian mixture model to divide the population into red and blue GCs. As has been found for the innermost regions of galaxies, LMXBs tend to form in red and bright GCs in intra-cluster space as well. We find, however, that the likelihood of a red GC to host an LMXB decreases with galactocentric distance, but it remains approximately constant for the blue GC population. Investigating the X-ray properties of the LMXBs residing in GCs, we find a difference in the X-ray luminosity function between the intra-cluster and host-galaxy sample: both follow a power-law down to $\sim 8.5 \times 10^{37} \text{ erg s}^{-1}$, which is consistent with field LMXBs for the intra-cluster sample, while the latter agree with previous estimates for LMXBs in GCs. We observe a deficiency of bright LMXBs in blue intra-cluster GCs, however. This might indicate a lack of black hole binaries in metal-poor systems. We find no differences between the LFs of field and GC-LMXBs, both following a single power law. We find the GC-LMXBs to contribute to the 17% of the total number of LMXBs in the cluster, with an integrated X-ray luminosity contributing to the 10% of the total observed X-ray luminosity. We further investigated the spectral properties of the GC-LMXBs through their hardness ratio. We detect a tentative difference in the hardness ratio

of two populations, where the intra-cluster GC-LMXBs appear to have harder spectra than the host-galaxy objects. We find the same trend when we compare red and blue GC-LMXBs: the spectra of the blue sample are harder spectra than those of the red sample. This result could suggest a relation between the spectral properties of LMXBs and the host GC color and therefore its metallicity. We discuss the possibilities of spatial biases due to uncertainties in the X-ray spectral response correction and due to contamination by background active galactic nuclei.

3.2 Introduction

Low-mass X-ray binaries (LMXBs) are stellar systems composed of an extremely dense object (a neutron star or black hole) that accretes mass from a secondary star (a main-sequence star of about one solar mass). They represent the dominant X-ray binary (XRB) population in early-type galaxies. It has been shown, in fact, that the amount of LMXBs, and thus their total X-ray emission, correlates with the stellar mass of the hosting early-type galaxy ((e.g. Gilfanov 2004; Kim et al. 2006; Lehmer et al. 2014. These results are supported by large scale population synthesis study performed by Fragos et al. (2013) that models the X-ray binary populations from the first galaxies of the Universe until today. These models give very accurate predictions of the number of XRB, and their emission, expected following an event of star formation. Although, these models only consider XRBs formed via the evolution of primordial isolated binaries, i.e. the field XRB population, neglecting dynamically formed population of LMXBs that can have a significant contribution to the integrated X-ray luminosity of some globular cluster rich elliptical galaxies.

It has been shown, in fact, that a significant fraction of LMXBs resides in GCs. This varies from 10%-20% in small galaxies and reaches $\sim 70\%$ in cD galaxies, depending on the morphological type of the galaxy and on the specific abundance of the GCs e.g. Kim et al., 2009. The GC-LMXB association is particularly interesting as the high stellar density near the center of GCs may trigger the formation of binaries either by three-body process or by tidal capture, formation channels that are not considered in population synthesis models of XRBs. It was observed that LMXBs tend to form in bright GCs, as expected if the luminosity is a proxy for the total number of stars they contain (Fabbiano 2006, and references therein). On the other hand, size, and concentration reflect the efficiency of dynamical interaction and favor binary formation in dense environments. Furthermore, the formation can also be influenced by the mass, size, and metallicity of GCs. Red metal-rich GCs are about three times more likely to host LMXB than blue (metal-poor) GCs, in part because red GCs are denser on average than the blue counterpart (Jordán et al. 2004, Fabbiano 2006, Paolillo et al. 2011, D'Ago et al. 2014 and references therein). However, the role played by metallicity in LMXB formation is still unclear, and understanding this connection would help us to know how these objects are formed, and if the properties of the environment (the host GC or the galaxy properties) can have an impact on the structure and emission of the LMXB.

The fact that the spatial distribution of GC-LMXBs in early-type galaxies usually follows the distribution of the host GC population well (Paolillo et al. 2011) suggests that the likelihood of LMXB formation is mainly driven by the internal GC properties. However, there have been claims that LMXBs may be less concentrated than GCs around giant ellipticals, suggesting that environmental effects may influence the formation and evolution of LMXBs. Unfortunately, most studies so far were limited to the central regions of galaxies because the area explored by past surveys

(*Hubble Space Telescope*) was limited and high-resolution imaging was lacking. This imaging is needed to select and measure the structural parameters of extragalactic GCs. This has prevented studies of the effect of the distance from the galaxy center on the formation of LMXBs inside GCs. Because the spatial distribution of the red and blue GCs changes according to the distance from the galaxy, moreover, wide-field observations are required to distinguish the different physical processes at work in a scenario in which red GCs are associated with the main body of the galaxy while the blue GCs are associated with the halo (Cantiello et al. 2018).

Significant populations of intra-cluster GCs have been discovered in the Virgo (Durrell et al. 2014) and in the Fornax galaxy cluster. Using the *VLT Survey Telescope* wide-field imaging obtained within the Fornax Deep Survey (FDS, Iodice et al. 2016) in the Fornax cluster, our collaboration has proved the existence of a vast population of intra-cluster stellar systems extending out to a significant fraction of the virial radius (D’Abrusco et al. 2016; Cantiello et al. 2018; Cantiello et al. 2020). This was found to match the distribution of the intra-cluster light (Iodice et al. 2017), thus tracing the past dynamical evolution of the galaxy cluster itself. In addition, Jin et al. (2019) discovered a population of field LMXBs throughout the cluster, around the dominant cD galaxy NGC1399, by analysing *Chandra* archival images.

In this work, we investigate the properties of LMXBs residing in this extended population of intra-cluster GCs making use of the latest FDS data release, combined with *Chandra* X-ray data covering the core of the Fornax galaxy cluster. Based on this, we study the GC-LMXB connection within the whole Fornax cluster and its dependence on host galaxy, environment, galactocentric distance, and metallicity.

3.3 Dataset

This work is based on the combination of VST and *Chandra* data. We briefly summarize the main properties of the datasets. We refer to the cited papers for more details.

3.3.1 Optical data

The optical data used were acquired as part of the Fornax FDS based on observations obtained in u , g , r , and i bands with the Survey Telescope (VST) of the Very Large Telescope at the ESO Paranal Observatory. The VST is a wide-field optical imaging telescope with a 2.6-meter aperture with a field of view (FoV) of 1 degree^2 . The telescope is equipped with the 268 megapixel OmegaCAM with a pixel scale of $0''.21 \text{ pixel}^{-1}$. The survey was designed to map the entire Fornax cluster out to the virial radius, and it also covered the NGC1316 subgroup (Iodice et al., 2017). Located at a distance of $D = 20.13 \pm 0.4 \text{ Mpc}$ (Blakeslee et al., 2009), this cluster is the second nearest to us after the Virgo cluster and therefore represents an ideal target for this type of study. The survey observed ~ 27 square degrees approximately centered on NGC1399 and NGC1316 (Cantiello et al. 2020), reaching magnitude limits for point-like sources of 24.1, 25.2, 24.6, and 23.6 in the u , g , r , and i bands, respectively (AB mag photometric system), while the median seeing of the observation ranges from 0.6 to 1.1 arcsec. We limit our analysis to the central 1.5 square degrees around NGC1399, which overlaps with the *Chandra* X-ray coverage of the cluster core. The data reduction was performed using the Astro-WISE pipeline see e.g. Venhola et al., 2019. This is a tool for the reduction of large field data to perform pre-reduction

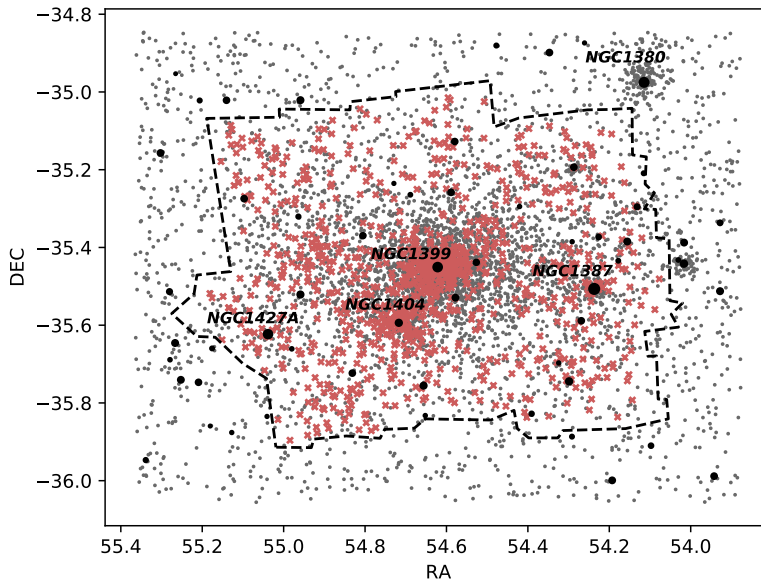


FIGURE 3.1: Spatial distribution of the GCs (grey points) and the X-ray sources (red crosses) centered on NGC1399. The solid black circles represent bright galaxies in the cluster from Ferguson (1997). The size is proportional to their effective radii. The dashed line highlights the FoV of *Chandra* observations.

(subtraction of bias, correction of flat), illumination, and edge correction and photometric and astrometric calibrations. To properly detect and study GCs, we need to minimize the contamination from the brightest galaxies in the cluster (e.g. NGC1399 and NGC1404). In order to model and subtract the galaxies, ELLIPSE task in IRAF STSDAS is used during the catalog preparation (Jedrzejewski et al. 1987). To produce a complete catalog of all sources present in the VST field of view, a combination of SExtractor (Bertin et al. 1996) and DAOPHOT (Stetson, 1987) was used on the galaxy-subtracted frame independently in each filter. For additional information on the data reduction and source photometry, we refer to Cantiello et al. (2020).

At the Fornax distance, GCs appear unresolved from the ground. They are therefore hard to separate from stars and compact background galaxies. The selection of the GC sample accordingly represents a crucial step in our analysis. In this case, we adopted the approach presented in Cantiello et al. (2018) applied to the improved FDS dataset (Cantiello et al. 2020). The GC selection criteria were defined using the training set of spectroscopically confirmed GCs published in Pota et al. (2018) and Schuberth et al. (2010). We refer to figure 1 of Pota et al. (2018) for the region covered by the confirmed GCs.

In order to minimize the contamination from foreground sources, we further discarded all sources with a g magnitude brighter than $M_{TO} - 3\sigma_{GCLF}$, where M_{TO} is defined as the absolute magnitude turn-off of the Gaussian GC luminosity distribution, assuming $\sigma_{GCLF} = 1.4 \pm 0.1 \text{ mag}$ and $M_{TO} = -7.4 \pm 0.2 \text{ mag}$ e.g. Villegas et al., 2010. At the distance of Fornax, the turn-over magnitude corresponds to $m_{TO} \sim 24.0 \text{ mag}$. The adopted selection criteria are given in Table 3.1.

The catalog of candidate GCs contains 5178 sources. Their spatial distribution is shown in Figure 3.1. The figure shows the extended distribution of GCs that

TABLE 3.1: Selection criteria for the GC candidates.

| Parameters | Values |
|---|----------------------------|
| magnitude | $19.8 \leq m_g \leq 26$ |
| concentration index ¹ | $0.8 \leq CI_n \leq 1.15$ |
| color | $0.6 \leq g - i \leq 1.45$ |
| | $1.35 \leq u - r \leq 3.5$ |
| Difference from model ² | ≤ 0.4 |

Notes: ¹ CI_n : normalized concentration index based on the difference in g -band magnitude between apertures of 6 and 12 pixels. ²Maximum distance from the best-fit population synthesis model for spectroscopically confirmed GCs in the color-color diagram.

TABLE 3.2: List of galaxies from Ferguson (1997) in the *Chandra* FoV.

| Name | RA (deg) | DEC (deg) | R_{eff} (kpc) |
|----------|------------|-----------|-----------------|
| NGC1387 | 54.2370 | -35.5066 | 4.86 |
| NGC1399 | 54.6216666 | -35.45055 | 3.61 |
| NGC1427A | 55.0383333 | -35.62305 | 3.52 |
| NGC1389 | 54.29875 | -35.74444 | 1.95 |
| NGC1404 | 54.7170833 | -35.59388 | 1.94 |
| NG115 | 54.1558333 | -35.38472 | 1.74 |
| NG6 | 54.83125 | -35.72333 | 1.61 |
| NGC1380B | 54.2870833 | -35.19361 | 1.58 |
| NG5 | 55.0970833 | -35.27444 | 1.54 |
| G72 | 54.8054166 | -35.36972 | 1.40 |
| NGC1381 | 54.1316666 | -35.29527 | 1.25 |
| NG8 | 54.26875 | -35.58861 | 1.17 |
| NG21 | 54.5779166 | -35.52916 | 1.14 |
| G79 | 54.22625 | -35.37305 | 1.10 |
| NG23 | 54.3908333 | -35.82777 | 0.99 |
| NGC1396 | 54.5266666 | -35.43833 | 0.95 |
| NG87 | 54.96375 | -35.32055 | 0.89 |
| NG7 | 54.5795833 | -35.1275 | 0.82 |
| NG116 | 54.1779166 | -35.43416 | 0.75 |
| NG72 | 54.68875 | -35.26444 | 0.74 |
| NG117 | 54.65625 | -35.75555 | 0.72 |
| NG111 | 54.98 | -35.66083 | 0.66 |
| D117 | 54.3241666 | -35.69722 | 0.62 |
| FCC197 | 54.29125 | -35.38527 | 0.61 |
| NG114 | 54.4204166 | -35.29472 | 0.61 |
| NG118 | 54.6520833 | -35.8325 | 0.60 |
| NG71 | 54.58875 | -35.25833 | 0.54 |
| D138 | 54.7291666 | -35.23527 | 0.54 |

was reported by D’Abrusco et al. (2016). While a large fraction of these GCs are clustered around the brightest galaxies, many GCs occupy the intra-cluster space, several effective radii (R_{eff}) away from any cluster galaxy member. The positions of cluster galaxies and their effective radii are extracted from Ferguson (1997). In Table 3.2 we show the R_{eff} of the galaxies in the FoV of the *Chandra* observations. We point out that the R_{eff} of NGC1399 and NGC1404 are considerably smaller than those reported in Iodice et al. (2016) and Iodice et al. (2019). These values were estimated using very deep observations probing very low surface brightnesses where the extended stellar halos of NGC1399 (and NGC1404) merge with the intra-cluster light and encompass most of the Fornax cluster. To identify intra-cluster sources, we therefore preferred to use the value provided by Ferguson (1997).

The completeness of the original gri catalog is $\sim 80\%$ for magnitudes $g \leq 24$ mag. However, the selection criteria introduced above in order to minimize the contamination of foreground/background sources combined with the use of the shallower u band constrain the actual completeness of our sample, as shown in Fig. 3.2. We note that because LMXBs tend to reside in bright GC, the final detection limit of $m_g \sim 25$

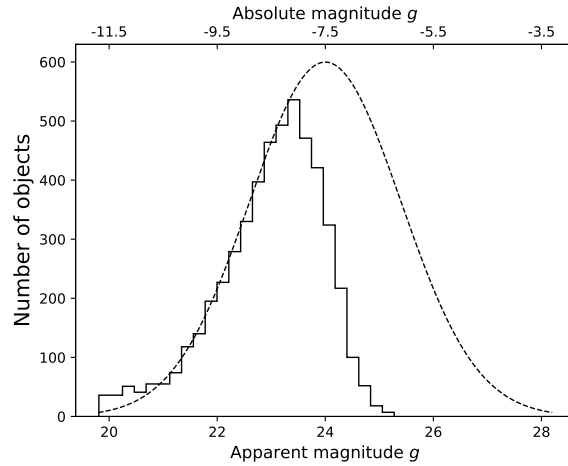


FIGURE 3.2: Luminosity function in g band for the sample of candidate GCs. The dashed black line corresponds to the expected theoretical GC luminosity function (with values $\mu = 24$ and $\sigma = 1.4$).

does not represent a significant limitation for our study.

The color distribution of GCs in the core of the Fornax cluster is known to be bimodal, mainly due to metallicity effects see e.g. D’Abrusco et al., 2016; Cantiello et al., 2018, and references therein. In order to study the possible differences between LMXBs formed in different environments, we used a *Gaussian mixture model* (GMM; Muratov et al. 2010) to divide the whole population into red and blue GCs. Using a $g - i \sim 1.00$ threshold, we find 2085 red GCs ($\sim 40\%$ of the total sample) and 3093 blue GCs ($\sim 60\%$ of the total sample). As discussed in more detail below, the relevance of each population is dependent on several factors, including the host galaxy properties, the galactocentric distance of the cluster, and the environment. We adopted a fixed color threshold as we intend to study the overall intra-cluster population, independently of the individual galaxies. We therefore ignored for the moment the variations in the GC color distribution as a function of the distance from the centers of the host galaxies (Kim et al. 2013; Cantiello et al. 2015) and the differences of the red/blue bimodality of the individual GCs (Jordán et al. 2015). In figure 3.3 we plot the GMM model over the g-i color distribution for the entire sample of candidate GCs. We point out that on cluster scales, the blue component dominates 3:2 of the total GC population. This is different from what has been reported close to individual galaxies, where red GCs are dominant e.g. Puzia et al., 2014. This agrees with the well-known trend for red and blue GC densities to have different radial gradients, the latter of which are shallower than the former. We note that the bulk of the blue GC population is redder than what was found for Fornax dwarf galaxies (Prole et al., 2019).

However, we tried to quantify the variation in the color distribution as a function of the distance by performing a GMM fit for different distances from each galaxy in terms of effective radius. We find a slight shift in the average value of each distribution towards more blue colors in progressively outer regions (Fig.3.4). The slope of the fit is found to be -0.0037 ± 0.0005 for the blue sample and -0.0037 ± 0.0017 for the red sample. This is inconsistent/marginally consistent ($\sim 2.2\sigma$), respectively, with a constant trend. This means that not only does the intra-cluster space host a larger fraction of blue GCs, but also that both distributions gradually become bluer with increasing distance. For this result, we do not expect any systematic effect from

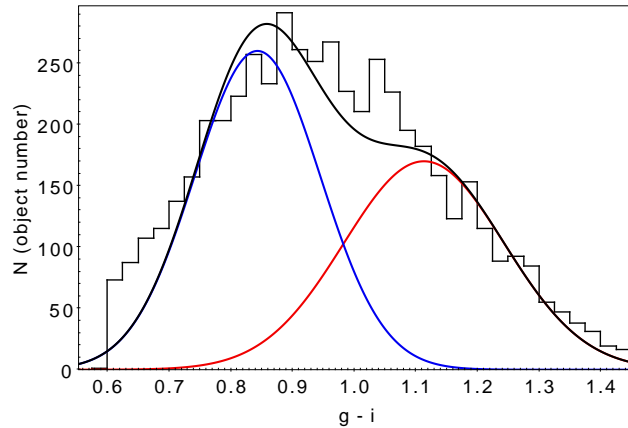


FIGURE 3.3: $g - i$ color distribution of GC candidates in the central square degree of the Fornax cluster. The smooth solid black, red, and blue lines show the GMM model for the total, red, and blue populations.

background galaxy light because it was removed during the catalog reduction process (Cantiello et al., 2020).

3.3.2 X-ray data

The X-ray data were extracted from 29 archival *Chandra* observations (given in Tab. 3.2 of Jin et al. (2019)) that were obtained with the *Advanced CCD Imaging Spectrometer* (ACIS) for a total exposure time of 1.3 Ms. This covers a large part of the central region of the Fornax cluster (Fig. 3.1). The details of the source detection procedure can be found in Jin et al. (2019). We briefly summarize the procedure here. The X-ray data were analyzed using the *Chandra* Interactive Analysis of Observation (CIAO) tool *Wavdetect*, producing counts and exposure maps, at the native pixel scale of 0.49, in three different bands: 0.5-2 (S-band), 2-8 (H-band), and 0.5-8 (F-band) KeV. The exposure maps were weighted by an assumed incident spectrum of an absorbed power law with a photon index of 1.7 and an absorption column density $N_H = 10^{21} \text{ cm}^{-2}$. This latter value is higher than the Galactic foreground absorption column ($\sim 1.5 \times 10^{20} \text{ cm}^{-2}$) but takes some intrinsic absorption of the LMXBs into account (see Jin et al. 2019)

The centroids of the sources were refined using a maximum likelihood method that iterates over the positions of the individual counts within the 90% of the *enclosed counts radius* (ECR). The photon fluxes in various bands were calculated using a circular opening of 90% of the ECR in non-crowded zones and 50% for the crowded zones to avoid contamination between nearby sources. The position uncertainty (PU) at the 68% confidence level was estimated following the empirical relation between PU, source counts, and source position in terms of the off-axis angle. At this point, a catalog of 1279 independent sources was obtained, of which 1177 are in the F band (0.5-8 KeV), 924 in S band (0.5-2 KeV), and 713 in H band (2-8 KeV). To derive the unabsorbed energy flux in the F band, a photon-to-flux conversion of $3.64 \times 10^{-9} \text{ erg/ph}$ was used, assuming the previously cited incident source spectrum.

In order to verify the quality and completeness of the catalog, we compared it to the *Chandra Source Catalog 2.0* (CSC master catalog, <http://cxc.harvard.edu/csc/>). The CSC uses a different approach to compute the source fluxes (based on the individual photon energy instead of assuming an average conversion factor) and the

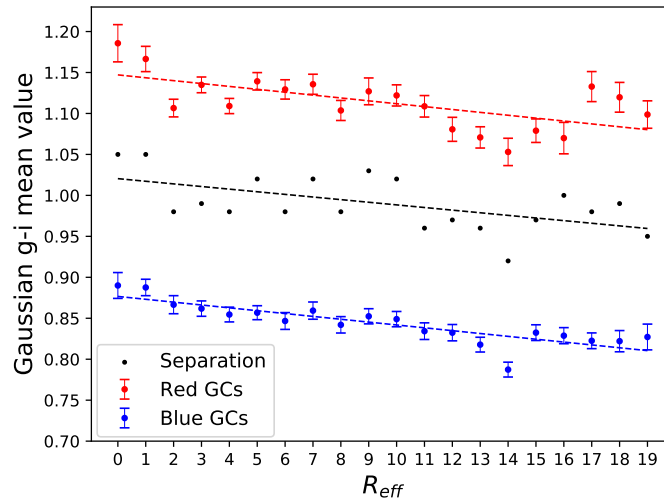


FIGURE 3.4: Mean values calculated by the GMM for different distances from each galaxy in terms of R_{eff} for red and blue GCs, and the separation performed by the GMM. The error bars correspond to the standard deviation of the mean.

exposure maps. In order to compare the two catalogs, we cross-matched the source positions and compared the fluxes of the sources in common, deriving the rescaling factor ($r = 1.41$) from CSC to Jin et al. (2019). In figure 3.5 we show the cumulative X-ray luminosity function of the two catalogs after correcting the CSC fluxes as explained above. Both catalogs follow a similar truncated power-law distribution down to $LF \simeq 3 \times 10^{38} \text{ erg/s}$, after which the CSC LF flattens more rapidly than the Jin catalog. The higher completeness of the Jin catalog is due to two main factors: first, the CSC contains observations up to 2014, while the catalog of Jin et al. (2019) is based on all available *Chandra* archived observations up to 2015. Of the 29 observations used in Jin et al. (2019), the CSC lacks the two identified with ObsIDs 17549 and 14529, which are centered on NGC1399 and NGC1404, where a large fraction of the GC population resides. Second, the CSC reports source properties in master, stack, and per-observation tables. A single source might then not be included in the master catalog (used here) but might have entries at the stack or observation level. We verified that when we include sources from all tables, we obtain a comparable number of sources between the CSC and Jin catalogs (1004 and 1177, respectively), and this considerably reduces the disagreement. However, in this case, the choice for the measured properties that are used becomes complex (see the detailed discussion at <https://cxc.cfa.harvard.edu/csc/organization.html>). For this reason, we mainly used the Jin et al. (2019) source catalog and reverted to the CSC for specific measurements and tests. Most of our results would be confirmed, although with lower significance, using the CSC catalog in any case, except for the hardness-ratio differences discussed in Sec.3.5.2

3.4 Identification of X-ray sources in GCs

In order to study the population of LMXBs residing in GCs, we performed a cross-match between the optical and the X-ray catalogs. To minimize the possibility of random matches, we employed the PU provided in the Jin et al. (2019) catalog as

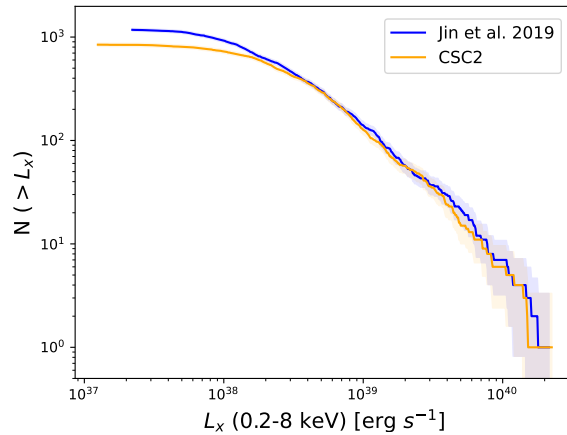


FIGURE 3.5: Cumulative X-ray luminosity function for the sources from the catalog of Jin et al. (2019) and for the CSC catalog. The shaded region represents the 1σ error.

the matching radius for the X-ray sources. This is different for each object. For the optical sources, we chose a matching radius of 0.5 arcsec that is typical of the VST astrometric accuracy (see e.g. Capaccioli et al. 2015). Two sources were considered to match when the separation between their positions did not exceed the sum of the two matching radii for the corresponding source. Based on the optical and X-ray source densities, we expect three false matches over the entire FoV. In addition, compact background galaxies hosting an active galactic nucleus (AGN) might be mistaken for GCs hosting an LMXB. This type of contamination is discussed in section 3.5.2. We identify 168 X-ray sources that are positionally coincident with GCs. We refer to these objects as GC-LMXBs.

To study the photometric properties of the intra-cluster population, we divided the GC-LMXBs sources into *host-galaxy* and *intra-cluster* objects based on their projected distance from the nearest galaxy in terms of R_{eff} . The choice on where to place the separation between the regions associated with the galaxy and the intra-cluster space is somewhat arbitrary.

Several authors considered $5 R_{eff}$ to be the upper limit for bound systems (Karthi et al. 2014, Forbes 2017, Caso et al. 2019). In order to obtain a nearly equal number of host-galaxy/intra-cluster sources, we considered as intra-cluster GCs those lying more than $6 R_{eff}$ from the nearest galaxy. In this way, we found 86 host-galaxy and 82 intra-cluster GC-LMXBs. Coincidentally for NGC1399, this limit roughly corresponds to the separation between the central region covered by *HST* data (Paolillo et al., 2011) and the outer cluster region that has only been studied with ground-based data so far. Due to projection effects, some intra-cluster sources will be included in the host-galaxy sample. However, our conservative choice should ensure that most of the sources that are classified as intra-cluster objects are loosely bound to individual galaxies. In Fig. 3.6 we show the distribution of intra-cluster and host-galaxy GC-LMXBs in our field of view. The majority of intra-cluster sources are located in the central cluster region around NGC1399.

In figure 3.7 we show the fraction of GC hosting LMXBs (XGC) as a function of the distance from the nearest galaxy in terms of R_{eff} for the entire GC sample, as well as red and blue GC subsamples. These fractions are normalized to the number of all, red, and blue GCs in the corresponding distance bin. We refer to this as f_{XGC} , f_{rXGC} ,

and f_{bXGC} for the total, red, and blue fractions of XGCs, respectively. We selected only GCs with a magnitude $g < 23.5$ (the 90% completeness limit of the GC catalog, see Fig. 3.2) in order to minimize the radial dependence on the optical completeness. We further verified that the same trends were confirmed when only LMXBs above the median sensitivity limit $L_x > 1.7 \times 10^{38} \text{ erg s}^{-1}$ of Jin et al. (2019) were selected (corresponding to a photon flux of $1.5 \times 10^{-6} \text{ ph s}^{-1} \text{ cm}^{-2}$ in their Fig.2). In this way, we also minimized the dependence on the variable X-ray completeness across the FoV.

Figure 3.7 shows that the likelihood of a red GC to host an LMXB decreases with galactocentric distance, but remains approximately constant for the blue GC population. We find the host-galaxy fraction of red XGC $f_{rXGC} = 0.154 \pm 0.017$ to be significantly different from the respective intra-cluster value $f_{rXGC} = 0.062 \pm 0.008$. On the other hand, the host-galaxy fraction of blue XGCs $f_{bXGC} = 0.021 \pm 0.006$ appears consistent within the errors but is still higher than that of the intra-cluster counterparts $f_{bXGC} = 0.013 \pm 0.003$. Because of the normalization we adopted, this result is independent of the known different radial distributions of red and blue GCs. The former follows the galaxy light more closely than the latter (which represents the dominant intra-cluster GC population). Thus, the clustering of LMXBs around bright galaxies is due to the combined effects of the steeper profile of the red GC population and the increased likelihood to host LMXBs close to the galaxy center. Previous studies targeting nearby elliptical galaxies on spatial scales comparable to ours, such as Kim et al. (2006), show that f_{rXGC} can range from 2.7% up to 13% from one galaxy to the next (the latter value refers to NGC1399), while f_{bXGC} remain relatively constant at $\sim 2\%$, except for NGC1399, where it reaches 5.8%. We thus find a strong agreement between our host-galaxy f_{rXGC} and the measurement carried out by Kim et al. (2006) on NGC1399, suggesting that our sample of host-galaxy red XGC is dominated by the population associated with the central cluster galaxy. In the case of blue XGCs, the fraction we measure is closer to the average, suggesting that blue GCs are more related to the overall cluster environment than to a single galaxy, as discussed in more detail below.

Because the formation of LMXBs is strongly influenced by the luminosity of the host GC, the drop in the fraction of GC-LMXB could be associated with an average decrease in the GC luminosity towards the outer regions. In Fig. 3.8 we show the GC g -band magnitude as a function of galactocentric distance. The dashed blue and red lines represent the mean magnitude for the blue and red samples, respectively. We can observe no clear decrease in the mean magnitude toward the outer regions, which might justify the drop of the GC-LMXB fraction. This might suggest that the LMXB formation is favored in the proximity of galaxies, or that it might also depend on other factors, such as the environment of the host galaxy.

3.5 Properties of GC-LMXBs

3.5.1 Optical properties of the host GCs

Because most of the previous works that focused on the GC-LMXB connection were restricted to the innermost regions of the galaxies, we verified whether the intra-cluster sample possesses the same properties as its host-galaxy counterpart. As a starting point, we investigated the dependence of the LMXB formation on the host GC luminosity. In Fig. 3.9 we present the fraction of GC-LMXB as a function of the GC apparent magnitude in the g band for three different galactocentric distances. We note a declining trend in the host-galaxy sample ($R_{eff} \leq 6$) as well as in the

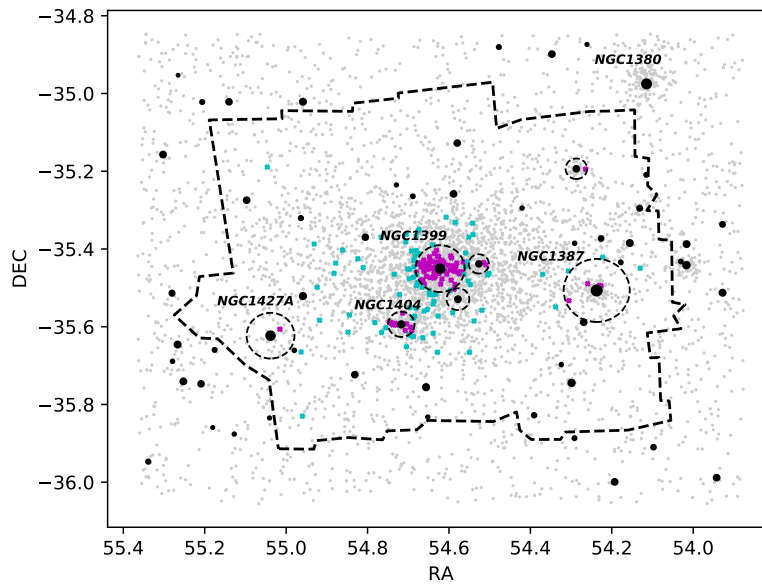


FIGURE 3.6: Spatial distribution of intra-cluster (cyan crosses) and host-galaxy (magenta crosses) GC-LMXBs. Cluster galaxies are solid black circles, and the sizes are proportional to their effective radii. The dashed circle shows the $6 R_{eff}$ distance from the galaxy center. The dashed line depicts the FoV of the *Chandra* observations.

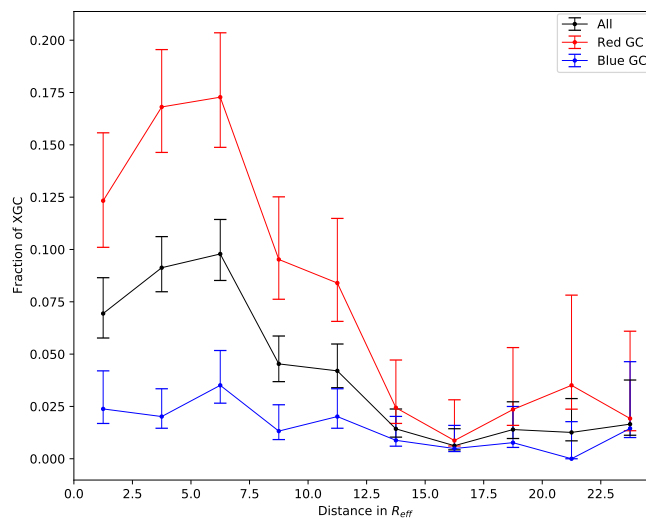


FIGURE 3.7: Fraction of XGC as a function of the distance in units of R_{eff} for the total, red, and blue sample of GCs. The fraction is defined as the number of total, red, or blue XGC divided by the respective total number of GCs in the distance bin. The distances on the X-axis are from the nearest galaxy to the object.

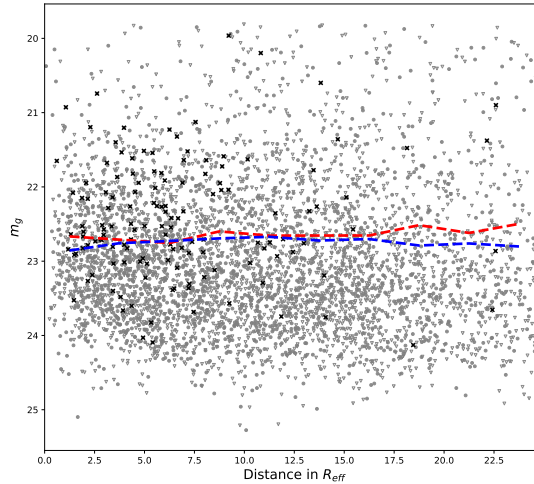


FIGURE 3.8: Magnitude in g band as a function of the distance in terms of R_{eff} . Grey circles and triangles represent red and blue GCs, respectively. Black crosses are GCs that host an LMXB. Dashed lines represent the mean g magnitude of the GC in each distance range for the red and blue sample. The dashed lines show a computer cut of the g magnitude at $g < 23.5$.

intra-cluster sample ($R_{eff} > 6$), suggesting that LMXBs tend to form in bright GCs in both environments. Fig. 3.10 (upper panel) confirms this result by comparing the magnitude distribution of GCs and GC-LMXBs for host-galaxy and intra-cluster sources. In both galactic and intra-cluster cases, a Kolmogorov-Smirnov (K-S) test confirms the difference between the distributions of GCs that hosting an LMXB or are without one at the 99.9% confidence level.

The LMXB formation efficiency was also shown to be dependent on the color of the host GC (see Sec.4.2), with a greater tendency for LMXBs to form in red GCs. To verify whether this trend also holds for intra-cluster GCs, we present in Fig. ?? the $g-i$ color distribution of intra-cluster and galactic GCs. Again, a K-S test confirms the difference in color between GCs with and without an LMXB at the 99.9% level in both environments.

3.5.2 X-ray properties of the GC-LMXB

Previous works (Jordán et al. 2004, Kim et al. 2004, Paolillo et al. 2011) showed that the X-ray properties of LMXBs, such as their X-ray luminosity function, do not depend on the properties of the stellar environment in which they form, such as the color, magnitude, or density of the host GC. In this section, we try to understand if these statements are valid for the intra-cluster population of GC-LMXBs. Furthermore, we explore the contribution of GC-LMXBs to the total X-ray luminosity of the cluster, in comparison with field LMXBs. In order to correct the completeness of our X-ray source catalog for the variable detection limit across the FoV due to hot gas emission near the brightest galaxies, the variable PSF with an off-axis angle, and the different exposure time across the X-ray mosaic, we used the X-ray sensitivity map produced by Jin et al. (2019) to weight X-ray sources according to the fraction of the GCs in which they could have been detected. In Figure 3.11 we show the

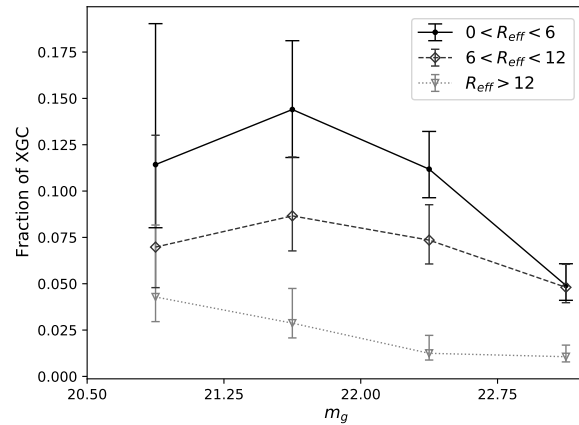


FIGURE 3.9: Fraction of GCs hosting LMXBs as a function of luminosity. The different types of lines correspond to different galactocentric distances. The magnitude range is restricted to $g \leq 23.5$. The fraction is defined as the number of XGCs divided by the number of GCs in the magnitude bin. The result for the inner region agrees with the results obtained in Paolillo et al. (2011). These authors covered almost the same FoV with *HST*.

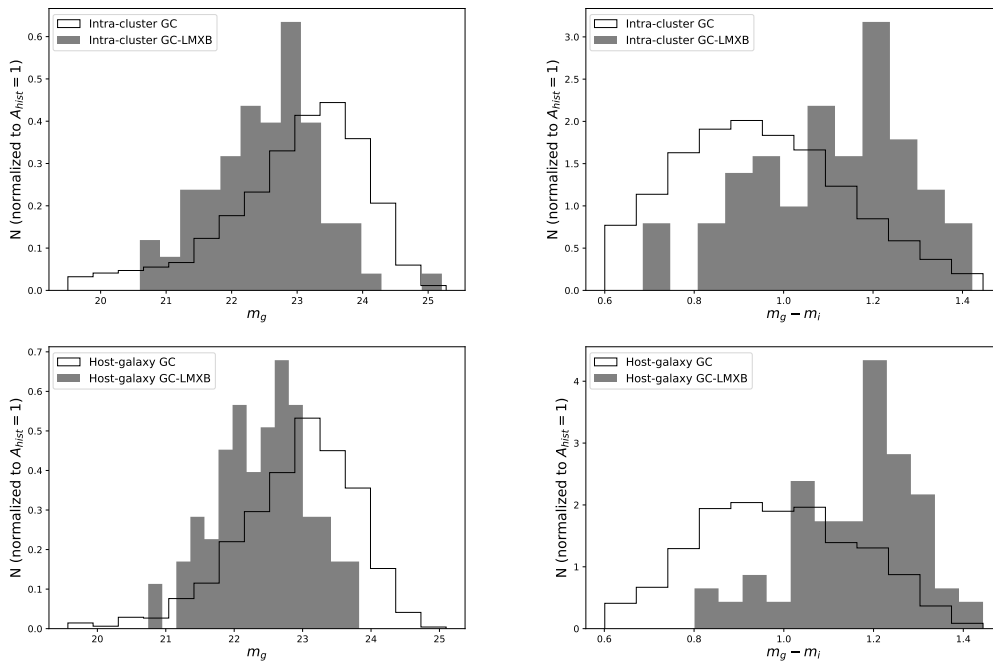


FIGURE 3.10: Left panels: Magnitude distribution of GCs hosting (grey shaded) and GCs without (black line) LMXBs in intra-cluster space (upper panel) and in the host-galaxy environment (lower panel). Right panels: Color distribution of GCs hosting (grey shaded) and GCs without (black line) LMXBs in intra-cluster space (upper panel) and in the host-galaxy environment (lower panel).

observed and completeness-corrected X-ray luminosity function of the intra-cluster and host-galaxy samples of GC-LMXBs. We found that the completeness-corrected intra-cluster and host-galaxy populations follow a single power law down to $L_x \simeq 8.5 \times 10^{37} \text{ erg s}^{-1}$. The intra-cluster sample is more affected by incompleteness because the sensitivity at the edges of the FoV is lower. Fitting the completeness-corrected distributions, we obtain an LF slope of $\alpha = 2.04 \pm 0.13$ for the host-galaxy sample (in agreement with the slopes found in previous works for GC-LMXBs belonging to galaxies, e.g. Kim et al. 2006, Paolillo et al. 2011, Jin et al. 2019), and $\alpha = 2.44 \pm 0.13$ for the intra-cluster sample. This is considerably steeper and consistent with the slope found for field LMXBs in Jin et al. (2019) ($\alpha = 2.30 \pm 0.12$) and in previous works (Paolillo et al. 2011). A K-S test confirms the difference of the two completeness-corrected LFs at the 99% confidence level.

Then, we studied the L_x distribution by dividing the sample of GC-LMXBs according to the host GC color (Fig. 3.12). The completeness-corrected red GC-LMXB follows a power-law distribution with a slope $\alpha = 2.37 \pm 0.12$ down to $L_x \simeq 8.5 \times 10^{37} \text{ erg s}^{-1}$. A possible lack of bright LMXBs is observed in the blue systems, which is found to be significant at the $\sim 2\sigma$ (97%) level according to a Poisson statistics. Fitting the entire sample of blue GC-LMXBs down to $L_x \simeq 8.5 \times 10^{37} \text{ erg s}^{-1}$ yields $\alpha = 2.21 \pm 0.18$. To further investigate this trend, we separated the red and blue sample into intra-cluster and host-galaxy sources (lower panel of Fig. 3.12). The population of blue intra-cluster GCs does not host LMXBs above $\sim 6 \times 10^{38} \text{ erg/s}$, although again the number of object is small for strong conclusions. The majority of objects above 10^{39} erg/s resides in red GCs possibly because multiple LMXBs reside in a single GC because it is easier to form LMXBs in these systems. However, previous studies often detected variability in systems like this, which argues against this possibility. On the other hand, this high luminosity break has already been observed in literature (Fabbiano 2006, and reference therein) and may reflect the transition between the most massive neutron stars and low-mass black hole systems, suggesting that blue environments are less likely to form binary systems with massive black holes. We point out, however, that considering the small statistics at high L_x , a small contamination by background AGNs randomly matched with GCs could be enough to cause the difference (see below). To verify that this is not linked to the different host GC distribution, we show in Fig. 3.13 the correlation between L_x and the color/galactocentric distance of the GCs for the red and blue sample of GC-LMXB. While red GC-LMXB are more centrally concentrated, as discussed before, the brightest sources with $L_x > 10^{39} \text{ erg s}^{-1}$ are uniformly distributed throughout the whole distance range. The small number of sources with $L_x > 10^{39} \text{ erg s}^{-1}$ does not allow us to draw definitive conclusions and therefore prevents us from excluding the effect of a background AGN contamination.

To assess the contribution of the GC-LMXBs to the total X-ray luminosity of the cluster, we study the XLF of the field LMXBs in comparison with the XLF of the full sample of GC-LMXBs (Fig. 3.14). We find the completeness corrected XLF for the full sample of GC-LMXBs follow a single power law with slope $\alpha = 2.37 \pm 0.10$ (in agreement with the slope found in previous works, e.g Kim et al. 2006; Pearson et al. 2018; Jin et al. 2019). For field LMXBs, it is not possible to perform the correction to the completeness, as we do not have information on the undetected sources we could have observed. A K-S test confirms no difference between the two observed LFs at a 99% confidence level. We find that the number of LMXBs residing in GCs

¹This limit yields the best power-law fit according to the algorithm of Newman (2005) as implemented in the R routine *powerlaw.R*.

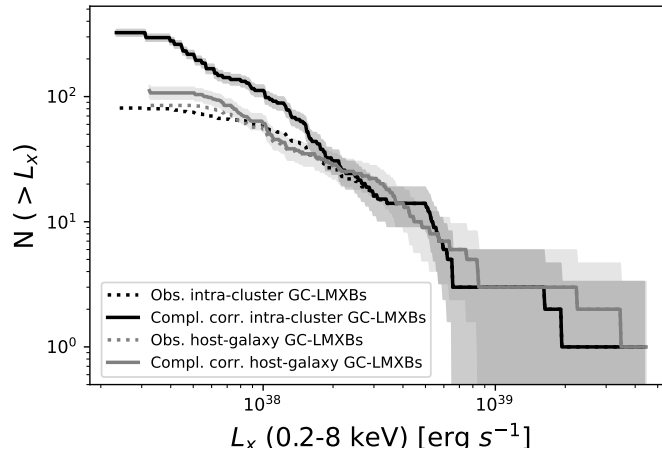


FIGURE 3.11: Cumulative X-ray luminosity function for the host-galaxy and intra-cluster sample of GC-LMXBs. The solid lines represent the completeness-corrected LFs, and the dotted lines show the observed LFs. The shaded region represents the 1σ error.

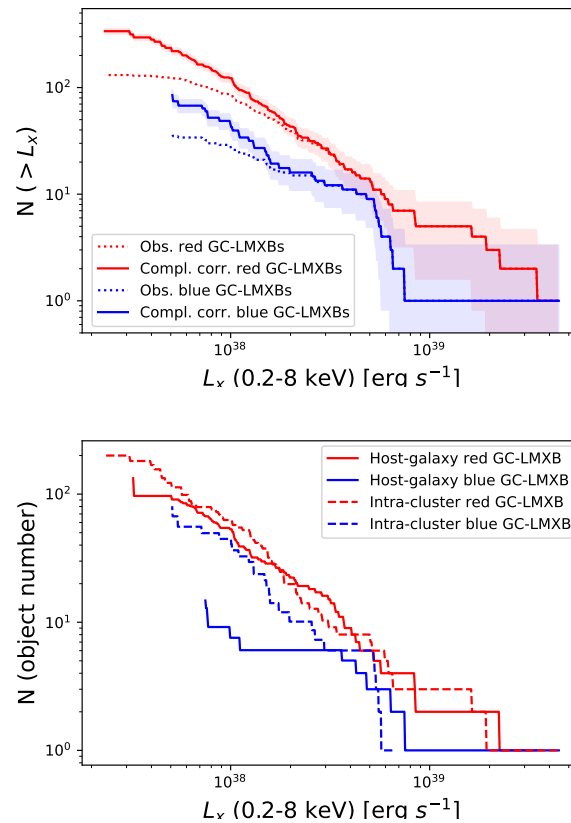


FIGURE 3.12: Cumulative X-ray luminosity functions comparison. *Upper panel*: red and blue samples of GC-LMXB. Lines and shaded areas are represented as in Figure 3.11. *Bottom panel*: completeness-corrected luminosity functions for red and blue intra-cluster and host-galaxy sources separately.

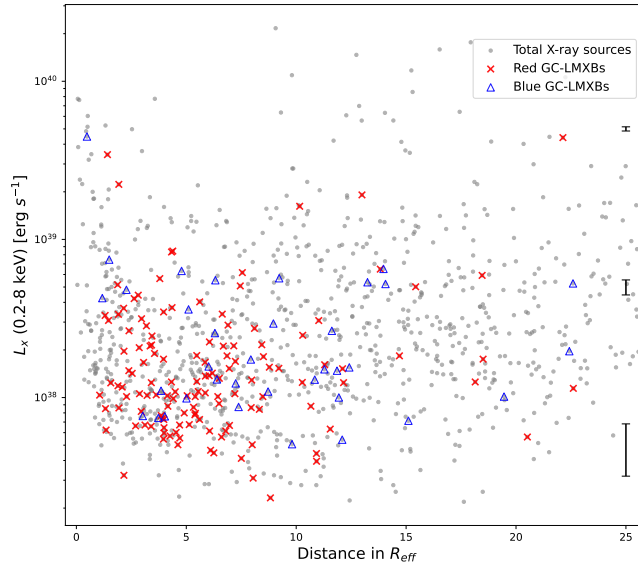


FIGURE 3.13: X-ray luminosity as a function of distance from each galaxy. Grey dots represent the whole sample of X-ray sources. Blue triangles and red crosses represent the respective GC-LMXBs. The mean errors in each X-ray luminosity order of magnitude are shown in black.

represents 17% of the total number of LMXBs in the cluster, with an integrated X-ray luminosity that contributes to 10% of the total X-ray luminosity of the cluster. This suggests that the observed scatter of the single sources from the empirical Lx-SFR scaling relation, in the low-SFR end (Kouroumpatzakis et al. 2020), is mainly driven by field LMXBs. In Fig. 3.14 we also show the X-ray luminosity of field and GC-LMXBs as a function of the distance from the nearest galaxy. We do not notice any statistical differences between the two samples, asserting that LMXBs formed in GCs have a comparable luminosity that the field LMXBs.

We further investigated the spectral properties of the LMXB population through their hardness-ratio (HR), defined as $HR = \frac{S_{Hard} - S_{Soft}}{S_{Hard} + S_{Soft}}$, with S_{hard} the photon flux in the hard band (2-8 KeV) and S_{soft} the photon flux in the soft band (0.5-2 Kev). In Fig. 3.15 we present the HR distribution of host-galaxy and intra-cluster sources. It is readily apparent that intra-cluster GC-LMXBs have harder spectra. A K-S test confirms that the two samples are drawn from different distributions. To understand this trend, we considered whether this systematic difference is related to the LMXB population itself or to their host GCs because we know from Sec.3.3.1 and from previous works that the GC population becomes increasingly blue with increasing galactocentric distance (Jordán et al., 2006; D’Abrusco et al., 2016; Cantiello et al., 2018, 2020).

In our case, 694 blue GCs (containing 10 LMXBs, i.e. 1.4% of the population) and 618 red GCs (72 LMXBs, i.e. 11.6% of the population) are associated with the main cluster galaxies, while the intra-cluster sample contains 2400 blue GCs (26 LMXBs, i.e. 1.1% of the population) against 1467 red (60 LMXBs, i.e. 4.1% of the population). The number of blue GCs therefore increases in the outer regions. As shown in Fig. 3.4, we also observe a shift in the average value of the red distribution towards bluer

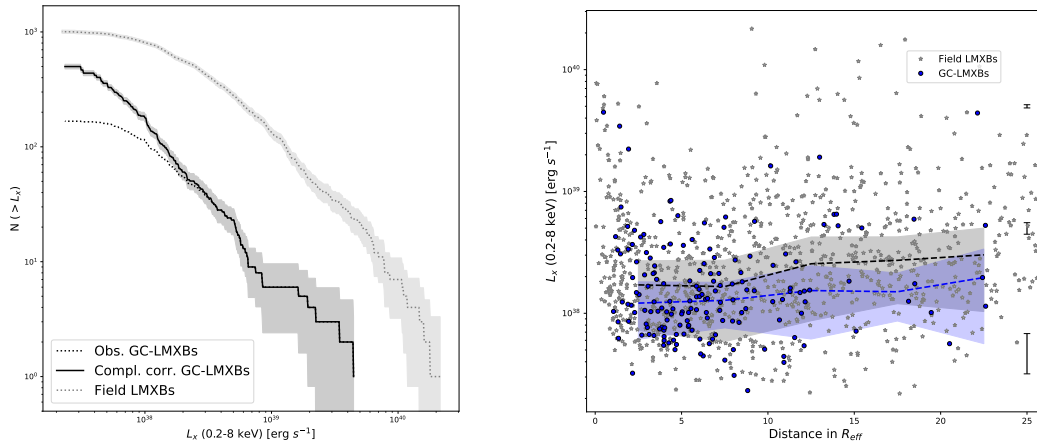


FIGURE 3.14: Left panel: Cumulative X-ray luminosity function for field and GC-LMXBs. The solid lines represent the completeness-corrected LF for the sample of GC-LMXBs, and the dotted lines show the observed LFs. The shaded region represents the 1σ error. Right panel: X-ray luminosity in the 0.5-8 KeV band in function of the distance from the nearest galaxy. Blue points represent the GC-LMXBs, while grey stars the field LMXBs. The dashed lines represent the median value of the X-ray luminosity in each bin of distance, with the shaded region representing the 1σ dispersion

colors, however. In Fig. 3.16 we show that LMXBs in blue GCs seem to have a harder spectrum than those in red GCs; the result is confirmed when red and blue GC-LMXBs are compared restricted to the intra-cluster sample alone².

To explain this result, we explored three possibilities: 1) Intra-cluster sources are more heavily contaminated by harder-background sources than the host-galaxy population. 2) The difference is due to uncertainties in the X-ray spectral response correction, which in turn is due to the combination of the multiple *Chandra* exposures with different off-axis angles and the presence of diffuse gas, which may affect the background estimate. Finally, 3) the difference is real.

To address the first possibility, we estimated the number of expected contaminants in our FoV. To this end, we used the COSMOS catalogs by Civano et al. (2014) and Laigle et al. (2016) to select X-ray sources within the same X-ray flux limit as was used for the catalog of Jin et al. (2019), and with optical counterparts obeying the same selection criteria in terms of limiting optical magnitude, colors, and concentration index as we adopted in Sec.3.3.1. We predict a contamination of about ten background X-ray sources with optical counterparts over our FoV. In addition, we expect three random superpositions of background sources without optical counterparts, as discussed in Sec.3.4. These contaminants do have harder average HR than the bulk of GC-LMXB sources, but they do not account for the entire excess observed in our sample. When we removed the ten hardest sources from the sample of intra-cluster GC-LMXBs, the result was unchanged.

Several factors can affect the derived hardness ratios in the spectral response, including different off-axis angles, detectors (ACIS-I versus ACIS-S), and observing

²Comparing red and blue GC-LMXBs restricted to the host-galaxy sample alone does not allow us to draw definitive conclusions because there are too few blue GC-LMXBs.

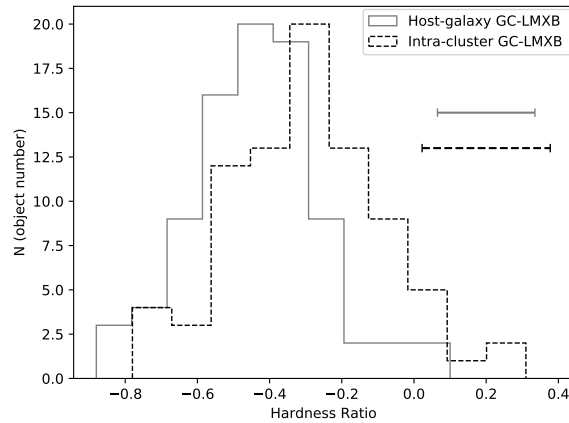


FIGURE 3.15: Hardness ratios between host-galaxy (grey) and intra-cluster (black) GC-LMXBs. The error bar is the median value of the errors associated with the HR of the sources.

epoch (due to the efficiency degradation of ACIS at low energies with time). We point out, however, that Jin et al. (2019) only used ACIS I0, I1, I2, I3, S2, and S3 chips in order to ensure an optimal source sensitivity. In addition, most intra-cluster sources are still located in the central region of the cluster, although at a greater distance from the main galaxies, and they are covered by multiple observations spanning several years (see Table 1 in Jin et al. 2019). These properties should reduce the potential systematic effects in the X-ray catalog. To evaluate how the catalog properties might affect our results, we compared the HR estimates used in this work with the estimate reported in the CSC catalog. In Fig. 3.17 we show the HR as a function of the distance from the nearest galaxy for X-ray sources with a counterpart in the CSC master catalog. We note a difference in the mean HR, mainly driven by *host-galaxy* sources, both considering GC-LMXBs and field X-ray sources. The higher HR in the CSC is higher on average than the HRs reported in the catalog used in this work. This suggests that the spectral corrections differ between the two catalogs, possibly due to the different data reduction strategy, source extraction method (see Sec.3.3.2), and the treatment of the contribution of the central diffuse emission.

Concerning the possibility that the observed difference might be real, it is known that the color mainly depends on metallicity in old GCs, where metal-rich GCs are significantly redder (Cantiello et al. 2018). This might suggest a relation between the spectral properties of LMXBs and the metallicity of the host GC. One model that discusses such a trend was presented by Maccarone et al. (2004), who proposed irradiation-induced winds in metal-poor stars that would cause absorption, mainly of the soft part of the X-ray spectra, which would produce higher HR values. The authors reported this trend for NGC4472 (Maccarone et al. 2003). In this case Fornax, would be the only other system in which this effect is directly observed so far.

3.6 Summary and conclusions

We performed an analysis of the properties of LMXBs residing in the population of intra-cluster GCs in the Fornax cluster. The main goal of this work was to study the GC-LMXB connection within the core of the Fornax cluster and its dependence on the environment in terms of galactocentric distance and host GC. For this purpose,

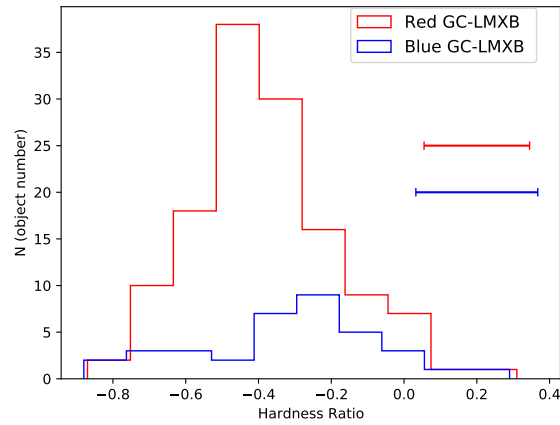


FIGURE 3.16: Hardness ratios between red (grey) and blue (black) GC-LMXBs. The error bar is the median value of the errors associated with the HR of the sources.

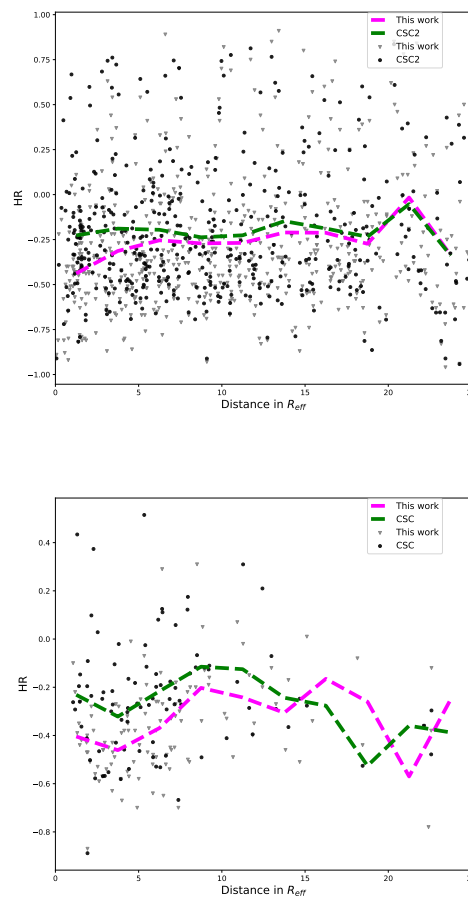


FIGURE 3.17: Hardness ratio as a function of the distance for field X-ray objects (upper panel) and GC-LMXBs (bottom panel) with counterparts in the CSC catalog. Black dots represent the HR estimates in the CSC catalog, and grey triangles show the HR we used. Dashed green and magenta lines again represent the mean value in each distance bin.

we used optical photometry of 5178 candidate GCs from the Fornax Deep Survey (Cantiello et al., 2020). In order to study the possible differences between LMXBs that formed in different GC environments, we performed a *Gaussian Mixture Model* fit on the $g-i$ color distribution, finding a separation threshold of $g-i \sim 1.00$ between red and blue that agrees with the threshold reported in previous works (D’Abrusco et al. 2016, Cantiello et al. 2020). We obtained 2085 red GCs and 3093 blue GCs. We further observe a tendency in the average $g-i$ color of becoming bluer with increasing galactocentric distance. Because the GC colors mainly depend on metallicity, this result suggests that the intra-cluster GCs have a lower metallicity on average.

The X-ray data employed in this work were extracted from archival *Chandra* observations. The source detection procedure together with the extraction of photometry was performed by Jin et al. (2019). In order to study the connection between LMXBs and GCs, we performed a cross-match between the optical and the X-ray catalogs. In this way, we identified 168 X-ray sources that are positionally coincident with GCs. We divided this population into *host-galaxy* and *intra-cluster* objects based on their projected distance from the nearest galaxy. We considered as *intra-cluster* objects the GC-LMXBs within more than $6 R_{eff}$ from the nearest galaxy and found 82 intra-cluster and 86 host-galaxy GC-LMXBs. Furthermore, considering the color division performed for the GC sample, we found 36 LMXBs to be associated with blue GCs and 132 LMXBs to be associated with red GCs.

We find the fraction of GC-LMXBs to be dependent on the galactocentric distance; this effect is particularly evident for the red population. Because the GC magnitude seems to be independent of the distance from the galaxies, we conclude that this result may suggest that the LMXBs formation channel in GCs may also depend on the host-galaxy environment. In the past, the evidence for a dependence of the LMXB formation likelihood on the local galaxy environment has been debated (see e.g. Kim et al. 2006 and Paolillo et al. 2011 for an opposing view), but these studies were essentially limited to the inner region of galaxies within a few R_{eff} . Even in this work, there is little evidence for a dependence like this within $\sim 6 R_{eff}$, which is visible only when the analysis is extended to the intra-cluster population. If this is confirmed, the enhanced LMXB formation rate in red GCs might be related to their orbital parameters, as suggested by Puzia et al. (2014), for instance, leading to a stronger influence of the external tidal field. Webb et al. (2016) found that the sizes of red GCs in NGC1399 are consistent with more radial orbits compared to blue GCs.

We confirm that intra-cluster LMXBs tend to form in red and bright GCs, as has been found for their host-galaxy counterparts. Furthermore, we studied the X-ray properties of the intra-cluster population of GC-LMXB to test whether they are independent of the properties of the host GC as for the host-galaxy sources. We find that the completeness-corrected X-ray luminosity function of the intra-cluster population of GC-LMXBs follows a power law with a slope that is marginally consistent ($\sim 2.2\sigma$) with the slope of the host-galaxy population, and it is consistent with the slope found for field LMXBs in the literature. A Kolmogorov-Smirnov test indicates a statistically significant difference between the *LF* of the intra-cluster and that of the host-galaxy sample. We cannot confirm any difference between the completeness-corrected LFs of the red and blue populations. We find a lack of bright LMXBs in blue GCs, however, which agrees with what has been found for host-galaxy sources and possibly indicates a lack of black hole binaries in metal-poor systems. We find no differences between the observed LFs of field and GC-LMXBs, both following a single power law with slopes consistent with what found in previous works. We find the GC-LMXBs to contribute to the 17% of the total LMXBs population of the cluster, with an integrated X-ray luminosity contributing to the 10% of the total luminosity

of the cluster.

Finally, we observed a puzzling difference in hardness ratio between intra-cluster and host-galaxy GC-LMXBs: the spectra of the intra-cluster sample are harder than those of the host-galaxy sample. Because intra-cluster GCs are bluer on average than the host-galaxy GCs, this result might suggest a relation between HR and the color of the host GC, and hence the metallicity. We explored different explanations for this difference, including residual systematics in the data and background contamination or a possible physical origin. We found that contamination alone seems unable to explain the observed trend. This result is still tentative, however, and a final conclusion will have to wait for a full spectral analysis of the host-galaxy and intra-cluster GC-LMXB populations.

4

X-ray luminosity - star formation rate scaling relation: constraints from the eROSITA Final Equatorial Depth Survey (eFEDS)

This chapter was submitted to the Astronomy & Astrophysics journal, as titled: "X-ray luminosity - star formation rate scaling relation: constraints from the eROSITA Final Equatorial Depth Survey (eFEDS)" (Riccio et al. 2023).

4.1 Abstract

We present measurements of the relation between X-ray luminosity and star formation activity for a sample of normal galaxies spanning the redshift range between 0 and 0.25. We use data acquired by SRG/eROSITA for the Performance-and-Verification-Phase program named the eROSITA Final Equatorial Depth Survey (eFEDS). The eFEDS galaxies are observed in the 0.2-2.3 keV band. Making use of a wide range of ancillary data, spanning from the ultraviolet (UV) to mid-infrared wavelengths (MIR), we estimate the star formation rate (SFR) and stellar mass (M_{star}) of 888 galaxies, using the Code Investigating GALaxy Emission (CIGALE). In order to study sources whose X-ray emission is dominated by X-ray binaries (XRBs), we classify galaxies into normal galaxies and Active Galactic Nuclei (AGN), by making use of the observed fluxes in the X-ray, optical, and MIR range and using the results from the SED fitting. To isolate the contribution of XRBs, that scale with the SFR and M_{star} , we subtract the contribution of hot gas, coronally active binaries and cataclysmic variables to the total X-ray emission. We divide our sample of normal galaxies in star-forming (SFGs) and quiescent galaxies according to their position on the main sequence. We confirm a linear correlation between the X-ray luminosity and the SFR for our sample of SFGs, shown previously in the literature. However, we find this relation to be strongly biased by the completeness limit of the eFEDS survey. Correcting for completeness, we find the fitted relation to be consistent with the literature. We investigate the relation between X-ray emission from both LMXBs and HMXBs populations with M_{star} and SFR, respectively. Even correcting for completeness, we find a consistently higher contribution of LMXBs than observed in previous works. We conclude that without performing a stacking process, it is not

possible to employ eFEDS data to study the redshift evolution of the LMXBs and HMXBs contributions due to completeness issues. Furthermore, we find our sources to largely scatter from the expected L_x/SFR vs specific SFR relation at high redshift. We discuss the dependence of the scatter from the stellar mass, the metallicity or the globular cluster content of the galaxy.

4.2 Introduction

In the past decades, one of the main efforts of the high-energy astronomy community has been focused on calibrating the galaxies' X-ray emission and source populations against the star formation rate (SFR) and the stellar mass (M_{star}) (Gilfanov 2004; Basu-Zych et al. 2013b; Mineo et al. 2014; Lehmer et al. 2016). X-ray binaries (XRBs), the hot ionized interstellar medium (ISM), and active galactic nuclei (AGNs) are the main contributors to the total X-ray emission of galaxies. XRBs are stellar systems composed of an extremely dense object (a neutron star or black hole) that accretes mass from a secondary star. They can be divided into two main categories: High mass X-ray binaries (HMXBs), when the donor star is an early-type star (OB star, or a supergiant), or Low mass X-ray binaries (LMXBs), when the secondary star is a later-type star (typically of M, K spectral type). It is well known that the X-ray emission from these objects traces the stellar population of the galaxy. In fact, the number of HMXBs and their collective X-ray luminosity was found to scale with the star formation rate (SFR) of the host galaxy (Grimm et al. 2003; Lehmer et al. 2010; Mineo et al. 2012, Mineo et al. 2014). This fact is well understood in terms of the short evolutionary time scales of HMXBs, and by the fact that the secondary star is a young supergiant (e.g. Verbunt et al. 1995, Shtykovskiyy et al. 2007). On the other hand, the number of LMXBs, and their X-ray luminosity, correlate with the M_{star} of the galaxy. Also, joint relations were found between the X-ray luminosity, the SFR, and the M_{star} (Lehmer et al. 2016). Fragos et al. (2013) employed local scaling relations data to restrict the predictions of theoretical XRB population-synthesis models. They found that the spectral energy distribution (hereafter, SED) of the XRBs remains relatively unchanged with redshift, despite a substantial evolution of its normalization, which occurs primarily due to changes in the cosmic star-formation rate. However, the particular X-ray output of XRBs is affected by metallicity and mean stellar age. In particular, the X-ray luminosity per unit of star-formation rate from HMXBs varies by order of magnitude when moving from solar metallicity to metallicity below 10%, while the X-ray luminosity per unit of stellar mass from LMXBs reaches a peak at the age of around 300 million years and then gradually decreases at later times (see Fig. 2 of Fragos et al. 2013). For mean stellar ages exceeding approximately 3 billion years, there is little variation in the X-ray luminosity from LMXBs. These relations provide analytical and tabulated guidelines for the energy output of XRBs, which can be directly integrated into cosmological simulations or models of the X-ray emission of galaxies.

The X-ray luminosity-SFR relation provides estimates of the SFR less affected by uncertainties due to dust and gas absorption, as the X-ray light is less affected by interstellar extinction than other traditional indicators. This characteristic makes it a valuable tool for cross-calibrating various SFR indicators and diagnosing star formation in galaxies. However, when observing distant galaxies, distinguishing the emission from HMXBs, LMXBs, or supermassive black holes is challenging. In fact, AGNs seem to dominate the total X-ray emission of bright galaxies (Xue et al. 2011, Lehmer et al. 2012) and they actively play a role in the star formation activity of the

host galaxy (Torbaniuk et al. 2021). Also, it is known that galaxies contain a considerable amount of ionized gas at temperatures of around sub-keV, which contribute to the total X-ray emission (Grimes et al. 2005, Tüllmann et al. 2006). This hot gas can form in different ways, from mass loss of old stellar populations (e.g., stellar winds from evolved stars, planetary nebulae, and Type Ia supernovae, accretion of the intergalactic medium, as well as mergers of small galaxies and can dominate the X-ray emission of the galaxy in the soft band (0.5-2 keV). As only the XRB emission correlates with stellar population properties, an extremely difficult challenge is to disentangle the contribution of each of these components, in order to probe the aforementioned scaling relations.

In this paper, we make use of the eROSITA Final Equatorial Depth Survey (eFEDS, Brunner et al. 2022) to study the correlation between SFR and X-ray luminosity. The extended ROentgen Survey with an Imaging Telescope Array (eROSITA; Merloni et al. 2012, Merloni et al. 2020, Predehl et al. 2021) as part of the Spectrum-Roentgen-Gamma (SRG, Sunyaev et al. 2021) mission, has become a crucial tool for investigating the X-ray characteristics of galaxies. The X-ray observations are combined with UV (GALEX), optical and near-IR (KiDS, HSC, VISTA/VHS), and mid-infrared (WISE) data (Salvato et al. 2022). These data are used to fit the SED of the galaxies to estimate their physical properties. The paper is organized as follows. In Section 4.3, we describe the dataset and the sample selection based on the quality of the photometry. In Section 4.4 we present the broadband SED fitting method and the first AGN selection based on photometry. In Section 4.5, we discuss the reliability of the estimated physical properties. We describe the subtraction of other X-ray components, such as hot gas, and a second AGN selection based on the SED fitting in Section 4.6. In Section 4.7, we discuss the results on the L_x -SFR and L_x -sSFR relations. The summary and conclusions are presented in Section 4.9. Throughout this paper we use the WMAP7 cosmology (Komatsu et al., 2011): $\Omega_m = 0.272$, $\Omega_\Lambda = 0.728$, and $H_0 = 70.4 \text{ km s}^{-1} \text{ Mpc}^{-1}$.

4.3 Data and sample selection

This work is based on a combination of eROSITA and ancillary data spanning from the ultraviolet (UV) to the mid-infrared (MIR). Here we briefly summarize the main properties of the catalog and refer the reader to the cited papers for more details.

The X-ray sources presented in this work are detected by eROSITA, the primary instrument aboard the SRG orbital observatory (Sunyaev et al. 2021). The main objective of the SRG mission is to perform a four-year survey of the full sky in continuous scanning mode. The sources taken into account in this work are part of the eFEDS, which scans ~ 140 square degrees of the sky as a verification phase ahead of the planned four years of all-sky scanning operations. With the exception of the all-sky surveys, eFEDS represents the largest contiguous X-ray survey in the soft X-rays band. A detailed explanation of the data processing and properties of the catalog can be found in Brunner et al. (2022). The catalog includes 27 910 X-ray sources detected in the band 0.2-2.3 keV, with detection likelihoods ≥ 6 , corresponding to a (point source) flux limit of $6.5 \times 10^{-15} \text{ erg s}^{-1} \text{ cm}^{-2}$ in the 0.5–2.0 keV energy band. To ensure the highest signal-to-noise ratio (SNR) of the X-ray sample used in this work, we exclude sources located at the border of the fields (INAREA90 flag, 3% of the total).

In order to estimate galaxies' physical parameters, multi-wavelength observations are required. Salvato et al. (2022) provides a catalog of multi-wavelength counterparts and redshifts of the X-ray sources presented in Brunner et al. (2022). Considering the large PSF (~ 16) and the small number of photons associated with a typical X-ray detection, the positional uncertainties of the sources can be in the order of the arcsecond, making the identification of the counterpart impossible to determine by the closest neighbor match alone. To overcome this problem Salvato et al. (2022) performed two different methods specifically developed to identify the correct counterparts to X-ray sources: 1) *NWAY* (Salvato et al. 2018), based on Bayesian statistics; 2) *ASTROMATCH* (Ruiz et al. 2018), based on maximum likelihood ratio (Sutherland et al. 1992). A detailed descriptions of these methods can be found in Salvato et al. (2022). The DESI Legacy Imaging Survey DR8 (LS8; Dey et al. 2019) was used for the optical counterpart identification. Together with LS8, UV, optical, and infrared photometry were included.

Each counterpart is assigned a quality flag, `CTP_QUALITY`, that characterizes the quality of the cross-match. To ensure reliable optical photometry for the SED fitting, we select only objects having `CTP_QUALITY > 2`, which are objects for which both methods agree on the counterpart but only one assigns to it a cross-match probability above the threshold (`CTP_QUALITY = 3`) or both agree on the counterpart and have assigned probability above the threshold (`CTP_QUALITY = 4`). In this way, we select 22 256 objects (81% of the total sample).

Sources are classified as Galactic or extra-Galactic (see detail in Section 5 of Salvato et al. 2022). To ensure the removal of foreground Galactic stars from the analysis we select only objects flagged as `SECURE EXTRAGALACTIC` (5100, 19% of the total sample). Furthermore, a redshift quality flag is given to the sources, `CTP_REDSHIFT_GRADE`, in a range from 5 (spectroscopy) to 0 (unreliable photo-z). Photometric redshifts are computed using *LePHARE* code (Arnouts et al. 1999; Ilbert et al. 2006) and the estimates are then compared with those obtained with *DNNz* (Nishizawa et al. in prep.), a machine learning method that uses HSC photometry. A detailed description of the method can be found in Salvato et al. (2022). In this work, we adopt the selection criteria `CTP_REDSHIFT_GRADE \geq 3`, which includes all previously selected sources (5100, 19% of the total sample).

In our analysis, galaxies' physical properties are estimated via SED fitting, which requires high-quality multi-wavelength measurements to ensure reliable results. The SFR especially requires high-quality IR observations to account for the amount of UV light absorbed and re-emitted by the dust. Therefore, we require the X-ray sources to have at least one available observation in each of the u, g, r, I, z, J, H, K bands, and WISE1 and WISE2 bands signal-to-noise $SNR \geq 2$ (3 367 sources, 12% of the total sample).

The main goal of this work is to analyze the properties of the eROSITA sample of normal galaxies (non-AGN system) that are expected to relatively have low X-ray luminosities ($L_x \leq 3 \times 10^{42}$ erg/s) compared to the AGN system (Luo et al. 2017, Lehmer et al. 2016). Such systems are hardly observed at high redshift, due to the limit on the sensitivity of the instrument (Fig. 4.3). Taking into account the eFEDS sensitivity limit, we restrict our analysis to the sources having $z < 0.35$ (888, 3.18% of the total sample). At the end of the selection criteria, we restrict our sample to 3% of the total initial sample, but we ensure the quality and reliability of the SED fitting process, explained in the next section. Table 4.1 shows the ancillary data associated with the X-ray sources. We stress that all the selected sources have reliable spectroscopic redshift (`CTP_REDSHIFT_QUALITY = 5`).

TABLE 4.1: List of photometry available as ancillary data for the X-ray sources. The number of detections corresponds to the sample of 888 galaxies initially selected as normal galaxies.

| Survey | Band | λ (μm) | Depth (AB mag) | Number of detections | Reference | |
|-------------|------|-----------------------------|----------------|----------------------|-----------------------|--------------------|
| GALEX | FUV | 0.15 | 19.9 | 248 | Bianchi (2014) | |
| | NUV | 0.23 | 20.8 | 323 | | |
| HSC | g | 0.48 | 26.8 | 830 | Aihara et al. (2018) | |
| | r | 0.62 | 26.4 | 573 | | |
| | i | 0.77 | 26.4 | 356 | | |
| | z | 0.91 | 25.5 | 834 | | |
| | y | 0.98 | 24.7 | 835 | | |
| KiDS/VIKING | u | 0.35 | 24.2 | 576 | Kuijken et al. (2019) | |
| | g | 0.48 | 25.1 | 576 | | |
| | r | 0.62 | 24.9 | 576 | | |
| | i | 0.76 | 23.7 | 575 | | |
| | J | 1.25 | 21.8 | 573 | | Edge et al. (2013) |
| | H | 1.64 | 21.1 | 573 | | |
| | K | 2.14 | 21.2 | 573 | | |
| LS8 | g | 0.48 | 24.0 | 888 | Dey et al. (2019) | |
| | r | 0.62 | 23.4 | 888 | | |
| | z | 0.91 | 22.5 | 888 | | |
| VISTA/VHS | Ks | 2.15 | 19.8 | 251 | McMahon et al. (2013) | |
| WISE | W1 | 3.35 | 21.0 | 888 | Meisner et al. (2019) | |
| | W2 | 4.60 | 20.1 | 888 | | |
| | W3 | 11.56 | 16.7 | 831 | | |
| | W4 | 22.08 | 14.5 | 712 | | |

4.4 Methodology

4.4.1 SED fitting

The SED fitting was performed with the Code Investigating GALaxy emission¹ (CIGALE, Noll et al. 2009, Boquien et al. 2019). We provide here a brief summary of the tool and refer to Boquien et al. (2019) for a detailed description. CIGALE is a Bayesian SED fitting code designed to estimate the physical properties of the galaxy (i.e. SFR, M_{star} , dust luminosity (hereafter, L_{dust}), etc.). It models the emission spectra of the stellar component and combines them with dust attenuation and emission. The latest version of CIGALE also extends to the X-ray domain, modeling the X-ray emission of the AGN, XRBs, and hot gas components of the galaxy (Yang et al., 2020; Yang et al., 2022). In the fitting process, CIGALE preserves the energy balance considering the energy emitted by young massive stars, which is partially absorbed by the dust grains and re-emitted in the MIR and far-IR (FIR). In this work, the SEDs are built as the superposition of six modeled components: star formation history (SFH), single stellar population (SSP), dust attenuation, dust emission, AGN and X-ray emission. Table 4.2 shows the main input parameters used in the SED fitting process. Figure 4.1 shows an example SED fitted with the adopted procedure.

Star formation history and SSP

As shown in previous works (Ciesla et al. 2015, Małek et al. 2018, Riccio et al. 2021), an SFH that models the bulk of the stellar population with the addition of a recent burst of star formation provides very good estimates of the SFR and M_{star} . This kind of SFH is in the form of a delayed exponential plus an exponential burst:

¹<https://cigale.lam.fr>

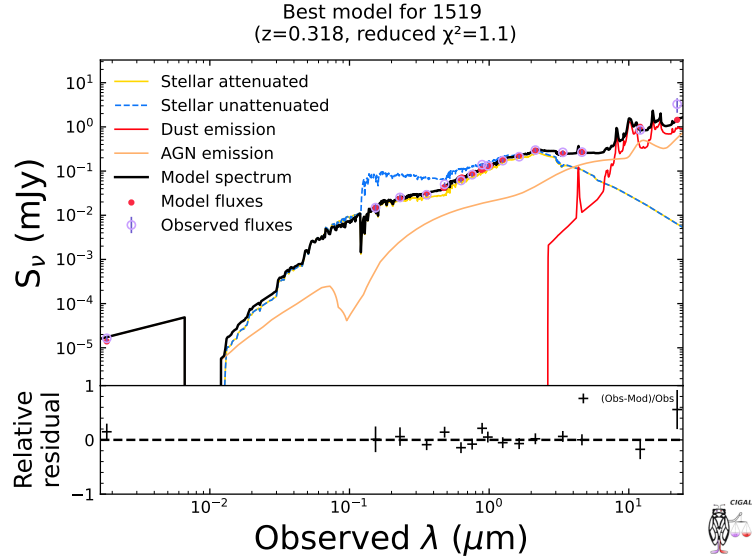


FIGURE 4.1: Exemplary SED fitted for an object at $z = 0.32$, adopting the procedure described in Section 4.4. The black solid line represents the total modeled spectrum, the red solid line the dust emission, the yellow solid line the attenuated stellar emission, the orange solid line the AGN emission and the dashed blue line the unattenuated stellar emission. The observed fluxes employed for the fitting are represented as purple empty circles, while the modeled fluxes are the red-filled circles. The bottom panel shows the residuals of the fit.

$$SFR(t) = t \times e^{(-t/\tau_{main})} / \tau_{main}^2 + t e^{-(t-t_{burst})/\tau_{burst}}, \quad (4.1)$$

where τ_{main} and τ_{burst} are the e-folding time of the main stellar and the late starburst populations, respectively.

After calculating the SFH, the following step involves computing the intrinsic stellar spectrum. This requires us to choose a library of single stellar populations. In this work, we adopt the SSP model by Bruzual et al. (2003) with the initial mass function given by Chabrier (2003). We set the metallicity of the model $Z = 0.02$. The spectrum of the composite stellar populations is calculated by computing the dot product of the SFH with the grid containing the evolution of the spectrum of an SSP with steps of 1 Myr.

Dust attenuation and emission

At this stage, the stellar populations are still dust-free. As dust attenuation law we use the Calzetti et al. (2000) law extended with Leitherer et al. (2002) curve between the Lyman break and 150 nm.

To model the dust emission employ Dale et al. (2014) model, based on a sample of SFGs presented in Dale et al. (2002). In their latest update, they improved the PAH emission and introduced an optional AGN component. The star-forming component is described with a single parameter α , which is defined as $dM_d(U) \propto U^\alpha U dU$, where M_d is the dust mass and U represents the intensity of the radiation field. The α parameter is closely related to the 60-100 μm color. The main strength of this model is its simplicity, with only one parameter, straightforward to interpret based on the observations.

AGN and X-ray emission

As shown by Liu et al. (2022), the eFEDS sample is mainly composed of AGN, especially at high redshift (Mountrichas et al. 2022). We derive the AGN contribution to the UV-to-IR emission of the galaxy using SKIRTOR model (Stalevski et al. 2012, Stalevski et al. 2016). The model considers the primary source of emission of the AGN, the accretion disc, surrounded by an optically and geometrically thick dusty torus. The model allows the user to set several parameters for the geometry of the torus, the extinction and emissivity of the polar dust, its temperature, etc.

In our analysis, we define a parameter called $f_{0.25\mu m}$. This parameter, as opposed to $AGN_{fraction}$ defined in default by CIGALE, as the ratio between the AGN luminosity to the total dust luminosity, describes the ratio of the AGN UV luminosity at $0.25 \mu m$ to the total UV luminosity at that wavelength. We explain the reason for using the UV estimate, instead of the default parameter in the IR, in Section 4.6.3. This parameter can be used to discriminate AGN systems from normal galaxies. We sample the $f_{0.25\mu m}$ from 0 to 0.7 to consider the strong contribution from nuclear sources in our sample. Allowing the code to consider high nuclear non-stellar contributions, we will be able to use this parameter to discriminate against AGN systems (see section 4.6.3).

The X-ray component is modeled as a superposition of XRBs, hot gas, and AGN. The HMXBs and LMXBs emission is modeled using the predictions from theoretical XRB population-synthesis models found by Fragos et al. (2013). However, these relations represent an approximation of the overall population of galaxies, and single galaxies can largely scatter around it. For this reason, the *xray* module of CIGALE includes two free parameters, δ_{HMXB} and δ_{LMXB} to account for the scatter from the scaling relations. More details about the module can be found in Yang et al. (2020) and Yang et al. (2022). We run the SED fitting setting δ_{HMXB} and δ_{LMXB} to 0 and discuss the possible scatter in the results. The AGN emission is modeled using the $\alpha_{ox} - L_{v,2500}$ relation from Just et al. (2007), where $L_{v,2500}$ is the intrinsic disk emission at 2500 Å at a viewing angle of 30° and α_{ox} is the AGN SED slope connecting $L_{v,2500}$ and $L_{v,2keV}$.

The full set of parameters employed in the SED fitting process is shown in Table 4.2. The quality of the fit is expressed by the best χ^2 (and a reduced best χ^2 defined as $\chi_r^2 = \chi^2 / (N - 1)$, with N the number of data points). The minimum value of χ_r^2 corresponds to the best model selected from the grid of all possible computed models from the input parameters. After the fit, we removed 164 galaxies with $\chi_r^2 > 10$ from the initial sample of 888 galaxies. From now on we refer to the remaining 724 sources as the final sample.

4.4.2 Identification of AGN systems

In order to study the properties of galaxies for which the X-ray emission is dominated by XRBs we need to reveal the presence of nuclear non-stellar emission. Given the presence of both nuclear and star-formation emissions, we use a combination of multi-wavelength techniques to identify the AGNs. We estimate the rest-frame X-ray luminosity in the 0.2-2.3 band using the formula:

$$\log(L_{0.2-2.3}) = \log(f_{0.2-2.3}) + 2\log(Dls) + \log(4\pi) - \log(E_{cor}) + \log(K_{cor}), \quad (4.2)$$

where E_{cor} and K_{cor} are corrections for the energy range and redshift respectively, Dls is the luminosity distance and $f_{0.2-2.3}$ is the flux detected in the 0.2-2.3 keV band. The assumed photon index is $\Gamma = 1.8$, indicated to reproduce emission from HMXBs (Lehmer et al. 2016).

TABLE 4.2: Input parameters for the code CIGALE.

| Parameters | Values |
|--|--|
| Star formation history: | |
| <i>Delayed star formation history + additional burst</i> | |
| e-folding time of the main stellar population model (Myr) | 1000, 3000, 5000 |
| e-folding time of the late starburst population model (Myr) | 50.0, 100 |
| Mass fraction of the late burst population | 0.0, 0.005, 0.015, 0.02, 0.05, 0.1, 0.15, 0.20 |
| Age (Myr) | 8000, 9000, 10000, 11000, 12000 |
| Age of the late burst (Myr) | 100, 150 |
| Single stellar population Bruzual et al. (2003) | |
| Initial mass function | Chabrier (2003) |
| Metallicities (solar metallicity) | 0.02 |
| Age of the separation between the young and the old star population (Myr) | 10 |
| Dust attenuation law Calzetti et al. (2000) | |
| $E(B - V)$: color excess of the nebular lines | 0.1, 0.3, 0.5, 0.7, 0.9 |
| $E(B - V)f$: reduction factor to compute the E(B-V) for the stellar continuum attenuation | 0.3, 0.5, 0.8, 1 |
| Dust emission: Dale et al. (2014) | |
| Fraction of AGN | 0 |
| α slope | 2.0 |
| AGN (UV-to-IR): Stalevski et al. (2016) | |
| Inclination, i.e. viewing angle (i) | 30, 70 |
| AGN contribution to UV luminosity ($f_{0.25\mu m}$) | 0.0, 0.001, 0.0025, 0.005, 0.0075, 0.01, 0.025, 0.05, 0.075 , 0.1, 0.2, 0.3, 0.4, 0.5, 0.6, 0.7 |
| Polar-dust color excess (E(B-V)) | 0, 0.2, 0.4 |
| X-ray emission: Yang et al. (2020) and Yang et al. (2022) | |
| Photon index of the AGN intrinsic X-ray spectrum (gam) | 1.8 |
| Power-law slope connecting L_ν at rest-frame 2500 and 2 keV (α_{ox}) | -1.9, -1.7, -1.5, -1.3, -1.1, -0.9 |
| Maximum allowed deviation of α_{ox} from the empirical $\alpha_{ox} - L_\nu(2500)$ | 0.2 |
| Deviation from the expected LMXB scaling relation (δ_{lmxb}) | 0.0 |
| Deviation from the expected HMXB scaling relation (δ_{hmxb}) | 0.0 |

Notes: The input values used for better sampling the $f_{0.25\mu m}$ are in boldface type (see Section 4.6.3).

We classify a source as AGN if it satisfies at least one of the following criteria:

1. X-ray luminosity of $L_{0.2-2.3} \geq 3 \times 10^{42}$ erg/s.
2. X-ray-to-optical flux ratio of $\log(f_X/f_r) > -1$ (where f_X is the flux detected in the 0.2-2.3 keV range, and f_r is the flux observed in the r band).
3. X-ray-to-NIR flux ratio of $\log(f_X/f_K) > -1.2$.

These first 3 criteria are described in section 4.4 of Xue et al. (2011).

The above selection criteria may still not identify highly obscured AGN. For this reason, making use of the MIR observations by WISE, we selected AGN sources following the color selection criteria presented in Assef et al. (2013). This method selects especially obscured AGN and has the advantage to make no use of the WISE4 band, which is often affected by low SNR. We select as AGN only objects having a 90% selection reliability.

Sources that do not meet any of these criteria are classified as "normal galaxies". We identify 405 AGN (55% of the final sample) and 319 normal galaxies (44% of the final sample). Figure 4.2 shows the X-ray/optical flux selection criteria in the r band (left panel) and the MIR selection criteria adopting WISE photometry. We notice that the majority of the AGNs are selected by X-ray luminosity, though a consistent number of obscured AGNs is selected with WISE selection criteria.

The redshift distribution of AGNs and normal galaxies is shown in Fig. 4.3. We notice that above redshift ~ 0.35 , we do not detect any normal galaxy due to the sensitivity limit of the instrument.

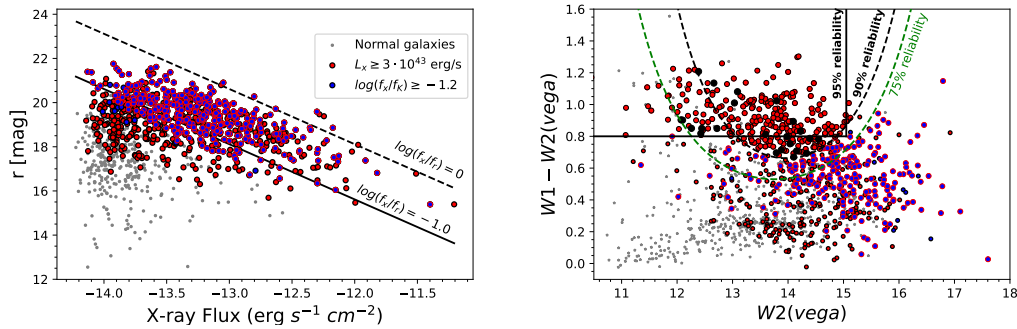


FIGURE 4.2: Left panel: Optical r-band AB magnitude vs the X-ray flux for the final selected sample. Diagonal lines indicate a constant flux ratio between the r-band and X-ray. Right panel: WISE1-WISE2 color vs WISE2-band VEGA magnitude. The lines represent the MIR WISE selection criteria, 95% reliability (solid line), 90% reliability (dashed black line) 75% reliability (dashed green), respectively. Black circles represent the WISE-selected AGNs in this work. For all panels, the grey circles represent the normal galaxies, the red circles the X-ray luminosity selected AGN, blue circles the K band selected AGNs.

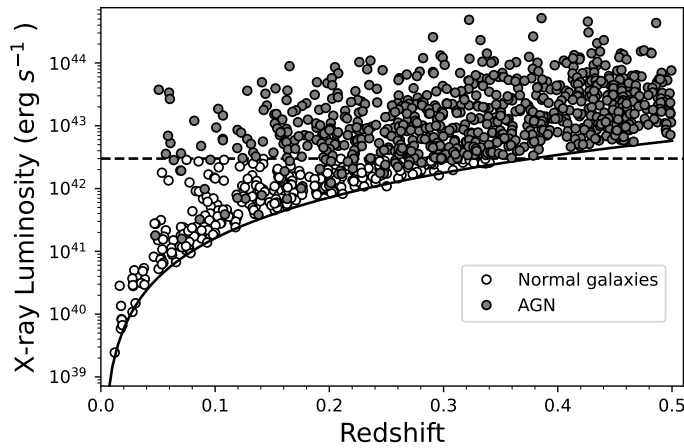


FIGURE 4.3: X-ray luminosity vs redshift for the selected final sample. The dashed black line indicates $L_x = 3 \times 10^{42} \text{ erg/s}$. The solid black line represent the eFEDS sensitivity limit of $f_{limit} = 6.5 \times 10^{-15} \text{ erg s}^{-1} \text{cm}^{-2}$ Brunner et al. (2022). Grey and white circles represent AGN and normal galaxies respectively for the final selected sample.

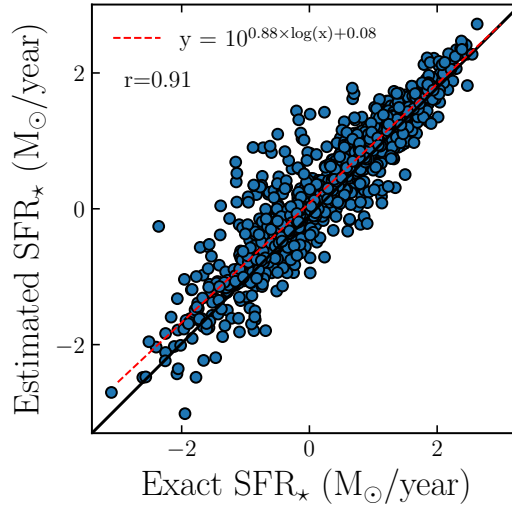


FIGURE 4.4: Comparison between the true value of the SFR provided by the best-fit model for the mock catalog (x-axis) and the value estimated by the code (y-axis). The Pearson product-moment correlation coefficient is given as the ‘r’ value. The black line corresponds to the 1:1 relation, while the red dashed line is the regression line with the equation given in the legend.

4.5 SFR estimates and reliability check

4.5.1 Mock analysis

To ensure the reliability of the computed SFR, a mock catalog is created using an option in CIGALE, which employs the best-fit model from the SED fitting to build an artificial object for each galaxy with known physical parameters. The process is described in detail in Giovannoli et al. (2011) and Lo Faro et al. (2017).

The physical properties are evaluated using a Bayesian method. This is done through a likelihood estimation. Each model in the grid of models built from the starting input parameters will have an associated likelihood taken as $\propto \exp(-\chi^2/2)$. This value is used as the weight to estimate the physical parameters as the likelihood-weighted mean of the physical parameters attributed to each model, while the related uncertainties are estimated as likelihood-weighted standard deviations of the physical parameters (see Section 4.3 of Boquien et al. 2019).

In Figure 4.4, we compare the output SFR of the mock catalog with the best values estimated by the code. The Pearson product-moment correlation coefficient (r) is used as a measure of the reliability of the obtained properties. We find a slight overestimation of the estimated values at low SFR, but statistically consistent with the exact value.

4.5.2 SFR estimates with FIR data

As was shown in previous works (i.e. Buat et al. 2019, Riccio et al. 2021), the lack of IR observations can lead to over or under-estimations of the SFR when broadband SED fitting methods are used. In particular, when FIR data are missing, it is not possible to constrain with sufficient precision the peak of the dust emission, making the estimate of the total dust luminosity incomplete. This could lead to inaccurate implementation of the energy balance and finally, to over or under-estimation of the

SFR. Even though Riccio et al. (2021) shows that a combination of optical and MIR data is enough to reliably estimate the SFR, to be as conservative as possible we validate our SFR estimates, when it is possible, using other indicators.

To validate SFRs obtained from the broad-band SED fitting we acquire data in the FIR wavelength, to improve the estimation of the dust luminosity. For this reason, we cross-matched our sample with observations performed by for the *Herschel Extragalactic Legacy Project* (HELP Shirley et al. 2021) survey in the GAMA09 field, that overlaps with the eROSITA data. *Herschel* was equipped with two imaging instruments, the Photodetector Array Camera and Spectrometer (PACS; Poglitsch et al. 2010), which observed the FIR at 100 and 160 μm , and the Spectral and Photometric Imaging Receiver (SPIRE; Griffin et al. 2010), which covered the 250, 350, and 500 μm wavelength ranges. In the GAMA09 field, we have found the detections only from the SPIRE instrument. We identify 53 matches to our sample adopting a 1 matching radius using coordinates from the optical observations. The cross-match is done only on galaxies that we flagged as ‘normal galaxies’ with the AGN selection discussed in Section 4.4.2. From now on we refer to the objects with HELP counterparts as the eROSITA_{G9} sample. To estimate the number of false matches, we shift the FoV of the eROSITA sample of 10 in all directions, each time performing the cross-match again. We find one possible false match between the two samples. We then perform the SED fitting on the eROSITA_{G9} sample using UV, optical, and WISE data from the initial sample, plus SPIRE data from HELP. We remove possibly failed fit cutting sources with $\chi_r^2 > 10$. This cut removes five galaxies from eROSITA_{G9} sample.

Figure 4.5 shows the results obtained with SED fitting using data up to WISE detections, with the one obtained for the eROSITA_{G9} sample. The top panel shows overall comparable results for the SFR, with a slight underestimation at $SFR > 1$. Furthermore, the employ of MIR observation without FIR detections can lead to a wrong differentiation between dust emission due to the AGN activity and due to star formation. Indeed, comparing the $f_{0.25\mu\text{m}}$ parameter between the two runs, we find higher values when only data up to the MIR wavelengths are used (bottom panel, Fig. 4.5). Constraining the FIR peak with SPIRE data, the code correctly attributes to the star formation activity part of the MIR emission assigned previously as AGN contribution, resulting in a lower $f_{0.25\mu\text{m}}$. As a result of the comparison, for the objects having HELP counterparts, we decide to update the values of the SFR, $f_{0.25\mu\text{m}}$, and the other physical parameters with those obtained from the SED fitting of the eROSITA_{G9} sample.

4.5.3 Spectral counterpart and BPT diagram

As discussed in Section 4.2, the emission from HMXBs directly traces the young stellar population. This makes the H_α SFR indicator the best to study the Lx-SFR relation, as it traces the emission from young stellar populations with the resolution of a few million years. For this reason, to further check the reliability of our SFR estimates, we cross-match our sample with the MPA/JHU catalog based on the *Sloan Digital Sky Survey* DR7 release (Abazajian et al. 2009), which provides images, imaging catalogs, spectra, and redshifts. We are interested in the spectral data of the catalog, especially the H_α line, whose specifications are explained in detail in Tremonti et al. (2004a). The cross-match is performed in the same way as the eROSITA_{G9} sample. We identify 106 matches to our sample adopting a 1 matching radius. Again, the cross-match is restricted only to galaxies flagged as ‘normal galaxies’. We identify one possible false match between the two samples. To avoid biases in the SFR

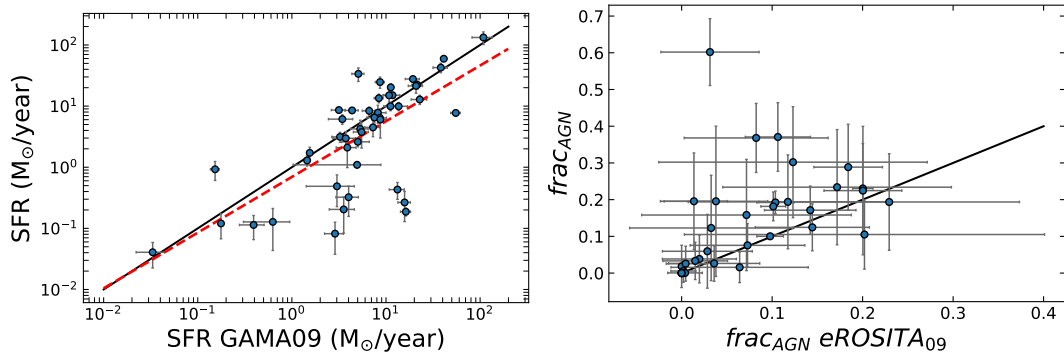


FIGURE 4.5: Left panel: Comparison between the SFR evaluated with data up to WISE (y-axis) and SFR estimated adding SPIRE FIR data (x-axis). The black solid line corresponds to the 1:1 relation, red dashed line to the linear fit of the data. Right panel: Comparison between $frac_{AGN}$ parameter estimated by the two runs. The solid line corresponds to the 1:1 relation.

estimates, we choose sources having $SNR > 3$ for the fluxes of all spectra, leaving us with 50 counterparts.

For the 50 galaxies, we corrected H_α , H_β , N_{II} , S_{II} , O_I , and O_{III} emission lines for attenuation from the measured Balmer decrement, assuming the case B recombination ($H_\alpha/H_\beta = 2.87$) and adopting Cardelli et al. (1989) law assuming $RV = 3.1$. A similar process was performed in Pistis et al. (2022). After correcting for the attenuation, we employ Kennicutt (1998) relation to estimate the SFR.

The top panel of Fig. 4.6 shows the comparison between derived from H_α (hereafter, $SFR_{H\alpha}$) and the one from the SED fitting up to WISE detection. This comparison shows a consistent difference between the two values of the SFR, with the SED fitting underestimating the SFR below $2 M_\odot yr^{-1}$, and overestimating above this value. To explain this trend, we examine the Baldwin-Phillips-Terlevich diagram (BPT, Baldwin et al. 1981) to further inspect the presence of nuclear activity due to SMBH accretion. The bottom panel of Fig. 4.6 shows the BPT diagram for the 50 sources flagged as ‘normal galaxies’ with SDSS spectra. Galaxies were classified using the optical emission line ratios $\log[N_{II}/H_\alpha]$, $\log[S_{II}/H_\alpha]$, $\log[O_I/H_\alpha]$, and $\log[O_{III}/H_\beta]$, as star forming galaxies (SFGs), *Low-ionization nuclear emission-line region* (LINER), Seyfert, and composite. We find that the majority of the galaxies that scatter from the 1:1 relation are classified as Seyfert or LINER. These galaxies are known to host ionization of the ISM, which can be powered both by star formation or AGN activity (Heckman 1980, Terlevich et al. 1985). However, most of these galaxies in the nearby Universe appear to have low levels of star formation activity (Larkin et al. 1998, Bendo et al. 2002), and the mid-infrared spectra do not appear similar to the spectra expected from star formation. For these objects, the H_α emission would be attributable to the activity of the SMBH and so would not be appropriate to use it as SFR indicator. For this reason, at the end of the analysis, we decide to update the SFR estimates with the one obtained with H_α only for the sources classified by the BPT diagram as star-forming and to exclude AGN and composite galaxies from our sample. Also, this investigation suggests that our sample of normal galaxies could be affected by a severe AGN contamination.

At the end of the process, 48 galaxies are updated with the SFR estimated using SPIRE data, eROSITA_{G9} sample, and four galaxies are updated with H_α estimated values, for a total of 52 sources (7.3% of the “normal galaxy” sample). We stress that

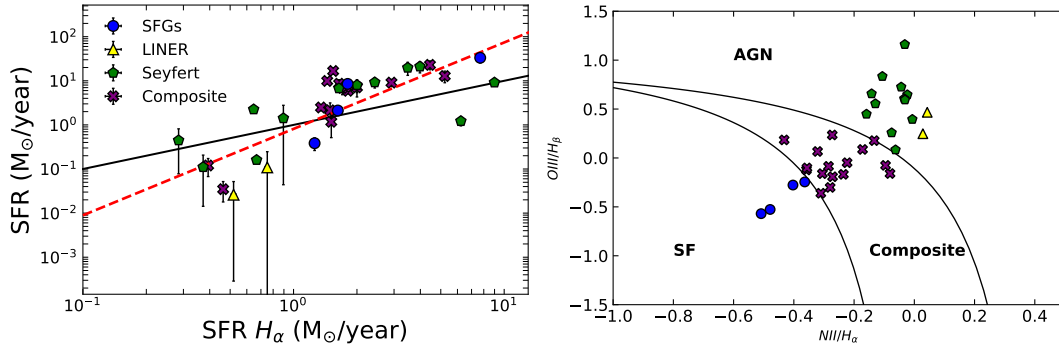


FIGURE 4.6: Left panel: Comparison between the SFR evaluated with the SED fitting up to WISE (y -axis) and SFR estimated using H_{α} lines (x -axis). The black solid line corresponds to the 1:1 relation, red dashed line to the linear fit of the data. Right panel: BPT diagram for the sources having spectral counterparts. The solid line delimits the division between SFG, AGNs, and composite. For both panels, the blue dots represent the SFGs, yellow triangles the LINERs, green pentagons the Seyferts and purple crosses the composite galaxies

the SDSS subsample and the eROSITA_{G9} sample do not have any common source.

4.5.4 Galaxies distribution on the SFR- M_* relation

It is known that the SFR- M_* plot of the galaxies highlights the existence of three different primary populations, according to their efficiency to form stars. In this plot Figure 4.7 shows the distribution of our sample of galaxies on the SFR- M_* plot. We classify them based on their SFRs relative to the evolving star-forming main sequence. We set the threshold between categories as 1.3 dex below (or above) the main sequence (MS) defined by Aird et al. (2017) and given by the equation:

$$\log \text{SFR}(z) [\text{M}_{\odot} \text{yr}^{-1}] = -7.6 + 0.76 \log \frac{M_*}{M_{\odot}} + 2.95 \log(1+z). \quad (4.3)$$

Galaxies 1.3 dex below the MS are categorized as quiescent or passive, those above 1.3 dex are classified as starburst, while those lying in between are labeled as SFGs. It is worth noting that the relation presented in Eq. 4.3 is redshift-dependent. To account for this dependence, we use the redshift of each individual object to classify it as passive, normal star-forming, or starbursting.

Using Eq. 4.3 we find that our final sample of 319 galaxies sample consists of 98 sources classified as star-forming (30% of the normal galaxy sample) and 221 as quiescent galaxies (70% of the normal galaxy sample). Our sample does not include any starbursting candidates.

The right panel of Fig. 4.7 shows the selected normal galaxies color-coded by $f_{0.25\mu\text{m}}$ parameter. We find a wide range of $f_{0.25\mu\text{m}}$ values. We stress that the majority of the sources with high $f_{0.25\mu\text{m}}$ values, higher than 0.2, reside in the region populated by the quiescent galaxies. This further suggests that our sample of normal galaxies can be strongly contaminated by nuclear activity. We will discuss this contamination in Section 4.6.3.

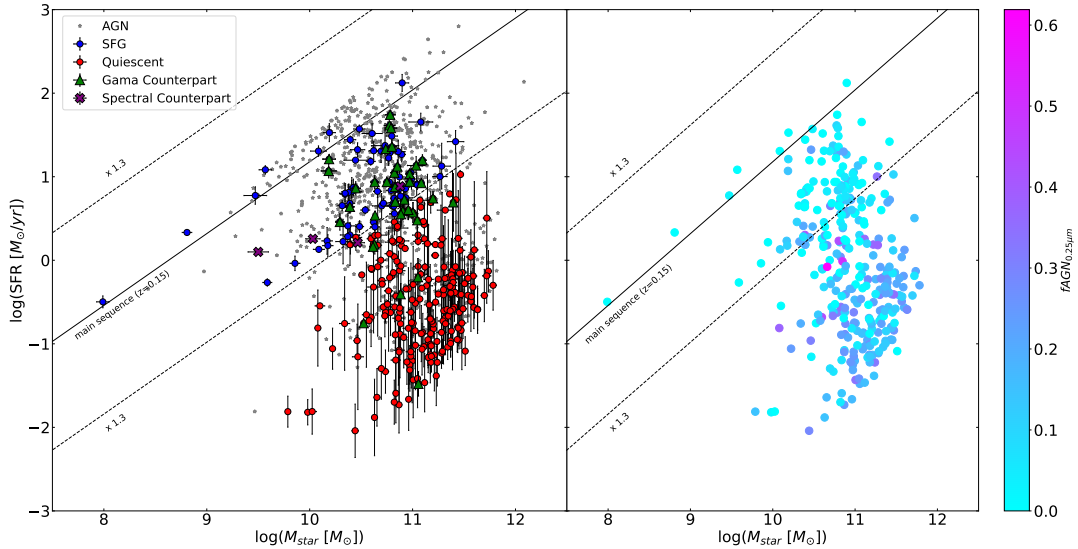


FIGURE 4.7: Left panel: 724 galaxies from the final sample shown in in the SFR- M_* plot. Blue points represent the SFGs, red points show the location of the quiescent galaxies, and grey points the AGNs classified as described in section 4.4.2. Right panel: the same plot showing star-forming and quiescent galaxies color-coded by the $f_{0.25\mu\text{m}}$ parameter. The solid black line represents the MS from Aird et al. (2017) at redshift 0.15 (the mean redshift of our sample of normal galaxies). The dashed line shows the threshold 1.3 dex above and below the MS.

4.6 Subtraction of other contributions to the total X-ray luminosity

As discussed in section 4.2, the X-ray emission of galaxies is the combination of the output of different sources, such as XRBs, hot gas, and AGNs. Different types of galaxies have varying contributions to their X-ray emissions. In normal SFGs, the XRBs typically dominate the total emission at energies $\sim 1 - 10$ keV, with LMXBs associated with the old stellar population in the bulge while HMXBs are linked to younger stellar population concentrated primarily in the disk or in the arms of the spiral. Conversely, as usually undergoing a prolonged period of quenching, elliptical galaxies have only one type of XRBs, which is the LMXBs. While the hard band (2-10 keV) is entirely dominated by XRBs in normal galaxies, the soft band (0.2-2 keV) can be significantly contaminated by hot gas emission, especially in elliptical galaxies. This contribution was found in the literature to scale with the SFR in SFGs (Mineo et al. 2012) and with K-band luminosity in ellipticals (Kim et al. 2013, Civano et al. 2014). Therefore, it is necessary to adjust the X-ray luminosity by accounting for the various types of galaxy populations.

Coronally active binaries (ABs) and cataclysmic variables (CVs) are additional types of stellar sources that can emit X-rays and hence make a contribution to the total X-ray luminosity of a galaxy. Although their X-ray luminosity was estimated in elliptical galaxies (e.g., Pellegrini 1994), their significance is often disregarded due to their relatively weaker luminosities compared to the more luminous LMXBs (see Fabbiano 2006 for a review). On top of that, even if not entirely dominated by AGNs, a nuclear contribution to the total X-ray luminosity can still be relevant. To account for all listed above sources of emission, we perform a correction of the X-ray luminosity of our sample, separately for the two populations of galaxies selected in

Section 4.5.4 (quiescent and SF).

4.6.1 Quiescent galaxies

To evaluate the contribution of the hot gas to the total X-ray emission of the passive galaxies we use the relation between X-ray emission and K-band luminosity in the form of $L_x \sim L_K^\alpha$ with an exponential slope of $\alpha = 4.5$ (Kim et al. 2013, Civano et al. 2014). As the K magnitude we use the VISTA/VHS K_S band available as ancillary data in the catalog from Salvato et al. (2022). We calculate the K band luminosity in units of solar luminosities using the equation from Civano et al. 2014:

$$L_K[L_\odot] = 10^{(-K-K_\odot)/2.5} \cdot (1+z)^{\alpha-1} \cdot (D_{L_S}/10)^2, \quad (4.4)$$

where K is the K_S magnitude from VISTA/VHS, z is the redshift, D_{L_S} is the luminosity distance in parsec and $K_\odot = 5.12$ is the absolute AB magnitude of the Sun in K-band. To estimate the luminosity, a spectral shape of the type $f_\nu = \nu^\alpha$ is assumed, where $\alpha = -(J-K)/\log(\nu_J/\nu_K)$ and $J-K$ is calculated from the magnitudes.

To account for the emission from ABs and CVs we use the relation found in Boroson et al. (2011) for the soft band (0.5-2 keV):

$$L_X[\text{erg/s}] = 4.4_{-0.9}^{+1.5} \times 10^{27} L_K[L_\odot]. \quad (4.5)$$

4.6.2 Star forming galaxies

For SFGs, it is of crucial importance to isolate the contribution produced by HMXBs to the total X-ray emission of the galaxy, as this component correlates directly with the SFR. For this reason, we estimate the X-ray contribution from LMXBs, hot gas and ABs/CVs.

To account for the contribution of LMXBs, we employ the relation between $L_{x,LMXBs}$ and M_* found by Gilfanov (2004). In this work, they study the properties of X-ray binaries in 11 local early and late-type galaxies, finding that, in late-type galaxies, the $L_{x,LMXBs}$ correlates with the M_* as:

$$\frac{L_{x,LMXBs}}{10^{40}} \text{erg/s} = \frac{M_*^{0.98} M_\odot}{10^{11} L_\odot}. \quad (4.6)$$

As well as early-type galaxies, SFGs are also known to possess a significant amount of hot ionized gas, which is the source of X-ray emission, that was found to correlate with their SFR. To account for this component, we make use of the relation found in Mineo et al. (2012). Using a sample of nearby late-type galaxies, they found that the X-ray luminosity due to hot gas correlates with the SFR as:

$$L_{0.5-2\text{keV}}^{\text{gas}}(\text{erg/s}) = (8.3 \pm 0.1) \times 10^{38} \cdot \text{SFR}(M_\odot \text{yr}^{-1}). \quad (4.7)$$

To determine the combined X-ray emission from AB+CV, we use the same relation as for quiescent galaxies. The X-ray luminosities estimated from Eqs. 4.5 and 4.7 are converted from the 0.5-2 keV to 0.2-2.3 keV band assuming a power law photon index of $\Gamma = 1.26$ (Boroson et al. 2011) and $\Gamma = 1$ (Mewe et al. 1986) respectively.

Figure 4.8 shows the redshift distribution of the sample of quiescent and SFGs after the subtractions discussed above. We notice that for SFGs at low redshift ($z = 0 - 0.1$), the subtracted X-ray luminosity attributed to hot gas, LMXBs, and CVs/ABs reaches on average 20% of the observed X-ray luminosity. This contribution drops to an average of 3% going to higher redshift. On the contrary, we observe

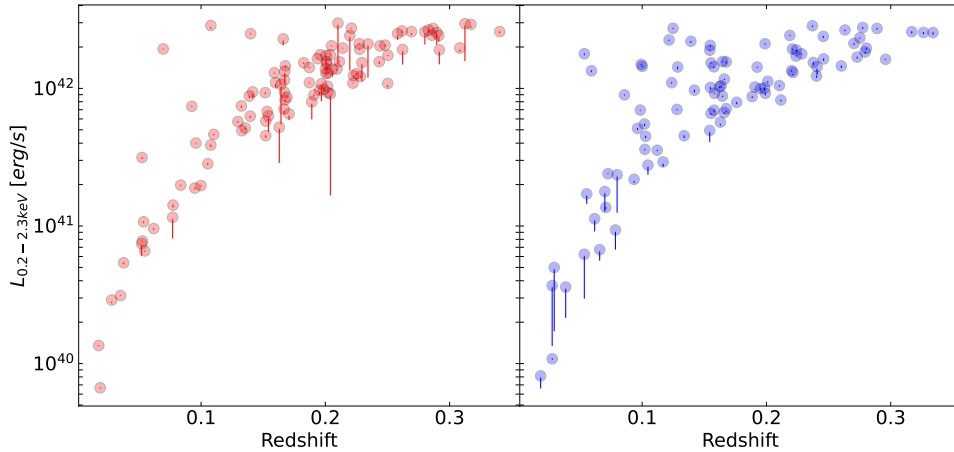


FIGURE 4.8: X-ray luminosity distribution over redshift for our sample of quiescent (left panel) and SFGs (right panel). The uncorrected values are presented as solid circles while the change in the L_x after the correction is shown by a solid line.

that our sample of quiescent galaxies is more contaminated by hot gas at high redshift (on average 10% of the observed X-ray emission), which drops moving to the very local Universe. At the end of the process, we expect to have X-ray emission only from LMXBs + possible AGN components for the quiescent galaxies and HMXBs + possible AGN components in SFGs. The AGN component will be discussed in the next section.

4.6.3 AGN contamination to the total X-ray luminosity

As discussed in section 4.5.3, some of the sources previously classified as "normal galaxies" are nevertheless identified as LINER or Seyfert galaxies by the BPT diagram. This makes clear that the classification carried out in section 4.4.2 is not enough to ensure a reliable sample of normal galaxies, and further investigations must be performed.

As described in section 4.4.1, the SED fitting process provides us further information, independent from the above, to classify AGNs, through the parameter $f_{0.25\mu\text{m}}$. A conservative choice often adopted in previous works (Małek et al. 2018, Ramos Padilla et al. 2022, Suleiman et al. 2022), defines galaxies with negligible AGN contribution the one having $AGN_{fraction} \leq 0.1 - 0.2$, depending on the work. However, this limit employed in the literature referred to the f_{AGN} parameter estimated in the IR range. In fact, as discussed in section 4.4.1, the $AGN_{fraction}$ parameter represents the fraction of the emission attributed to the AGN over the total emission of the galaxy in a specific wavelength, which can be set in CIGALE. Thus, as we estimate the parameter in the UV range (at $0.25 \mu\text{m}$), we have no previous literature feedback to identify a limit to safely select AGN systems. Therefore, further investigation must be carried out. We present the results as a function of $f_{0.25\mu\text{m}}$, estimated at $0.25 \mu\text{m}$, for two primary reasons:

1. Our objective is to obtain information on the X-ray emission of these sources, and since CIGALE computes this emission using the L_{2500} , the $f_{0.25\mu\text{m}}$ is directly linked to the $L_{X,AGN,0.2-2.3}$.

2. Probing the $f_{0.25\mu\text{m}}$ parameter allows us to identify Seyfert 1 galaxies, which are the main type of AGNs expected to contaminate our sample of normal galaxies. In fact, obscured AGNs (Seyfert 2) are expected to be well classified with the WISE band selection, with expected reliability of $\sim 90\%$ (Section 4.4.2, and Fig. 4.2 right panel). Also, highly obscured AGNs for which it is not possible to observe the broad line region (and therefore the $f_{0.25\mu\text{m}}$ would lead to wrong findings) are expected to be considerably obscured in the X-ray regime.

The basic idea presented in this Section is to select a sample of normal galaxies having the parameter $\text{fracAGN}_{0.2-2.3\text{keV}}$ defined as:

$$\text{fracAGN}_{0.2-2.3\text{keV}} = L_{\text{AGN},0.2-2.3\text{keV}} / L_{\text{total},0.2-2.3\text{keV}}, \quad (4.8)$$

less than an arbitrary threshold. Unfortunately, the standard version of CIGALE does not directly allow to estimate the f in the X-ray band due to its structure: the *xray* module is added to the SED fitting process after the AGN module when the $f_{0.25\mu\text{m}}$ is already computed. For this reason, we add the possibility to estimate $\text{fracAGN}_{0.2-2.3\text{keV}}$ in the *xray* module as part of the Bayesian evaluation process. This parameter will be strictly connected to the $f_{0.25\mu\text{m}}$ through the $L_{\text{AGN},0.2-2.3\text{keV}}$ luminosity, making clear the importance of a reliable estimate of this parameter. Therefore, we run the SED fitting process again, only on the sample of normal galaxies, better sampling the $f_{0.25\mu\text{m}}$ for low values². We limit the set of parameters to low values as we want to increase the quality of the $\text{fracAGN}_{0.2-2.3\text{keV}}$ estimates for $f_{0.25\mu\text{m}}$ lower than 0.1. With this set of parameters, all the sources previously best-fitted with $f_{0.25\mu\text{m}} > 0.1$ will have catastrophic fits and will be removed from the sample.

As our goal is to select sources with minimal $\text{fracAGN}_{0.2-2.3\text{keV}}$ contribution, to study the relation between SFR and the L_x for normal galaxies, the cleaning described above will not affect the final results. Furthermore, the estimates of SFR and M_{star} will not be significantly affected by the change since their estimation depends mostly on the SFH, SSPs and dust-related modules. In Fig. 4.9 we show the mock analysis for the computed values of $L_{\text{AGN},0.2-2.3\text{keV}}$, $L_{\text{XRB},0.2-2.3\text{keV}}$ and $\text{fracAGN}_{0.2-2.3\text{keV}}$. We notice that the AGNs and XRBs contributions to the X-ray luminosity are statistically well estimated by the SED fitting. Instead, we find a slight difference between the estimated and the exact values for the $\text{fracAGN}_{0.2-2.3\text{keV}}$ parameter, with a Pearson correlation coefficient of $r = 0.77$. However, the difference is mainly carried out by sources with estimated $\text{fracAGN}_{0.2-2.3\text{keV}}$ greater than 0.2, which will be removed at the end of the process. This result can be explained by considering the functioning of the Bayesian method. The sources far from the 1:1 relation have considerably higher values of $\text{fracAGN}_{0.2-2.3\text{keV}}$ estimated from the best-fit SED compared to the one estimated by the Bayesian method. For these sources, many models predicting low values of $\text{fracAGN}_{0.2-2.3\text{keV}}$ equally well fit the photometry. Consequently, these models will be associated with a high weight in the weighted estimation of the physical properties, considerably lowering the value of the estimated $\text{fracAGN}_{0.2-2.3\text{keV}}$. On the other hand, as we expected, the majority of the sources that are clustered on the right part of the plot are associated with a value of $f_{0.25\mu\text{m}}$ higher than 0.1 in the initial run described in Section 4.4. Therefore, the sources we are interested in are in the bottom left part of the diagram. We stress that

²The list of the $f_{0.25\mu\text{m}}$ parameters used for this second, refined SED fitting, is marked with bold values in the Table 4.2

this region of the plot, where the sources have estimated $fracAGN_{0.2-2.3keV} \sim 0$ (but never exactly 0) consists of 44 galaxies (magenta star in Fig. 4.9).

To be conservative, we decide to select as normal galaxies those expected to have an AGN contribution to the X-ray luminosity less than 10% ($fracAGN_{0.2-2.3keV} < 0.1$). With this limit not only we cut the majority of the outliers of the mock analysis, but we are confident to analyze only the stellar component of the X-ray emission. In this way, we select 49 sources: 34 SF and 15 quiescent galaxies. Only seven of these sources have an exact value of $fracAGN_{0.2-2.3keV}$ larger than 0.1. We stress that all the sources below the threshold have estimated $f_{0.25\mu m} \sim 0$.

4.7 Lx-SFR relation

As discussed in Section 4.2, our primary goal is to constrain the connection between X-ray luminosity and star formation activity for the sample of X-ray detected normal galaxies observed in the eFEDS survey. This can be achieved by fitting the empirical scaling relation between X-ray luminosity and SFR and comparing it with those inferred for local and distant galaxies. We limit this analysis only to the SFGs, as it was shown to have a strict dependence on the SFR. In Fig. 4.10 we present the measured X-ray luminosity, $L_{0.2-2.3keV}$, versus the SFR estimated using the broadband SED fitting method for our sample of SFGs. As already found in previous works, we find a positive correlation between X-ray luminosity and SFR. We perform a fit of our sample of SFG using the linear model:

$$\log(L_x) = A + B \cdot \log(\text{SFR}), \quad (4.9)$$

where L_x is in units of erg s^{-1} and SFR is in units of $M_\odot \text{ yr}^{-1}$. We derive the fitting constants $A = 40.67 \pm 0.21$ and $B = 0.57 \pm 0.20$. Despite the correlation between the two parameters, due to the scatter of the sources, the fit does not yield statistically robust results, with a $\chi_r^2 = 11.32$. The scaling relation from Lehmer et al. (2016) is plotted as a dashed black line representing the XRBs emission of a sample of normal galaxies in the local universe ($z \sim 0$). This sample was obtained as a combination of local normal galaxies and stacked sub-samples of normal galaxies in the $\sim 7\text{Ms}$ Chandra Deep Field-South (CDF-S) survey (Luo et al. 2017). The local normal galaxies subset analyzed by Lehmer et al. (2016) was observed at rest-frame emissions above 2keV. Therefore, Lehmer et al. (2016) corrected for the 0.5-2 keV emission range and added the hot gas contribution, which was determined based on the findings of Mineo et al. (2012). Moreover, the CDF-S stacked sub-samples were generated based on the observed frame 0.5-1 keV emission, which probes the rest-frame 0.5-2 keV band emission and includes the total hot gas and XRB emission. We notice that the majority of our SFGs lie above the Lx/SFR relation found by Lehmer et al. (2016), but the trend of the relation seems to be very similar. This is reflected in the fitting parameters, with B being consistent with the slope found in Lehmer et al. (2016) at 0.27σ while A is found to be not consistent at 4.3σ .

To explain the observed scatter of the SFGs sample from the literature relation, we take into account two possible scenarios: 1) The scatter is due to differences in the intrinsic properties of the sources, such as different metallicity, intrinsic X-ray absorption or contribution from LMXBs and hot gas that do not follow the empirical relations employed in Section 4.6. 2) The scatter is a consequence of the eROSITA sensitivity limit, which could preclude the detection of low Lx/SFR sources at higher redshift. In fact, in Fig. 4.10 we can notice an alleged dependence of the Lx/SFR relation on redshift, as $L_{0.2-2.3keV}/\text{SFR}$ seems to increase going to higher redshift,

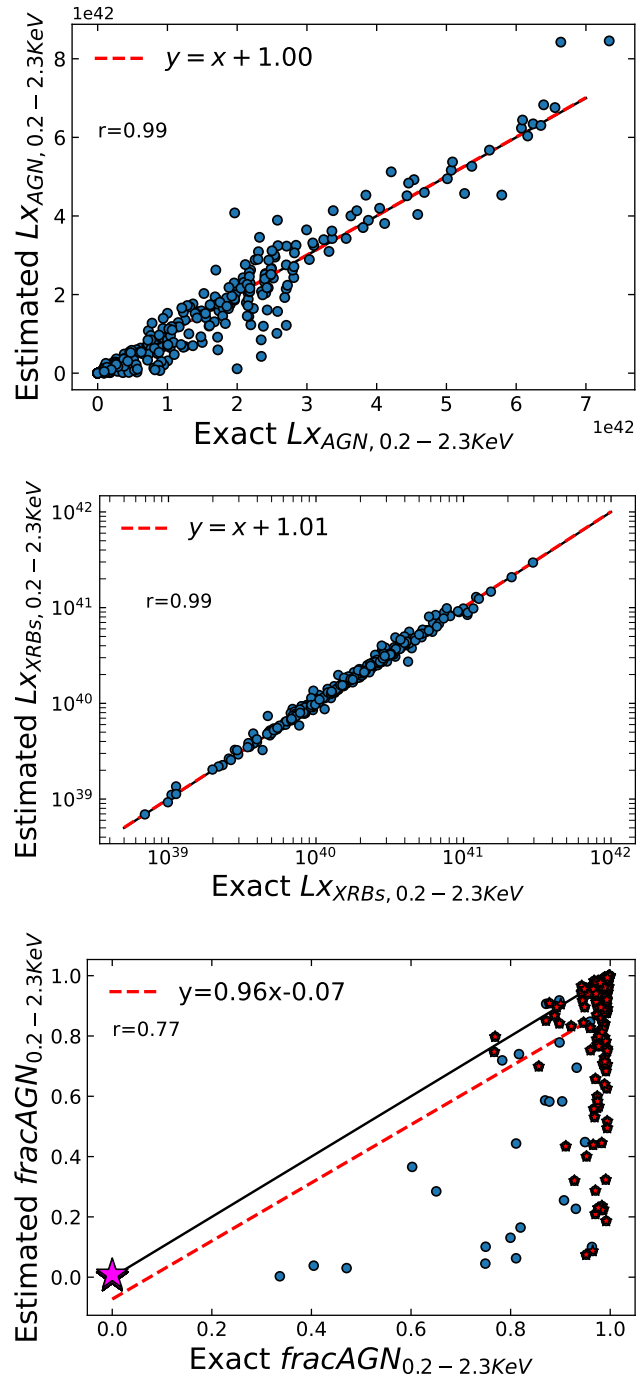


FIGURE 4.9: Mock analysis for the $L_{AGN,0.2-2.3keV}$ (top panel), $L_{XRB,0.2-2.3keV}$ (middle panel) and $fracAGN_{0.2-2.3keV}$ (bottom panel). The Pearson product-moment correlation coefficient is given as an ‘r’ value. The black solid line corresponds to the 1:1 relation, while the red dashed line is the regression line with the equation given in the legend. The magenta star represents the superposition of 44 sources. The red stars are the sources having $f_{0.25\mu m} > 0.1$ from the initial run described in Section 4.4.

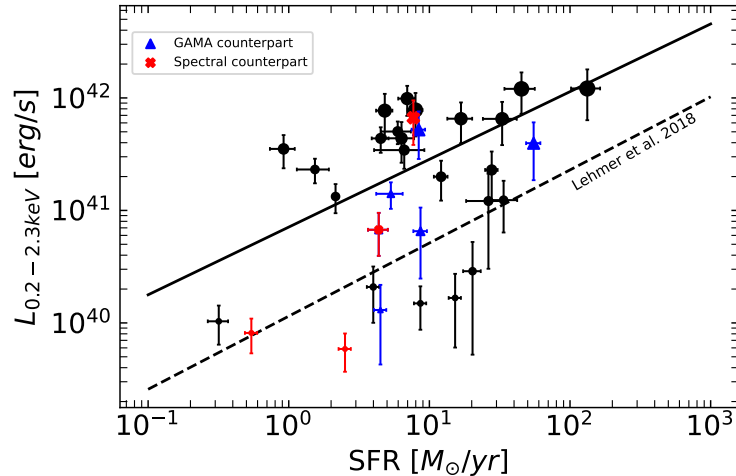


FIGURE 4.10: X-ray luminosity as a function of the SFR. Black dots represent the full sample of SFGs. Red crosses and blue triangles represent the sources having *Herschel* and SDSS counterparts respectively. The solid black line represents the fit of our sample of data, while Lehmer et al. (2016) scaling relation is represented by the dashed black line. The size of the dots is proportional to the redshift of the sources.

at fixed SFRs. Such dependence was indeed already observed and predicted, as we expected an evolution of HMXBs and LMXBs populations with cosmic time (Basu-Zych et al. 2013b, Lehmer et al. 2016). However, the evolution found in these works is only significant at $z > 1$ and is not steep enough to address the rapid increase in the L_x/SFR with redshift observed in this work.

To address the first possibility, we estimate the metallicity of the sources having counterparts in the MPA/JHU catalog, using Tremonti et al. (2004b) calibration. Indeed, we find that the sources with higher $L_{0.2-2.3keV}$ have lower metallicity (of about 0.6 dex), as expected due to HMXBs being more numerous and more luminous with decreasing metallicity, since weaker stellar winds allow more mass retention and tighter binary orbits, as demonstrated in X-ray binary population synthesis models (Linden et al. 2010, Fragos et al. 2013, Basu-Zych et al. 2016). Unfortunately, as only four sources have SDSS counterparts, this result is not statistically robust, motivating the need for a full spectroscopic follow-up of the galaxies observed by the eFEDS survey.

Concerning the possibility that the observed difference might be due to the sensitivity limit of the eFEDS survey, we explore the evolution of the L_x/SFR scaling relation with redshift. In Fig. 4.11, we show the $L_{0.2-2.3keV}/SFR$ ratio as a function of redshift in three SFR intervals. We observe a considerable increase in the L_x/SFR relation with increasing redshift, much steeper than the one found previously in the literature (Lehmer et al. 2016). However, we notice that the trend found in this work very well follows the X-ray luminosity limit of the eFEDS sample, represented in the figure by the solid black line. This confirms that our results are affected by completeness biases.

To address this problem, we correct the results for completeness. To do that, we make use of the MPA/JHU catalog to identify SFGs in our FoV that do not have X-ray counterparts in the eFEDS catalog. As the MPA/JHU catalog provides the emission lines of the sources, we use the BPT diagram to select 1833 SFGs in our

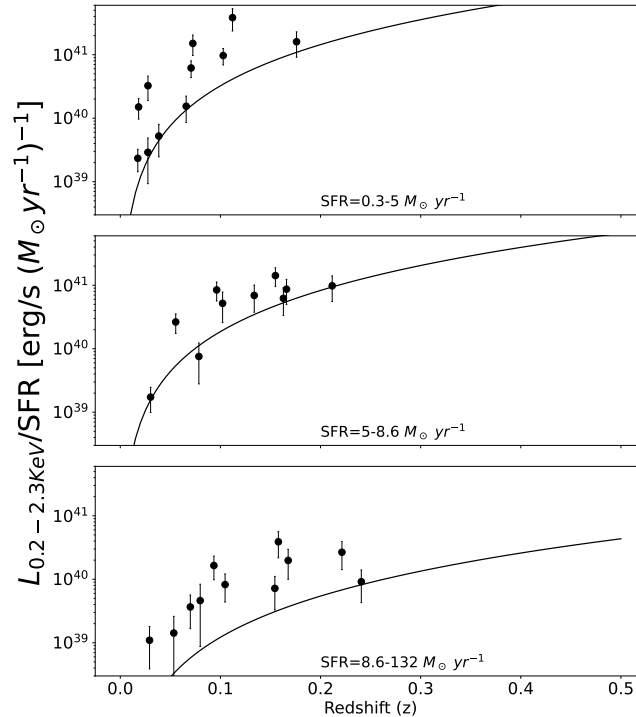


FIGURE 4.11: X-ray luminosity per SFR unit ($L_{0.2-2.3keV}/SFR$) in the function of redshift for the sample of SFGs. The solid black line represents the X-ray luminosity sensitivity limit of the eFEDS sample, rescaled by the max value of the SFR in each interval.

FoV. In order to correct for completeness, we weigh the X-ray sources according to the fraction of SFGs, selected with the MPA/JHU catalog, in which they could have been detected. In Fig. 4.12 we show the observed and the completeness-corrected X-ray luminosity function (XLF) for our sample of SFGs. We can notice that the observed XLF flattens due to completeness already at $L_{0.2-2.3keV} \sim 10^{41}$ erg/s. Fig. 4.12 also shows the $L_{0.2-2.3keV}$ -SFR scaling relation corrected for completeness (red solid line). We derive the fitting constants for the completeness corrected curve as $A_{c.c} = 40.05 \pm 0.05$ and $B_{c.c} = 0.52 \pm 0.06$, consistent with the one found by Lehmer et al. (2016) at 0.08σ and 1.60σ respectively.

4.8 L_x -sSFR relation

In the previous Section, we discussed the relation between the X-ray luminosity and star formation activity for the sample of 34 SFGs detected in the eFEDS FoV. But, as discussed in Section 4.2, the X-ray emission of normal galaxies is not only dominated by the contribution of HMXBs, which is expected to scale with the SFR, but also by the contribution of LMXBs, which is expected to scale with the M_{star} . It was shown that the ratio of HMXB-to-LMXB emission is sensitive to the specific SFR (sSFR), and can be quantified with the scaling factors $\alpha \equiv L_{x,LMXB}/M_{star}$ and $\beta \equiv L_{x,HMXB}/SFR$, obtained as fitting constants of the empirical relation in the form (Mineo et al. 2014, Lehmer et al. 2016):

$$L_x = \alpha M_{star} + \beta SFR. \quad (4.10)$$

Figure 4.13 shows the $L_{0.2-2.3keV}$ as a function of the sSFR for our sample of normal galaxies. We stress that for this plot we removed only the hot gas, ABs and CVs

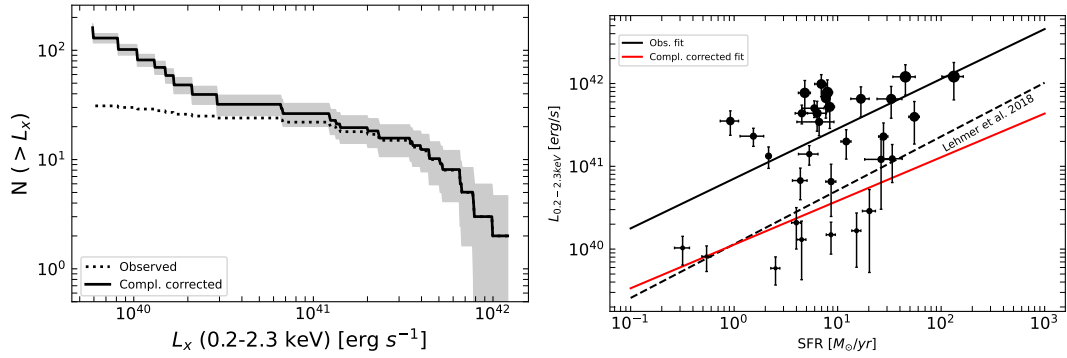


FIGURE 4.12: Right panel: Cumulative X-ray luminosity function for the sample of SFGs. The black solid line represents the completeness-corrected XLF, while the dotted line shows the observed XLF. The shaded region represents the 1σ error. Right panel: X-ray luminosity in the 0.2-2.3 keV band as a function of the SFR. The size of the dots is proportional to the redshift of the sources. The red line shows the linear fit corrected for completeness, while the black line is the observed fit already shown in Fig. 4.10.

components as described in Section 4.6, leaving the HMXBs and LMXBs emissions untouched. The scaling relation of Lehmer et al. (2016) at the mean redshift of our sample ($z \sim 0.09$) is plotted as the dashed black line, with dispersion in gray. Figure 4.13 shows a large dispersion from the relation, both for quiescent and SF galaxies. In the low-sSFR end, we do not notice any trend of the scatter with the redshift, having the sources from the entire redshift range clumped in the same region. Nevertheless, considering the large uncertainties on the L_x/SFR and sSFR, the sources in the low-sSFR regime are consistent with the locus of the scaling relation. For the SFGs, the scatter is much more accentuated and depends on redshift as already observed for the L_x -SFR scaling relation. In Fig. 4.13 we show both the observed and the completeness-corrected fits, as black and red solid lines respectively. We can notice that correcting for completeness lowers the relation, but still, the fit lies above the one previously observed by Lehmer et al. (2016). For the completeness-corrected fit, we estimate the fitting parameters $\alpha = 29.83 \pm 0.14$ and $\beta = 39.91 \pm 0.04$, that are respectively consistent at 3.6σ and 1.5σ with the parameters estimated in Lehmer et al. (2016). Thus, analyzing the full sample of normal galaxies selected in this work, we obtain a considerably higher contribution by LMXBs (as the α parameter is defined as $\alpha = L_{\text{LMXB}}/M_{\text{star}}$) than observed before.

To understand the role of the redshift on the estimated fitting parameters, in Fig. 4.14 we show the $L_{0.2-2.3\text{keV}}/\text{SFR}$ as a function of the sSFR for three redshift bins. We divide our sample in order to have the same number of objects in each bin. We notice that for the lowest redshift bin, where the sample is the most complete, our fitted relation is consistent with what was found previously in the literature. Being incomplete in the highest ranges of redshift, we do not perform any statistical analysis on the evolution of the scaling relation with redshift. However, as complete enough, we report the fitting parameters $\alpha = 28.81 \pm 0.25$ and $\beta = 39.19 \pm 0.3$ in the range $z = 0 - 0.07$. Table 4.3 shows the best-fit parameters, corrected by completeness, for both the L_x -SFR and L_x/SFR -sSFR scaling relations.

We stress that for each panel, the plotted literature relation is estimated according to the mean value of redshift in the bin. Thus, even considering the completeness, it is interesting to notice that all objects in the highest redshift bin are clustered

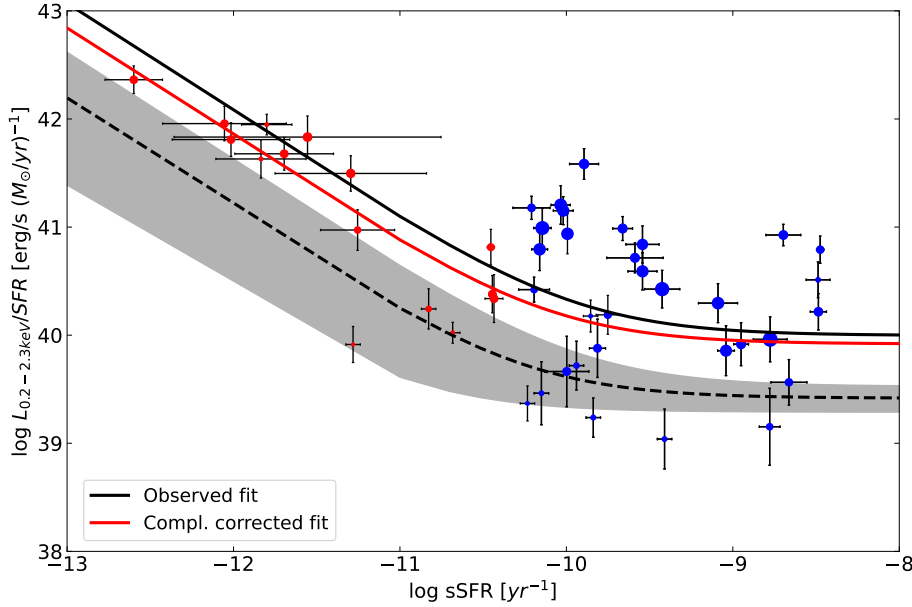


FIGURE 4.13: X-ray luminosity in the 0.2-2.3 keV band scaled by the SFR in the function of the sSFR for the full sample of normal galaxies, selected in this work, both quiescent (red dots) and SFGs (blue dots). The solid black line represents the observed fit of the sources, while the red solid line represents the completeness corrected fit. Lehmer et al. (2016) fit at $z = 0.09$ is pictured as a black dashed line, with the shaded region representing the 3σ dispersion. The size of the dots scales with the redshift of the sources.

TABLE 4.3: Summary of the fits performed on the completeness corrected eFEDS sample.

| Function | Parameter | Fitted value | z | Literature comparison (Lehmer et al. 2016) |
|-------------------------------------|-----------|------------------|----------|--|
| $\log(L_x) = A + B \cdot \log(SFR)$ | A | 40.05 ± 0.05 | 0 - 0.23 | 40.06 ± 0.05 |
| | B | 0.52 ± 0.06 | 0 - 0.23 | 0.65 ± 0.04 |
| $L_x = \alpha M_{star} + \beta SFR$ | α | 29.83 ± 0.14 | 0 - 0.23 | 29.04 ± 0.17 |
| | | 28.81 ± 0.25 | 0 - 0.07 | |
| | β | 39.91 ± 0.04 | 0 - 0.23 | 39.66 ± 0.03 |
| | | 39.19 ± 0.03 | 0 - 0.07 | |

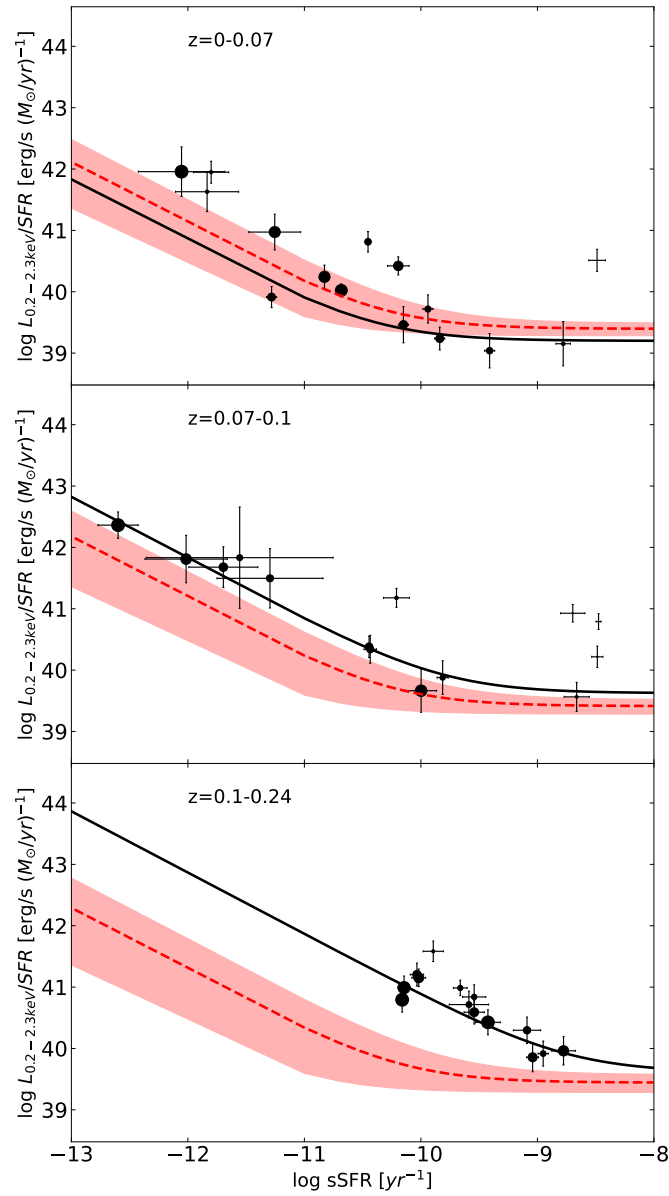


FIGURE 4.14: X-ray luminosity in the 0.2-2.3 keV band scaled by the SFR in the function of the sSFR for the full sample of normal galaxies divided into three redshift bins. The points size is scaled by the M_{star} , The solid black lines represent the observed fit of the sources, while the red dashed lines represent Lehmer et al. (2016) relation estimated at the mean value of the redshift for each bin. The shaded red region represents the 3σ dispersion.

above the scaling relation. Vulic et al. 2022 found a similar trend for a sample of low redshift SFGs detected by the Heraklion Extragalactic Catalogue (HECATE) in the eFEDS field. They found that high sSFR dwarf galaxies tended to have higher values of the $L_{0.5-2.0keV}/SFR$ than expected by the scaling relation. For this reason, in Fig. 4.14 we scale the size of the symbols according to their M_{star} . In the redshift range $z=0.07-0.1$ we notice a slight preference of less massive galaxies ($\sim 10^{10} M_{\odot}$) to scatter from the relation, at high sSFR. However, we do not find any statistically significant trend with the size of the galaxies, with all of our sources having comparable M_{star} , distributed between $10^{10}-10^{11} M_{\odot}$. Thus, the scatter of the sources at higher redshift should be traced back to other reasons, such as metallicity differences or an enhanced contribution of LMXBs per unit of M_{star} , that reflects in the high value of the fitted α parameter. To address the first possibility, as already discussed in the previous section, an accurate spectral analysis is necessary. Instead, regarding the second possibility, one explanation of this hypothetical enhanced contribution may be the presence of a large population of globular clusters (GC). In fact, it is known that the formation of LMXBs in GCs is favored as the high stellar density near the center of GCs may trigger the formation of binaries either by three-body process or by tidal capture. This component is usually not taken into account in theoretical XRB population-synthesis models. To have a rough idea of the GC population of our sample of galaxies, we use the empirical relation presented in Harris et al. (2013), which relates the V-band absolute magnitude to the total number of GCs (see their Eq. 4). The relation is in the form:

$$SN \equiv N_{GC} \times 10^{0.4(M_V^T + 15)} \quad (4.11)$$

where SN is the specific frequency of GCs and M_V^T is the absolute magnitude in the V-band. They calibrated this relation on a sample of 422 sources, composed by elliptical, spiral and irregular galaxies. As we do not have measurements of the specific frequency of GCs, we assume $SN = 1$, as the V-band luminosity range of our sample lies in the region where the "U" shaped relation flatten to unity (see Fig. 10 in Harris et al. 2013). In Fig. 4.15 we show again the same subsample presented in the bottom panel of Fig. 4.14 but color coded by the number of GCs estimated with Harris et al. (2013) formula. We do not notice any significant increase in the $L_{0.2-2.3keV}/SFR$ according to different GC populations. The same result is found for the other two redshift ranges.

To conclude, it is clear that a statistical analysis on normal galaxies carried out with eROSITA will be inevitably affected by severe completeness biases. Thus, to perform an accurate study of the evolution of the XRB contribution to the X-ray emission of galaxies, a stacking process as already performed in previous works (Lehmer et al. 2016), is essential. In this way, one would trade the information about the sources to have a more accurate statistical sample of faint X-ray sources, being able to populate the low $L_{0.2-2.3keV}/SFR$ at higher redshift. A straightforward follow-up of this work moves in this direction.

4.9 Summary and conclusions

We performed an analysis of the X-ray properties of a sample of normal galaxies with negligible AGN contribution observed by SRG/eROSITA for the eROSITA Final Equatorial Depth Survey. The main goal of this work is to explore the contribution to the total X-ray emission given by HMXBs and LMXBs, and how it scales on SFR and M_{star} . For this purpose, we make use of X-ray photometry in the 0.2-2.3

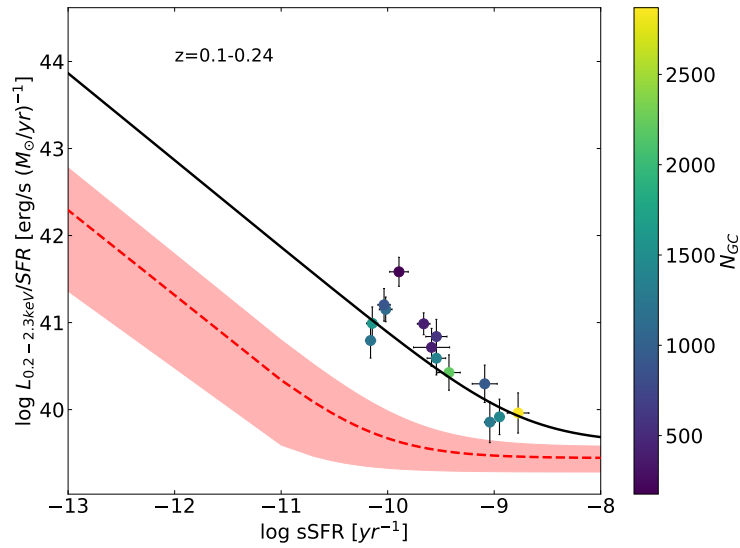


FIGURE 4.15: X-ray luminosity in the 0.2-2.3 keV band scaled by the SFR as a function of the sSFR, color-coded by the number of globular clusters. The lines are the same as Fig. 4.14.

keV band for a sample of 27 369 sources in the eFEDS field (Brunner et al. 2022). In order to estimate the physical parameters, we make use of ancillary data from the UV to the MIR provided in Salvato et al. (2022) to fit the SED of the galaxies, using the CIGALE code (Section 4.4). To guarantee the quality of the fit and to remove possible foreground Galactic sources, we performed several quality cuts discussed in Section 4.3, narrowing the sample to 888 galaxies.

To ensure the reliability of the SFR estimates we validated our results, when possible, using other indicators. To do so, we cross-matched our sample with the *Herschel Extragalactic Legacy Project* (HELP) survey in the GAMA09 field and with MPA/JHU catalog based on the Sloan Digital Sky Survey DR7 release (Abazajian et al. 2009). In this way, we acquired FIR and spectral data for 48 and 50 sources, respectively. We found consistent estimates with the SFR resulting from the fit of the SED up to SPIRE FIR photometry. On the other hand, we found a consistent difference between the SFR estimated with the H_{α} line and the one resulting from the fit of the SED up to MIR photometry. Making use of the BPT diagram to classify these objects, we found the difference to be driven by LINER and Seyfert galaxies, which are the cause of the H_{α} emission for the low-SFR sources. At the end of the process, we updated the physical properties of 48 galaxies with the results from the fit of the SED up to the FIR, and the SFR of 5 galaxies selected by the BPT diagram as star-forming with the SFR from the H_{α} line.

To isolate the contribution of XRBs we subtracted the X-ray emission from hot gas, CVs, and ABs. For quiescent galaxies, we used the K-band luminosity to estimate the contribution from hot gas, following the prescription discussed in Civano et al. (2014). For SFGs, we employ the relation between $L_{x,LMXBs}$ and M_* found by Gilfanov (2004) to estimate the contribution from LMXBs (Eq. 4.6). We account to the hot gas using Mineo et al. (2012) (Eq. 4.7). For both types, we use the relation from Boroson et al. (2011) to account for CVs and ABs (Eq 4.5). These contributions are subtracted from the observed X-ray luminosity to accordingly isolate the emission

from HMXBs and LMXBs.

After removing the contribution from hot gas, ABs and CVs, in order to study the properties of galaxies for which the X-ray emission is dominated by XRBs we need to reveal the presence of non-stellar nuclear emission. To achieve this, we used a combination of observed photometry in the X-ray, optical, and MIR range, together with a selection based on the SED fitting. The criteria to select AGNs can be summarized as follow:

- $L_{0.2-2.3keV} \geq 3 \times 10^{42}$ erg/s.
- X-ray-to-optical flux ratio of $\log(f_X/f_r) > -1$.
- X-ray-to-NIR flux ratio of $\log(f_X/f_{Ks}) > -1.2$.
- MIR WISE photometry selection described in Assef et al. (2013).
- AGN contribution to the total X-ray emission estimated with the SED fitting $fracAGN_{0.2-2.3keV} < 0.1$.

At the end of the process, we are left with the final sample of 49 normal galaxies: 34 SFGs and 15 quiescent galaxies.

To study the HMXBs contribution to the X-ray luminosity we measured the constants A and B of the empirical relation already found in literature between $L_{0.2-2.3keV}$ and SFR (in the form of Eq. 4.9). We stress that for this analysis, we subtract the LMXBs, hot gas, ABs and CVs contributions to the total X-ray emission. We derived the fitting constants $A = 40.67 \pm 0.21$ and $B = 0.57 \pm 0.20$. Despite the correlation, the fit did not yield statistically robust results. We found that the majority of our SFGs lie above the L_X/SFR relation found previously in the literature (Lehmer et al. 2016). This is reflected in the fitting parameter A, found to be not consistent with previous measures at 4.3σ . To investigate this result, we discussed the possibility of a dependence on the completeness limit of the eFEDS survey which could preclude the detection of low L_X/SFR sources at higher redshift. Correcting for completeness using SFGs detected in the MPA/JHU catalog, we found very good agreement between the completeness corrected fitting constants and the literature. We derive $A_{c.c} = 40.05 \pm 0.05$ and $B_{c.c} = 0.52 \pm 0.06$, consistent at 0.08σ and 1.60σ respectively with previous measurements. We conclude that the overall connection between X-ray luminosity and SFR of our population of SFGs is highly biased by completeness issues, but the scatter of the sources from the literature relation can be traced back to physical differences between the galaxies, such as metallicity differences, LMXBs contribution or intrinsic X-ray absorption.

In order to study the ratio of HMXBs-to-LMXBs emission, that was shown to scale with the sSFR, we quantified the scaling factors $\alpha \equiv L_{x,LMXB}/M_{star}$ and $\beta \equiv L_{x,HMXB}/SFR$, fitting the empirical relation presented in Eq. 4.10. For this analysis, for both quiescent and SFGs, we subtract the hot gas, ABs and CVs contributions to the X-ray luminosity. Correcting the full sample of normal galaxies for completeness, we derive the fitting parameters $\alpha = 29.83 \pm 0.14$ and $\beta = 39.91 \pm 0.04$, respectively consistent at 3.6σ and 1.5σ with the parameters estimated in Lehmer et al. (2016). Thus, we observe a higher contribution of LMXBs than observed before. We found that this higher contribution is mainly carried out by high redshift sources, concluding that the statistical trend of the empirical relation is highly biased by completeness. However, for the lowest redshift range where we are the most complete, we found consistent results with the literature. Even though it was not possible to study the redshift evolution of the empirical relation due to completeness issues, at high

redshift we found a consistent scatter of the sources from the relation for that specific redshift range. We discuss the possibility of an enhanced LMXBs contribution due to an overpopulation of GCs, which would favor the formation of binary systems. We address this possibility by estimating the expected number of GCs employing the relation presented in Harris et al. (2013) (Eq. 4.11). We do not find any statistical correlation between the L_X/SFR and the number of GCs. We concluded that an accurate study of the evolution of the XRB contribution to the X-ray emission of galaxies carried out with eROSITA must be performed combined with a stacking procedure, to overcome the severe completeness biases. Furthermore, to investigate the scatter of the sources from the predicted relations, a full spectral follow-up of the eFEDS survey is necessary. Future work must be carried out in these directions.

5

Summary

In the present work, several significant results were achieved. In this chapter, I summarize the conclusions and mark possible future perspectives.

I first inspect how LSST will be able to estimate galaxies' physical parameters, most importantly SFR and M_{star} . To do so, I simulate *Legacy Survey of Space and Time* (LSST) photometry for a sample of ~ 50000 real galaxies observed by the *Herschel Extragalactic Legacy Project* and estimate their physical parameters by employing Spectral Energy Distribution (SED) fitting methods using CIGALE software. Due to the high-quality optical observations, with LSST I am able to obtain reliable estimates of the M_{star} , while I find an overestimation of the SFR, L_{dust} and M_{dust} parameters. Considering how the physical properties are evaluated by the Bayesian method, I conclude that the results are due to an overestimation of the A_{FUV} when only LSST data are employed. Furthermore, I find these results to be highly dependent on redshift, obtaining reliable estimates of the SFR (and the other dust-related parameters) moving to higher redshift. Since the UV spectrum traces the young stellar populations, the estimates of the SFR from the SED fitting significantly improve when this range of wavelengths is constrained by observations. Moving to higher redshifts, the LSST bands are almost entirely shifted to the rest-frame UV band, which results in a better estimation of the A_{FUV}/SFR . Furthermore, I explore possible ways to correct the SFR estimates obtained with LSST. The most efficient and straightforward way is to add MIR (for example IRAC data) or UV (GALEX) observations. Unfortunately, considering the huge amount of data that LSST will provide, I expect that the majority of galaxies observed will not have available auxiliary data in the MIR or UV wavelengths. For this reason, other methods of correcting the estimates of the physical parameters are needed. In this work, I show another efficient way to correct for the SFR, by employing a prior knowledge of the A_{FUV} , based on the $A_{FUV}-M_{star}$ empirical relation. The incredible advantage of this method is the possibility to use only the M_{star} , well estimated by LSST, to reliably constrain the SFR. The drawback of this approach is the uncertainty associated with the empirical relation, which depends on several factors, such as the type of galaxies observed or the statistical sample used to calibrate it. For this reason, as a future project, I plan to make use of the huge statistical sample of galaxies expected from LSST to better constrain the $A_{FUV} - M_{star}$ relation.

However, LSST is not the only next-generation survey expected to revolutionize our understanding of galaxies' physical parameters. In this thesis, I also discussed the importance of the X-ray emission to understand the processes that take place in the galactic environment. Empirical relations such as $L_x\text{-SFR}$ and $L_x\text{-}M_{star}$ not only

give us insight into the mechanisms that lead to the formation of XRBs but also represent promising alternative methods for estimating the galaxies' properties. The problem with these approaches is the difficulty of detecting X-ray photons, which significantly lowers the sensitivity of X-ray observatories compared to optical or UV ones. As a result, these relations are calibrated on small statistical samples, which inevitably affects their uncertainty. For this reason, next-generation X-ray observatories are crucial for studying the high-energy Universe. In this context, I study the connection between galaxies' X-ray emission and their physical properties, giving a glimpse into the future of X-ray astronomy: the eROSITA survey.

One of the major problems of the empirical relation between SFR and X-ray luminosity is that it fails in the low-SFR regime. This may be due to several factors, including a non-negligible contribution of low mass X-ray binaries hosted in globular clusters (GC-LMXBs). In fact, the GC-LMXB association is particularly interesting as the high stellar density near the center of GCs may trigger the formation of binaries either by the three-body process or by tidal capture. This channel of formation is often neglected in theoretical XRB population synthesis models, making the constraint of this contribution of great importance. For this reason, in this work, I present an analysis of the properties of LMXBs residing in the population of globular clusters in the Fornax cluster. The main goals of this work are to study the contribution of the sources to the X-ray luminosity of the cluster and to inspect the dependencies of individual object properties on the environment. For this purpose, I make use of a combination of X-ray *Chandra* and optical VST observations, to study the properties of both LMXBs and the GCs that host them. I find a deep connection between the formation of LMXBs and the environment. LMXBs tend to form in red and bright GCs, as the color and the luminosity are a proxy of the density and of the number of stars hosted by the GC. This result does not depend on the distance of the GCs from the center of the host galaxy. Furthermore, I find the fraction of GC-LMXBs to be dependent on the galactocentric distance, especially for the red population. This result may suggest that the LMXBs formation channel in GCs may depend on the host-galaxy environment. I also observe a puzzling difference in hardness ratio between intra-cluster and host-galaxy GC-LMXBs: the spectra of the intra-cluster sample are harder than those of the host-galaxy sample. I discuss that this might suggest a relation between the emitted spectra of the LMXBs and the metallicity of the hosting GC. I find the total X-ray luminosity of the cluster to be dominated by field LMXBs. In fact, the LMXBs hosted in GCs represent the $\sim 20\%$ of the total number of LMXBs in the cluster, with an integrated luminosity that contributes to the $\sim 10\%$ of the total X-ray luminosity.

Studying the Fornax cluster, I asserted the properties and the role of LMXBs in an environment mainly populated by quiescent galaxies. But, to explore how the contribution to the total X-ray emission given by HMXBs and LMXBs scales with the SFR and M_{star} for a general sample of normal galaxies, it is necessary to make use of a bigger statistical sample. For this reason, I employ pre-release data acquired by SRG/eROSITA for the Performance-and-Verification-Phase program named the eROSITA Final Equatorial Depth Survey in order to parameterize the L_x -SFR and L_x - M_{star} scaling relations. The eROSITA survey is expected to detect a number of normal galaxies never observed by other wide-field X-ray surveys, and this study represents an anticipation of what can be achieved with it. I perform an accurate analysis of the components contributing to the total X-ray emission of the galaxies, in order to safely study only the XRBs component, that scale with SFR and M_{star} . I subtract the X-ray emission from the hot ISM, cataclysmic variables (CVs), and coronally active binaries (ABs) using empirical relations. However, the most sensitive

part of this analysis is the identification and removal of the sources dominated by nuclear non-stellar emission. To achieve this, we used a combination of observed photometry in the X-ray, optical, and MIR range, together with a selection based on the SED fitting. At the end of the process, we are confident to study only galaxies dominated by XRBs emission. To study the HMXBs' contribution to the total X-ray luminosity, I constrained the L_x -SFR scaling relation. I find a linear relation that predicts higher L_x /SFR ratios than observed in previous works, and I find a dependence on the completeness limit of the eFEDS survey which precludes the detection of low L_x /SFR sources at higher redshift. Correcting for this bias, I obtain an empirical relation in agreement with what was found in previous works. In order to study the ratio of HMXBs-to-LMXBs emission, that was shown to scale with the sSFR, I quantified the scaling factors $\alpha \equiv L_{x,LMXB}/M_{star}$ and $\beta \equiv L_{x,HMXB}/SFR$. I find that even correcting for completeness, I observe a higher contribution of LMXBs than observed before. I discuss the possibility of an enhanced LMXB contribution due to an overpopulation of GCs, which would favor the formation of binary systems, but I do not find any statistical correlation between the L_x /SFR ratio and the number of GCs. I conclude that an accurate statistical analysis of the XRBs emission and its evolution with redshift cannot be performed with eROSITA due to severe completeness biases. To overcome this problem, a stacking of the observations must be carried out. Furthermore, to investigate the scatter of the single sources from the predicted relation, a full spectral follow-up of the eROSITA survey is necessary. In future works, I plan to move in both the directions mentioned above.

To summarize the results of my thesis, a comprehensive study of the possibilities of the next-generation surveys in the estimation of the physical parameters was carried out. The results achieved will give future researchers a useful idea of how to approach these surveys in their studies. I have shown how the A_{FUV} -Mstar relation can be of great help in estimating the SFR for galaxies observed only by LSST. If calibrated in a more general way, it could have a big impact on the scientific development of this field in the coming years. Furthermore, I have shown how the study of the X-ray regime can give important information on the star formation activity of the galaxies. Taking a look at the next generation of wide-field X-ray observatories, I discovered a puzzling picture in the connection between physical parameters and X-ray luminosity. The hypothesized enhanced emission by LMXBs had not been previously predicted and will have to be ascertained with further studies on the galaxies observed by eROSITA. Unfortunately, a statistical analysis of the evolution of the contribution of HMBXs and LMXBs was not possible due to completeness issues, but these results represent a starting point for future work.

Bibliography

- Einstein, A. (Jan. 1916). Die Grundlage der allgemeinen Relativitätstheorie. Annalen der Physik 354.7, pp. 769–822. DOI: [10.1002/andp.19163540702](https://doi.org/10.1002/andp.19163540702).
- Hubble, E. P. (Dec. 1926). Extragalactic nebulae. 64, pp. 321–369. DOI: [10.1086/143018](https://doi.org/10.1086/143018).
- Salpeter, Edwin E. (Jan. 1955). The Luminosity Function and Stellar Evolution. 121, p. 161. DOI: [10.1086/145971](https://doi.org/10.1086/145971).
- Holmberg, E. (Jan. 1958). A photographic photometry of extragalactic nebulae. Meddelanden fran Lunds Astronomiska Observatorium 136, p. 1.
- X-ray astronomy (Jan. 1974). DOI: [10.1007/978-94-010-2105-0](https://doi.org/10.1007/978-94-010-2105-0).
- Miller, G. E. et al. (Nov. 1979). The Initial Mass Function and Stellar Birthrate in the Solar Neighborhood. 41, p. 513. DOI: [10.1086/190629](https://doi.org/10.1086/190629).
- Heckman, T. M. (July 1980). An Optical and Radio Survey of the Nuclei of Bright Galaxies - Activity in the Normal Galactic Nuclei. 87, p. 152.
- Baldwin, J. A. et al. (Feb. 1981). Classification parameters for the emission-line spectra of extragalactic objects. 93, pp. 5–19. DOI: [10.1086/130766](https://doi.org/10.1086/130766).
- Kennicutt R. C., Jr. et al. (Aug. 1983). A survey of H-alpha emission in normal galaxies. 88, pp. 1094–1107. DOI: [10.1086/113399](https://doi.org/10.1086/113399).
- Leger, A. et al. (Aug. 1984). Identification of the Unidentified Infrared Emission Features of Interstellar Dust. 137, pp. L5–L8.
- Allamandola, L. J. et al. (Mar. 1985). Polycyclic aromatic hydrocarbons and the unidentified infrared emission bands: auto exhaust along the milky way. 290, pp. L25–L28. DOI: [10.1086/184435](https://doi.org/10.1086/184435).
- Terlevich, R. et al. (Apr. 1985). Warmers : the missing link between Starburst and Seyfert galaxies. 213, pp. 841–856. DOI: [10.1093/mnras/213.4.841](https://doi.org/10.1093/mnras/213.4.841).
- Trinchieri, G. et al. (Sept. 1985). A statistical analysis of the Einstein normal galaxy sample. II. Elliptical and SO galaxies. 296, pp. 447–457. DOI: [10.1086/163463](https://doi.org/10.1086/163463).
- Mewe, R. et al. (Sept. 1986). Calculated X-radiation from optically thin plasmas. VI - Improved calculations for continuum emission and approximation formulae for nonrelativistic average Gaunt factors. 65, pp. 511–536.
- Jedrzejewski, Robert I. et al. (Dec. 1987). CCD Surface Photometry of the Bright Elliptical Galaxies NGC 720, NGC 1052, and NGC 4697. 94, p. 1508. DOI: [10.1086/114584](https://doi.org/10.1086/114584).
- Stetson, Peter B. (Mar. 1987). DAOPHOT: A Computer Program for Crowded-Field Stellar Photometry. 99, p. 191. DOI: [10.1086/131977](https://doi.org/10.1086/131977).
- Cardelli, Jason A. et al. (Oct. 1989). The Relationship between Infrared, Optical, and Ultraviolet Extinction. 345, p. 245. DOI: [10.1086/167900](https://doi.org/10.1086/167900).
- Fabbiano, G. (Jan. 1989). X-rays from normal galaxies. 27, pp. 87–138. DOI: [10.1146/annurev.aa.27.090189.000511](https://doi.org/10.1146/annurev.aa.27.090189.000511).
- Buat, V. (Oct. 1992). Global recent star formation in normal galaxies from a multi-wavelength study. Comparison with their gas content. 264, pp. 444–454.
- Kennicutt Robert C., Jr. (Apr. 1992). A Spectrophotometric Atlas of Galaxies. 79, p. 255. DOI: [10.1086/191653](https://doi.org/10.1086/191653).

- Sutherland, Will et al. (Dec. 1992). On the likelihood ratio for source identification. 259, pp. 413–420. DOI: [10.1093/mnras/259.3.413](https://doi.org/10.1093/mnras/259.3.413).
- Calzetti, Daniela et al. (July 1994). Dust Extinction of the Stellar Continua in Starburst Galaxies: The Ultraviolet and Optical Extinction Law. 429, p. 582. DOI: [10.1086/174346](https://doi.org/10.1086/174346).
- Kennicutt Robert C., Jr. et al. (Nov. 1994). Past and Future Star Formation in Disk Galaxies. 435, p. 22. DOI: [10.1086/174790](https://doi.org/10.1086/174790).
- Pellegrini, S. (Dec. 1994). ROSAT PSPC observation of the X-ray faint early-type galaxy NGC 5866. 292, pp. 395–403. DOI: [10.48550/arXiv.astro-ph/9407008](https://doi.org/10.48550/arXiv.astro-ph/9407008). arXiv: [astro-ph/9407008](https://arxiv.org/abs/astro-ph/9407008) [astro-ph].
- Roberts, Morton S. et al. (Jan. 1994). Physical Parameters along the Hubble Sequence. 32, pp. 115–152. DOI: [10.1146/annurev.aa.32.090194.000555](https://doi.org/10.1146/annurev.aa.32.090194.000555).
- Verbunt, F. et al. (Jan. 1995). Formation and evolution of neutron stars and black holes in binaries. *X-ray Binaries*, pp. 457–494.
- Bertin, E. et al. (June 1996). SExtractor: Software for source extraction. 117, pp. 393–404. DOI: [10.1051/aas:1996164](https://doi.org/10.1051/aas:1996164).
- Ferguson, H. C. (July 1997). VizieR Online Data Catalog: Galaxies in Fornax Cluster and five nearby groups (Ferguson+ 1990). *VizieR Online Data Catalog*, VII/180, pp. VII/180.
- Li, A. et al. (July 1997). A unified model of interstellar dust. 323, pp. 566–584.
- Arnaboldi, M. et al. (Sept. 1998). VST: VLT Survey Telescope. *The Messenger* 93, pp. 30–35.
- Kennicutt Robert C., Jr. (Jan. 1998). Star Formation in Galaxies Along the Hubble Sequence. 36, pp. 189–232. DOI: [10.1146/annurev.astro.36.1.189](https://doi.org/10.1146/annurev.astro.36.1.189). arXiv: [astro-ph/9807187](https://arxiv.org/abs/astro-ph/9807187) [astro-ph].
- Larkin, J. E. et al. (Jan. 1998). A Near-Infrared Spectroscopic Survey of LINER Galaxies. 114.1, pp. 59–72. DOI: [10.1086/313063](https://doi.org/10.1086/313063). arXiv: [astro-ph/9708097](https://arxiv.org/abs/astro-ph/9708097) [astro-ph].
- Madau, Piero et al. (May 1998). The Star Formation History of Field Galaxies. 498.1, pp. 106–116. DOI: [10.1086/305523](https://doi.org/10.1086/305523). arXiv: [astro-ph/9708220](https://arxiv.org/abs/astro-ph/9708220) [astro-ph].
- Riess, Adam G. et al. (Sept. 1998). Observational Evidence from Supernovae for an Accelerating Universe and a Cosmological Constant. 116.3, pp. 1009–1038. DOI: [10.1086/300499](https://doi.org/10.1086/300499). arXiv: [astro-ph/9805201](https://arxiv.org/abs/astro-ph/9805201) [astro-ph].
- Silva, Laura et al. (Dec. 1998). Modeling the Effects of Dust on Galactic Spectral Energy Distributions from the Ultraviolet to the Millimeter Band. 509.1, pp. 103–117. DOI: [10.1086/306476](https://doi.org/10.1086/306476).
- Arnouts, S. et al. (Dec. 1999). Measuring and modelling the redshift evolution of clustering: the Hubble Deep Field North. 310.2, pp. 540–556. DOI: [10.1046/j.1365-8711.1999.02978.x](https://doi.org/10.1046/j.1365-8711.1999.02978.x). arXiv: [astro-ph/9902290](https://arxiv.org/abs/astro-ph/9902290) [astro-ph].
- Perlmutter, S. et al. (June 1999). Measurements of Ω and Λ from 42 High-Redshift Supernovae. 517.2, pp. 565–586. DOI: [10.1086/307221](https://doi.org/10.1086/307221). arXiv: [astro-ph/9812133](https://arxiv.org/abs/astro-ph/9812133) [astro-ph].
- Bolzonella, M. et al. (Nov. 2000). Photometric redshifts based on standard SED fitting procedures. 363, pp. 476–492. arXiv: [astro-ph/0003380](https://arxiv.org/abs/astro-ph/0003380) [astro-ph].
- Brinchmann, Jarle et al. (June 2000). The Mass Assembly and Star Formation Characteristics of Field Galaxies of Known Morphology. 536.2, pp. L77–L80. DOI: [10.1086/312738](https://doi.org/10.1086/312738). arXiv: [astro-ph/0005120](https://arxiv.org/abs/astro-ph/0005120) [astro-ph].
- Calzetti, Daniela et al. (Apr. 2000). The Dust Content and Opacity of Actively Star-forming Galaxies. 533.2, pp. 682–695. DOI: [10.1086/308692](https://doi.org/10.1086/308692). arXiv: [astro-ph/9911459](https://arxiv.org/abs/astro-ph/9911459) [astro-ph].

- Charlot, Stéphane et al. (Aug. 2000). A Simple Model for the Absorption of Starlight by Dust in Galaxies. 539.2, pp. 718–731. DOI: [10.1086/309250](https://doi.org/10.1086/309250). arXiv: [astro-ph/0003128](https://arxiv.org/abs/astro-ph/0003128) [astro-ph].
- Oliver, Seb et al. (Aug. 2000). The European Large Area ISO Survey - I. Goals, definition and observations. 316.4, pp. 749–767. DOI: [10.1046/j.1365-8711.2000.03550.x](https://doi.org/10.1046/j.1365-8711.2000.03550.x). arXiv: [astro-ph/0003263](https://arxiv.org/abs/astro-ph/0003263) [astro-ph].
- Popescu, C. C. et al. (Oct. 2000). Modelling the spectral energy distribution of galaxies. I. Radiation fields and grain heating in the edge-on spiral NGC 891. 362, pp. 138–150. DOI: [10.48550/arXiv.astro-ph/0008098](https://doi.org/10.48550/arXiv.astro-ph/0008098). arXiv: [astro-ph/0008098](https://arxiv.org/abs/astro-ph/0008098) [astro-ph].
- Gordon, Karl D. et al. (Apr. 2001). The DIRTY Model. I. Monte Carlo Radiative Transfer through Dust. 551.1, pp. 269–276. DOI: [10.1086/320082](https://doi.org/10.1086/320082). arXiv: [astro-ph/0011575](https://arxiv.org/abs/astro-ph/0011575) [astro-ph].
- Sarazin, Craig L. et al. (Aug. 2001). Chandra X-Ray Observations of the X-Ray Faint Elliptical Galaxy NGC 4697. 556.2, pp. 533–555. DOI: [10.1086/321618](https://doi.org/10.1086/321618). arXiv: [astro-ph/0104070](https://arxiv.org/abs/astro-ph/0104070) [astro-ph].
- Bendo, George J. et al. (Sept. 2002). Star Formation in the Infrared Space Observatory Atlas of Bright Spiral Galaxies. 124.3, pp. 1380–1392. DOI: [10.1086/342283](https://doi.org/10.1086/342283). arXiv: [astro-ph/0206299](https://arxiv.org/abs/astro-ph/0206299) [astro-ph].
- Dale, Daniel A. et al. (Sept. 2002). The Infrared Spectral Energy Distribution of Normal Star-forming Galaxies: Calibration at Far-Infrared and Submillimeter Wavelengths. 576.1, pp. 159–168. DOI: [10.1086/341632](https://doi.org/10.1086/341632). arXiv: [astro-ph/0205085](https://arxiv.org/abs/astro-ph/0205085) [astro-ph].
- Leitherer, Claus et al. (July 2002). Ultraviolet Spectra of Star-forming Galaxies with Time-dependent Dust Obscuration. 574.1, pp. 114–125. DOI: [10.1086/340902](https://doi.org/10.1086/340902).
- Bruzual, G. et al. (Oct. 2003). Stellar population synthesis at the resolution of 2003. 344.4, pp. 1000–1028. DOI: [10.1046/j.1365-8711.2003.06897.x](https://doi.org/10.1046/j.1365-8711.2003.06897.x). arXiv: [astro-ph/0309134](https://arxiv.org/abs/astro-ph/0309134) [astro-ph].
- Chabrier, Gilles (July 2003). Galactic Stellar and Substellar Initial Mass Function. 115.809, pp. 763–795. DOI: [10.1086/376392](https://doi.org/10.1086/376392). arXiv: [astro-ph/0304382](https://arxiv.org/abs/astro-ph/0304382) [astro-ph].
- Draine, B. T. (Jan. 2003). Interstellar Dust Grains. 41, pp. 241–289. DOI: [10.1146/annurev.astro.41.011802.094840](https://doi.org/10.1146/annurev.astro.41.011802.094840). arXiv: [astro-ph/0304489](https://arxiv.org/abs/astro-ph/0304489) [astro-ph].
- Grimm, H. J. et al. (Mar. 2003). High-mass X-ray binaries as a star formation rate indicator in distant galaxies. 339.3, pp. 793–809. DOI: [10.1046/j.1365-8711.2003.06224.x](https://doi.org/10.1046/j.1365-8711.2003.06224.x). arXiv: [astro-ph/0205371](https://arxiv.org/abs/astro-ph/0205371) [astro-ph].
- Lonsdale, Carol J. et al. (Aug. 2003). SWIRE: The SIRTf Wide-Area Infrared Extragalactic Survey. 115.810, pp. 897–927. DOI: [10.1086/376850](https://doi.org/10.1086/376850). arXiv: [astro-ph/0305375](https://arxiv.org/abs/astro-ph/0305375) [astro-ph].
- Maccarone, Thomas J. et al. (Apr. 2003). The Low-Mass X-Ray Binary-Globular Cluster Connection. II. NGC 4472 X-Ray Source Properties and Source Catalogs. 586.2, pp. 814–825. DOI: [10.1086/367886](https://doi.org/10.1086/367886). arXiv: [astro-ph/0210143](https://arxiv.org/abs/astro-ph/0210143) [astro-ph].
- Brinchmann, J. et al. (July 2004). The physical properties of star-forming galaxies in the low-redshift Universe. 351.4, pp. 1151–1179. DOI: [10.1111/j.1365-2966.2004.07881.x](https://doi.org/10.1111/j.1365-2966.2004.07881.x). arXiv: [astro-ph/0311060](https://arxiv.org/abs/astro-ph/0311060) [astro-ph].
- Gilfanov, M. (Mar. 2004). Low-mass X-ray binaries as a stellar mass indicator for the host galaxy. 349.1, pp. 146–168. DOI: [10.1111/j.1365-2966.2004.07473.x](https://doi.org/10.1111/j.1365-2966.2004.07473.x). arXiv: [astro-ph/0309454](https://arxiv.org/abs/astro-ph/0309454) [astro-ph].
- Jordán, Andrés et al. (Sept. 2004). The ACS Virgo Cluster Survey. III. Chandra and Hubble Space Telescope Observations of Low-Mass X-Ray Binaries and Globular Clusters in M87. 613.1, pp. 279–301. DOI: [10.1086/422545](https://doi.org/10.1086/422545). arXiv: [astro-ph/0405188](https://arxiv.org/abs/astro-ph/0405188) [astro-ph].

- Kewley, Lisa J. et al. (Apr. 2004). [O II] as a Star Formation Rate Indicator. 127.4, pp. 2002–2030. DOI: [10.1086/382723](https://doi.org/10.1086/382723). arXiv: [astro-ph/0401172](https://arxiv.org/abs/astro-ph/0401172) [astro-ph].
- Kim, Dong-Woo et al. (Aug. 2004). X-Ray Luminosity Function and Total Luminosity of Low-Mass X-Ray Binaries in Early-Type Galaxies. 611.2, pp. 846–857. DOI: [10.1086/422210](https://doi.org/10.1086/422210). arXiv: [astro-ph/0312104](https://arxiv.org/abs/astro-ph/0312104) [astro-ph].
- Maccarone, Thomas J. et al. (May 2004). An Explanation for Metallicity Effects on X-Ray Binary Properties. 606.1, pp. 430–435. DOI: [10.1086/382937](https://doi.org/10.1086/382937). arXiv: [astro-ph/0401333](https://arxiv.org/abs/astro-ph/0401333) [astro-ph].
- Tremonti, Christy A. et al. (Oct. 2004a). The Origin of the Mass-Metallicity Relation: Insights from 53,000 Star-forming Galaxies in the Sloan Digital Sky Survey. 613.2, pp. 898–913. DOI: [10.1086/423264](https://doi.org/10.1086/423264). arXiv: [astro-ph/0405537](https://arxiv.org/abs/astro-ph/0405537) [astro-ph].
- (Oct. 2004b). The Origin of the Mass-Metallicity Relation: Insights from 53,000 Star-forming Galaxies in the Sloan Digital Sky Survey. 613.2, pp. 898–913. DOI: [10.1086/423264](https://doi.org/10.1086/423264). arXiv: [astro-ph/0405537](https://arxiv.org/abs/astro-ph/0405537) [astro-ph].
- Tuffs, R. J. et al. (June 2004). Modelling the spectral energy distribution of galaxies. III. Attenuation of stellar light in spiral galaxies. 419, pp. 821–835. DOI: [10.1051/0004-6361:20035689](https://doi.org/10.1051/0004-6361:20035689). arXiv: [astro-ph/0401630](https://arxiv.org/abs/astro-ph/0401630) [astro-ph].
- Valencic, Lynne A. et al. (Dec. 2004). Ultraviolet Extinction Properties in the Milky Way. 616.2, pp. 912–924. DOI: [10.1086/424922](https://doi.org/10.1086/424922). arXiv: [astro-ph/0408409](https://arxiv.org/abs/astro-ph/0408409) [astro-ph].
- Zubko, Viktor et al. (June 2004). Interstellar Dust Models Consistent with Extinction, Emission, and Abundance Constraints. 152.2, pp. 211–249. DOI: [10.1086/382351](https://doi.org/10.1086/382351). arXiv: [astro-ph/0312641](https://arxiv.org/abs/astro-ph/0312641) [astro-ph].
- Buat, V. et al. (Jan. 2005). Dust Attenuation in the Nearby Universe: A Comparison between Galaxies Selected in the Ultraviolet and in the Far-Infrared. 619.1, pp. L51–L54. DOI: [10.1086/423241](https://doi.org/10.1086/423241). arXiv: [astro-ph/0411343](https://arxiv.org/abs/astro-ph/0411343) [astro-ph].
- Burgarella, D. et al. (July 2005). Star formation and dust attenuation properties in galaxies from a statistical ultraviolet-to-far-infrared analysis. 360.4, pp. 1413–1425. DOI: [10.1111/j.1365-2966.2005.09131.x](https://doi.org/10.1111/j.1365-2966.2005.09131.x). arXiv: [astro-ph/0504434](https://arxiv.org/abs/astro-ph/0504434) [astro-ph].
- Cid Fernandes, Roberto et al. (Apr. 2005). Semi-empirical analysis of Sloan Digital Sky Survey galaxies - I. Spectral synthesis method. 358.2, pp. 363–378. DOI: [10.1111/j.1365-2966.2005.08752.x](https://doi.org/10.1111/j.1365-2966.2005.08752.x). arXiv: [astro-ph/0412481](https://arxiv.org/abs/astro-ph/0412481) [astro-ph].
- Grimes, J. P. et al. (July 2005). A Chandra X-Ray Investigation of the Violent Interstellar Medium: From Dwarf Starbursts to Ultraluminous Infrared Galaxies. 628.1, pp. 187–204. DOI: [10.1086/430692](https://doi.org/10.1086/430692). arXiv: [astro-ph/0503685](https://arxiv.org/abs/astro-ph/0503685) [astro-ph].
- Le Floc'h, Emeric et al. (Oct. 2005). Infrared Luminosity Functions from the Chandra Deep Field-South: The Spitzer View on the History of Dusty Star Formation at 0 z $\lesssim 1$. 632.1, pp. 169–190. DOI: [10.1086/432789](https://doi.org/10.1086/432789). arXiv: [astro-ph/0506462](https://arxiv.org/abs/astro-ph/0506462) [astro-ph].
- Martin, D. Christopher et al. (Jan. 2005). The Galaxy Evolution Explorer: A Space Ultraviolet Survey Mission. 619.1, pp. L1–L6. DOI: [10.1086/426387](https://doi.org/10.1086/426387). arXiv: [astro-ph/0411302](https://arxiv.org/abs/astro-ph/0411302) [astro-ph].
- Newman, M. E. J. (Sept. 2005). Power laws, Pareto distributions and Zipf's law. *Contemporary Physics* 46.5, pp. 323–351. DOI: [10.1080/00107510500052444](https://doi.org/10.1080/00107510500052444). arXiv: [cond-mat/0412004](https://arxiv.org/abs/cond-mat/0412004) [cond-mat.stat-mech].
- Stauffer, J. R. et al. (Dec. 2005). Spitzer Space Telescope Observations of the Pleiades: Debris Disks and Brown Dwarfs. *American Astronomical Society Meeting Abstracts*. Vol. 207. American Astronomical Society Meeting Abstracts, 63.11, p. 63.11.
- Stern, D. et al. (Sept. 2005). Mid-Infrared Selection of Active Galaxies. 631, pp. 163–168. DOI: [10.1086/432523](https://doi.org/10.1086/432523). eprint: [astro-ph/0410523](https://arxiv.org/abs/astro-ph/0410523).

- Takeuchi, T. T. et al. (Sept. 2005). The evolution of the ultraviolet and infrared luminosity densities in the universe at $0 < z < 1$. 440.2, pp. L17–L20. DOI: [10.1051/0004-6361:200500158](https://doi.org/10.1051/0004-6361:200500158). arXiv: [astro-ph/0508124](https://arxiv.org/abs/astro-ph/0508124) [astro-ph].
- Dalton, G. B. et al. (June 2006). The VISTA infrared camera. *Society of Photo-Optical Instrumentation Engineers*. Ed. by Ian S. McLean et al. Vol. 6269. Society of Photo-Optical Instrumentation Engineers (SPIE) Conference Series, 62690X, p. 62690X. DOI: [10.1117/12.670018](https://doi.org/10.1117/12.670018).
- Emerson, J. et al. (Dec. 2006). Visible and Infrared Survey Telescope for Astronomy: Progress Report. *The Messenger* 126, pp. 41–42.
- Fabbiano, G. (Sept. 2006). Populations of X-Ray Sources in Galaxies. 44.1, pp. 323–366. DOI: [10.1146/annurev.astro.44.051905.092519](https://doi.org/10.1146/annurev.astro.44.051905.092519). arXiv: [astro-ph/0511481](https://arxiv.org/abs/astro-ph/0511481) [astro-ph].
- Gardner, Jonathan P. et al. (Apr. 2006). The James Webb Space Telescope. 123.4, pp. 485–606. DOI: [10.1007/s11214-006-8315-7](https://doi.org/10.1007/s11214-006-8315-7). arXiv: [astro-ph/0606175](https://arxiv.org/abs/astro-ph/0606175) [astro-ph].
- Ilbert, O. et al. (Oct. 2006). Accurate photometric redshifts for the CFHT legacy survey calibrated using the VIMOS VLT deep survey. 457.3, pp. 841–856. DOI: [10.1051/0004-6361:20065138](https://doi.org/10.1051/0004-6361:20065138). arXiv: [astro-ph/0603217](https://arxiv.org/abs/astro-ph/0603217) [astro-ph].
- Jordán, Andrés et al. (Nov. 2006). Trends in the Globular Cluster Luminosity Function of Early-Type Galaxies. 651.1, pp. L25–L28. DOI: [10.1086/509119](https://doi.org/10.1086/509119). arXiv: [astro-ph/0609371](https://arxiv.org/abs/astro-ph/0609371) [astro-ph].
- Kim, Eunhyeuk et al. (Aug. 2006). Low-Mass X-Ray Binaries in Six Elliptical Galaxies: Connection to Globular Clusters. 647.1, pp. 276–292. DOI: [10.1086/505261](https://doi.org/10.1086/505261). arXiv: [astro-ph/0510817](https://arxiv.org/abs/astro-ph/0510817) [astro-ph].
- Renzini, Alvio (Sept. 2006). Stellar Population Diagnostics of Elliptical Galaxy Formation. 44.1, pp. 141–192. DOI: [10.1146/annurev.astro.44.051905.092450](https://doi.org/10.1146/annurev.astro.44.051905.092450). arXiv: [astro-ph/0603479](https://arxiv.org/abs/astro-ph/0603479) [astro-ph].
- Tüllmann, R. et al. (Mar. 2006). The multi-phase gaseous halos of star forming late-type galaxies. I. XMM-Newton observations of the hot ionized medium. 448.1, pp. 43–75. DOI: [10.1051/0004-6361:20052936](https://doi.org/10.1051/0004-6361:20052936). arXiv: [astro-ph/0510079](https://arxiv.org/abs/astro-ph/0510079) [astro-ph].
- Calzetti, D. et al. (Sept. 2007). The Calibration of Mid-Infrared Star Formation Rate Indicators. 666.2, pp. 870–895. DOI: [10.1086/520082](https://doi.org/10.1086/520082). arXiv: [0705.3377](https://arxiv.org/abs/0705.3377) [astro-ph].
- Daddi, E. et al. (Nov. 2007). Multiwavelength Study of Massive Galaxies at $z \sim 2$. I. Star Formation and Galaxy Growth. 670.1, pp. 156–172. DOI: [10.1086/521818](https://doi.org/10.1086/521818). arXiv: [0705.2831](https://arxiv.org/abs/0705.2831) [astro-ph].
- Draine, B. T. et al. (Mar. 2007). Infrared Emission from Interstellar Dust. IV. The Silicate-Graphite-PAH Model in the Post-Spitzer Era. 657.2, pp. 810–837. DOI: [10.1086/511055](https://doi.org/10.1086/511055). arXiv: [astro-ph/0608003](https://arxiv.org/abs/astro-ph/0608003) [astro-ph].
- Faber, S. M. et al. (Aug. 2007). Galaxy Luminosity Functions to $z \sim 1$ from DEEP2 and COMBO-17: Implications for Red Galaxy Formation. 665.1, pp. 265–294. DOI: [10.1086/519294](https://doi.org/10.1086/519294). arXiv: [astro-ph/0506044](https://arxiv.org/abs/astro-ph/0506044) [astro-ph].
- Fitzpatrick, E. L. et al. (July 2007). An Analysis of the Shapes of Interstellar Extinction Curves. V. The IR-through-UV Curve Morphology. 663.1, pp. 320–341. DOI: [10.1086/518158](https://doi.org/10.1086/518158). arXiv: [0705.0154](https://arxiv.org/abs/0705.0154) [astro-ph].
- Just, D. W. et al. (Aug. 2007). The X-Ray Properties of the Most Luminous Quasars from the Sloan Digital Sky Survey. 665.2, pp. 1004–1022. DOI: [10.1086/519990](https://doi.org/10.1086/519990). arXiv: [0705.3059](https://arxiv.org/abs/0705.3059) [astro-ph].
- Lawrence, A. et al. (Aug. 2007). The UKIRT Infrared Deep Sky Survey (UKIDSS). 379.4, pp. 1599–1617. DOI: [10.1111/j.1365-2966.2007.12040.x](https://doi.org/10.1111/j.1365-2966.2007.12040.x). arXiv: [astro-ph/0604426](https://arxiv.org/abs/astro-ph/0604426) [astro-ph].

- Martin, D. Christopher et al. (Dec. 2007). The Star Formation and Extinction Coevolution of UV-Selected Galaxies over $0.05 < z < 1.2$. 173.2, pp. 415–431. DOI: [10.1086/522088](https://doi.org/10.1086/522088). arXiv: [0709.0730](https://arxiv.org/abs/0709.0730) [astro-ph].
- Noeske, K. G. et al. (May 2007). Star Formation in AEGIS Field Galaxies since $z=1.1$: The Dominance of Gradually Declining Star Formation, and the Main Sequence of Star-forming Galaxies. 660.1, pp. L43–L46. DOI: [10.1086/517926](https://doi.org/10.1086/517926). arXiv: [astro-ph/0701924](https://arxiv.org/abs/astro-ph/0701924) [astro-ph].
- Shtykovskiy, P. E. et al. (July 2007). High-mass X-ray binaries and recent star formation history of the Small Magellanic Cloud. *Astronomy Letters* 33.7, pp. 437–454. DOI: [10.1134/S106377370707002X](https://doi.org/10.1134/S106377370707002X). arXiv: [0710.3059](https://arxiv.org/abs/0710.3059) [astro-ph].
- Tojeiro, R. et al. (Nov. 2007). Recovering galaxy star formation and metallicity histories from spectra using VESPA. 381.3, pp. 1252–1266. DOI: [10.1111/j.1365-2966.2007.12323.x](https://doi.org/10.1111/j.1365-2966.2007.12323.x). arXiv: [0704.0941](https://arxiv.org/abs/0704.0941) [astro-ph].
- Xu, C. Kevin et al. (Dec. 2007). IR and UV Galaxies at $z = 0.6$: Evolution of Dust Attenuation and Stellar Mass as Revealed by SWIRE and GALEX. 173.2, pp. 432–440. DOI: [10.1086/516641](https://doi.org/10.1086/516641). arXiv: [astro-ph/0701737](https://arxiv.org/abs/astro-ph/0701737) [astro-ph].
- Brammer, Gabriel B. et al. (Oct. 2008). EAZY: A Fast, Public Photometric Redshift Code. 686.2, pp. 1503–1513. DOI: [10.1086/591786](https://doi.org/10.1086/591786). arXiv: [0807.1533](https://arxiv.org/abs/0807.1533) [astro-ph].
- da Cunha, Elisabete et al. (Aug. 2008). A simple model to interpret the ultraviolet, optical and infrared emission from galaxies. 388.4, pp. 1595–1617. DOI: [10.1111/j.1365-2966.2008.13535.x](https://doi.org/10.1111/j.1365-2966.2008.13535.x). arXiv: [0806.1020](https://arxiv.org/abs/0806.1020) [astro-ph].
- Franzetti, P. et al. (Aug. 2008). GOSSIP, a New VO Compliant Tool for SED Fitting. *Astronomical Data Analysis Software and Systems XVII*. Ed. by R. W. Argyle et al. Vol. 394. Astronomical Society of the Pacific Conference Series, p. 642. arXiv: [0801.2518](https://arxiv.org/abs/0801.2518) [astro-ph].
- Lehmer, B. D. et al. (July 2008). Tracing the Mass-Dependent Star Formation History of Late-Type Galaxies Using X-Ray Emission: Results from the Chandra Deep Fields. 681.2, pp. 1163–1182. DOI: [10.1086/588459](https://doi.org/10.1086/588459). arXiv: [0803.3620](https://arxiv.org/abs/0803.3620) [astro-ph].
- Revnitsev, M. et al. (Oct. 2008). Universal X-ray emissivity of the stellar population in early-type galaxies: unresolved X-ray sources in NGC 3379. 490.1, pp. 37–43. DOI: [10.1051/0004-6361:200809889](https://doi.org/10.1051/0004-6361:200809889). arXiv: [0804.0319](https://arxiv.org/abs/0804.0319) [astro-ph].
- Tielens, A. G. G. M. (Sept. 2008). Interstellar polycyclic aromatic hydrocarbon molecules. 46, pp. 289–337. DOI: [10.1146/annurev.astro.46.060407.145211](https://doi.org/10.1146/annurev.astro.46.060407.145211).
- Abazajian, Kevork N. et al. (June 2009). The Seventh Data Release of the Sloan Digital Sky Survey. 182.2, pp. 543–558. DOI: [10.1088/0067-0049/182/2/543](https://doi.org/10.1088/0067-0049/182/2/543). arXiv: [0812.0649](https://arxiv.org/abs/0812.0649) [astro-ph].
- Blakeslee, John P. et al. (Mar. 2009). The ACS Fornax Cluster Survey. V. Measurement and Recalibration of Surface Brightness Fluctuations and a Precise Value of the Fornax-Virgo Relative Distance. 694.1, pp. 556–572. DOI: [10.1088/0004-637X/694/1/556](https://doi.org/10.1088/0004-637X/694/1/556). arXiv: [0901.1138](https://arxiv.org/abs/0901.1138) [astro-ph.CO].
- Blanton, Michael R. et al. (Sept. 2009). Physical Properties and Environments of Nearby Galaxies. 47.1, pp. 159–210. DOI: [10.1146/annurev-astro-082708-101734](https://doi.org/10.1146/annurev-astro-082708-101734). arXiv: [0908.3017](https://arxiv.org/abs/0908.3017) [astro-ph.GA].
- Buat, V. et al. (Nov. 2009). The infrared emission of ultraviolet-selected galaxies from $z = 0$ to $z = 1$. 507.2, pp. 693–704. DOI: [10.1051/0004-6361/200912024](https://doi.org/10.1051/0004-6361/200912024). arXiv: [0907.2819](https://arxiv.org/abs/0907.2819) [astro-ph.CO].
- Gordon, Karl D. et al. (Nov. 2009). FUSE Measurements of Far-Ultraviolet Extinction. III. The Dependence on $R(V)$ and Discrete Feature Limits from 75 Galactic Sightlines. 705.2, pp. 1320–1335. DOI: [10.1088/0004-637X/705/2/1320](https://doi.org/10.1088/0004-637X/705/2/1320). arXiv: [0909.3087](https://arxiv.org/abs/0909.3087) [astro-ph.GA].

- Ibert, O. et al. (Jan. 2009). Cosmos Photometric Redshifts with 30-Bands for 2-deg². 690.2, pp. 1236–1249. DOI: [10.1088/0004-637X/690/2/1236](https://doi.org/10.1088/0004-637X/690/2/1236). arXiv: [0809.2101](https://arxiv.org/abs/0809.2101) [astro-ph].
- Kennicutt Robert C., Jr. et al. (Oct. 2009). Dust-corrected Star Formation Rates of Galaxies. I. Combinations of H α and Infrared Tracers. 703.2, pp. 1672–1695. DOI: [10.1088/0004-637X/703/2/1672](https://doi.org/10.1088/0004-637X/703/2/1672). arXiv: [0908.0203](https://arxiv.org/abs/0908.0203) [astro-ph.CO].
- Kim, D. W. et al. (Sept. 2009). Comparing GC and Field LMXBs in Elliptical Galaxies with Deep Chandra and Hubble Data. 703.1, pp. 829–844. DOI: [10.1088/0004-637X/703/1/829](https://doi.org/10.1088/0004-637X/703/1/829). arXiv: [0902.2343](https://arxiv.org/abs/0902.2343) [astro-ph.CO].
- Kormendy, John et al. (May 2009). Structure and Formation of Elliptical and Spheroidal Galaxies. 182.1, pp. 216–309. DOI: [10.1088/0067-0049/182/1/216](https://doi.org/10.1088/0067-0049/182/1/216). arXiv: [0810.1681](https://arxiv.org/abs/0810.1681) [astro-ph].
- LSST Science Collaboration et al. (Dec. 2009). LSST Science Book, Version 2.0. [arXiv e-prints](https://arxiv.org/abs/0912.0201), arXiv:0912.0201, arXiv:0912.0201. arXiv: [0912.0201](https://arxiv.org/abs/0912.0201) [astro-ph.IM].
- Noll, S. et al. (Dec. 2009). Analysis of galaxy spectral energy distributions from far-UV to far-IR with CIGALE: studying a SINGS test sample. 507.3, pp. 1793–1813. DOI: [10.1051/0004-6361/200912497](https://doi.org/10.1051/0004-6361/200912497). arXiv: [0909.5439](https://arxiv.org/abs/0909.5439) [astro-ph.CO].
- Salvato, M. et al. (Jan. 2009). Photometric Redshift and Classification for the XMM-COSMOS Sources. 690.2, pp. 1250–1263. DOI: [10.1088/0004-637X/690/2/1250](https://doi.org/10.1088/0004-637X/690/2/1250). arXiv: [0809.2098](https://arxiv.org/abs/0809.2098) [astro-ph].
- Williams, Rik J. et al. (Feb. 2009). Detection of Quiescent Galaxies in a Bicolor Sequence from Z = 0–2. 691.2, pp. 1879–1895. DOI: [10.1088/0004-637X/691/2/1879](https://doi.org/10.1088/0004-637X/691/2/1879). arXiv: [0806.0625](https://arxiv.org/abs/0806.0625) [astro-ph].
- da Cunha, E. et al. (Nov. 2010). Exploring the physical properties of local star-forming ULIRGs from the ultraviolet to the infrared. 523, A78, A78. DOI: [10.1051/0004-6361/201014498](https://doi.org/10.1051/0004-6361/201014498). arXiv: [1008.2000](https://arxiv.org/abs/1008.2000) [astro-ph.CO].
- Eales, S. et al. (May 2010). The Herschel ATLAS. 122.891, p. 499. DOI: [10.1086/653086](https://doi.org/10.1086/653086). arXiv: [0910.4279](https://arxiv.org/abs/0910.4279) [astro-ph.CO].
- Elbaz, D. et al. (July 2010). Herschel unveils a puzzling uniformity of distant dusty galaxies. 518, L29, p. L29. DOI: [10.1051/0004-6361/201014687](https://doi.org/10.1051/0004-6361/201014687). arXiv: [1005.2859](https://arxiv.org/abs/1005.2859) [astro-ph.CO].
- Griffin, M. J. et al. (July 2010). The Herschel-SPIRE instrument and its in-flight performance. 518, L3, p. L3. DOI: [10.1051/0004-6361/201014519](https://doi.org/10.1051/0004-6361/201014519). arXiv: [1005.5123](https://arxiv.org/abs/1005.5123) [astro-ph.IM].
- Hildebrandt, H. et al. (Nov. 2010). PHAT: PHoto-z Accuracy Testing. 523, A31, A31. DOI: [10.1051/0004-6361/201014885](https://doi.org/10.1051/0004-6361/201014885). arXiv: [1008.0658](https://arxiv.org/abs/1008.0658) [astro-ph.CO].
- Lehmer, B. D. et al. (Nov. 2010). A Chandra Perspective on Galaxy-wide X-ray Binary Emission and its Correlation with Star Formation Rate and Stellar Mass: New Results from Luminous Infrared Galaxies. 724.1, pp. 559–571. DOI: [10.1088/0004-637X/724/1/559](https://doi.org/10.1088/0004-637X/724/1/559). arXiv: [1009.3943](https://arxiv.org/abs/1009.3943) [astro-ph.CO].
- Linden, T. et al. (Dec. 2010). The Effect of Starburst Metallicity on Bright X-ray Binary Formation Pathways. 725.2, pp. 1984–1994. DOI: [10.1088/0004-637X/725/2/1984](https://doi.org/10.1088/0004-637X/725/2/1984). arXiv: [1005.1639](https://arxiv.org/abs/1005.1639) [astro-ph.CO].
- Mo, Houjun et al. (2010). [Galaxy Formation and Evolution](https://arxiv.org/abs/1002.1325).
- Muratov, Alexander L. et al. (Aug. 2010). Modeling the Metallicity Distribution of Globular Clusters. 718.2, pp. 1266–1288. DOI: [10.1088/0004-637X/718/2/1266](https://doi.org/10.1088/0004-637X/718/2/1266). arXiv: [1002.1325](https://arxiv.org/abs/1002.1325) [astro-ph.GA].
- Poglitsch, A. et al. (July 2010). The Photodetector Array Camera and Spectrometer (PACS) on the Herschel Space Observatory. 518, L2, p. L2. DOI: [10.1051/0004-6361/201014535](https://doi.org/10.1051/0004-6361/201014535). arXiv: [1005.1487](https://arxiv.org/abs/1005.1487) [astro-ph.IM].

- Schuberth, Y. et al. (Apr. 2010). The globular cluster system of NGC 1399. V. dynamics of the cluster system out to 80 kpc. 513, A52, A52. DOI: [10.1051/0004-6361/200912482](https://doi.org/10.1051/0004-6361/200912482). arXiv: [0911.0420](https://arxiv.org/abs/0911.0420) [astro-ph.CO].
- Villegas, Daniela et al. (July 2010). The ACS Fornax Cluster Survey. VIII. The Luminosity Function of Globular Clusters in Virgo and Fornax Early-type Galaxies and Its Use as a Distance Indicator. 717.2, pp. 603–616. DOI: [10.1088/0004-637X/717/2/603](https://doi.org/10.1088/0004-637X/717/2/603). arXiv: [1004.2883](https://arxiv.org/abs/1004.2883) [astro-ph.CO].
- Baes, Maarten et al. (Oct. 2011). Efficient Three-dimensional NLTE Dust Radiative Transfer with SKIRT. 196.2, 22, p. 22. DOI: [10.1088/0067-0049/196/2/22](https://doi.org/10.1088/0067-0049/196/2/22). arXiv: [1108.5056](https://arxiv.org/abs/1108.5056) [astro-ph.CO].
- Boroson, Bram et al. (Mar. 2011). Revisiting with Chandra the Scaling Relations of the X-ray Emission Components (Binaries, Nuclei, and Hot Gas) of Early-type Galaxies. 729.1, 12, p. 12. DOI: [10.1088/0004-637X/729/1/12](https://doi.org/10.1088/0004-637X/729/1/12). arXiv: [1011.2529](https://arxiv.org/abs/1011.2529) [astro-ph.HE].
- Giovannoli, E. et al. (Jan. 2011). Population synthesis modelling of luminous infrared galaxies at intermediate redshift. 525, A150, A150. DOI: [10.1051/0004-6361/201014898](https://doi.org/10.1051/0004-6361/201014898). arXiv: [1006.5555](https://arxiv.org/abs/1006.5555) [astro-ph.CO].
- González-Solares, E. A. et al. (Sept. 2011). Wide-field optical imaging on ELAIS N1, ELAIS N2, First Look Survey and Lockman Hole: observations and source catalogues. 416.2, pp. 927–940. DOI: [10.1111/j.1365-2966.2011.19082.x](https://doi.org/10.1111/j.1365-2966.2011.19082.x).
- Hao, Cai-Na et al. (Nov. 2011). Dust-corrected Star Formation Rates of Galaxies. II. Combinations of Ultraviolet and Infrared Tracers. 741.2, 124, p. 124. DOI: [10.1088/0004-637X/741/2/124](https://doi.org/10.1088/0004-637X/741/2/124). arXiv: [1108.2837](https://arxiv.org/abs/1108.2837) [astro-ph.CO].
- Komatsu, E. et al. (Feb. 2011). Seven-year Wilkinson Microwave Anisotropy Probe (WMAP) Observations: Cosmological Interpretation. 192.2, 18, p. 18. DOI: [10.1088/0067-0049/192/2/18](https://doi.org/10.1088/0067-0049/192/2/18). arXiv: [1001.4538](https://arxiv.org/abs/1001.4538) [astro-ph.CO].
- Paolillo, Maurizio et al. (Aug. 2011). Probing the GC-LMXB Connection in NGC 1399: A Wide-field Study with the Hubble Space Telescope and Chandra. 736.2, 90, p. 90. DOI: [10.1088/0004-637X/736/2/90](https://doi.org/10.1088/0004-637X/736/2/90). arXiv: [1105.2561](https://arxiv.org/abs/1105.2561) [astro-ph.HE].
- Popescu, C. C. et al. (Mar. 2011). Modelling the spectral energy distribution of galaxies. V. The dust and PAH emission SEDs of disk galaxies. 527, A109, A109. DOI: [10.1051/0004-6361/201015217](https://doi.org/10.1051/0004-6361/201015217). arXiv: [1011.2942](https://arxiv.org/abs/1011.2942) [astro-ph.CO].
- Rodighiero, G. et al. (Oct. 2011). The Lesser Role of Starbursts in Star Formation at $z = 2$. 739.2, L40, p. L40. DOI: [10.1088/2041-8205/739/2/L40](https://doi.org/10.1088/2041-8205/739/2/L40). arXiv: [1108.0933](https://arxiv.org/abs/1108.0933) [astro-ph.CO].
- Walcher, Jakob et al. (Jan. 2011). Fitting the integrated spectral energy distributions of galaxies. 331, pp. 1–52. DOI: [10.1007/s10509-010-0458-z](https://doi.org/10.1007/s10509-010-0458-z). arXiv: [1008.0395](https://arxiv.org/abs/1008.0395) [astro-ph.CO].
- Wild, Vivienne et al. (2011). Empirical determination of the shape of dust attenuation curves in star-forming galaxies. *Monthly Notices of the Royal Astronomical Society* 417.3, pp. 1760–1786. DOI: [10.1111/j.1365-2966.2011.19367.x](https://doi.org/10.1111/j.1365-2966.2011.19367.x).
- Xue, Y. Q. et al. (July 2011). The Chandra Deep Field-South Survey: 4 Ms Source Catalogs. 195.1, 10, p. 10. DOI: [10.1088/0067-0049/195/1/10](https://doi.org/10.1088/0067-0049/195/1/10). arXiv: [1105.5643](https://arxiv.org/abs/1105.5643) [astro-ph.CO].
- Zhang, Z. et al. (Sept. 2011). Luminosity functions of LMXBs in different stellar environments. 533, A33, A33. DOI: [10.1051/0004-6361/201116936](https://doi.org/10.1051/0004-6361/201116936). arXiv: [1103.4486](https://arxiv.org/abs/1103.4486) [astro-ph.HE].
- Béthermin, Matthieu et al. (Oct. 2012). A Unified Empirical Model for Infrared Galaxy Counts Based on the Observed Physical Evolution of Distant Galaxies. 757.2, L23, p. L23. DOI: [10.1088/2041-8205/757/2/L23](https://doi.org/10.1088/2041-8205/757/2/L23). arXiv: [1208.6512](https://arxiv.org/abs/1208.6512) [astro-ph.CO].

- Buat, V. et al. (Sept. 2012). GOODS-Herschel: dust attenuation properties of UV selected high redshift galaxies. 545, A141, A141. DOI: [10 . 1051 / 0004 - 6361 / 201219405](https://doi.org/10.1051/0004-6361/201219405). arXiv: [1207.3528](https://arxiv.org/abs/1207.3528) [astro-ph.CO].
- Calzetti, D. et al. (June 2012). Star Formation Laws: The Effects of Gas Cloud Sampling. 752.2, 98, p. 98. DOI: [10 . 1088 / 0004 - 637X / 752 / 2 / 98](https://doi.org/10.1088/0004-637X/752/2/98). arXiv: [1204 . 5659](https://arxiv.org/abs/1204.5659) [astro-ph.GA].
- Donley, J. L. et al. (Apr. 2012). Identifying Luminous Active Galactic Nuclei in Deep Surveys: Revised IRAC Selection Criteria. 748.2, 142, p. 142. DOI: [10 . 1088 / 0004 - 637X / 748 / 2 / 142](https://doi.org/10.1088/0004-637X/748/2/142). arXiv: [1201 . 3899](https://arxiv.org/abs/1201.3899) [astro-ph.CO].
- Lehmer, B. D. et al. (June 2012). The 4 Ms Chandra Deep Field-South Number Counts Apportioned by Source Class: Pervasive Active Galactic Nuclei and the Ascent of Normal Galaxies. 752.1, 46, p. 46. DOI: [10 . 1088 / 0004 - 637X / 752 / 1 / 46](https://doi.org/10.1088/0004-637X/752/1/46). arXiv: [1204 . 1977](https://arxiv.org/abs/1204.1977) [astro-ph.CO].
- Mauduit, J. C. et al. (July 2012). The Spitzer Extragalactic Representative Volume Survey (SERVS): Survey Definition and Goals. 124.917, p. 714. DOI: [10 . 1086 / 666945](https://doi.org/10.1086/666945). arXiv: [1206 . 4060](https://arxiv.org/abs/1206.4060) [astro-ph.CO].
- Merloni, A. et al. (Sept. 2012). eROSITA Science Book: Mapping the Structure of the Energetic Universe. arXiv e-prints, arXiv:1209.3114, arXiv:1209.3114. DOI: [10 . 48550 / arXiv . 1209 . 3114](https://doi.org/10.48550/arXiv.1209.3114). arXiv: [1209 . 3114](https://arxiv.org/abs/1209.3114) [astro-ph.HE].
- Mineo, S. et al. (Jan. 2012). X-ray emission from star-forming galaxies - I. High-mass X-ray binaries. 419.3, pp. 2095–2115. DOI: [10 . 1111 / j . 1365 - 2966 . 2011 . 19862 . x](https://doi.org/10.1111/j.1365-2966.2011.19862.x). arXiv: [1105 . 4610](https://arxiv.org/abs/1105.4610) [astro-ph.HE].
- Oliver, S. J. et al. (Aug. 2012). The Herschel Multi-tiered Extragalactic Survey: HerMES. 424.3, pp. 1614–1635. DOI: [10 . 1111 / j . 1365 - 2966 . 2012 . 20912 . x](https://doi.org/10.1111/j.1365-2966.2012.20912.x). arXiv: [1203 . 2562](https://arxiv.org/abs/1203.2562) [astro-ph.CO].
- Stalevski, Marko et al. (Mar. 2012). 3D radiative transfer modelling of the dusty tori around active galactic nuclei as a clumpy two-phase medium. 420.4, pp. 2756–2772. DOI: [10 . 1111 / j . 1365 - 2966 . 2011 . 19775 . x](https://doi.org/10.1111/j.1365-2966.2011.19775.x). arXiv: [1109 . 1286](https://arxiv.org/abs/1109.1286) [astro-ph.CO].
- Whitaker, Katherine E. et al. (Aug. 2012). The Star Formation Mass Sequence Out to $z = 2.5$. 754.2, L29, p. L29. DOI: [10 . 1088 / 2041 - 8205 / 754 / 2 / L29](https://doi.org/10.1088/2041-8205/754/2/L29). arXiv: [1205 . 0547](https://arxiv.org/abs/1205.0547) [astro-ph.CO].
- Arnouts, S. et al. (Oct. 2013). Encoding of the infrared excess in the NUVrK color diagram for star-forming galaxies. 558, A67, A67. DOI: [10 . 1051 / 0004 - 6361 / 201321768](https://doi.org/10.1051/0004-6361/201321768). arXiv: [1309 . 0008](https://arxiv.org/abs/1309.0008) [astro-ph.CO].
- Assef, R. J. et al. (July 2013). Mid-infrared Selection of Active Galactic Nuclei with the Wide-field Infrared Survey Explorer. II. Properties of WISE-selected Active Galactic Nuclei in the NDWFS Boötes Field. 772.1, 26, p. 26. DOI: [10 . 1088 / 0004 - 637X / 772 / 1 / 26](https://doi.org/10.1088/0004-637X/772/1/26). arXiv: [1209 . 6055](https://arxiv.org/abs/1209.6055) [astro-ph.CO].
- Basu-Zych, Antara R. et al. (Sept. 2013a). Evidence for Elevated X-Ray Emission in Local Lyman Break Galaxy Analogs. 774.2, 152, p. 152. DOI: [10 . 1088 / 0004 - 637X / 774 / 2 / 152](https://doi.org/10.1088/0004-637X/774/2/152). arXiv: [1306 . 0906](https://arxiv.org/abs/1306.0906) [astro-ph.CO].
- Basu-Zych, Antara R. et al. (Jan. 2013b). The X-Ray Star Formation Story as Told by Lyman Break Galaxies in the 4 Ms CDF-S. 762.1, 45, p. 45. DOI: [10 . 1088 / 0004 - 637X / 762 / 1 / 45](https://doi.org/10.1088/0004-637X/762/1/45). arXiv: [1210 . 3357](https://arxiv.org/abs/1210.3357) [astro-ph.CO].
- Burgarella, D. et al. (June 2013). Herschel PEP/HerMES: the redshift evolution ($0 \leq z \leq 4$) of dust attenuation and of the total (UV+IR) star formation rate density. 554, A70, A70. DOI: [10 . 1051 / 0004 - 6361 / 201321651](https://doi.org/10.1051/0004-6361/201321651). arXiv: [1304 . 7000](https://arxiv.org/abs/1304.7000) [astro-ph.CO].
- Conroy, Charlie (Aug. 2013). Modeling the Panchromatic Spectral Energy Distributions of Galaxies. 51.1, pp. 393–455. DOI: [10 . 1146 / annurev - astro - 082812 - 141017](https://doi.org/10.1146/annurev-astro-082812-141017). arXiv: [1301 . 7095](https://arxiv.org/abs/1301.7095) [astro-ph.CO].

- Domínguez, A. et al. (Feb. 2013). Dust Extinction from Balmer Decrements of Star-forming Galaxies at $0.75 \leq z \leq 1.5$ with Hubble Space Telescope/Wide-Field-Camera 3 Spectroscopy from the WFC3 Infrared Spectroscopic Parallel Survey. 763.2, 145, p. 145. DOI: [10.1088/0004-637X/763/2/145](https://doi.org/10.1088/0004-637X/763/2/145). arXiv: [1206.1867](https://arxiv.org/abs/1206.1867) [astro-ph.CO].
- Edge, A. et al. (Dec. 2013). The VISTA Kilo-degree Infrared Galaxy (VIKING) Survey: Bridging the Gap between Low and High Redshift. *The Messenger* 154, pp. 32–34.
- Fragos, T. et al. (Oct. 2013). Energy Feedback from X-Ray Binaries in the Early Universe. 776.2, L31, p. L31. DOI: [10.1088/2041-8205/776/2/L31](https://doi.org/10.1088/2041-8205/776/2/L31). arXiv: [1306.1405](https://arxiv.org/abs/1306.1405) [astro-ph.CO].
- Graham, Alister W. (2013). Elliptical and Disk Galaxy Structure and Modern Scaling Laws. *Planets, Stars and Stellar Systems. Volume 6: Extragalactic Astronomy and Cosmology*. Ed. by Terry D. Oswalt et al. Vol. 6, pp. 91–140. DOI: [10.1007/978-94-007-5609-0_2](https://doi.org/10.1007/978-94-007-5609-0_2).
- Harris, William E. et al. (Aug. 2013). A Catalog of Globular Cluster Systems: What Determines the Size of a Galaxy’s Globular Cluster Population? 772.2, 82, p. 82. DOI: [10.1088/0004-637X/772/2/82](https://doi.org/10.1088/0004-637X/772/2/82). arXiv: [1306.2247](https://arxiv.org/abs/1306.2247) [astro-ph.GA].
- Kim, D. W. et al. (Feb. 2013). Metallicity Effect on Low-mass X-Ray Binary Formation in Globular Clusters. 764.1, 98, p. 98. DOI: [10.1088/0004-637X/764/1/98](https://doi.org/10.1088/0004-637X/764/1/98). arXiv: [1208.5952](https://arxiv.org/abs/1208.5952) [astro-ph.HE].
- McMahon, R. G. et al. (Dec. 2013). First Scientific Results from the VISTA Hemisphere Survey (VHS). *The Messenger* 154, pp. 35–37.
- Mitchell, Peter D. et al. (Oct. 2013). How well can we really estimate the stellar masses of galaxies from broad-band photometry? 435.1, pp. 87–114. DOI: [10.1093/mnras/stt1280](https://doi.org/10.1093/mnras/stt1280). arXiv: [1303.7228](https://arxiv.org/abs/1303.7228) [astro-ph.CO].
- Steinacker, Jürgen et al. (2013). Three-Dimensional Dust Radiative Transfer. *Annual Review of Astronomy and Astrophysics* 51.1, pp. 63–104. DOI: [10.1146/annurev-astro-082812-141042](https://doi.org/10.1146/annurev-astro-082812-141042). eprint: <https://doi.org/10.1146/annurev-astro-082812-141042>. URL: <https://doi.org/10.1146/annurev-astro-082812-141042>.
- Swinbank, A. M. (Jan. 2013). The UKIDSS Deep eXtra-Galactic Survey. *Thirty Years of Astronomical Discoveries* Vol. 37, p. 299. DOI: [10.1007/978-94-007-7432-2_28](https://doi.org/10.1007/978-94-007-7432-2_28).
- Bianchi, Luciana (Nov. 2014). The Galaxy Evolution Explorer (GALEX). Its legacy of UV surveys, and science highlights. 354.1, pp. 103–112. DOI: [10.1007/s10509-014-1935-6](https://doi.org/10.1007/s10509-014-1935-6). arXiv: [1404.4882](https://arxiv.org/abs/1404.4882) [astro-ph.GA].
- Brown, Michael J. I. et al. (June 2014). An Atlas of Galaxy Spectral Energy Distributions from the Ultraviolet to the Mid-infrared. 212.2, 18, p. 18. DOI: [10.1088/0067-0049/212/2/18](https://doi.org/10.1088/0067-0049/212/2/18). arXiv: [1312.3029](https://arxiv.org/abs/1312.3029) [astro-ph.CO].
- Civano, F. et al. (July 2014). Early-type Galaxies in the Chandra COSMOS Survey. 790.1, 16, p. 16. DOI: [10.1088/0004-637X/790/1/16](https://doi.org/10.1088/0004-637X/790/1/16). arXiv: [1405.7039](https://arxiv.org/abs/1405.7039) [astro-ph.GA].
- D’Ago, G. et al. (July 2014). Luminosity function of low-mass X-ray binaries in the globular cluster system of <ASTROBJ>NGC 1399</ASTROBJ>. 567, A2, A2. DOI: [10.1051/0004-6361/201322722](https://doi.org/10.1051/0004-6361/201322722). arXiv: [1405.0618](https://arxiv.org/abs/1405.0618) [astro-ph.HE].
- Dale, Daniel A. et al. (Mar. 2014). A Two-parameter Model for the Infrared/Submillimeter/Radio Spectral Energy Distributions of Galaxies and Active Galactic Nuclei. 784.1, 83, p. 83. DOI: [10.1088/0004-637X/784/1/83](https://doi.org/10.1088/0004-637X/784/1/83). arXiv: [1402.1495](https://arxiv.org/abs/1402.1495) [astro-ph.GA].
- Dobbs, Clare et al. (Sept. 2014). Dawes Review 4: Spiral Structures in Disc Galaxies. 31, e035, e035. DOI: [10.1017/pasa.2014.31](https://doi.org/10.1017/pasa.2014.31). arXiv: [1407.5062](https://arxiv.org/abs/1407.5062) [astro-ph.GA].
- Draine, B. T. et al. (Jan. 2014). Andromeda’s Dust. 780.2, 172, p. 172. DOI: [10.1088/0004-637X/780/2/172](https://doi.org/10.1088/0004-637X/780/2/172). arXiv: [1306.2304](https://arxiv.org/abs/1306.2304) [astro-ph.CO].

- Durrell, Patrick R. et al. (Oct. 2014). The Next Generation Virgo Cluster Survey. VIII. The Spatial Distribution of Globular Clusters in the Virgo Cluster. 794.2, 103, p. 103. DOI: [10.1088/0004-637X/794/2/103](https://doi.org/10.1088/0004-637X/794/2/103). arXiv: [1408.2821](https://arxiv.org/abs/1408.2821) [astro-ph.GA].
- Han, Yunkun et al. (Nov. 2014). BayeSED: A General Approach to Fitting the Spectral Energy Distribution of Galaxies. 215.1, 2, p. 2. DOI: [10.1088/0067-0049/215/1/2](https://doi.org/10.1088/0067-0049/215/1/2). arXiv: [1408.6399](https://arxiv.org/abs/1408.6399) [astro-ph.GA].
- Kartha, Sreeja S. et al. (Jan. 2014). The SLUGGS survey: the globular cluster systems of three early-type galaxies using wide-field imaging. 437.1, pp. 273–292. DOI: [10.1093/mnras/stt1880](https://doi.org/10.1093/mnras/stt1880). arXiv: [1310.1979](https://arxiv.org/abs/1310.1979) [astro-ph.CO].
- Lehmer, B. D. et al. (July 2014). The X-Ray Luminosity Functions of Field Low-mass X-Ray Binaries in Early-type Galaxies: Evidence for a Stellar Age Dependence. 789.1, 52, p. 52. DOI: [10.1088/0004-637X/789/1/52](https://doi.org/10.1088/0004-637X/789/1/52). arXiv: [1405.2069](https://arxiv.org/abs/1405.2069) [astro-ph.GA].
- Madau, Piero et al. (Aug. 2014). Cosmic Star-Formation History. 52, pp. 415–486. DOI: [10.1146/annurev-astro-081811-125615](https://doi.org/10.1146/annurev-astro-081811-125615). arXiv: [1403.0007](https://arxiv.org/abs/1403.0007) [astro-ph.CO].
- Mineo, S. et al. (Jan. 2014). X-ray emission from star-forming galaxies - III. Calibration of the L_X -SFR relation up to redshift $z \approx 1.3$. 437.2, pp. 1698–1707. DOI: [10.1093/mnras/stt1999](https://doi.org/10.1093/mnras/stt1999). arXiv: [1207.2157](https://arxiv.org/abs/1207.2157) [astro-ph.HE].
- Puzia, Thomas H. et al. (May 2014). Wide-field Hubble Space Telescope Observations of the Globular Cluster System in NGC 1399. 786.2, 78, p. 78. DOI: [10.1088/0004-637X/786/2/78](https://doi.org/10.1088/0004-637X/786/2/78). arXiv: [1402.6714](https://arxiv.org/abs/1402.6714) [astro-ph.GA].
- Speagle, J. S. et al. (Oct. 2014). A Highly Consistent Framework for the Evolution of the Star-Forming “Main Sequence” from $z \sim 0$ –6. 214.2, 15, p. 15. DOI: [10.1088/0067-0049/214/2/15](https://doi.org/10.1088/0067-0049/214/2/15). arXiv: [1405.2041](https://arxiv.org/abs/1405.2041) [astro-ph.GA].
- Cantiello, Michele et al. (Mar. 2015). VEGAS-SSS. A VST early-type galaxy survey: analysis of small stellar systems. Testing the methodology on the globular cluster system in NGC 3115. 576, A14, A14. DOI: [10.1051/0004-6361/201425165](https://doi.org/10.1051/0004-6361/201425165). arXiv: [1412.0469](https://arxiv.org/abs/1412.0469) [astro-ph.GA].
- Capaccioli, Massimo et al. (Sept. 2015). VEGAS: A VST Early-type Galaxy Survey. I. Presentation, wide-field surface photometry, and substructures in NGC 4472. 581, A10, A10. DOI: [10.1051/0004-6361/201526252](https://doi.org/10.1051/0004-6361/201526252). arXiv: [1507.01336](https://arxiv.org/abs/1507.01336) [astro-ph.GA].
- Ciesla, L. et al. (Apr. 2015). Constraining the properties of AGN host galaxies with spectral energy distribution modelling. 576, A10, A10. DOI: [10.1051/0004-6361/201425252](https://doi.org/10.1051/0004-6361/201425252). arXiv: [1501.03672](https://arxiv.org/abs/1501.03672) [astro-ph.GA].
- Jones, Mark H. et al. (2015). *An Introduction to Galaxies and Cosmology*.
- Jordán, Andrés et al. (Nov. 2015). The ACS Fornax Cluster Survey. XI. Catalog of Globular Cluster Candidates. 221.1, 13, p. 13. DOI: [10.1088/0067-0049/221/1/13](https://doi.org/10.1088/0067-0049/221/1/13).
- Schreiber, C. et al. (Mar. 2015). The Herschel view of the dominant mode of galaxy growth from $z = 4$ to the present day. 575, A74, A74. DOI: [10.1051/0004-6361/201425017](https://doi.org/10.1051/0004-6361/201425017). arXiv: [1409.5433](https://arxiv.org/abs/1409.5433) [astro-ph.GA].
- Timmons, N. et al. (Dec. 2015). Multi-wavelength lens reconstruction of a Planck & *Herschel*-detected starbursting galaxy. *The Astrophysical Journal* 829. DOI: [10.3847/0004-637X/829/1/21](https://doi.org/10.3847/0004-637X/829/1/21).
- Vulcani, Benedetta et al. (Jan. 2015). From Blue Star-forming to Red Passive: Galaxies in Transition in Different Environments. 798.1, 52, p. 52. DOI: [10.1088/0004-637X/798/1/52](https://doi.org/10.1088/0004-637X/798/1/52). arXiv: [1410.6481](https://arxiv.org/abs/1410.6481) [astro-ph.GA].
- Whitaker, Katherine E. et al. (Sept. 2015). Galaxy Structure as a Driver of the Star Formation Sequence Slope and Scatter. 811.1, L12, p. L12. DOI: [10.1088/2041-8205/811/1/L12](https://doi.org/10.1088/2041-8205/811/1/L12). arXiv: [1508.04771](https://arxiv.org/abs/1508.04771) [astro-ph.GA].

- Basu-Zych, Antara R. et al. (Feb. 2016). Exploring the Overabundance of ULXs in Metal- and Dust-poor Local Lyman Break Analogs. 818.2, 140, p. 140. DOI: [10 . 3847/0004-637X/818/2/140](https://doi.org/10.3847/0004-637X/818/2/140). arXiv: [1601.00644](https://arxiv.org/abs/1601.00644) [astro-ph.GA].
- Chambers, K. C. et al. (Dec. 2016). The Pan-STARRS1 Surveys. *arXiv e-prints*, arXiv:1612.05560, arXiv:1612.05560. arXiv: [1612.05560](https://arxiv.org/abs/1612.05560) [astro-ph.IM].
- Ciesla, L. et al. (Jan. 2016). The imprint of rapid star formation quenching on the spectral energy distributions of galaxies. 585, A43, A43. DOI: [10 . 1051/0004-6361/201527107](https://doi.org/10.1051/0004-6361/201527107). arXiv: [1510.07657](https://arxiv.org/abs/1510.07657) [astro-ph.GA].
- D'Abrusco, R. et al. (Mar. 2016). The Extended Spatial Distribution of Globular Clusters in the Core of the Fornax Cluster. 819.2, L31, p. L31. DOI: [10 . 3847/2041-8205/819/2/L31](https://doi.org/10.3847/2041-8205/819/2/L31). arXiv: [1602.06076](https://arxiv.org/abs/1602.06076) [astro-ph.GA].
- Iodice, E. et al. (Mar. 2016). The Fornax Deep Survey with VST. I. The Extended and Diffuse Stellar Halo of NGC 1399 out to 192 kpc. 820.1, 42, p. 42. DOI: [10 . 3847/0004-637X/820/1/42](https://doi.org/10.3847/0004-637X/820/1/42). arXiv: [1602.02149](https://arxiv.org/abs/1602.02149) [astro-ph.GA].
- Laigle, C. et al. (June 2016). The COSMOS2015 Catalog: Exploring the 1 < z < 6 Universe with Half a Million Galaxies. 224.2, 24, p. 24. DOI: [10 . 3847/0067-0049/224/2/24](https://doi.org/10.3847/0067-0049/224/2/24). arXiv: [1604.02350](https://arxiv.org/abs/1604.02350) [astro-ph.GA].
- Lehmer, B. D. et al. (July 2016). The Evolution of Normal Galaxy X-Ray Emission through Cosmic History: Constraints from the 6 MS Chandra Deep Field-South. 825.1, 7, p. 7. DOI: [10 . 3847/0004-637X/825/1/7](https://doi.org/10.3847/0004-637X/825/1/7). arXiv: [1604.06461](https://arxiv.org/abs/1604.06461) [astro-ph.GA].
- Salim, Samir et al. (Nov. 2016). GALEX-SDSS-WISE Legacy Catalog (GSWLC): Star Formation Rates, Stellar Masses, and Dust Attenuations of 700,000 Low-redshift Galaxies. 227.1, 2, p. 2. DOI: [10 . 3847/0067-0049/227/1/2](https://doi.org/10.3847/0067-0049/227/1/2). arXiv: [1610.00712](https://arxiv.org/abs/1610.00712) [astro-ph.GA].
- Schreiber, C. et al. (May 2016). Observational evidence of a slow downfall of star formation efficiency in massive galaxies during the past 10 Gyr. 589, A35, A35. DOI: [10 . 1051/0004-6361/201527200](https://doi.org/10.1051/0004-6361/201527200). arXiv: [1601.04226](https://arxiv.org/abs/1601.04226) [astro-ph.GA].
- Stalevski, Marko et al. (May 2016). The dust covering factor in active galactic nuclei. 458.3, pp. 2288–2302. DOI: [10 . 1093/mnras/stw444](https://doi.org/10.1093/mnras/stw444). arXiv: [1602.06954](https://arxiv.org/abs/1602.06954) [astro-ph.GA].
- Tacchella, Sandro et al. (Apr. 2016). The confinement of star-forming galaxies into a main sequence through episodes of gas compaction, depletion and replenishment. 457.3, pp. 2790–2813. DOI: [10 . 1093/mnras/stw131](https://doi.org/10.1093/mnras/stw131). arXiv: [1509.02529](https://arxiv.org/abs/1509.02529) [astro-ph.GA].
- Webb, Jeremy J. et al. (2016). Globular cluster scale sizes in giant galaxies: orbital anisotropy and tidally underfilling clusters in M87, NGC 1399 and NGC 5128. *Monthly Notices of the Royal Astronomical Society* 460.2, pp. 2129–2142. ISSN: 0035-8711. DOI: [10 . 1093/mnras/stw1115](https://doi.org/10.1093/mnras/stw1115). arXiv: [1605.03191](https://arxiv.org/abs/1605.03191). URL: <http://arxiv.org/abs/1605.03191><http://dx.doi.org/10.1093/mnras/stw1115><http://mnras.oxfordjournals.org/lookup/doi/10.1093/mnras/stw1115>.
- Aird, J. et al. (Mar. 2017). X-rays across the galaxy population - I. Tracing the main sequence of star formation. 465.3, pp. 3390–3415. DOI: [10 . 1093/mnras/stw2932](https://doi.org/10.1093/mnras/stw2932). arXiv: [1611.03508](https://arxiv.org/abs/1611.03508) [astro-ph.GA].
- B  thermin, Matthieu et al. (Nov. 2017). The impact of clustering and angular resolution on far-infrared and millimeter continuum observations. 607, A89, A89. DOI: [10 . 1051/0004-6361/201730866](https://doi.org/10.1051/0004-6361/201730866). arXiv: [1703.08795](https://arxiv.org/abs/1703.08795) [astro-ph.GA].
- Forbes, Duncan A. (Nov. 2017). How large are the globular cluster systems of early-type galaxies and do they scale with galaxy halo properties? 472.1, pp. L104–L108. DOI: [10 . 1093/mnrasl/slx148](https://doi.org/10.1093/mnrasl/slx148). arXiv: [1710.01324](https://arxiv.org/abs/1710.01324) [astro-ph.GA].

- Hurley, P. D. et al. (Jan. 2017). HELP: XID+, the probabilistic de-blender for Herschel SPIRE maps. 464.1, pp. 885–896. DOI: [10.1093/mnras/stw2375](https://doi.org/10.1093/mnras/stw2375). arXiv: [1606.05770](https://arxiv.org/abs/1606.05770) [astro-ph.GA].
- Iodice, E. et al. (Apr. 2017). The Fornax Deep Survey with VST. II. Fornax A: A Two-phase Assembly Caught in the Act. 839.1, 21, p. 21. DOI: [10.3847/1538-4357/aa6846](https://doi.org/10.3847/1538-4357/aa6846). arXiv: [1703.07989](https://arxiv.org/abs/1703.07989) [astro-ph.GA].
- Leja, Joel et al. (Mar. 2017). Deriving Physical Properties from Broadband Photometry with Prospector: Description of the Model and a Demonstration of its Accuracy Using 129 Galaxies in the Local Universe. 837.2, 170, p. 170. DOI: [10.3847/1538-4357/aa5ffe](https://doi.org/10.3847/1538-4357/aa5ffe). arXiv: [1609.09073](https://arxiv.org/abs/1609.09073) [astro-ph.GA].
- Lo Faro, B. et al. (Dec. 2017). Characterizing the UV-to-NIR shape of the dust attenuation curve of IR luminous galaxies up to $z \sim 2$. 472.2, pp. 1372–1391. DOI: [10.1093/mnras/stx1901](https://doi.org/10.1093/mnras/stx1901). arXiv: [1707.09805](https://arxiv.org/abs/1707.09805) [astro-ph.GA].
- Luo, B. et al. (Jan. 2017). The Chandra Deep Field-South Survey: 7 Ms Source Catalogs. 228.1, 2, p. 2. DOI: [10.3847/1538-4365/228/1/2](https://doi.org/10.3847/1538-4365/228/1/2). arXiv: [1611.03501](https://arxiv.org/abs/1611.03501) [astro-ph.GA].
- Miettinen, O. et al. (Sept. 2017). An ALMA survey of submillimetre galaxies in the COSMOS field: Physical properties derived from energy balance spectral energy distribution modelling. 606, A17, A17. DOI: [10.1051/0004-6361/201730762](https://doi.org/10.1051/0004-6361/201730762). arXiv: [1707.00637](https://arxiv.org/abs/1707.00637) [astro-ph.GA].
- Trayford, James W. et al. (Sept. 2017). Optical colours and spectral indices of $z = 0.1$ eagle galaxies with the 3D dust radiative transfer code skirt. 470.1, pp. 771–799. DOI: [10.1093/mnras/stx1051](https://doi.org/10.1093/mnras/stx1051). arXiv: [1705.02331](https://arxiv.org/abs/1705.02331) [astro-ph.GA].
- Whitaker, Katherine E. et al. (Dec. 2017). The Constant Average Relationship between Dust-obscured Star Formation and Stellar Mass from $z = 0$ to $z = 2.5$. 850.2, 208, p. 208. DOI: [10.3847/1538-4357/aa94ce](https://doi.org/10.3847/1538-4357/aa94ce). arXiv: [1710.06872](https://arxiv.org/abs/1710.06872) [astro-ph.GA].
- Aihara, Hiroaki et al. (Jan. 2018). The Hyper Suprime-Cam SSP Survey: Overview and survey design. 70, S4, S4. DOI: [10.1093/pasj/psx066](https://doi.org/10.1093/pasj/psx066). arXiv: [1704.05858](https://arxiv.org/abs/1704.05858) [astro-ph.IM].
- Buat, V. et al. (Nov. 2018). Dust attenuation and H α emission in a sample of galaxies observed with Herschel at $0.6 < z < 1.6$. 619, A135, A135. DOI: [10.1051/0004-6361/201833841](https://doi.org/10.1051/0004-6361/201833841). arXiv: [1809.00161](https://arxiv.org/abs/1809.00161) [astro-ph.GA].
- Cantiello, Michele et al. (Apr. 2018). VEGAS-SSS. II. Comparing the globular cluster systems in NGC 3115 and NGC 1399 using VEGAS and FDS survey data. The quest for a common genetic heritage of globular cluster systems. 611, A93, A93. DOI: [10.1051/0004-6361/201730649](https://doi.org/10.1051/0004-6361/201730649). arXiv: [1711.00750](https://arxiv.org/abs/1711.00750) [astro-ph.GA].
- Duncan, Kenneth J. et al. (Jan. 2018). Photometric redshifts for the next generation of deep radio continuum surveys - I. Template fitting. 473.2, pp. 2655–2672. DOI: [10.1093/mnras/stx2536](https://doi.org/10.1093/mnras/stx2536). arXiv: [1709.09183](https://arxiv.org/abs/1709.09183) [astro-ph.GA].
- Elbaz, D. et al. (Aug. 2018). Starbursts in and out of the star-formation main sequence. 616, A110, A110. DOI: [10.1051/0004-6361/201732370](https://doi.org/10.1051/0004-6361/201732370). arXiv: [1711.10047](https://arxiv.org/abs/1711.10047) [astro-ph.GA].
- Leja, Joel et al. (Feb. 2018). Hot Dust in Panchromatic SED Fitting: Identification of Active Galactic Nuclei and Improved Galaxy Properties. 854.1, 62, p. 62. DOI: [10.3847/1538-4357/aaa8db](https://doi.org/10.3847/1538-4357/aaa8db). arXiv: [1709.04469](https://arxiv.org/abs/1709.04469) [astro-ph.GA].
- Małek, K. et al. (Nov. 2018). HELP: modelling the spectral energy distributions of Herschel detected galaxies in the ELAIS N1 field. 620, A50, A50. DOI: [10.1051/0004-6361/201833131](https://doi.org/10.1051/0004-6361/201833131). arXiv: [1809.00529](https://arxiv.org/abs/1809.00529) [astro-ph.GA].
- Pearson, W. J. et al. (July 2018). Main sequence of star forming galaxies beyond the Herschel confusion limit. 615, A146, A146. DOI: [10.1051/0004-6361/201832821](https://doi.org/10.1051/0004-6361/201832821). arXiv: [1804.03482](https://arxiv.org/abs/1804.03482) [astro-ph.GA].

- Pota, V. et al. (Dec. 2018). The Fornax Cluster VLT Spectroscopic Survey - I. VIMOS spectroscopy of compact stellar systems in the Fornax core region. 481.2, pp. 1744–1756. DOI: [10.1093/mnras/sty2149](https://doi.org/10.1093/mnras/sty2149). arXiv: [1803.03275](https://arxiv.org/abs/1803.03275) [astro-ph.GA].
- Ruiz, A. et al. (Oct. 2018). XMMPZCAT: A catalogue of photometric redshifts for X-ray sources. 618, A52, A52. DOI: [10.1051/0004-6361/201833117](https://doi.org/10.1051/0004-6361/201833117). arXiv: [1807.04526](https://arxiv.org/abs/1807.04526) [astro-ph.GA].
- Salim, Samir et al. (May 2018). Dust Attenuation Curves in the Local Universe: Demographics and New Laws for Star-forming Galaxies and High-redshift Analogs. 859.1, 11, p. 11. DOI: [10.3847/1538-4357/aabf3c](https://doi.org/10.3847/1538-4357/aabf3c). arXiv: [1804.05850](https://arxiv.org/abs/1804.05850) [astro-ph.GA].
- Salvato, M. et al. (Feb. 2018). Finding counterparts for all-sky X-ray surveys with NWAY: a Bayesian algorithm for cross-matching multiple catalogues. 473.4, pp. 4937–4955. DOI: [10.1093/mnras/stx2651](https://doi.org/10.1093/mnras/stx2651). arXiv: [1705.10711](https://arxiv.org/abs/1705.10711) [astro-ph.GA].
- Schreiber, C. et al. (Jan. 2018). Dust temperature and mid-to-total infrared color distributions for star-forming galaxies at $0 < z < 4$. 609, A30, A30. DOI: [10.1051/0004-6361/201731506](https://doi.org/10.1051/0004-6361/201731506). arXiv: [1710.10276](https://arxiv.org/abs/1710.10276) [astro-ph.GA].
- Silverman, J. D. et al. (Nov. 2018). The Molecular Gas Content and Fuel Efficiency of Starbursts at $z \sim 1.6$ with ALMA. 867.2, 92, p. 92. DOI: [10.3847/1538-4357/aae25e](https://doi.org/10.3847/1538-4357/aae25e). arXiv: [1810.01596](https://arxiv.org/abs/1810.01596) [astro-ph.GA].
- Siudek, M. et al. (Sept. 2018). The VIMOS Public Extragalactic Redshift Survey (VIPERS). The complexity of galaxy populations at $0.4 < z < 1.3$ revealed with unsupervised machine-learning algorithms. 617, A70, A70. DOI: [10.1051/0004-6361/201832784](https://doi.org/10.1051/0004-6361/201832784). arXiv: [1805.09904](https://arxiv.org/abs/1805.09904) [astro-ph.GA].
- Boquien, M. et al. (Feb. 2019). CIGALE: a python Code Investigating GALaxy Emission. 622, A103, A103. DOI: [10.1051/0004-6361/201834156](https://doi.org/10.1051/0004-6361/201834156). arXiv: [1811.03094](https://arxiv.org/abs/1811.03094) [astro-ph.GA].
- Buat, V. et al. (Dec. 2019). Cold dust and stellar emissions in dust-rich galaxies observed with ALMA: a challenge for SED-fitting techniques. 632, A79, A79. DOI: [10.1051/0004-6361/201936643](https://doi.org/10.1051/0004-6361/201936643).
- Caso, Juan P. et al. (Oct. 2019). Scaling relations for globular cluster systems in early-type galaxies. 488.4, pp. 4504–4519. DOI: [10.1093/mnras/stz2039](https://doi.org/10.1093/mnras/stz2039). arXiv: [1908.01807](https://arxiv.org/abs/1908.01807) [astro-ph.GA].
- Dey, Arjun et al. (May 2019). Overview of the DESI Legacy Imaging Surveys. 157.5, 168, p. 168. DOI: [10.3847/1538-3881/ab089d](https://doi.org/10.3847/1538-3881/ab089d). arXiv: [1804.08657](https://arxiv.org/abs/1804.08657) [astro-ph.IM].
- Fioc, Michel et al. (Mar. 2019). PÉGASE.3: A code for modeling the UV-to-IR/submm spectral and chemical evolution of galaxies with dust. 623, A143, A143. DOI: [10.1051/0004-6361/201833556](https://doi.org/10.1051/0004-6361/201833556). arXiv: [1902.07929](https://arxiv.org/abs/1902.07929) [astro-ph.GA].
- Iodice, E. et al. (2019). The Fornax Deep Survey with VST. V. Exploring the faintest regions of the bright early-type galaxies inside the virial radius. *Astronomy Astrophysics* 623, A1. ISSN: 0004-6361. DOI: [10.1051/0004-6361/201833741](https://doi.org/10.1051/0004-6361/201833741). arXiv: [1812.01050](https://arxiv.org/abs/1812.01050). URL: <https://www.aanda.org/10.1051/0004-6361/201833741><http://arxiv.org/abs/1812.01050><http://dx.doi.org/10.1051/0004-6361/201833741>.
- Ivezić, Željko et al. (Mar. 2019). LSST: From Science Drivers to Reference Design and Anticipated Data Products. 873.2, 111, p. 111. DOI: [10.3847/1538-4357/ab042c](https://doi.org/10.3847/1538-4357/ab042c). arXiv: [0805.2366](https://arxiv.org/abs/0805.2366) [astro-ph].
- Jin, Xiangyu et al. (May 2019). Chandra Detection of Intracluster X-Ray Sources in Fornax. 876.1, 53, p. 53. DOI: [10.3847/1538-4357/ab064f](https://doi.org/10.3847/1538-4357/ab064f). arXiv: [1902.03733](https://arxiv.org/abs/1902.03733) [astro-ph.GA].
- Kuijken, K. et al. (May 2019). The fourth data release of the Kilo-Degree Survey: ugr imaging and nine-band optical-IR photometry over 1000 square degrees. 625, A2, A2. DOI: [10.1051/0004-6361/201834918](https://doi.org/10.1051/0004-6361/201834918). arXiv: [1902.11265](https://arxiv.org/abs/1902.11265) [astro-ph.GA].

- Meisner, A. M. et al. (Dec. 2019). unWISE Coadds: The Five-year Data Set. 131.1006, p. 124504. DOI: [10.1088/1538-3873/ab3df4](https://doi.org/10.1088/1538-3873/ab3df4). arXiv: [1909.05444](https://arxiv.org/abs/1909.05444) [astro-ph.IM].
- Prole, D. J. et al. (Apr. 2019). Halo mass estimates from the globular cluster populations of 175 low surface brightness galaxies in the Fornax cluster. 484.4, pp. 4865–4880. DOI: [10.1093/mnras/stz326](https://doi.org/10.1093/mnras/stz326). arXiv: [1901.09648](https://arxiv.org/abs/1901.09648) [astro-ph.GA].
- Shirley, Raphael et al. (Nov. 2019). HELP: a catalogue of 170 million objects, selected at 0.36–4.5 μm , from 1270 deg^2 of prime extragalactic fields. 490.1, pp. 634–656. DOI: [10.1093/mnras/stz2509](https://doi.org/10.1093/mnras/stz2509). arXiv: [1909.04003](https://arxiv.org/abs/1909.04003) [astro-ph.GA].
- Venhola, Aku et al. (May 2019). The Fornax Deep Survey (FDS) with VST. VI. Optical properties of the dwarf galaxies in the Fornax cluster. 625, A143, A143. DOI: [10.1051/0004-6361/201935231](https://doi.org/10.1051/0004-6361/201935231). arXiv: [1904.08660](https://arxiv.org/abs/1904.08660) [astro-ph.GA].
- Bogdanoska, Jana et al. (Aug. 2020). UV dust attenuation as a function of stellar mass and its evolution with redshift. 496.4, pp. 5341–5349. DOI: [10.1093/mnras/staa1928](https://doi.org/10.1093/mnras/staa1928). arXiv: [2006.16700](https://arxiv.org/abs/2006.16700) [astro-ph.GA].
- Cantiello, Michele et al. (July 2020). The Fornax Deep Survey with VST. IX. Catalog of sources in the FDS area with an example study for globular clusters and background galaxies. 639, A136, A136. DOI: [10.1051/0004-6361/202038137](https://doi.org/10.1051/0004-6361/202038137). arXiv: [2005.12085](https://arxiv.org/abs/2005.12085) [astro-ph.GA].
- Donevski, D. et al. (Dec. 2020). In pursuit of giants. I. The evolution of the dust-to-stellar mass ratio in distant dusty galaxies. 644, A144, A144. DOI: [10.1051/0004-6361/202038405](https://doi.org/10.1051/0004-6361/202038405). arXiv: [2008.09995](https://arxiv.org/abs/2008.09995) [astro-ph.GA].
- Kouroumpatzakis, K. et al. (June 2020). Sub-galactic scaling relations between X-ray luminosity, star formation rate, and stellar mass. 494.4, pp. 5967–5984. DOI: [10.1093/mnras/staa1063](https://doi.org/10.1093/mnras/staa1063). arXiv: [2004.09873](https://arxiv.org/abs/2004.09873) [astro-ph.GA].
- Merloni, Andrea et al. (June 2020). eROSITA's X-ray eyes on the Universe. *Nature Astronomy* 4, pp. 634–636. DOI: [10.1038/s41550-020-1133-0](https://doi.org/10.1038/s41550-020-1133-0).
- Yang, G. et al. (Jan. 2020). X-CIGALE: Fitting AGN/galaxy SEDs from X-ray to infrared. 491.1, pp. 740–757. DOI: [10.1093/mnras/stz3001](https://doi.org/10.1093/mnras/stz3001). arXiv: [2001.08263](https://arxiv.org/abs/2001.08263) [astro-ph.GA].
- Predehl, P. et al. (Mar. 2021). The eROSITA X-ray telescope on SRG. 647, A1, A1. DOI: [10.1051/0004-6361/202039313](https://doi.org/10.1051/0004-6361/202039313). arXiv: [2010.03477](https://arxiv.org/abs/2010.03477) [astro-ph.HE].
- Riccio, G. et al. (Sept. 2021). Preparing for LSST data. Estimating the physical properties of $z < 2.5$ main-sequence galaxies. 653, A107, A107. DOI: [10.1051/0004-6361/202140854](https://doi.org/10.1051/0004-6361/202140854). arXiv: [2106.12573](https://arxiv.org/abs/2106.12573) [astro-ph.GA].
- Shirley, R. et al. (Oct. 2021). HELP: the Herschel Extragalactic Legacy Project. 507.1, pp. 129–155. DOI: [10.1093/mnras/stab1526](https://doi.org/10.1093/mnras/stab1526). arXiv: [2105.05659](https://arxiv.org/abs/2105.05659) [astro-ph.GA].
- Sunyaev, R. et al. (Dec. 2021). SRG X-ray orbital observatory. Its telescopes and first scientific results. 656, A132, A132. DOI: [10.1051/0004-6361/202141179](https://doi.org/10.1051/0004-6361/202141179). arXiv: [2104.13267](https://arxiv.org/abs/2104.13267) [astro-ph.HE].
- Torbaniuk, O. et al. (Sept. 2021). The connection between star formation and supermassive black hole activity in the local Universe. 506.2, pp. 2619–2637. DOI: [10.1093/mnras/stab1794](https://doi.org/10.1093/mnras/stab1794). arXiv: [2106.11079](https://arxiv.org/abs/2106.11079) [astro-ph.GA].
- Weaver, J. R. et al. (Jan. 2021). COSMOS2020: A next-generation catalog to explore the $1 < z < 8$ universe. *American Astronomical Society Meeting Abstracts*. Vol. 53. American Astronomical Society Meeting Abstracts, 215.06, p. 215.06.
- Brunner, H. et al. (May 2022). The eROSITA Final Equatorial Depth Survey (eFEDS). X-ray catalogue. 661, A1, A1. DOI: [10.1051/0004-6361/202141266](https://doi.org/10.1051/0004-6361/202141266). arXiv: [2106.14517](https://arxiv.org/abs/2106.14517) [astro-ph.HE].
- Euclid Collaboration et al. (June 2022). Euclid preparation. I. The Euclid Wide Survey. 662, A112, A112. DOI: [10.1051/0004-6361/202141938](https://doi.org/10.1051/0004-6361/202141938). arXiv: [2108.01201](https://arxiv.org/abs/2108.01201) [astro-ph.CO].

- Figueira, M. et al. (Nov. 2022). SFR estimations from $z = 0$ to $z = 0.9$. A comparison of SFR calibrators for star-forming galaxies. 667, A29, A29. DOI: [10.1051/0004-6361/202141701](https://doi.org/10.1051/0004-6361/202141701). arXiv: [2209.04390](https://arxiv.org/abs/2209.04390) [astro-ph.GA].
- Liu, Teng et al. (May 2022). The eROSITA Final Equatorial-Depth Survey (eFEDS). The AGN catalog and its X-ray spectral properties. 661, A5, A5. DOI: [10.1051/0004-6361/202141643](https://doi.org/10.1051/0004-6361/202141643). arXiv: [2106.14522](https://arxiv.org/abs/2106.14522) [astro-ph.HE].
- Mountrichas, G. et al. (July 2022). Comparison of the star formation in X-ray-selected AGN in eFEDS with that of star-forming galaxies. 663, A130, A130. DOI: [10.1051/0004-6361/202243254](https://doi.org/10.1051/0004-6361/202243254). arXiv: [2205.01451](https://arxiv.org/abs/2205.01451) [astro-ph.GA].
- Pistis, F. et al. (July 2022). The fundamental metallicity relation from SDSS ($z \sim 0$) to VIPERS ($z \sim 0.7$). Data selection or evolution. 663, A162, A162. DOI: [10.1051/0004-6361/202142430](https://doi.org/10.1051/0004-6361/202142430). arXiv: [2206.02458](https://arxiv.org/abs/2206.02458) [astro-ph.GA].
- Ramos Padilla, Andrés F. et al. (Feb. 2022). The viewing angle in AGN SED models: a data-driven analysis. 510.1, pp. 687–707. DOI: [10.1093/mnras/stab3486](https://doi.org/10.1093/mnras/stab3486). arXiv: [2108.10899](https://arxiv.org/abs/2108.10899) [astro-ph.GA].
- Riccio, G. et al. (Aug. 2022). Properties of intra-cluster low-mass X-ray binaries in Fornax globular clusters. 664, A41, A41. DOI: [10.1051/0004-6361/202142894](https://doi.org/10.1051/0004-6361/202142894). arXiv: [2206.14207](https://arxiv.org/abs/2206.14207) [astro-ph.HE].
- Salvato, M. et al. (May 2022). The eROSITA Final Equatorial-Depth Survey (eFEDS). Identification and characterization of the counterparts to point-like sources. 661, A3, A3. DOI: [10.1051/0004-6361/202141631](https://doi.org/10.1051/0004-6361/202141631). arXiv: [2106.14520](https://arxiv.org/abs/2106.14520) [astro-ph.HE].
- Suleiman, Nofoz et al. (Oct. 2022). The statistical properties of 28 IR-bright dust-obscured galaxies and SED modelling using CIGALE. 74.5, pp. 1157–1185. DOI: [10.1093/pasj/psac061](https://doi.org/10.1093/pasj/psac061).
- Vulic, N. et al. (May 2022). The eROSITA Final Equatorial-Depth Survey (eFEDS). Presenting the demographics of X-ray emission from normal galaxies. 661, A16, A16. DOI: [10.1051/0004-6361/202141641](https://doi.org/10.1051/0004-6361/202141641). arXiv: [2106.14526](https://arxiv.org/abs/2106.14526) [astro-ph.GA].
- Yang, Guang et al. (Mar. 2022). Fitting AGN/Galaxy X-Ray-to-radio SEDs with CIGALE and Improvement of the Code. 927.2, 192, p. 192. DOI: [10.3847/1538-4357/ac4971](https://doi.org/10.3847/1538-4357/ac4971). arXiv: [2201.03718](https://arxiv.org/abs/2201.03718) [astro-ph.GA].
- Hamed, M. et al. (Apr. 2023). The slippery slope of dust attenuation curves: Correlation of dust attenuation laws with star-to-dust compactness up to $z = 4$. arXiv e-prints, arXiv:2304.13713, arXiv:2304.13713. DOI: [10.48550/arXiv.2304.13713](https://doi.org/10.48550/arXiv.2304.13713). arXiv: [2304.13713](https://arxiv.org/abs/2304.13713) [astro-ph.GA].
- Pacifici, Camilla et al. (Feb. 2023). The Art of Measuring Physical Parameters in Galaxies: A Critical Assessment of Spectral Energy Distribution Fitting Techniques. 944.2, 141, p. 141. DOI: [10.3847/1538-4357/acacff](https://doi.org/10.3847/1538-4357/acacff). arXiv: [2212.01915](https://arxiv.org/abs/2212.01915) [astro-ph.GA].